
Director-based continuum modeling and analysis of damage mechanics and coupled micro-magneto-mechanics

Dissertation

by Christian Dorn
from Pfaffenhofen a.d.Ilm

in partial fulfillment of the requirements for the degree of
Doctor of Engineering (Dr.-Ing.)

submitted to the Faculty of Engineering of
Kiel University

Examiners:	Prof. Dr.-Ing. Stephan Wulfinghoff Prof. Dr.-Ing. Marc-André Keip
------------	--

Date of submission:	31.01.2024
---------------------	------------

Date of oral examination:	30.10.2024
---------------------------	------------

Eidesstattliche Erklärung

Ich versichere hiermit an Eides statt, dass ich die vorliegende Dissertation nach Inhalt und Form eigenständig verfasst habe. Ich habe dabei keine unzulässige fremde Hilfe erhalten und keine anderen als die angegebenen Quellen und Hilfsmittel verwendet. Die Arbeit hat bisher weder ganz noch teilweise einer anderen Stelle im Rahmen eines Prüfungsverfahrens vorgelegen. In Teilen wurde der Inhalt der vorliegenden Arbeit bereits in wissenschaftlichen Publikationen veröffentlicht. Letzteres ist an den relevanten Stellen in der Arbeit kenntlich gemacht. Die Arbeit ist nach bestem Wissen und Gewissen im Einklang mit den Regeln guter wissenschaftlicher Praxis der Deutschen Forschungsgemeinschaft entstanden. Mir wurde kein akademischer Grad entzogen.

Kiel, den 31.01.2024

Christian Dorn

Acknowledgments

Before delving into the contents of the present dissertation, I want to take a moment to thank everyone who directly or indirectly contributed to this work, supported it or made it possible in one way or another.

First and foremost, I owe deep thanks and gratitude to my supervisor and mentor Prof. Dr.-Ing. Stephan Wulfinghoff. To put it briefly and succinctly, I just learned a lot from him. In particular, he really helped me understand how the finite element method works and sharpened my focus for understanding what happens in a material (model). Furthermore, he gave me both freedom to pursue my own plans and ideas as well as and guidance in difficult situations to get myself out of tight spots. I am deeply grateful that Stephan accepted me into his working group at one of the most difficult times of my early career.

Furthermore, credit is due to my colleagues from CRC 1261 *Magnetoelectric Sensors: From Composite Materials to Biomagnetic Diagnostics* for great discussions, scientific exchange and valuable input to motivate and advance my work.

I am thrilled and grateful that Prof. Dr.-Ing. Marc-André Keip agreed to be the second reviewer for the present thesis.

When I was new to Kiel and Kiel university, Marian Hörsting showed me how everything works. I really appreciate the great scientific and technical conversations we had, for example, about where to find tiny details in our code and the best ways to improve them. Furthermore, I thoroughly enjoyed our *thinker's pauses* at the billiard table.

I would also like to thank my colleagues Jan Dittmann, Muhammad Babar Shamim and Hauke Goldbeck for the great time in the office. We had many amusing conversations, for example, on the multiple occasions of Jan *deciding* to leave his coffee utensils in the office.

Finally, I want to thank my family and in particular my parents for their love and support not just during my studies but throughout my entire life.

Zusammenfassung

Komplexes Materialverhalten beinhaltet häufig eine lokale Materialorientierung, die sich zeitabhängig verändert. Ein Beispiel für eine solche Orientierung ist die Magnetisierungsrichtung in magnetischen Materialien. Um dieses Materialverhalten in einem Kontinuumsmodell abzubilden, wird jeder Punkt des Materials (beschrieben durch einen Ortsvektor) zusätzlich mit einer Orientierung und zugehörigen Bilanzgleichungen ausgestattet. In vielen Fällen kann die besagte Orientierung durch einen Einheitsvektor (*Direktor* genannt) dargestellt werden, der nur Richtungs-, aber keine Betragsinformation enthält. Das Beschränken des Orientierungsvektors auf eine konstante Länge ist eine numerisch herausfordernde Nebenbedingung. Mit der vorliegenden Dissertation soll ein Beitrag zur Weiterentwicklung der Materialmodellierung und –simulation mithilfe von Direktoren geleistet werden. Dieser Beitrag soll sich insbesondere in den Bereich der Modellierung magnetischer Materialien mit Kontinuumsmodellen (sowohl numerisch als auch analytisch) erstrecken.

Die vorliegende Dissertation ist als kumulative Arbeit angelegt und umfasst zwei begutachtete Publikationen (Publikationen 1 und 2) sowie ein zur Veröffentlichung vorbereitetes Manuskript (Manuskript 3). Wir beginnen mit einer kurzen Einführung in unsere Auffassung von Kontinuumsmodellen mit einem Direktor. Neben der Einführung grundlegender Zusammenhänge diskutieren wir auch Beispiele für Materialmodelle mit einem Direktor sowie Beispiele für numerische Strategien zur Umsetzung der Norm–Nebenbedingung für Direktoren. Anschließend werden die zwei Publikationen und das Manuskript vorgestellt.

In der ersten begutachteten Publikation wird ein gradientenerweitertes Phasenfeldmodell für Schädigung im Rahmen der generalisierten Standardmaterialien entwickelt. Um die schädigungsbedingte Zug–Druck–Asymmetrie zu behandeln und um anisotropes Rissverhalten abbilden zu können, wird das Phasenfeldmodell durch ein Rissorientierungsvektorfeld erweitert. Letzteres wird als Feld von Einheitsvektoren eingeführt, die wir als Direktoren betrachten. Wir erreichen eine normerhaltende Aktualisierung des Rissorientierungsdirektors mithilfe der Exponentialabbildung.

Der Fokus der zweiten begutachteten Publikation liegt auf numerischen Techniken für ein gekoppeltes Modell, welches mikromagnetisches und linear elastisches Materialverhalten bei kleinen Deformationen umfasst. Abseits der numerischen Techniken, dreht sich die Publikation um die Untersuchung des Barkhausenrauschens. Der im mikromagnetischen Modell beinhaltete Magnetisierungsvektor wird als Einheitsvektor angenommen und wir betrachten diesen als Direktor. Wir erfüllen die Norm–Nebenbedingung mithilfe der Exponentialabbildung in Kombination mit dem normerhaltenden modifizierten Crank–Nicolson Zeitintegrationsverfahren, welches die Fehlerordnung zwei aufweist.

Das letzte Manuskript (zur Veröffentlichung vorbereitet) befasst sich ebenfalls mit der gekoppelten Mikromagnetomechanik. Der Schwerpunkt liegt auf einer Domänen (Sub–)Struktur, welche wir als *Wellung* bezeichnen. Es wird eine analytische Theorie entwickelt, um die Stabilität von Störungen in der magnetischen Mikrostruktur zu beurteilen, welche zu Wellungen

führen können. Im magnetischen Teil des Modells tritt der Magnetisierungsdirektor auf, welcher zunächst in Polarkoordinaten angegeben wird. Numerischen Techniken zur Normerhaltung sind in dieser Arbeit nicht von Interesse, da das rein analytische Modell nicht in einem numerischen Verfahren implementiert ist. Nach der Formulierung des Modells (Kontinuum mit Direktor), linearisieren wir die Magnetisierung um eine vorgegebene Richtung, um die Stabilitätsanalyse durchzuführen.

Abstract

Complex material behavior often involves a local material orientation that is subject to evolution over time. One example of such an orientation is the direction of magnetization in magnetic materials. To represent this behavior in a continuum model, each material point (described by a position vector) is additionally endowed with an orientation and associated balance equations. In many cases, the aforementioned orientation can be represented by a unit vector (called *director*) which only contains directional but no magnitude information. Enforcing the length of the orientation vector to remain constant is a numerically challenging constraint. The aim of the present dissertation is to contribute to the advancement of material modeling and simulation involving directors. In particular, this contribution is intended to stretch into the realm of modeling magnetic materials with continuum models (both numerically and analytically).

The dissertation at hand is organized as a cumulative thesis and comprises two peer-reviewed publications (publications 1 and 2) and a manuscript which has been prepared for publication (manuscript 3). We begin with a short introduction to our view on continuum models with a director. Besides introducing the fundamental relations, we also discuss examples of material models with a director as well as examples of numerical strategies to enforce the norm constraint of directors. Subsequently, the two publications and the manuscript are presented.

In the first peer-reviewed publication, a gradient-extended phase-field damage model is proposed using the framework of generalized standard materials. To approach the damage related tension-compression asymmetry and to enable the representation of anisotropic fracture behavior, the phase-field model is enhanced by a crack orientation vector field. The latter is introduced as a field of unit vectors which we consider as directors. We achieve the norm conserving update of the crack orientation director using the exponential map.

The focus of the second peer-reviewed publication is on numerical techniques for a coupled model including micromagnetics and small strain linear elasticity. Beyond the numerical techniques, the publication pivots on the investigation of Barkhausen noise. The magnetization vector included in the micromagnetic model is assumed to be a unit vector and we regard it as a director. We fulfill the norm constraint by means of the exponential map which is combined with the norm conserving and second order accurate modified Crank-Nicolson time integration scheme.

The last manuscript (prepared for publication) also deals with coupled micro-magneto-mechanics. The focus is on a domain (sub-)structure which we call *undulations*. An analytical theory is developed to assess the stability of perturbations in the magnetic microstructure which can lead to undulations. In the magnetic part of the model, the magnetization director occurs which is initially given in polar coordinates. Numerical techniques for norm conservation are not of interest in this work because the purely analytical model is not implemented in a numerical scheme. After the model setup (continuum with a director), we linearize the magnetization around a fixed direction to perform the stability analysis.

Contents

1	Introduction	1
1.1	The director continuum	1
1.2	Fundamental idea and kinematics	1
1.3	Thermodynamics perspective on the director continuum	3
1.4	Director continuum from the perspective of generalized standard materials . .	6
1.5	Examples of continuum models with a director	8
1.6	Examples of numerical treatment	9
1.7	Properties of the exponential map	10
1.8	Algorithmic approach using the exponential map	14
1.9	Relevance of the director continuum for the chapters of this thesis	15
2	Publication 1: A gradient–extended large–strain anisotropic damage model	17
2.1	Introduction	18
2.2	Kinematics	19
2.3	Formulation as a generalized standard material	23
2.4	Treatment of internal variables and linearization of residuals	28
2.4.1	Stationarity condition for internal variables \underline{c}	28
2.4.2	Traction free crack surface	29
2.4.3	Linearization of residual for internal variables \underline{c}	30
2.4.4	Stationarity condition for damage D	32
2.4.5	Linearization of residuals G_u , G_N and G_{D_χ}	34
2.5	Implementation and finite element method	37
2.6	Numerical experiments	39
2.6.1	Single notched edge test (SNET)	40
2.6.2	Double notched edge test (DNET)	45

2.6.3	Comparison to spectral tension–compression split	48
2.7	Summary and outlook	50
2.A	Primal and dual quantities	51
2.B	Recurring relations	52
2.C	Derivation and linearization of the residual G_u	54
2.D	Derivation and linearization of the residual G_N	58
2.E	Derivation and linearization of the residual G_{D_χ}	65
2.F	Linearization of the stationarity conditions for internal variables	67
3	Publication 2: Computing Barkhausen noise spectra	71
3.1	Introduction	72
3.2	Geometry, kinematics and boundary conditions	74
3.3	Generalized standard material formulation	76
3.4	Departure from the GSM framework to include precession	79
3.5	Implementation and finite element method	80
3.5.1	Overview	80
3.5.2	Time discretization	81
3.5.3	Magnetization magnitude in the Gauss points	82
3.5.4	Remarks on quadrature	82
3.6	Computing magnetic noise by ensemble averaging	83
3.7	Numerical examples	87
3.7.1	Software details and material parameters	87
3.7.2	Single element	88
3.7.3	Influence of precession on noise	90
3.7.4	Influence of surface roughness height on noise	92
3.7.5	Influence of inhomogeneous material properties on noise	94
3.7.6	Influence of inhomogeneous eigenstrain on noise	96
3.7.7	Remark on comparison with experiments	97
3.8	Summary and Outlook	98
3.A	Divergence theorem for a domain with singular surface	99
3.B	Accuracy of modified Crank–Nicolson scheme	99
3.C	Time and space discrete magnetization residual	103
3.D	Linearization of the time and space discrete magnetization residual	107
3.E	Fourier transform	113
4	Manuscript 3: Stability analysis of undulating magnetization states in thin films	115
4.1	Introduction	116
4.2	Kinematics	117
4.3	Potential formulation and stationarity conditions	119
4.3.1	Magnetic equilibrium	119

4.3.2	Magnetic non-equilibrium states	120
4.4	Linearization of the Landau–Lifshitz–Gilbert equation	120
4.5	Evaluation of the linear momentum balance	122
4.6	Stability analysis of the trivial solution for the coupled problem	125
4.7	An energetic view on stability	130
4.8	Results	132
4.8.1	Qualitative conclusions from the stability criterion	132
4.8.2	Stability maps	133
4.8.3	Undulation wavelength and stability limit of alignment constant . . .	135
4.9	Conclusion	136
4.A	Vanishing magnetic potential	137
5	Summary and outlook	139
	Bibliography	143

CHAPTER 1

Introduction

1.1 The director continuum

The common theme of all three publications in this thesis is the consideration of continuum models whose local material behavior is characterized by a unit vector (director). For brevity, we refer to such continuum models as *director continua*. Examples for directors are the crack orientation director (Publication 1) and the magnetization (Publication 2 and Manuscript 3). In the course of Chapter 1, we will discuss further examples of such continuum models. Furthermore, we will illustrate a particular challenge arising from the director (unit constraint) and how this challenge can be approached numerically. Special attention will be devoted to one of the approaches, the exponential map. We start by giving a short introduction to our view on what we call the director continuum.

1.2 Fundamental idea and kinematics

The idea of continua with a local orientation has occupied the mechanics community since the late 19th century, see, e.g., [1, 2]. Overviews on Cosserat-type and micropolar continua, in particular in the context of rods, plates and shells, can be found, e.g., in [3, 4]. In what we call a director continuum, each material point is characterized by a position vector $\mathbf{x} \in V$ and a local orientation $\{\mathbf{a}_1, \mathbf{a}_2, \mathbf{d}\}$, see Fig. 1.1. The three directions \mathbf{a}_1 , \mathbf{a}_2 and \mathbf{d} are orthonormal, i.e., in particular $\|\mathbf{d}\| = \|\mathbf{a}_i\| = 1$. The prominent director which determines the local material orientation is the distinguished direction \mathbf{d} . The perpendicular directions \mathbf{a}_1 and \mathbf{a}_2 are used to accompany \mathbf{d} but their specific orientation is not of profound

interest. To realize that \mathbf{a}_1 and \mathbf{a}_2 are of minor interest, consider a vector $\mathbf{b} = b_1\mathbf{a}_1 + b_2\mathbf{a}_2$,

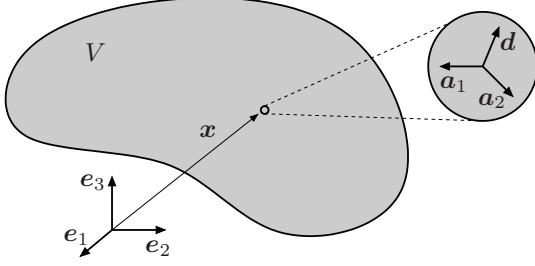


Fig. 1.1: Continuum consists of material points with a position vector $\mathbf{x} \in V$ and an orientation $\{\mathbf{a}_1, \mathbf{a}_2, \mathbf{d}\}$.

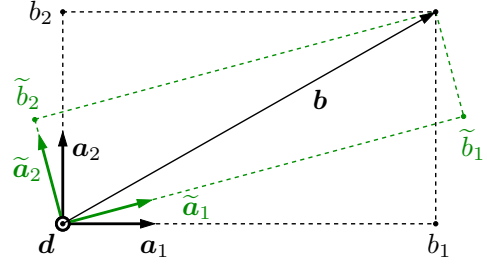


Fig. 1.2: Equivalent description of the vector \mathbf{b} in the systems $\{\mathbf{a}_1, \mathbf{a}_2, \mathbf{d}\}$ and $\{\tilde{\mathbf{a}}_1, \tilde{\mathbf{a}}_2, \mathbf{d}\}$.

perpendicular to \mathbf{d} . We can find $\{\tilde{\mathbf{a}}_1, \tilde{\mathbf{a}}_2\}$ with $(\tilde{b}_1, \tilde{b}_2)$ such that $\mathbf{b} = b_1\mathbf{a}_1 + b_2\mathbf{a}_2 = \tilde{b}_1\tilde{\mathbf{a}}_1 + \tilde{b}_2\tilde{\mathbf{a}}_2$, see Fig. 1.2. While the orientation of \mathbf{b} is unique, the orientation of $\{\mathbf{a}_1, \mathbf{a}_2\}$ is not. If we wanted to describe a rotation of the vector \mathbf{b} around the director \mathbf{d} , we could achieve this by rotating the system $\{\mathbf{a}_1, \mathbf{a}_2\}$ or by changing the coordinates (b_1, b_2) or both. To avoid this ambiguity, we require that drilling rotations of the system $\{\mathbf{a}_1, \mathbf{a}_2, \mathbf{d}\}$ around \mathbf{d} must vanish. The local orientation, as described above, could be considered as a surface with normal \mathbf{d} and non-unique (but predetermined) in-plane direction vectors $\{\mathbf{a}_1, \mathbf{a}_2\}$.

The field $\mathbf{d}(\mathbf{x}, t)$ associates with every point $\mathbf{x} \in V$ at every time $t \in [0, T]$ a unit vector $\mathbf{d} \in \mathcal{S}^2$, where the latter denotes the unit sphere in \mathbb{R}^3 . To ensure that the director \mathbf{d}

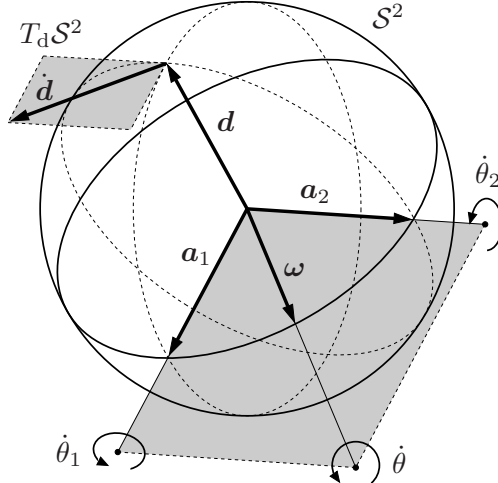


Fig. 1.3: Director \mathbf{d} on the unit sphere \mathcal{S}^2 , time derivative $\dot{\mathbf{d}}$ in tangent space $T_d\mathcal{S}^2$ and angular velocity vector $\dot{\theta}\boldsymbol{\omega} = (\dot{\theta}_1\mathbf{a}_1 + \dot{\theta}_2\mathbf{a}_2) \perp \mathbf{d}$.

remains on the unit sphere, its time derivative $\dot{\mathbf{d}}$ is required to be perpendicular to \mathbf{d} , i.e., $\dot{\mathbf{d}} \in T_d\mathcal{S}^2$, where the latter denotes the tangent space on \mathcal{S}^2 which is spanned by \mathbf{a}_1 and \mathbf{a}_2 , see Fig. 1.3. We express the change of the director \mathbf{d} using the angular velocity vector $\dot{\theta}\boldsymbol{\omega}$

$$(\|\boldsymbol{\omega}\| = 1)$$

$$\dot{\mathbf{d}} = \dot{\theta} \boldsymbol{\omega} \times \mathbf{d} . \quad (1.1)$$

Note that, with a little abuse of notation, we denote the angular velocity vector by $\dot{\theta} \boldsymbol{\omega}$. We choose the notation with separated magnitude $\dot{\theta}$ and direction $\boldsymbol{\omega}$ since this simplifies the exposition later on, see, e.g., Section 1.7. The angle θ strictly speaking does not exist because the angular velocity $\dot{\theta}$ would continuously increase it (even beyond the limits of $[0, 2\pi)$). As mentioned above, we require drilling rotations around the director \mathbf{d} to vanish, i.e., $\dot{\theta} \boldsymbol{\omega} \perp \mathbf{d}$ or equivalently

$$\dot{\theta} \boldsymbol{\omega} = \dot{\theta}_1 \mathbf{a}_1 + \dot{\theta}_2 \mathbf{a}_2 . \quad (1.2)$$

The relation in Eq.(1.1) applies to all three orientation vectors $\{\dot{\mathbf{a}}_1, \dot{\mathbf{a}}_2, \dot{\mathbf{d}}\} = \dot{\theta} \boldsymbol{\omega} \times \{\mathbf{a}_1, \mathbf{a}_2, \mathbf{d}\}$.

1.3 Thermodynamics perspective on the director continuum

We start with the dissipation inequality, cf., e.g., [5],

$$\mathcal{D} = \mathcal{P} - \dot{\Psi} \geq 0 , \quad (1.3)$$

where \mathcal{D} denotes dissipation, \mathcal{P} describes the power of external forces, $\dot{\Psi} = \int_V \dot{\psi} dv$ denotes the rate of the free energy, and ψ is the free energy density per unit volume. For details on the thermodynamic underpinnings, see, e.g., [6, 7, 8, 9]. In the case with vanishing dissipation, the material stores all of the external power ($\dot{\Psi} = \mathcal{P}$). By contrast, in the (more realistic) case including dissipation, the material can only store less ($\dot{\Psi} < \mathcal{P}$). The difference between external power \mathcal{P} and storage rate $\dot{\Psi}$ is dissipated and must, in general, be greater or equal to zero $\mathcal{D} = \mathcal{P} - \dot{\Psi} \geq 0$.

We consider two contributions to the power of external forces $\mathcal{P} = \mathcal{P}_t + \mathcal{P}_\Xi$ related to displacement \mathbf{u} and the director \mathbf{d} . For the power of mechanical forces, we write

$$\mathcal{P}_t = \int_{\partial V_t} \dot{\mathbf{u}} \cdot \bar{\mathbf{t}} da \quad \text{with} \quad \bar{\mathbf{t}} = \boldsymbol{\sigma} \mathbf{n} , \quad (1.4)$$

where the latter relation is an assumption (Cauchy's theorem). In Eq. (1.4), $\bar{\mathbf{t}}$ denotes the traction vector, $\boldsymbol{\sigma}$ is the Cauchy stress tensor, \mathbf{n} refers to the exterior normal of the material volume V and the boundary $\partial V = \partial V_t \cup \partial V_u$ is decomposed into a Neumann and a Dirichlet part. In analogy, we assume for the external power related to the director \mathbf{d}

$$\mathcal{P}_\Xi = \int_{\partial V_\Xi} \dot{\mathbf{d}} \cdot \bar{\boldsymbol{\Xi}} da \quad \text{with} \quad \bar{\boldsymbol{\Xi}} = \boldsymbol{\xi} \mathbf{n} , \quad (1.5)$$

where $\bar{\Xi}$ and ξ are the generalized stress vector and microstress dual to \mathbf{d} in the sense of [5]. Again, the boundary $\partial V = \partial V_{\Xi} \cup \partial V_d$ is decomposed into a Neumann and a Dirichlet part. Assuming $\dot{\mathbf{u}} = \mathbf{0}$ on ∂V_u and $\dot{\mathbf{d}} = \mathbf{0}$ on ∂V_d (to not violate the Dirichlet boundary conditions), we obtain

$$\mathcal{D} = \int_{\partial V} (\boldsymbol{\sigma}^\top \dot{\mathbf{u}}) \cdot \mathbf{n} \, da + \int_{\partial V} (\xi^\top \dot{\mathbf{d}}) \cdot \mathbf{n} \, da - \dot{\Psi} \geq 0 , \quad (1.6)$$

which reads with divergence theorem

$$\mathcal{D} = \int_V \left\{ \dot{\mathbf{u}} \cdot \operatorname{div}(\boldsymbol{\sigma}) + \boldsymbol{\sigma} : \operatorname{grad}(\dot{\mathbf{u}}) + \dot{\mathbf{d}} \cdot \operatorname{div}(\xi) + \xi : \operatorname{grad}(\dot{\mathbf{d}}) - \dot{\psi} \right\} dv \geq 0 . \quad (1.7)$$

The former inequality has to hold not only for the volume V but for every subvolume. By decreasing the subvolume size to a point, we can argue that the following dissipation inequality has to hold locally

$$\dot{\mathbf{u}} \cdot \operatorname{div}(\boldsymbol{\sigma}) + \boldsymbol{\sigma} : \operatorname{grad}(\dot{\mathbf{u}}) + \dot{\mathbf{d}} \cdot \operatorname{div}(\xi) + \xi : \operatorname{grad}(\dot{\mathbf{d}}) - \dot{\psi} \geq 0 . \quad (1.8)$$

In the following, we use that the Cauchy stress tensor $\boldsymbol{\sigma}$ is symmetric and hence we write for simplicity of exposition $\boldsymbol{\sigma} : \operatorname{grad}(\dot{\mathbf{u}}) = \boldsymbol{\sigma} : \dot{\boldsymbol{\varepsilon}}$. The quantity $\boldsymbol{\varepsilon}$ denotes the strain tensor (symmetric part of the displacement gradient). We model the material behavior using the free energy density ψ according to

$$\psi = \psi(\boldsymbol{\varepsilon}, \mathbf{d}, \operatorname{grad}(\mathbf{d})) , \quad (1.9)$$

where ψ cannot depend on the displacement \mathbf{u} or on the skew symmetric part of the displacement gradient $\operatorname{skw}(\operatorname{grad}(\mathbf{u}))$ for objectivity reasons. For the dissipation inequality, Eq. (1.8), we obtain

$$\dot{\mathbf{u}} \cdot \operatorname{div}(\boldsymbol{\sigma}) + \left(\boldsymbol{\sigma} - \frac{\partial \psi}{\partial \boldsymbol{\varepsilon}} \right) : \dot{\boldsymbol{\varepsilon}} + \left(\xi - \frac{\partial \psi}{\partial \operatorname{grad}(\mathbf{d})} \right) : \operatorname{grad}(\dot{\mathbf{d}}) + \left(\operatorname{div}(\xi) - \frac{\partial \psi}{\partial \mathbf{d}} \right) \cdot \dot{\mathbf{d}} \geq 0 . \quad (1.10)$$

Applying the Coleman–Noll procedure [6], we obtain from the first three terms in Eq. (1.10)

$$\operatorname{div}(\boldsymbol{\sigma}) = \mathbf{0} , \quad \boldsymbol{\sigma} = \frac{\partial \psi}{\partial \boldsymbol{\varepsilon}} , \quad \xi = \frac{\partial \psi}{\partial \operatorname{grad}(\mathbf{d})} . \quad (1.11)$$

The remaining dissipation inequality is subject to the kinematic constraint $\dot{\mathbf{d}} = \dot{\boldsymbol{\theta}} \boldsymbol{\omega} \times \mathbf{d}$, see Eq. (1.1), which yields (using the relation $\mathbf{a} \cdot (\mathbf{b} \times \mathbf{c}) = \mathbf{b} \cdot (\mathbf{c} \times \mathbf{a}) = \mathbf{c} \cdot (\mathbf{a} \times \mathbf{b})$)

$$\dot{\boldsymbol{\theta}} \boldsymbol{\omega} \cdot \left[\mathbf{d} \times \left(\operatorname{div}(\xi) - \frac{\partial \psi}{\partial \mathbf{d}} \right) \right] = \dot{\boldsymbol{\theta}} \boldsymbol{\omega} \cdot \mathbf{T} \geq 0 . \quad (1.12)$$

We interpret the quantity $\mathbf{T} = \mathbf{d} \times (\operatorname{div}(\boldsymbol{\xi}) - \partial\psi/\partial\mathbf{d})$ as the dissipative driving force conjugate to $\dot{\boldsymbol{\omega}}$. To proceed, we make the constitutive assumption that a convex and differentiable dual dissipation potential $\phi^*(\mathbf{T})$ exists such that

$$\dot{\boldsymbol{\omega}} = \frac{\partial\phi^*(\mathbf{T})}{\partial\mathbf{T}} . \quad (1.13)$$

Since ϕ^* is convex, the remaining dissipation inequality Eq. (1.12) is automatically fulfilled

$$\mathbf{T} \cdot \dot{\boldsymbol{\omega}} = \mathbf{T} \cdot \frac{\partial\phi^*(\mathbf{T})}{\partial\mathbf{T}} \geq 0 , \quad (1.14)$$

see [10] (and hence the second law of thermodynamics is automatically fulfilled). A one-dimensional illustration is given in Fig. 1.4. The Legendre transform of the dual dissipation

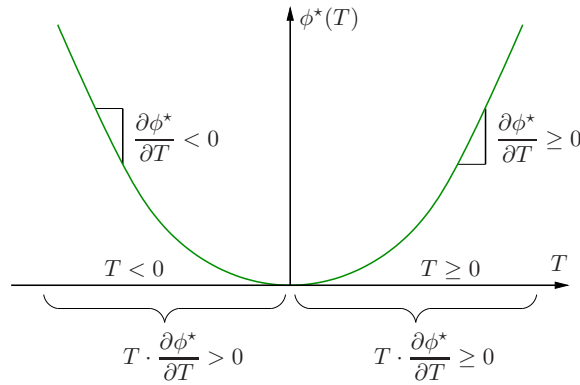


Fig. 1.4: The convex dual dissipation potential $\phi^*(\mathbf{T})$ ensures vanishing or positive dissipation (one-dimensional sketch).

potential $\phi^*(\mathbf{T})$ reads

$$\phi(\dot{\boldsymbol{\omega}}) = \sup_{\mathbf{T}} \left\{ \mathbf{T} \cdot \dot{\boldsymbol{\omega}} - \phi^*(\mathbf{T}) \right\} \quad (1.15)$$

and we compute the corresponding derivative according to

$$\frac{\partial\phi}{\partial\dot{\boldsymbol{\omega}}} = \mathbf{T} , \quad (1.16)$$

see [10]. Typically, the dissipation potential ϕ is formulated in $\dot{\mathbf{d}}$ rather than $\dot{\boldsymbol{\omega}}$ (e.g., $\phi \sim \|\dot{\mathbf{d}}\|^2$, easier to interpret). From this formulation, we obtain with Eq. (1.1)

$$\mathbf{T} = \frac{\partial\phi}{\partial\dot{\boldsymbol{\omega}}} = \frac{\partial\phi}{\partial\dot{\mathbf{d}}} \cdot \frac{\partial\dot{\mathbf{d}}}{\partial\dot{\boldsymbol{\omega}}} = \frac{\partial\phi}{\partial\dot{\mathbf{d}}} \cdot \boldsymbol{\epsilon} \cdot \mathbf{d} = \mathbf{d} \times \frac{\partial\phi}{\partial\dot{\mathbf{d}}} , \quad (1.17)$$

where ϵ denotes the third order permutation tensor. The original relation for the dissipative driving force \mathbf{T} in Eq. (1.12) together with the relation in Eq. (1.17) yields

$$\mathbf{d} \times \left(\operatorname{div}(\boldsymbol{\xi}) - \frac{\partial \psi}{\partial \mathbf{d}} - \frac{\partial \phi}{\partial \dot{\mathbf{d}}} \right) = \mathbf{0} \quad (1.18)$$

which can be interpreted as a kinematically constrained version of a microforce balance, cf. [5]. To summarize, in a thermodynamically consistent model of the director continuum, the material is governed by the following set of equations

$$\mathbf{0} = \operatorname{div}(\boldsymbol{\sigma}) , \quad \boldsymbol{\sigma} = \frac{\partial \psi}{\partial \boldsymbol{\epsilon}} , \quad (1.19)$$

$$\mathbf{0} = \mathbf{d} \times \left(\operatorname{div}(\boldsymbol{\xi}) - \frac{\partial \psi}{\partial \mathbf{d}} - \frac{\partial \phi}{\partial \dot{\mathbf{d}}} \right) , \quad \boldsymbol{\xi} = \frac{\partial \psi}{\partial \operatorname{grad}(\mathbf{d})} . \quad (1.20)$$

Note that, while the mechanical and the director-related problem are coupled due to constitutive assumptions (i.e., due to the choice $\psi(\boldsymbol{\epsilon}, \mathbf{d}, \operatorname{grad}(\mathbf{d}))$) and therefore influence each other, they do not contribute to each other's balance equations explicitly (beyond the constitutive relations). In particular, the director-related microforce is not a mechanical force and hence does not occur in the linear or angular momentum balance as an additional contribution. A dedicated evaluation of the angular momentum balance (as for polar continua) is not necessary.

1.4 Director continuum from the perspective of generalized standard materials

An equivalent description to Sec. 1.3, resulting in the same set of governing equations, can be obtained by considering the potential

$$\Pi = \dot{\Psi} + \Phi - \mathcal{P} \quad \text{with} \quad \Phi = \int_V \phi \, dv \quad (1.21)$$

and computing the associated stationary points (see below). This thermodynamically consistent description of a material (i.e., dissipation $\mathcal{D} \geq 0$) using the rate potential Π is the core idea behind the *generalized standard material* [11] and the *standard dissipative solid* [10] (subsequently referred to as GSM). In the following, we briefly outline this approach for a director continuum.

The process starts by formulating the rate potential

$$\Pi = \int_V \dot{\psi} + \phi \, dv - \int_{\partial V_t} \bar{\mathbf{t}} \cdot \dot{\mathbf{u}} \, da - \int_{\partial V_\Xi} \bar{\boldsymbol{\Xi}} \cdot \dot{\mathbf{d}} \, da \quad (1.22)$$

with prescribed tractions $\bar{\mathbf{t}}$ and $\bar{\mathbf{\Xi}}$ on the respective boundaries. To compute the following stationary points

$$\int_V \frac{\partial \psi}{\partial \boldsymbol{\varepsilon}} : \dot{\boldsymbol{\varepsilon}} + \frac{\partial \psi}{\partial \dot{\mathbf{d}}} \cdot \dot{\mathbf{d}} + \frac{\partial \psi}{\partial \text{grad}(\dot{\mathbf{d}})} : \text{grad}(\dot{\mathbf{d}}) + \phi(\dot{\mathbf{d}}) dv - \int_{\partial V_t} \bar{\mathbf{t}} \cdot \dot{\mathbf{u}} da - \int_{\partial V_\Xi} \bar{\mathbf{\Xi}} \cdot \dot{\mathbf{d}} da \longrightarrow_{\dot{\mathbf{u}}, \dot{\mathbf{d}}} \text{stat} ,$$

we first set the variational derivative w.r.t. $\dot{\mathbf{u}}$ to zero

$$\delta_{\dot{\mathbf{u}}} \Pi = 0 = \int_V \frac{\partial \psi}{\partial \boldsymbol{\varepsilon}} : \text{grad}(\delta \dot{\mathbf{u}}) dv - \int_{\partial V_t} \bar{\mathbf{t}} \cdot \delta \dot{\mathbf{u}} da . \quad (1.23)$$

Using divergence theorem, identifying $\boldsymbol{\sigma} = \partial \psi / \partial \boldsymbol{\varepsilon}$ and requiring the expression Eq. (1.23) to vanish for arbitrary variation $\delta \dot{\mathbf{u}}$, yields the same governing mechanical equations as in Sec. 1.3

$$\mathbf{0} = \text{div}(\boldsymbol{\sigma}) \quad \text{in } V, \quad \text{with} \quad \boldsymbol{\sigma} = \frac{\partial \psi}{\partial \boldsymbol{\varepsilon}} \quad (1.24)$$

and in addition the boundary condition

$$\boldsymbol{\sigma} \mathbf{n} = \bar{\mathbf{t}} \quad \text{on } \partial V_t . \quad (1.25)$$

After setting the variational derivative w.r.t. $\dot{\mathbf{d}}$ to zero

$$\delta_{\dot{\mathbf{d}}} \Pi = 0 = \int_V \frac{\partial \psi}{\partial \dot{\mathbf{d}}} \cdot \delta \dot{\mathbf{d}} + \frac{\partial \psi}{\partial \text{grad}(\dot{\mathbf{d}})} : \text{grad}(\delta \dot{\mathbf{d}}) + \frac{\partial \phi}{\partial \dot{\mathbf{d}}} \cdot \delta \dot{\mathbf{d}} dv - \int_{\partial V_\Xi} \bar{\mathbf{\Xi}} \cdot \delta \dot{\mathbf{d}} da , \quad (1.26)$$

we follow the same steps as in the mechanical case and again obtain the same governing equations as in Sec. 1.3

$$\mathbf{0} = \dot{\mathbf{d}} \times \left(\text{div}(\boldsymbol{\xi}) - \frac{\partial \psi}{\partial \dot{\mathbf{d}}} - \frac{\partial \phi}{\partial \dot{\mathbf{d}}} \right) \quad \text{in } V, \quad \text{with} \quad \boldsymbol{\xi} = \frac{\partial \psi}{\partial \text{grad}(\dot{\mathbf{d}})} \quad (1.27)$$

and furthermore the boundary condition

$$\dot{\mathbf{d}} \times (\boldsymbol{\xi} \mathbf{n} - \bar{\mathbf{\Xi}}) = \mathbf{0} \quad \text{on } \partial V_\Xi . \quad (1.28)$$

Hence, the GSM approach is equivalent to the thermodynamically consistent formulation in Sec. 1.3, albeit the derivations follow different lines of reasoning. The approach in Sec. 1.3 assumes Cauchy's theorem, see Eqs. (1.4) and (1.5), and yields the energetic relations, see Eq. (1.11). The GSM approach in Sec. 1.4, on the other hand, assumes the energetic relations, see Eqs. (1.23) and (1.26), and yields Cauchy's theorem, see Eqs. (1.25) and (1.28).

1.5 Examples of continuum models with a director

To counter the impression that director continua are a purely academic niche topic, we discuss examples of continua with a director in the following.

We start with liquid crystals described by the Oseen–Frank model. The model is named after the seminal publications by Oseen [12] and Frank [13]. Liquid crystals consist of big elongated and fairly rigid molecules, which arrange in one of three types of orientation, see, e.g., [14]. In the simplest case with uniaxial nematic orientation, for example, all molecules tend to align with their neighbors, but can otherwise arrange freely [15, 14]. In an average sense, the orientation of these molecules can be identified with the so-called *optic axis*. Since the latter is described by a unit vector, the Oseen–Frank model of liquid crystals can be considered as a director continuum. An exhaustive review of liquid crystals can be found, e.g., in [16].

Next, we turn our attention to fiber reinforced composites, or more specifically, their production process. During the molding process of fiber composites, the fibers are subject to reorientation processes induced by the flow of the (still liquid) matrix material, see [17]. Each fiber can be understood as a director whose evolution can be described by Jeffery’s equation [18, 19]. The latter is valid for ellipsoidal particles which are assumed to not disturb the fluid flow. Furthermore, in the original version of Jeffery’s equation, the interaction of fibers is neglected. Jeffery’s equation is length preserving in the sense that the time derivative of the director is perpendicular to the director (i.e., director on the unit sphere and derivative in tangent space). An overview of different approaches to describe and model fiber orientation can be found, e.g., in [20]. Note that the description of fiber composites based on individual fibers is rather unusual. Instead, fiber orientation tensors are more common.

The term *director* has a strong connection with classical structural elements such as rods, plates and shells. Therefore, we briefly discuss the role of directors in the context of these structural elements in the following. A rod is a slender structure with two dimensions smaller than the third. Conversely, plates and shells exhibit a small thickness compared to the other two dimensions. Plates refer to planar structures while shells are curved. As these structural elements are classic objects of study in continuum mechanics, there is a plethora of work on the topic of rods, plates and shells. A historic overview going back as far as 1691 can be found in [3] and for a more recent review see [4]. Typically, rods are described by two sets of quantities [21, 22, 23]. The first is the position vector of the cross section centroids (i.e., the position vector along the rod axis). The second is a set of three orthonormal vectors describing the cross section orientation. The latter gives rise to the consideration as a director continuum. The situation is similar for shells, where a position vector is used to characterize the shell mid-surface (surface sandwiched in between the two large-area exterior surfaces) [24]. Furthermore, a unit normal vector (director) at every point of the mid-surface describes the orientation. Thus, a shell can be considered as a one-director Cosserat surface [25]. In modern applications, shell theory is used, e.g., in flexible multi-body dynamics [26] and cloth

simulation [27].

The last example we want to discuss is low-temperature isothermal micromagnetics. On the atomic scale, all materials exhibit elementary magnetic moments due to angular momentum of electrons around the nucleus and due to spin moment of electrons [28]. In most materials, these elementary magnetic moments cancel out while in magnetic materials a resultant magnetic moment persists. In a continuum sense, these magnetic moments are represented by the magnetization vector field on the microscopic scale, which associates with every point in space a magnetization vector. Typically, authors assume the microscopic magnetization to have constant magnitude equal to the spontaneous magnetization (or the normalized field to have norm one), see, e.g., [29]. Hence, the magnetization can be considered as a director. In terms of magnetics, the material is sometimes considered to be locally saturated [30]. It is important to note that this constraint is only valid for constant temperature below the Curie point. With respect to the relation between the norm constraint and temperature, James and Kinderlehrer [31] mention the work of Weiss [32] and Landau–Lifshitz [33]. The norm constraint of the magnetization is sometimes referred to as *Heisenberg–Weiss constraint* [34, 35, 36].

1.6 Examples of numerical treatment

The abovementioned norm constraint on directors is numerically challenging. Without dedicated techniques, this constraint will typically not be satisfied. Authors from different communities have devised a multitude of approaches to preserve the norm of vector fields in numerical methods. In the following, we give a brief overview of norm conservation techniques. The exposition is not ordered by topic as many of the techniques are utilized across disciplines and communities. An exhaustive review and comparative simulations within the scope of micromagnetics can be found in [37].

A straightforward approach to retain the length of a director is to divide by its norm, see [38, 39] for examples in the context of liquid crystals and [40] for micromagnetics. More sophisticated types of renormalization can be found in [41] and [42, 43]. In the former, the magnetization update including renormalization is only accepted if the energy is decreased w.r.t. the previous step, and in latter, an operator split is employed which contains and unconstrained predictor and a corrector based on renormalization. However, as Lewis and Nigam [44] pointed out, renormalization must be applied with caution as it changes the mathematical problem and can lead to physically inconsistent solutions.

An alternative approach is to use a norm conserving time integration scheme. One example is the midpoint rule, which is used in conjunction with both finite element [45, 46, 47] and finite difference [48, 49] techniques.

One of the main problems of straightforward renormalization is that it is unclear how the energy behaves during the renormalization (and if the solution is subsequently still the minimum). This led Alouges [50] to construct a new method in which the minimum is searched

for in a subspace perpendicular to the previous solution (i.e., the update is in the tangent space) and the updated solution is subsequently projected to the unit sphere. This method was originally introduced for liquid crystals [50] and has later been transferred to micromagnetics [34, 51, 52, 53] and even Bose–Einstein condensates [54].

Another straightforward approach to conserve the director norm is to express it in spherical coordinates (polar and azimuthal angle, constant radius) [55, 56, 57, 58]. This method has the added benefit that the number of degrees of freedom is decreased by one. However, as pointed out by Reichel et al. [37], this approach has to be applied with caution. Firstly, the value range of the angles has to be constrained and secondly, in case of the finite element method, the interpolation of angles can produce unphysical results.

The norm restriction to a fixed value can also be enforced by changing the energy landscape such that energy minimization can only yield those solutions which obey the constraint. The penalty method adopts this strategy and introduces an additional energy which penalizes any deviation of the director norm from the desired value [59, 60]. Particularly noteworthy is the approach by Landis [61, 62] in which the penalty parameter depends on the magnetic susceptibility. Hence, paramagnetic or diamagnetic behavior can be represented.

Similar to the penalty method, the method of Lagrange multipliers alters the energy landscape to enforce the norm constraint. The method of Lagrange multipliers can be understood as a penalty method in which the penalty parameter is introduced as an additional degree of freedom [37]. An application of Lagrange multipliers to micromagnetics can be found in [63] and a modified Lagrange multiplier method is presented in [64] (perturbed Lagrange approach to avoid singular system matrix).

The last method we want to discuss, is the exponential map. The gist is to update the director using a rotation matrix, e.g., in the form of Rodrigues’s rotation formula. The exponential map is geometrically exact and reduces the number of degrees of freedom by one (because the director is parameterized by the angles which characterize the rotation matrix). Examples for the exponential map in computational methods include applications to rods and shells [23, 24, 65] and micromagnetics [44, 35].

1.7 Properties of the exponential map

In both numerical papers (Publications 1 and 2), we use the exponential map to fulfill the unit length constraint on the director. Hence, in the following, we introduce the exponential map and some interesting properties in detail.

The exact update of the director \mathbf{d} due to rotation around the vector $\boldsymbol{\omega}_\Delta$, $\|\boldsymbol{\omega}_\Delta\| = 1$, with angle $\Delta\theta$ is given by the rotation tensor $\mathbf{Q}(\Delta\theta, \boldsymbol{\omega}_\Delta)$ (exponential map)

$$\mathbf{d}' = \mathbf{Q}(\Delta\theta, \boldsymbol{\omega}_\Delta) \mathbf{d} . \quad (1.29)$$

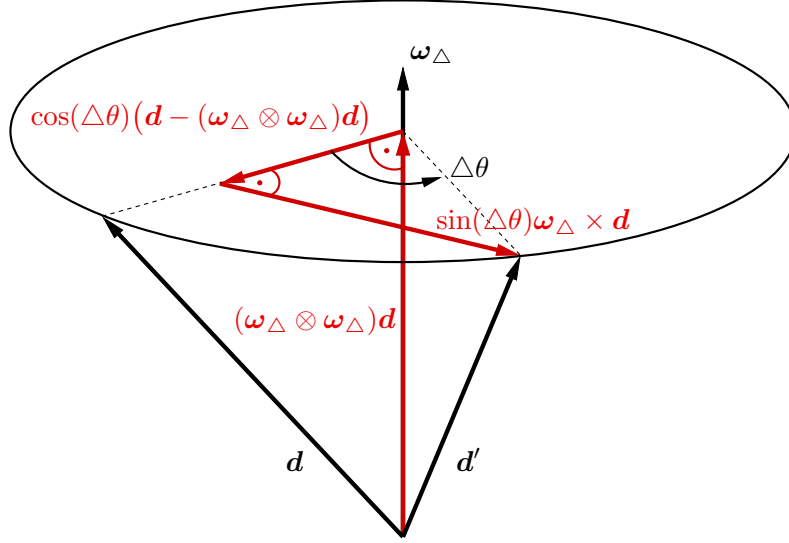


Fig. 1.5: Decomposition of the rotation tensor \mathbf{Q} into individual contributions.

Note that we write $\Delta\theta\boldsymbol{\omega}_\Delta$ for the rotation vector to distinguish it from the angular velocity vector $\dot{\theta}\boldsymbol{\omega}$ and its variational version $\delta\theta\boldsymbol{\omega}_\delta$. To construct the tensor \mathbf{Q} , we consider Fig. 1.5 and introduce the skew symmetric second order tensor $\hat{\boldsymbol{\omega}}_\Delta$ related to the cross product

$$\hat{\boldsymbol{\omega}}_\Delta \mathbf{d} = \boldsymbol{\omega}_\Delta \times \mathbf{d} \quad \text{with} \quad \hat{\boldsymbol{\omega}}_\Delta = -\boldsymbol{\epsilon} : \boldsymbol{\omega}_\Delta \quad \text{and} \quad \hat{\boldsymbol{\omega}}_\Delta^\top = -\hat{\boldsymbol{\omega}}_\Delta, \quad (1.30)$$

where $\boldsymbol{\epsilon}$ denotes the third order permutation tensor. The inverse relation reads

$$\boldsymbol{\omega}_\Delta = -\frac{1}{2}\boldsymbol{\epsilon} : \hat{\boldsymbol{\omega}}_\Delta. \quad (1.31)$$

Collecting all contributions in Fig. 1.5, the rotated director can be expressed as

$$\mathbf{d}' = (\boldsymbol{\omega}_\Delta \otimes \boldsymbol{\omega}_\Delta)\mathbf{d} + \cos(\Delta\theta)(\mathbf{I} - \boldsymbol{\omega}_\Delta \otimes \boldsymbol{\omega}_\Delta)\mathbf{d} + \sin(\Delta\theta)\hat{\boldsymbol{\omega}}_\Delta \mathbf{d} \quad (1.32)$$

and thus the rotation tensor $\mathbf{Q}(\Delta\theta, \boldsymbol{\omega}_\Delta)$ reads

$$\mathbf{Q}(\Delta\theta, \boldsymbol{\omega}_\Delta) = \boldsymbol{\omega}_\Delta \otimes \boldsymbol{\omega}_\Delta + \cos(\Delta\theta)(\mathbf{I} - \boldsymbol{\omega}_\Delta \otimes \boldsymbol{\omega}_\Delta) + \sin(\Delta\theta)\hat{\boldsymbol{\omega}}_\Delta \quad (1.33)$$

(Rodrigues's rotation formula). Using the relation $\hat{\boldsymbol{\omega}}_\Delta^2 = \hat{\boldsymbol{\omega}}_\Delta \hat{\boldsymbol{\omega}}_\Delta = \boldsymbol{\omega}_\Delta \otimes \boldsymbol{\omega}_\Delta - \mathbf{I}$, an alternative form of Eq. (1.33) reads

$$\mathbf{Q}(\Delta\theta, \boldsymbol{\omega}_\Delta) = \mathbf{I} + \sin(\Delta\theta)\hat{\boldsymbol{\omega}}_\Delta + (1 - \cos(\Delta\theta))\hat{\boldsymbol{\omega}}_\Delta^2 \quad (1.34)$$

which is the matrix exponential of $\Delta\theta\hat{\boldsymbol{\omega}}_\Delta$ (hence the update $\mathbf{d} \leftarrow \mathbf{Q}\mathbf{d}$ is called *exponential map*). The relation with the matrix exponential can be motivated by considering the series

representation of the exponential

$$\begin{aligned} \exp(\Delta\theta\boldsymbol{\omega}_\Delta) &= \sum_{k=1}^{\infty} \frac{1}{k!} (\Delta\theta\hat{\boldsymbol{\omega}}_\Delta)^k \\ &= \mathbf{I} + \Delta\theta\hat{\boldsymbol{\omega}}_\Delta + \frac{1}{2}\Delta\theta^2\hat{\boldsymbol{\omega}}_\Delta^2 + \frac{1}{6}\Delta\theta^3\hat{\boldsymbol{\omega}}_\Delta^3 + \frac{1}{24}\Delta\theta^4\hat{\boldsymbol{\omega}}_\Delta^4 + \frac{1}{120}\Delta\theta^5\hat{\boldsymbol{\omega}}_\Delta^5 + \dots \end{aligned} \quad (1.35)$$

To proceed, we use the cyclic property of the tensor $\hat{\boldsymbol{\omega}}_\Delta$ together with $\|\boldsymbol{\omega}_\Delta\| = 1$

$$\hat{\boldsymbol{\omega}}_\Delta \mathbf{d} = \boldsymbol{\omega}_\Delta \times \mathbf{d} \quad (1.36)$$

$$\hat{\boldsymbol{\omega}}_\Delta^2 \mathbf{d} = \boldsymbol{\omega}_\Delta \times (\boldsymbol{\omega}_\Delta \times \mathbf{d}) = (\boldsymbol{\omega}_\Delta \cdot \mathbf{d})\boldsymbol{\omega}_\Delta - \|\boldsymbol{\omega}_\Delta\|^2 \mathbf{d} \quad (1.37)$$

$$\hat{\boldsymbol{\omega}}_\Delta^3 \mathbf{d} = \boldsymbol{\omega}_\Delta \times (\hat{\boldsymbol{\omega}}_\Delta^2 \mathbf{d}) = -\boldsymbol{\omega}_\Delta \times \mathbf{d} = -\hat{\boldsymbol{\omega}}_\Delta \mathbf{d} \quad (1.38)$$

$$\hat{\boldsymbol{\omega}}_\Delta^4 \mathbf{d} = \hat{\boldsymbol{\omega}}_\Delta (\hat{\boldsymbol{\omega}}_\Delta^3 \mathbf{d}) = -\hat{\boldsymbol{\omega}}_\Delta^2 \mathbf{d} \quad (1.39)$$

$$\hat{\boldsymbol{\omega}}_\Delta^5 \mathbf{d} = \hat{\boldsymbol{\omega}}_\Delta (\hat{\boldsymbol{\omega}}_\Delta^4 \mathbf{d}) = -\hat{\boldsymbol{\omega}}_\Delta^3 \mathbf{d} = \hat{\boldsymbol{\omega}}_\Delta \mathbf{d} \quad (1.40)$$

from which we obtain for the matrix exponential

$$\exp(\Delta\theta\boldsymbol{\omega}_\Delta) = \mathbf{I} + \left(\Delta\theta - \frac{1}{6}\Delta\theta^3 + \frac{1}{120}\Delta\theta^5 + \dots \right) \hat{\boldsymbol{\omega}}_\Delta + \left(\frac{1}{2}\Delta\theta^2 - \frac{1}{24}\Delta\theta^4 + \dots \right) \hat{\boldsymbol{\omega}}_\Delta^2. \quad (1.41)$$

Without proof, we use the following series representations for the prefactors

$$\exp(\Delta\theta\boldsymbol{\omega}_\Delta) = \mathbf{I} + \left(\sum_{k=0}^{\infty} (-1)^k \frac{\Delta\theta^{2k+1}}{(2k+1)!} \right) \hat{\boldsymbol{\omega}}_\Delta + \left(1 - \sum_{k=0}^{\infty} (-1)^k \frac{\Delta\theta^{2k}}{(2k)!} \right) \hat{\boldsymbol{\omega}}_\Delta^2 \quad (1.42)$$

$$= \mathbf{I} + \sin(\Delta\theta)\hat{\boldsymbol{\omega}}_\Delta + (1 - \cos(\Delta\theta))\hat{\boldsymbol{\omega}}_\Delta^2 \quad (1.43)$$

and obtain the desired relation between the matrix exponential and Rodrigues's rotation tensor. Using $\cos(2\Delta\theta) = 1 - 2\sin^2(\Delta\theta)$, a common alternative form can be obtained from Eq. (1.43)

$$\exp(\Delta\theta\boldsymbol{\omega}_\Delta) = \mathbf{I} + \frac{\sin(\Delta\theta)}{\Delta\theta} (\Delta\theta\hat{\boldsymbol{\omega}}_\Delta) + \frac{1}{2} \left(\frac{\sin(\Delta\theta/2)}{\Delta\theta/2} \right)^2 (\Delta\theta\hat{\boldsymbol{\omega}}_\Delta)^2. \quad (1.44)$$

Irrespective of the form, the matrix exponential maps skew symmetric tensors to proper orthogonal tensors, i.e., $\exp : \Delta\theta\hat{\boldsymbol{\omega}}_\Delta \mapsto \mathbf{Q}$ with $(\Delta\theta\hat{\boldsymbol{\omega}}_\Delta)^\top = -\Delta\theta\hat{\boldsymbol{\omega}}_\Delta$ and $\det(\mathbf{Q}) = 1$, $\mathbf{Q}\mathbf{Q}^\top = \mathbf{Q}^\top\mathbf{Q} = \mathbf{I}$. To illustrate proper orthogonality, we first compute the determinant of $\mathbf{Q} = \exp(\Delta\theta\hat{\boldsymbol{\omega}}_\Delta)$ by considering the following limit expression for the exponential

$$\exp(\Delta\theta\hat{\boldsymbol{\omega}}_\Delta) = \lim_{k \rightarrow \infty} \left(\mathbf{I} + \frac{\Delta\theta\hat{\boldsymbol{\omega}}_\Delta}{k} \right)^k \quad (1.45)$$

$$\det(\exp(\Delta\theta\hat{\boldsymbol{\omega}}_\Delta)) = \lim_{k \rightarrow \infty} \det \left(\mathbf{I} + \frac{\Delta\theta\hat{\boldsymbol{\omega}}_\Delta}{k} \right)^k, \quad (1.46)$$

where we used that the determinant is a continuous function and further that $\det(\mathbf{A}^k) = \det(\mathbf{A})^k$. To obtain the determinant of $\mathbf{I} + \Delta\theta\hat{\boldsymbol{\omega}}_\Delta/k$, we compute

$$\det\left(\mathbf{I} + \frac{\Delta\theta\hat{\boldsymbol{\omega}}_\Delta}{k}\right) = \det\begin{bmatrix} 1 & -\frac{\Delta\theta}{k}\omega_3^\Delta & \frac{\Delta\theta}{k}\omega_2^\Delta \\ \frac{\Delta\theta}{k}\omega_3^\Delta & 1 & -\frac{\Delta\theta}{k}\omega_1^\Delta \\ -\frac{\Delta\theta}{k}\omega_2^\Delta & \frac{\Delta\theta}{k}\omega_1^\Delta & 1 \end{bmatrix} = 1 + \left(\frac{\Delta\theta}{k}\right)^2. \quad (1.47)$$

Hence, the determinant of the matrix exponential reads

$$\det(\exp(\Delta\theta\hat{\boldsymbol{\omega}}_\Delta)) = \lim_{k \rightarrow \infty} \left(1 + \left(\frac{\Delta\theta}{k}\right)^2\right)^k \quad (1.48)$$

$$= \lim_{k \rightarrow \infty} \exp\left(k \ln\left(1 + \left(\frac{\Delta\theta}{k}\right)^2\right)\right) \quad (1.49)$$

$$= \lim_{l \rightarrow 0} \exp\left(\frac{\ln(1 + \Delta\theta^2 l^2)}{l}\right). \quad (1.50)$$

Since the exponential is a continuous function at $l = 0$, we can pull the limit inside

$$\det(\exp(\Delta\theta\hat{\boldsymbol{\omega}}_\Delta)) = \exp\left(\lim_{l \rightarrow 0} \frac{\ln(1 + \Delta\theta^2 l^2)}{l}\right) \quad (1.51)$$

and subsequently apply L'Hôpital's rule

$$\det(\exp(\Delta\theta\hat{\boldsymbol{\omega}}_\Delta)) = \exp\left(\lim_{l \rightarrow 0} \frac{2\Delta\theta^2 l}{1 + \Delta\theta^2 l^2}\right) = \exp(0) = 1. \quad (1.52)$$

Alternatively, we could use $\det(\exp(\mathbf{A})) = \exp(\text{tr}(\mathbf{A}))$, see, e.g., [66], together with $\text{tr}(\Delta\theta\hat{\boldsymbol{\omega}}_\Delta) = 0$. To illustrate the second part of proper orthogonality, $\mathbf{Q}\mathbf{Q}^\top = \mathbf{I}$, we simply compute the single contraction of tensors (while using Eqs. (1.30) and (1.39))

$$\begin{aligned} \mathbf{Q}\mathbf{Q}^\top &= \left(\mathbf{I} + \sin(\Delta\theta)\hat{\boldsymbol{\omega}}_\Delta + (1 - \cos(\Delta\theta))\hat{\boldsymbol{\omega}}_\Delta^2\right) \left(\mathbf{I} + \sin(\Delta\theta)\hat{\boldsymbol{\omega}}_\Delta + (1 - \cos(\Delta\theta))\hat{\boldsymbol{\omega}}_\Delta^2\right)^\top \\ &= \mathbf{I} + 2(1 - \cos(\Delta\theta))\hat{\boldsymbol{\omega}}_\Delta^2 - \sin^2(\Delta\theta)\hat{\boldsymbol{\omega}}_\Delta^2 - (1 - \cos(\Delta\theta))^2\hat{\boldsymbol{\omega}}_\Delta^2 \end{aligned} \quad (1.53)$$

$$= \mathbf{I}. \quad (1.54)$$

As mentioned above, Rodrigues's rotation formula associates with every pair $(\Delta\theta, \boldsymbol{\omega}_\Delta)$ a proper orthogonal tensor \mathbf{Q} . We can invert the relation (in the sense of obtaining $(\Delta\theta, \boldsymbol{\omega}_\Delta)$ from \mathbf{Q}) as follows. We start with the formulation of Rodrigues's rotation tensor in Eq. (1.33)

$$\mathbf{Q} = \cos(\Delta\theta)\mathbf{I} + (1 - \cos(\Delta\theta))\boldsymbol{\omega}_\Delta \otimes \boldsymbol{\omega}_\Delta + \sin(\Delta\theta)\hat{\boldsymbol{\omega}}_\Delta. \quad (1.55)$$

To obtain the angle $\Delta\theta$, we compute

$$\text{tr}(\mathbf{Q}) = \cos(\Delta\theta)\text{tr}(\mathbf{I}) + (1 - \cos(\Delta\theta))\text{tr}(\boldsymbol{\omega}_\Delta \otimes \boldsymbol{\omega}_\Delta) + \sin(\Delta\theta)\text{tr}(\hat{\boldsymbol{\omega}}_\Delta) \quad (1.56)$$

$$= 3 \cos(\Delta\theta) + (1 - \cos(\Delta\theta)) \quad (1.57)$$

$$\Leftrightarrow \cos(\Delta\theta) = \frac{1}{2} (\text{tr}(\mathbf{Q}) - 1) . \quad (1.58)$$

For the vector $\boldsymbol{\omega}_\Delta$, we consider the skew symmetric part of \mathbf{Q} together with Eq. (1.31)

$$\frac{1}{2} (\mathbf{Q} - \mathbf{Q}^\top) = \text{skw}(\mathbf{Q}) = \sin(\Delta\theta) \widehat{\boldsymbol{\omega}}_\Delta \quad (1.59)$$

$$\Leftrightarrow \boldsymbol{\omega}_\Delta = -\frac{1}{2 \sin(\Delta\theta)} \boldsymbol{\epsilon} : \text{skw} \mathbf{Q} . \quad (1.60)$$

1.8 Algorithmic approach using the exponential map

Having introduced the exponential map and some interesting properties in Sec. 1.7, we now turn our attention to its application in the finite element context. To this end, we consider the weak form of the microforce balance, Eqs. (1.26) and (1.27), with vanishing traction $\bar{\mathbf{E}}$

$$G_d^e = \int_{V^e} [\boldsymbol{\xi} : \text{grad}(\delta \dot{\mathbf{d}}) + \mathbf{S} \cdot \delta \dot{\mathbf{d}}] dv , \quad (1.61)$$

where $(\bullet)^e$ denotes quantities in element e and $\mathbf{S} = \partial\psi/\partial\mathbf{d} + \partial\phi/\partial\dot{\mathbf{d}}$. The ideas discussed in the following for the element residual (weak form) also apply to the element stiffness. With the interpolations

$$\delta \dot{\mathbf{d}} = \underline{N}_d \underline{\delta \dot{d}}^e \quad \text{and} \quad \text{grad}(\delta \dot{\mathbf{d}}) = \underline{B}_d \underline{\delta \dot{d}}^e , \quad (1.62)$$

where underlined quantities denote matrix equivalents of tensors, the element residual reads

$$G_d^e = (\underline{\delta \dot{d}}^e)^\top \int_{V^e} [\underline{B}_d^\top \widehat{\boldsymbol{\xi}} + \underline{N}_d^\top \underline{S}] dv . \quad (1.63)$$

The quantity $\widehat{\boldsymbol{\xi}}$ is the (9×1) equivalent of the (3×3) tensor $\boldsymbol{\xi}$ (Voigt notation). Since we use the exponential map, the degree of freedom is not \mathbf{d} but rather the two angle increments $(\Delta\theta_1, \Delta\theta_2)$ used in the exponential map

$$\mathbf{d} \leftarrow \exp(\Delta\theta \widehat{\boldsymbol{\omega}}_\Delta) \mathbf{d} \quad (1.64)$$

$$\Delta\theta \widehat{\boldsymbol{\omega}}_\Delta = -\boldsymbol{\epsilon} \cdot \Delta\theta \boldsymbol{\omega}_\Delta \quad (1.65)$$

$$\Delta\theta \boldsymbol{\omega}_\Delta = \Delta\theta_1 \mathbf{a}_1 + \Delta\theta_2 \mathbf{a}_2 , \quad (1.66)$$

where (in the time continuous setting) the angle increments can be understood as the angular velocity $\dot{\theta}$ integrated over a fixed time period. To adjust the formulation of the element residual accordingly, we use the variational equivalent of Eq. (1.1) in node I

$$\delta \dot{\mathbf{d}}_I = \delta \dot{\theta}_I \boldsymbol{\omega}_{\delta I} \times \mathbf{d}_I = \delta \dot{\theta}_{2I} \mathbf{a}_{1I} - \delta \dot{\theta}_{1I} \mathbf{a}_{2I} . \quad (1.67)$$

Hence, we can find a matrix \underline{G} which translates the director variations into the variations of angular velocity, i.e., $\delta \dot{\underline{d}}^e = \underline{G} \delta \dot{\underline{\theta}}^e$, see [35]. For the element residual \underline{r}_θ^e , we finally obtain

$$G_d^e = (\delta \dot{\underline{\theta}}^e)^\top \underline{G}^\top \int_{V^e} [\underline{B}_d^\top \hat{\underline{\xi}} + \underline{N}_d^\top \underline{S}] dv = (\delta \dot{\underline{\theta}}^e)^\top \underline{r}_\theta^e. \quad (1.68)$$

The algorithmic treatment involving the exponential map is summarized in Algo. 1.1.

Algo. 1.1: Director update with exponential map.

- (1) Initialize $\{\mathbf{a}_1, \mathbf{a}_2, \mathbf{d}\}$ according to the desired initial conditions and initialize $\{\theta_1, \theta_2\}$ with zero.
- (2) Compute the residual \underline{r}_θ and associated stiffness $\underline{K}_{\theta\theta}$ (assembled from \underline{r}_θ^e and $\underline{K}_{\theta\theta}^e$) using the current orientation $\{\mathbf{a}_1, \mathbf{a}_2, \mathbf{d}\}$.
- (3) Solve the global system for the new angles $\{\theta_1, \theta_2\}$ and obtain the increments $\{\Delta\theta_1, \Delta\theta_2\}$ w.r.t. the previous Newton step.
- (4) Rotate $\{\mathbf{a}_1, \mathbf{a}_2, \mathbf{d}\}$ by increments $\{\Delta\theta_1, \Delta\theta_2\}$ using the exponential map

$$\Delta\theta \hat{\underline{\omega}}_\Delta \leftarrow -\epsilon \cdot (\Delta\theta_1 \mathbf{a}_1 + \Delta\theta_2 \mathbf{a}_2) \quad (1.69)$$

$$\{\mathbf{a}_1, \mathbf{a}_2, \mathbf{d}\} \leftarrow \exp(\Delta\theta \hat{\underline{\omega}}_\Delta) \{\mathbf{a}_1, \mathbf{a}_2, \mathbf{d}\}. \quad (1.70)$$

- (5) Repeat steps (2)–(4) until convergence.
 - (6) If applicable, go to the next time step and repeat steps (2)–(5).
-

1.9 Relevance of the director continuum for the chapters of this thesis

In Chapter 2, we present the first peer-reviewed publication in which a phase-field damage model is formulated. In order to allow for anisotropic fracture behavior and to capture the damage related tension-compression asymmetry, the phase-field model is extended by a crack orientation vector. With regard to kinematics, the crack orientation field allows to locally represent fracture modes *I*, *II* and *III*. We introduce the crack orientation vector as a unit vector and hence consider it as a director. In the numerical implementation, we employ the exponential map.

The second peer-reviewed publication appears in Chapter 3. Here, the focus is on numerical techniques for a coupled micro-magneto-mechanical model and its application for Barkhausen noise computation. In this publication, the magnetization vector is introduced as a unit vector and we therefore regard it as a director. The exponential map in conjunction with the norm conserving modified Crank-Nicolson time integration scheme is used to retain the magnetization norm in the computational scheme.



In Chapter 4, we showcase a manuscript which has been prepared for publication. Similar to Chapter 3, this manuscript deals with coupled micro-magneto-mechanics. However, the focus

is not on Barkhausen noise but on the stability analysis of a domain (sub-)structure which we call *undulations*. The magnetization director is initially formulated in polar coordinates. After setting up the model, we subsequently linearize the magnetization orientation around a prescribed direction to proceed with the stability analysis. In this work, computational approaches to retain the director norm are not relevant since the model is purely analytical, i.e., there is no computational update which could violate the constraint.

CHAPTER 2

Publication 1: A gradient–extended large–strain anisotropic damage model with crack orientation director

This work was published as:

Dorn, C.  and Wulfinghoff, S.  [2021], 'A gradient–extended large–strain anisotropic damage model with crack orientation director', *Computer Methods in Applied Mechanics and Engineering* **387**, 114123.

Reproduced from [67], with the permission of Elsevier.

Own contributions to the following article:

- Conceptualization (small contribution)
- Planning (large contribution)
- Methodology (large contribution)
- Software implementation and validation (large contribution)
- Investigation (large contribution)
- Interpretation of results (large contribution)
- Manuscript writing (large contribution)

Abstract

Tension-compression splits are frequently introduced to remedy the symmetric behavior of phase-field models of fracture. These splits can suffer from an overly stiff model response. We propose a gradient-extended damage model with crack orientation director which locally represents the kinematics of fracture modes *I*, *II* and *III*. The kinematics of the model are asymmetric in tension and compression. Other authors which follow this approach are often times concerned with cleavage systems with well-known cleavage planes. In our model, the crack surface orientation is not known a priori and thus treated as a degree of freedom. The formulation within the generalized standard material framework yields thermodynamic consistency. Two outstanding features of our approach are the straightforward implementation of anisotropic damage behavior and the traction free crack surface which emerges from the model. We demonstrate our findings with numerical examples for different load cases, different sample geometries and isotropic as well as anisotropic damage behavior. We showcase advantages of our approach when compared to a model which features a spectral tension-compression split.

Keywords: Anisotropic damage, Tension-compression asymmetry, Generalized standard material, Micromorphic approach, Director

2.1 Introduction

Consideration of damage mechanisms in engineering materials is crucial for the prediction of component lifetime. State of the art computational approaches have proven to be powerful tools in this respect. One of the most prominent computational approaches is the phase-field model of fracture, which is based on the theory of brittle fracture by Griffith [68] and emerged from the variational approach of fracture by Francfort and Marigo [69] in the regularized setting by Ambrosio and Tortorelli [70]. This classical phase-field model of fracture leads to an unphysically symmetric behavior in tension and compression, see Amor et al. [71] and Freddi and Royer-Carfagni [72]. As possible remedies for this behavior, a spectral tension-compression split, see, e.g., Miehe et al. [73, 74] and a volumetric-deviatoric tension-compression split, see, e.g., Amor et al. [71] and Strobl and Seelig [75] were proposed. These tension-compression splits can lead to an overly stiff model response which was demonstrated by Strobl and Seelig [76]. Moreover Strobl and Seelig [77] noted that tension-compression splits can also suffer from other pitfalls like the violation of traction free crack surfaces. A different idea to rectify the symmetric tension-compression behavior is to introduce an additional energy contribution into the phase-field functional. This additional contribution is intended to cause non-symmetric behavior due to kinematic constraints as done by, e.g., Shanthraj et al. [78] and Bryant and Sun [79]. A possible application for this idea are materials with single crystal cleavage systems and predetermined cleavage planes,

see Aslan and Forest [80, 81], Sabnis et al. [82] and Shanthraj et al. [78].

In this article, we want to follow the route of introducing an energy contribution to obtain non-symmetric behavior kinematically. However, in contrast to the referenced previous works, we are concerned with materials where the crack surface orientation is not known a priori. This means that we have to treat the crack surface orientation as a degree of freedom.

2.2 Kinematics

Before we start with the kinematics, we introduce some non-standard notation. First, we define the following products

$$\mathbf{A} \square \mathbf{B} : \mathbf{C} = \mathbf{ACB} \quad (2.1)$$

$$\mathbf{A} \overset{s}{\square} \mathbf{B} : \mathbf{C} = \mathbf{A} \operatorname{sym}(\mathbf{C}) \mathbf{B} \quad (2.2)$$

$$\mathbf{A} \underset{s}{\square} \mathbf{B} : \mathbf{C} = \operatorname{sym}(\mathbf{ACB}) \quad (2.3)$$

$$\mathbf{A} \overset{T}{\square} \mathbf{B} : \mathbf{C} = \mathbf{AC}^T \mathbf{B} , \quad (2.4)$$

where \mathbf{A} , \mathbf{B} and \mathbf{C} are second order tensors and $\mathbf{A} \square \mathbf{B}$, $\mathbf{A} \overset{s}{\square} \mathbf{B}$, $\mathbf{A} \underset{s}{\square} \mathbf{B}$ and $\mathbf{A} \overset{T}{\square} \mathbf{B}$ are fourth order tensors. Furthermore, for a third order tensor $\mathbf{a} = a_{ijk} \mathbf{e}_i \otimes \mathbf{e}_j \otimes \mathbf{e}_k$ we define the transpose as

$$\mathbf{a}^T = a_{jki} \mathbf{e}_i \otimes \mathbf{e}_j \otimes \mathbf{e}_k . \quad (2.5)$$

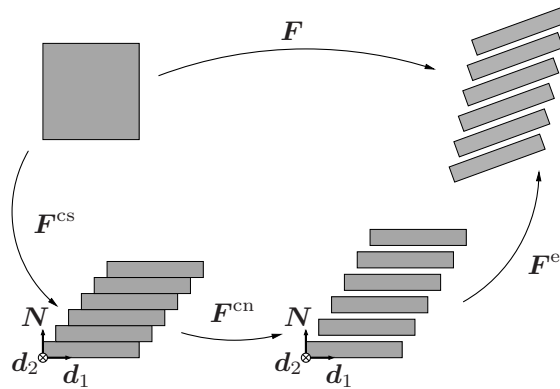


Fig. 2.1: Multiplicative decomposition of the deformation gradient \mathbf{F} into a normal crack contribution \mathbf{F}^{cn} , a shear crack contribution \mathbf{F}^{cs} and an elastic contribution \mathbf{F}^e .

We consider a material body $\Omega_0 \subset \mathbb{R}^3$ with boundary $\partial\Omega_0 \subset \mathbb{R}^2$ in the reference configuration and denote the same body in the current configuration by $\Omega \subset \mathbb{R}^3$ with boundary $\partial\Omega \subset \mathbb{R}^2$. The equation of motion χ describes the motion of a material point $\mathbf{X} : [0, T] \rightarrow \Omega_0$ from the

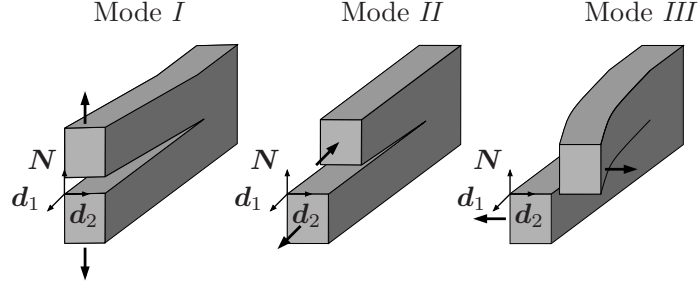


Fig. 2.2: Fracture mode *I* described by normal crack contribution \mathbf{F}^{cn} and modes *II* and *III* described by shear crack contribution \mathbf{F}^{cs} , figure adapted from Shanthraj et al. [78].

reference configuration to the current configuration $\mathbf{x} : [0, T] \rightarrow \Omega$, where $[0, T]$ is the time range and $\mathbf{x} = \chi(\mathbf{X}, t)$. We assume the deformation gradient $\mathbf{F} = \partial \mathbf{x} / \partial \mathbf{X}$ to be composed of a shear crack contribution \mathbf{F}^{cs} , a normal crack contribution \mathbf{F}^{cn} and an elastic contribution \mathbf{F}^{e} in a multiplicative fashion

$$\mathbf{F} = \mathbf{F}^{\text{e}} \mathbf{F}^{\text{cn}} \mathbf{F}^{\text{cs}}, \quad (2.6)$$

cf. Fig. 2.1. Further, we assume each material point to behave like a stack of layers with normal vector \mathbf{N} and in-plane vectors \mathbf{d}_1 and \mathbf{d}_2 . Kinematically, these layers accommodate fracture mode *I* via the deformation gradient \mathbf{F}^{cn} and fracture modes *II* and *III* via the deformation gradient \mathbf{F}^{cs} , see Fig. 2.2. We construct \mathbf{F}^{cn} such that it describes the mapping of a line element $d\mathbf{X}$ onto a line element $d\mathbf{x}$, the tip of which is (relatively) displaced in the direction of the normal vector \mathbf{N}

$$d\mathbf{x} = d\mathbf{X} + \varepsilon(d\mathbf{X} \cdot \mathbf{N})\mathbf{N} = (\mathbf{I} + \varepsilon\mathbf{N} \otimes \mathbf{N}) \cdot d\mathbf{X} = \mathbf{F}^{\text{cn}} \cdot d\mathbf{X}, \quad (2.7)$$

cf. Fig. 2.3. Here, \mathbf{I} denotes the second order identity tensor. Similarly, \mathbf{F}^{cs} describes the

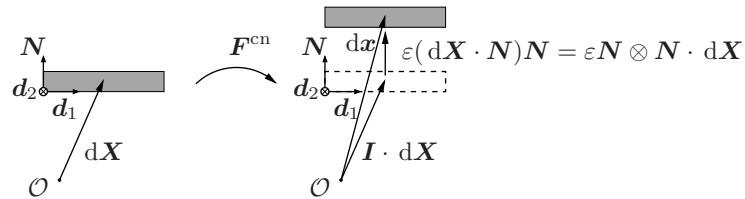


Fig. 2.3: Normal crack contribution \mathbf{F}^{cn} .

mapping of a line element $d\mathbf{X}$ onto a line element $d\mathbf{x}$, the tip of which is (relatively) displaced in the direction of the two in-plane vectors \mathbf{d}_1 and \mathbf{d}_2

$$d\mathbf{x} = d\mathbf{X} + \sum_{i=1}^2 \gamma_i(d\mathbf{X} \cdot \mathbf{N})\mathbf{d}_i = \left(\mathbf{I} + \sum_{i=1}^2 \gamma_i \mathbf{d}_i \otimes \mathbf{N} \right) \cdot d\mathbf{X} = \mathbf{F}^{\text{cs}} \cdot d\mathbf{X}, \quad (2.8)$$

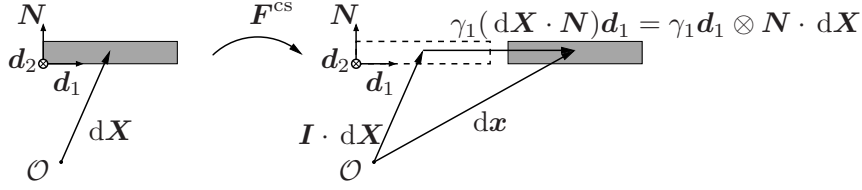


Fig. 2.4: Shear crack contribution \mathbf{F}^{cs} , example for displacement in direction \mathbf{d}_1 .

cf. Fig. 2.4. We summarize the two contributions \mathbf{F}^{cn} and \mathbf{F}^{cs} into the crack deformation gradient

$$\mathbf{F}^{\text{c}} = \mathbf{F}^{\text{cn}} \mathbf{F}^{\text{cs}} = \mathbf{I} + \varepsilon \mathbf{N} \otimes \mathbf{N} + \sum_{i=1}^2 \gamma_i \mathbf{d}_i \otimes \mathbf{N} , \quad (2.9)$$

the inverse of which is given by

$$\mathbf{F}^{\text{c-1}} = \mathbf{I} - \frac{\varepsilon}{1 + \varepsilon} \mathbf{N} \otimes \mathbf{N} - \sum_{i=1}^2 \frac{\gamma_i}{1 + \varepsilon} \mathbf{d}_i \otimes \mathbf{N} . \quad (2.10)$$

Furthermore, we summarize the variables γ_1 , γ_2 and ε in the vector $\underline{\varepsilon} = (\gamma_1, \gamma_2, \varepsilon)^\top$. The total deformation gradient \mathbf{F} , the crack contribution \mathbf{F}^{c} and the elastic deformation gradient \mathbf{F}^{e} are connected via the relation $\mathbf{F} = \mathbf{F}^{\text{e}} \mathbf{F}^{\text{c}}$. Hence, it is only necessary to compute two of the quantities \mathbf{F} , \mathbf{F}^{c} and \mathbf{F}^{e} because the third one follows immediately from the multiplicative connection. We decide to work with \mathbf{F} and \mathbf{F}^{c} and treat \mathbf{F}^{e} as the resulting dependent quantity.

The vectors \mathbf{d}_1 , \mathbf{d}_2 and \mathbf{N} are orthonormal vectors, i.e., they have to retain norm 1. The

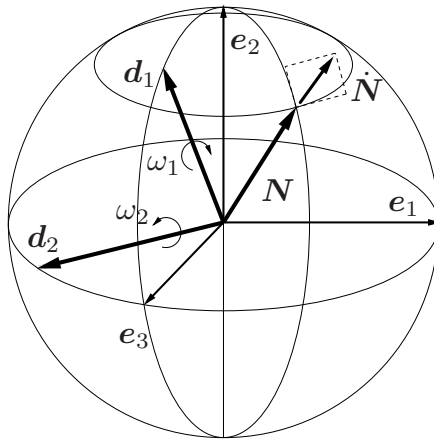


Fig. 2.5: Kinematics of \mathbf{d}_1 , \mathbf{d}_2 and \mathbf{N} on the unit sphere.

restriction of these vectors to the unit sphere makes the treatment challenging. Similar challenges arise for the shell director in shell theory (see, e.g., Simo et al. [24, 65]) and

for the magnetization vector in micromagnetics (see, e.g., Lewis and Nigam [44] and Miehe and Ethiraj [35]). The norm constraint entails the following kinematic relationships. Since we require $\|\mathbf{N}\| = 1$ at all times, the vector \mathbf{N} only has two instead of three independent components. We describe the orientation of the normal vector \mathbf{N} using the angular velocities ω_1 and ω_2 in the angular velocity vector $\boldsymbol{\omega} = \omega_1 \mathbf{d}_1 + \omega_2 \mathbf{d}_2$, see Fig. 2.5. We do not consider any rotation around the vector \mathbf{N} because it yields an equivalent configuration $\gamma' \mathbf{d}' = \sum_{i=1}^2 \gamma_i \mathbf{d}_i = \sum_{i=1}^2 \tilde{\gamma}_i \tilde{\mathbf{d}}_i$, where $\tilde{\mathbf{d}}_i$ and $\tilde{\gamma}_i$ ($i = 1, 2$) are the rotated vectors and corresponding components. Thus, while $\{\gamma_1, \gamma_2\}$ and $\{\mathbf{d}_1, \mathbf{d}_2\}$ are not unique, the resulting vector $\gamma' \mathbf{d}'$ is unique. From Fig. 2.5, it becomes apparent that $\dot{\mathbf{N}}$ can be expressed as

$$\dot{\mathbf{N}} = \omega_2 \mathbf{d}_1 - \omega_1 \mathbf{d}_2 = \omega_2 (\mathbf{d}_2 \times \mathbf{N}) - \omega_1 (-\mathbf{d}_1 \times \mathbf{N}) = \boldsymbol{\omega} \times \mathbf{N} \quad (2.11)$$

and similarly $\dot{\mathbf{d}}_i$ can be expressed as

$$\dot{\mathbf{d}}_i = \boldsymbol{\omega} \times \mathbf{d}_i, \quad i = 1, 2. \quad (2.12)$$

Furthermore, the variations of Eqs. (2.11) and (2.12) are obtained by multiplying Eqs. (2.11) and (2.12) by the time increment dt

$$d\mathbf{N} = (\omega_1 dt \mathbf{d}_1 + \omega_2 dt \mathbf{d}_2) \times \mathbf{N} = (\omega_{d1} \mathbf{d}_1 + \omega_{d2} \mathbf{d}_2) \times \mathbf{N} = \boldsymbol{\omega}_d \times \mathbf{N} = \hat{\boldsymbol{\omega}}_d \mathbf{N} \quad (2.13)$$

$$d\mathbf{d}_i = \boldsymbol{\omega}_d \times \mathbf{d}_i = \hat{\boldsymbol{\omega}}_d \mathbf{d}_i, \quad i = 1, 2, \quad (2.14)$$

where $\hat{\boldsymbol{\omega}}_d = -\boldsymbol{\epsilon} \cdot \boldsymbol{\omega}_d$ with $\boldsymbol{\epsilon}$ the permutation tensor. Note that we consider the infinitesimal case $\omega_i dt = \omega_{di} \rightarrow 0$. Moreover, the following variation of $\boldsymbol{\omega}_d$ will prove to be useful later on

$$\begin{aligned} \delta \boldsymbol{\omega}_d &= d\omega_1 \delta \mathbf{d}_1 + d\omega_2 \delta \mathbf{d}_2 = \boldsymbol{\omega}_\delta \times (d\omega_1 \mathbf{d}_1 + d\omega_2 \mathbf{d}_2) \\ &= \boldsymbol{\omega}_\delta \times \boldsymbol{\omega}_d, \end{aligned} \quad (2.15)$$

where it is important to note that $\delta \neq d$. The dual formulation reads $d\boldsymbol{\omega}_\delta = \boldsymbol{\omega}_d \times \boldsymbol{\omega}_\delta$.

In the algorithmic procedure (with time step Δt , see Section 2.3), we want to compute updates of the vectors $\{\mathbf{d}_1, \mathbf{d}_2, \mathbf{N}\}$ such that they remain on the unit sphere. To account for this requirement, we use the exponential map

$$\{\mathbf{d}_1, \mathbf{d}_2, \mathbf{N}\} \leftarrow \exp(\hat{\boldsymbol{\omega}} \Delta t) \cdot \{\mathbf{d}_1, \mathbf{d}_2, \mathbf{N}\} \quad (2.16)$$

$$\exp(\hat{\boldsymbol{\omega}} \Delta t) = \mathbf{I} + \sin \|\boldsymbol{\omega} \Delta t\| \frac{\hat{\boldsymbol{\omega}} \Delta t}{\|\boldsymbol{\omega} \Delta t\|} + \left(1 - \cos \|\boldsymbol{\omega} \Delta t\|\right) \frac{\hat{\boldsymbol{\omega}}^2 \Delta t^2}{\|\boldsymbol{\omega} \Delta t\|^2} \quad (2.17)$$

with $\hat{\boldsymbol{\omega}}^2 \mathbf{v} = \boldsymbol{\omega} \times (\boldsymbol{\omega} \times \mathbf{v})$ for arbitrary vector \mathbf{v} . An initial set $\{\mathbf{d}_1, \mathbf{d}_2, \mathbf{N}\}$ has to be chosen. For details on the exponential map we refer to Lewis and Nigam [44] and Miehe and Ethiraj [35].

2.3 Formulation as a generalized standard material

In order to achieve thermodynamic consistency, we formulate our material model within the framework of generalized standard materials [11]. We choose the free energy density ψ as follows

$$\begin{aligned} \psi = & g(D)\psi_{e0}(\mathbf{C}) + (1 - g(D_\chi))(\psi_{e0}(\mathbf{C}^e) + \psi_k(\underline{\varepsilon})) + \psi_h(D) + \psi_\chi(D_\chi - D) \\ & + \psi_{\text{pin}}(\mathbf{N} - \mathbf{N}^*) + \psi_{\text{aniso}}(\mathbf{N}) + \psi_{g\chi}(\text{Grad}(D_\chi)) + \psi_{gN}(\text{Grad}(\mathbf{N})) , \end{aligned} \quad (2.18)$$

where D_χ is the micro-damage degree of freedom, $\mathbf{C} = \mathbf{F}^\top \mathbf{F}$ and $\mathbf{C}^e = \mathbf{F}^{e\top} \mathbf{F}^e$ are the respective right Cauchy–Green tensors, $\underline{\varepsilon} = (\gamma_1, \gamma_2, \varepsilon)^\top$ are the internal variables (see Section 2.2), D is a damage variable, \mathbf{N} is the crack surface normal and $\text{Grad}(\cdot) = \partial(\cdot)/\partial \mathbf{X}$.

The elastic energy ψ_{e0} is split into an undamaged contribution $g\psi_{e0}(\mathbf{C})$ and a damaged contribution $(1 - g)\psi_{e0}(\mathbf{C}^e)$ via the degradation function g , see Pham et al. [83] for properties of g . We choose the quadratic polynomial $g(D) = (1 - D)^2$ for the degradation function. In the completely undamaged case ($g = 1$), only $\psi_{e0}(\mathbf{C})$ is active because \mathbf{C} is fully elastic. In the completely damaged case ($g = 0$), only $\psi_{e0}(\mathbf{C}^e)$ is active because we do not want any inelastic contributions in \mathbf{C} to cause an elastic energy. In between the two extreme states, the linear combination of both contributions is active. For technical reasons we use $g(D_\chi)$ for the damaged and $g(D)$ for the undamaged case, see Section 2.5.

In order to prevent interpenetration for fracture mode I (see Section 2.2) and to provide some residual stiffness in the fully damaged case, we introduce

$$\psi_k = \begin{cases} \infty, & \varepsilon < 0 \\ \frac{1}{2}k \left(\varepsilon^2 + \sum_{i=1}^2 \gamma_i^2 \right), & \text{else} \end{cases} = \begin{cases} \infty, & \varepsilon < 0 \\ \frac{1}{2}k \underline{\varepsilon} \cdot \underline{\varepsilon}, & \text{else} \end{cases} . \quad (2.19)$$

In case $\varepsilon < 0$, which characterizes interpenetration for fracture mode I , we activate a large penalty parameter. In every other case, we prescribe a quadratic energy. Next, we introduce the damage hardening energy ψ_h similar to a hardening energy in plasticity to prevent an infinite crack width. A simple choice for ψ_h is

$$\psi_h = \frac{1}{2}HD^2 . \quad (2.20)$$

Following the micromorphic approach by Forest [84], the next contribution ψ_χ is introduced to establish a coupling between the damage variable D and the micro-damage degree of freedom D_χ , i.e., to keep them in close vicinity of each other. We choose

$$\psi_\chi = \frac{1}{2}H_\chi(D_\chi - D)^2 , \quad (2.21)$$

where H_χ is very large such that D and D_χ are virtually identical. We further include ψ_{pin} in the free energy density to stop the crack orientation \mathbf{N} from evolving any further in case D or

$D_\chi \geq 1 - \epsilon$ where $\epsilon > 0$ is small. Thus, we are pinning the orientation. Without this pinning, a fully evolved crack ($D \geq 1 - \epsilon$) could change its local crack orientation \mathbf{N} after the crack evolution finished. We consider this as unphysical behavior. The quadratic energy

$$\psi_{\text{pin}} = \begin{cases} \frac{1}{2} H_N (\mathbf{N} - \mathbf{N}^*) \cdot (\mathbf{N} - \mathbf{N}^*), & D \text{ or } D_\chi \geq 1 - \epsilon \\ 0, & \text{else} \end{cases} \quad (2.22)$$

penalizes deviations of the orientation \mathbf{N} from the orientation \mathbf{N}^* which prevailed at the point where the condition D or $D_\chi \geq 1 - \epsilon$ was first fulfilled. In order to represent anisotropic damage behavior, we include the contribution ψ_{aniso} in the free energy density. For the special case of orthonormal preferential directions, we choose

$$\begin{aligned} \psi_{\text{aniso}} &= \sum_{m=1}^3 \frac{1}{2} \beta_m (\mathbf{N} \cdot \mathbf{p}_m)^2 = \frac{1}{2} \mathbf{N} \cdot \left(\sum_{m=1}^3 \beta_m \mathbf{p}_m \otimes \mathbf{p}_m \right) \cdot \mathbf{N} \\ &= \frac{1}{2} \mathbf{N} \cdot \mathbf{A} \cdot \mathbf{N} . \end{aligned} \quad (2.23)$$

We condense ψ_{aniso} into the short notation in Eq. (2.23) using the spectral decomposition of symmetric tensors into the eigenvalues β_m and the orthonormal eigenvectors \mathbf{p}_m ($m = 1, 2, 3$). The eigenvalues β_m and eigenvectors \mathbf{p}_m are visualized in Fig. 2.6 for the two-dimensional case. In case \mathbf{N} points in the direction $\pm \mathbf{p}_m$, the energy contribution $\beta_m/2$ is active. Since we

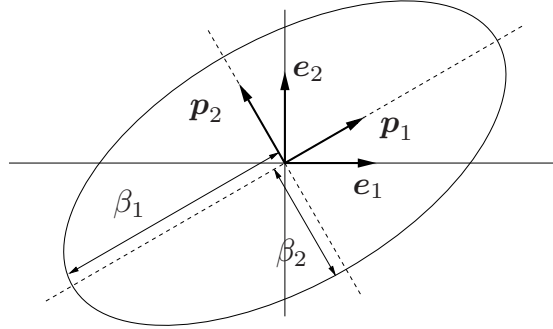


Fig. 2.6: Eigenvalues β_m and eigenvectors \mathbf{p}_m of the symmetric second order tensor \mathbf{A} .

are ultimately minimizing the energy, the direction \mathbf{p}_m with the smallest energy contribution β_m is the preferred direction. Finally, we introduce the gradient energies $\psi_{g\chi}$ and ψ_{gN} to regularize the solution. Following the micromorphic approach by Forest [84], we choose a quadratic gradient energy for the micro-damage D_χ

$$\psi_{g\chi} = \frac{1}{2} K_{g\chi} \text{Grad}(D_\chi) \cdot \text{Grad}(D_\chi) \quad (2.24)$$

and analogously for the crack surface normal \mathbf{N}

$$\psi_{gN} = \frac{1}{2} K_{gN} \text{Grad}(\mathbf{N}) : \text{Grad}(\mathbf{N}) . \quad (2.25)$$

We introduce gradient terms in both variables because we anticipate that regularization of either one of the variables will not carry over to the other one. According to the generalized standard materials framework, we also prescribe a dissipation potential

$$\phi = \frac{1}{2} \eta_D \dot{D}^2 + \frac{1}{2} \eta_N \dot{\mathbf{N}} \cdot \dot{\mathbf{N}} \quad (2.26)$$

in order to introduce viscous behavior in the damage variable D and the crack surface orientation \mathbf{N} . Note that choosing the two ingredients ψ and ϕ , where ϕ is convex, according to the generalized standard materials framework ensures thermodynamic consistency. The second law of thermodynamics is readily fulfilled, see Miehe [10]. The dissipation is non-negative. With the two ingredients, the free energy density ψ and the dissipation potential ϕ , we can formulate the rate potential

$$\pi = \dot{\psi} + \phi . \quad (2.27)$$

The primal and dual variables (constitutive equations) in the time-continuous case are given in appendix 2.A. In lieu of the time-continuous potential, we consider the time-discrete version which ultimately allows us to solve the problem numerically. We discretize the continuous time range $[0, T]$ into discrete points in time $0, t_1, \dots, t_n, t_{n+1}, \dots, T$ and call the distance between two of these points *time step* $\Delta t = t_{n+1} - t_n$. Further, we denote quantities at the previous point in time t_n with $(\cdot)_n$ while we drop the index $n+1$ for quantities at the current point in time t_{n+1} . The quantities at the previous time t_n are assumed to be known. The time discrete rate potential reads

$$\pi_\Delta = \psi - \underbrace{\psi_n}_{\text{const.}} + \underbrace{\Delta t \phi}_{=:\phi_\Delta} \quad (2.28)$$

$$\phi_\Delta = \frac{\eta_D}{2\Delta t} (D - D_n)^2 + \frac{\eta_N}{2\Delta t} (\mathbf{N} - \mathbf{N}_n) \cdot (\mathbf{N} - \mathbf{N}_n) , \quad (2.29)$$

where we used forward difference schemes to approximate the time derivatives. For $\Delta t \rightarrow 0$, the continuous problem is recovered. We assume stationarity of the following expression

$$\Pi_\Delta = \int_{\Omega_0} \pi_\Delta \, d\Omega - \int_{\partial\Omega_{0t}} \hat{\mathbf{t}} \cdot (\mathbf{u} - \mathbf{u}_n) \, dS - \int_{\Omega_0} \rho_0 \mathbf{b} \cdot (\mathbf{u} - \mathbf{u}_n) \, d\Omega \quad (2.30)$$

which balances the rate potential of the material with the external work done by the prescribed traction vector $\hat{\mathbf{t}}$ and the body force $\rho_0 \mathbf{b}$. Note that it would be possible to include external power due generalized tractions in Eq. (2.30) (i.e., tractions due to generalized stresses conjugate to $\text{Grad}(D_\chi)$ and $\text{Grad}(\mathbf{N})$). The generalized tractions are however assumed to

vanish on $\partial\Omega_0$. The vector \mathbf{u} denotes the displacement degree of freedom and $\partial\Omega_{0t}$ denotes the subset of $\partial\Omega_0$ where we prescribe the traction vector $\hat{\mathbf{t}}$ (Neumann boundary condition). Finding a stationary point means finding the point where the variation is zero

$$\Pi_\Delta \rightarrow_{\mathbf{u}, \mathbf{N}, D_\chi, D, \underline{c}}^{\text{stat}} \iff \delta\Pi_\Delta = 0. \quad (2.31)$$

Thus, we want to find the point where

$$\delta\Pi_\Delta = \delta_u\Pi_\Delta + \delta_\omega\Pi_\Delta + \delta_{D_\chi}\Pi_\Delta + \delta_D\Pi_\Delta + \delta_c\Pi_\Delta = 0$$

which is satisfied if all the summands are zero individually. The first three requirements $\delta_u\Pi_\Delta = 0$, $\delta_\omega\Pi_\Delta = 0$ and $\delta_{D_\chi}\Pi_\Delta = 0$ are treated as residuals for the global FEM system since we choose \mathbf{u} , \mathbf{N} and D_χ to be degrees of freedom, see Section 2.5. More precisely, we do not use the orientation \mathbf{N} as a degree of freedom but rather the angular velocity vector $\boldsymbol{\omega}$. The two descriptions are equivalent. \mathbf{N} gives the crack orientation immediately while $\boldsymbol{\omega}$ gives it via the exponential map, see Eq. (2.16). The advantage of $\boldsymbol{\omega}$ as degree of freedom is that it only delivers orientations \mathbf{N} that have norm 1 (by virtue of the exponential map). Note that variation with respect to the crack surface normal \mathbf{N} is computed equivalently with respect to the angular velocity vector $\boldsymbol{\omega}$, see Eq. (2.125). The next stationarity condition $\delta_D\Pi_\Delta = 0$ is used as the residual for a Newton–Raphson scheme which computes updates of D , see Sections 2.4 and 2.5. Moreover, this requirement yields an expression for dD which is used in the linearizations of the FEM residuals. Finally, the stationarity condition $\delta_c\Pi_\Delta = 0$ serves as the residual for a Newton–Raphson scheme which updates the internal variables \underline{c} , see Sections 2.4 and 2.5. First, we consider the variation with respect to the displacement \mathbf{u}

$$\delta_u\Pi_\Delta = \int_{\Omega_0} \delta_u\pi_\Delta \, d\Omega - \int_{\partial\Omega_{0t}} \hat{\mathbf{t}} \cdot \delta\mathbf{u} \, dS - \int_{\Omega_0} \rho_0\mathbf{b} \cdot \delta\mathbf{u} \, d\Omega$$

from which we finally obtain the residual

$$\begin{aligned} G_u &= \int_{\Omega_0} \left[g(D)\boldsymbol{\tau}^v + (1 - g(D_\chi))\boldsymbol{\tau}^0 \right] : \mathbf{d}_\delta \, d\Omega - \int_{\partial\Omega_{0t}} \hat{\mathbf{t}} \cdot \delta\mathbf{u} \, dS - \int_{\Omega_0} \rho_0\mathbf{b} \cdot \delta\mathbf{u} \, d\Omega \quad (2.32) \\ \boldsymbol{\tau}^v &= 2\mathbf{F} \frac{\partial\psi_{e0}(\mathbf{C})}{\partial\mathbf{C}} \mathbf{F}^\top, \quad \boldsymbol{\tau}^0 = 2\mathbf{F}^e \frac{\partial\psi_{e0}(\mathbf{C}^e)}{\partial\mathbf{C}^e} \mathbf{F}^{e\top}, \end{aligned}$$

where $\boldsymbol{\tau}^v$ and $\boldsymbol{\tau}^0$ denote the Kirchhoff-like stresses associated with \mathbf{C} and \mathbf{C}^e , respectively, and $\mathbf{d}_\delta = (\delta\mathbf{F}\mathbf{F}^{-1} + \mathbf{F}^{-\top}\delta\mathbf{F}^\top)/2$ can be thought of as the variational version of the symmetric part of the spatial velocity gradient $\mathbf{d} = (\dot{\mathbf{F}}\mathbf{F}^{-1} + \mathbf{F}^{-\top}\dot{\mathbf{F}}^\top)/2$. The full derivation is given in appendix 2.C. Using Gauss’s theorem, the local form of $G_u = 0$ in Eq. (2.32) reads

$$0 = \text{Div} \left(\left[g(D)\boldsymbol{\tau}^v + (1 - g(D_\chi))\boldsymbol{\tau}^0 \right] \mathbf{F}^{-\top} \right) + \rho_0\mathbf{b} \quad \text{in } \Omega_0 \quad (2.33)$$

$$\hat{\mathbf{t}} = \left[g(D)\boldsymbol{\tau}^v + (1 - g(D_\chi))\boldsymbol{\tau}^0 \right] \mathbf{F}^{-\top} \cdot \mathcal{N} \quad \text{at } \partial\Omega_{0t}, \quad (2.34)$$

where \mathcal{N} denotes the outer normal vector of Ω_0 . Note that, in general, $\mathbf{N} \neq \mathcal{N}$. Moreover, we prescribe the displacement $\mathbf{u} = \hat{\mathbf{u}}$ at $\partial\Omega_0 \setminus \partial\Omega_{0t}$ (Dirichlet boundary condition). Next, we inspect the variation with respect to the crack surface normal \mathbf{N}

$$\delta_\omega \Pi_\Delta = \int_{\Omega_0} \delta_\omega \pi_\Delta \, d\Omega$$

which yields the residual

$$G_N = \int_{\Omega_0} \left(\left[\left(1 - g(D_\chi) \right) \mathbf{M}_0 + \mathbf{N} \times \frac{\partial}{\partial \mathbf{N}} \left(\psi_{\text{pin}} + \psi_{\text{aniso}} + \phi_\Delta \right) \right] \cdot \boldsymbol{\omega}_\delta + \boldsymbol{\xi}_N : \text{Grad}(\delta \mathbf{N}) \right) d\Omega, \quad (2.35)$$

where \mathbf{M}_0 denotes the stress-like quantity dual to $\boldsymbol{\omega}$ and $\boldsymbol{\xi}_N = \partial\psi_{gN}/\partial\text{Grad}(\mathbf{N})$. In case of our choices for ψ and ϕ_Δ , we obtain

$$G_N = \int_{\Omega_0} \left(\left[\left(1 - g(D_\chi) \right) \mathbf{M}_0 + \begin{cases} H_N \mathbf{N}^* \times \mathbf{N}, & D \text{ or } D_\chi \geq 1 - \epsilon \\ 0, & \text{else} \end{cases} + \frac{\eta_N}{\Delta t} \mathbf{N}_n \times \mathbf{N} \right. \right. \\ \left. \left. + \sum_{m=1}^3 \beta_m (\mathbf{N} \cdot \mathbf{p}_m) (\mathbf{N} \times \mathbf{p}_m) \right] \cdot \boldsymbol{\omega}_\delta + \boldsymbol{\xi}_N : \text{Grad}(\delta \mathbf{N}) \right) d\Omega, \quad (2.36)$$

where

$$\mathbf{M}_0 = -\mathbf{L}_\omega^{\text{c}\top} : \boldsymbol{\Sigma}^e, \quad \mathbf{L}_\omega^{\text{c}\top} = -\epsilon : (\mathbb{I} - \mathbf{F}^{\text{c}\top} \square \mathbf{F}^{\text{c}-\top}) \quad \text{and} \quad \boldsymbol{\xi}_N = K_{gN} \text{Grad}(\mathbf{N}). \quad (2.37)$$

$\boldsymbol{\Sigma}^e = \mathbf{C}^e \mathbf{S}^{0e}$ denotes a Mandel-like stress tensor with respect to the intermediate configuration, \mathbb{I} denotes the fourth order identity tensor and \square denotes the product defined in Eq. (2.1). For the third order tensor $\mathbf{L}_\omega^{\text{c}\top}$, the transpose given in Eq. (2.5) is used. The full derivation is given in appendix 2.D. The local form of $G_N = 0$ in Eq. (2.36) is obtained using Gauss's theorem and reads

$$0 = \text{Div}(\boldsymbol{\xi}_N) \times \mathbf{N} + \left(1 - g(D_\chi) \right) \mathbf{M}_0 + \begin{cases} H_N \mathbf{N}^* \times \mathbf{N}, & D \text{ or } D_\chi \geq 1 - \epsilon \\ 0, & \text{else} \end{cases} \\ + \frac{\eta_N}{\Delta t} \mathbf{N}_n \times \mathbf{N} + \sum_{m=1}^3 \beta_m (\mathbf{N} \cdot \mathbf{p}_m) (\mathbf{N} \times \mathbf{p}_m), \quad \text{in } \Omega_0 \quad (2.38)$$

$$0 = \mathbf{N} \times (\boldsymbol{\xi}_N \cdot \mathcal{N}), \quad \text{at } \partial\Omega_0, \quad (2.39)$$

where \mathcal{N} denotes the outer normal vector of Ω_0 . The last residual G_{D_χ} results from the variation with respect to D_χ

$$\delta_{D_\chi} \Pi_\Delta = \int_{\Omega_0} \delta_{D_\chi} \pi_\Delta \, d\Omega$$

and reads

$$G_{D_\chi} = \int_{\Omega_0} \left(\left[-g'(D_\chi)(\psi_{e0}(\mathbf{C}^e) + \psi_k(\underline{c})) + \frac{\partial \psi_\chi}{\partial D_\chi} \right] \delta D_\chi + \boldsymbol{\xi}_{D_\chi} \cdot \text{Grad}(\delta D_\chi) \right) d\Omega, \quad (2.40)$$

where $\boldsymbol{\xi}_{D_\chi} = \partial \psi_{g\chi} / \partial \text{Grad}(D_\chi)$. In case of our choices for ψ , we obtain

$$G_{D_\chi} = \int_{\Omega_0} \left(\left[-g'(D_\chi)(\psi_{e0}(\mathbf{C}^e) + \psi_k(\underline{c})) + H_\chi(D_\chi - D) \right] \delta D_\chi + \boldsymbol{\xi}_{D_\chi} \cdot \text{Grad}(\delta D_\chi) \right) d\Omega, \quad (2.41)$$

where $\boldsymbol{\xi}_{D_\chi} = K_{g\chi} \text{Grad}(D_\chi)$. We give the full derivation in appendix 2.E. For the local form of $G_{D_\chi} = 0$ in Eq. (2.41), we write

$$0 = -\text{Div}(\boldsymbol{\xi}_{D_\chi}) - g'(D_\chi)(\psi_{e0}(\mathbf{C}^e) + \psi_k(\underline{c})) + H_\chi(D_\chi - D) \quad \text{in } \Omega_0 \quad (2.42)$$

$$0 = \boldsymbol{\xi}_{D_\chi} \cdot \mathcal{N} \quad \text{at } \partial\Omega_0. \quad (2.43)$$

2.4 Treatment of internal variables and linearization of residuals

2.4.1 Stationarity condition for internal variables \underline{c}

From the stationarity of the incremental potential in Eq. (2.31), we have so far obtained three residuals (Eqs. (2.32), (2.36) and (2.41)) for the global FEM system. The last two conditions that we have not yet evaluated, are $\delta_c \Pi_\Delta = 0$ and $\delta_D \Pi_\Delta = 0$. In order to derive the stationarity conditions with respect to the internal variables \underline{c} from the condition $\delta_c \Pi_\Delta = 0$, we consider

$$\delta_c \Pi_\Delta = \int_{\Omega_0} \delta_c \pi_\Delta d\Omega = \int_{\Omega_0} (1 - g(D_\chi)) \delta_c (\psi_{e0}(\mathbf{C}^e) + \psi_k(\underline{c})) d\Omega = 0$$

which is fulfilled if

$$0 = \delta_c \tilde{\psi} = \frac{\partial \tilde{\psi}}{\partial \underline{c}} \cdot \delta \underline{c} = \tilde{\psi}_c \cdot \delta \underline{c} = \delta_c \psi_{e0}(\mathbf{C}^e) + \delta_c \psi_k(\underline{c}), \quad (2.44)$$

where we used $\tilde{\psi} = \psi_{e0}(\mathbf{C}^e) + \psi_k(\underline{c})$. For the second summand in Eq. (2.44), we consider $\varepsilon \geq 0$ because $\varepsilon < 0$ entails $\psi_k \rightarrow \infty$ which cannot be the stationary point we are searching for. Thus, we write

$$\delta_c \psi_k(\underline{c}) = \delta_c \left(\frac{1}{2} k \underline{c} \cdot \underline{c} \right) = k \underline{c} \cdot \delta \underline{c}.$$

For the first summand, we consider

$$\delta_c \psi_{e0}(\mathbf{C}^e) = \frac{\partial \psi_{e0}(\mathbf{C}^e)}{\partial \mathbf{C}^e} : \delta_c \mathbf{C}^e = \frac{1}{2} \mathbf{S}^{0e} : \delta_c \mathbf{C}^e.$$

For $\delta_c \mathbf{C}^e$, we use Eq. (2.102). However, instead of computing the variation of \mathbf{F}^c with respect to the crack surface normal \mathbf{N} (or $\boldsymbol{\omega}$, as in Eq. (2.103)), we compute it with respect to the internal variables \underline{c} . The resulting expression for $\delta_c \mathbf{F}^c \mathbf{F}^{c-1}$, using Eqs. (2.9) and (2.10), reads

$$\begin{aligned} \delta_c \mathbf{F}^c \mathbf{F}^{c-1} &= \left(\delta \varepsilon \mathbf{N} \otimes \mathbf{N} + \sum_{i=1}^2 \delta \gamma_i \mathbf{d}_i \otimes \mathbf{N} \right) \left(\mathbf{I} - \frac{\varepsilon}{1+\varepsilon} \mathbf{N} \otimes \mathbf{N} - \sum_{i=1}^2 \frac{\gamma_i}{1+\varepsilon} \mathbf{d}_i \otimes \mathbf{N} \right) \\ &= \frac{\delta \varepsilon}{1+\varepsilon} \mathbf{N} \otimes \mathbf{N} + \sum_{i=1}^2 \frac{\delta \gamma_i}{1+\varepsilon} \mathbf{d}_i \otimes \mathbf{N} \end{aligned} \quad (2.45)$$

which yields

$$\delta_c \psi_{e0}(\mathbf{C}^e) = -\boldsymbol{\Sigma}^e : \left(\frac{\delta \varepsilon}{1+\varepsilon} \mathbf{N} \otimes \mathbf{N} + \sum_{i=1}^2 \frac{\delta \gamma_i}{1+\varepsilon} \mathbf{d}_i \otimes \mathbf{N} \right).$$

Thus, we obtain from Eq. (2.44) the following stationarity conditions

$$\begin{aligned} 0 &= \delta \varepsilon \left(k\varepsilon - \frac{\mathbf{N} \cdot \boldsymbol{\Sigma}^e \cdot \mathbf{N}}{1+\varepsilon} \right) + \sum_{i=1}^2 \delta \gamma_i \left(k\gamma_i - \frac{\mathbf{d}_i \cdot \boldsymbol{\Sigma}^e \cdot \mathbf{N}}{1+\varepsilon} \right) \quad \forall \delta \varepsilon, \delta \gamma_i, \quad i = 1, 2 \\ \Leftrightarrow k\varepsilon &= \frac{\mathbf{N} \cdot \boldsymbol{\Sigma}^e \cdot \mathbf{N}}{1+\varepsilon} \end{aligned} \quad (2.46)$$

$$k\gamma_i = \frac{\mathbf{d}_i \cdot \boldsymbol{\Sigma}^e \cdot \mathbf{N}}{1+\varepsilon}, \quad i = 1, 2. \quad (2.47)$$

2.4.2 Traction free crack surface

An interesting conclusion can be drawn from the case where we choose $k = 0$ and assume $(1+\varepsilon) \neq 0$. In that case, the stationarity conditions for \underline{c} are fulfilled if

$$\begin{aligned} 0 &= \underbrace{\left(u\mathbf{N} + \sum_{i=1}^2 v_i \mathbf{d}_i \right)}_{=\mathbf{w}} \cdot \boldsymbol{\Sigma}^e \cdot \mathbf{N} \\ &= \mathbf{w} \cdot \mathbf{F}^{e\top} \mathbf{F}^e \mathbf{S}^{0e} \mathbf{F}^{e\top} \mathbf{F}^{e-\top} \cdot \mathbf{N} \\ &= \mathbf{F}^e \mathbf{w} \cdot \mathbf{F}^e \mathbf{S}^{0e} \mathbf{F}^{e\top} \cdot \mathbf{F}^{e-\top} \mathbf{N} \\ &= \tilde{\mathbf{w}} \cdot \mathbf{F}^e \mathbf{S}^{0e} \mathbf{F}^{e\top} \cdot \mathbf{F}^{e-\top} \mathbf{N} \end{aligned} \quad (2.48)$$

for arbitrary $u, v_i \in \mathbb{R}$ ($i = 1, 2$) or arbitrary vectors \mathbf{w} and $\tilde{\mathbf{w}}$. In order to find an expression for $\mathbf{F}^{e-\top} \mathbf{N}$, we consider the mapping property of \mathbf{F} for surface elements (Nanson's relation [85]). The surface element $\mathbf{n} da$ in current configuration is related to the surface element $\mathbf{N} dA$ in reference configuration via

$$\mathbf{n} da = \det(\mathbf{F}) \mathbf{F}^{-\top} \mathbf{N} dA$$

$$= \det(\mathbf{F}^e) \mathbf{F}^{e-\top} \det(\mathbf{F}^c) \mathbf{F}^{c-\top} \mathbf{N} \, dA . \quad (2.49)$$

The crack deformation gradient \mathbf{F}^c does not change the orientation of \mathbf{N} , see Section 2.2. Thus, $\det(\mathbf{F}^c) \mathbf{F}^{c-\top} \mathbf{N} \, dA$ maps the surface element $\mathbf{N} \, dA$ to a scaled surface element $\alpha \mathbf{N} \, dA$ ($\alpha \in \mathbb{R}_{>0}$) with the same orientation. Together with Eq. (2.49), this yields for the orientation \mathbf{n} in the current configuration

$$\mathbf{n} = \frac{\alpha \det(\mathbf{F}^e) \, dA}{da} \mathbf{F}^{e-\top} \mathbf{N} .$$

Multiplying the stationarity condition in Eq. (2.48) with $\alpha \, dA / da \neq 0$ yields

$$\begin{aligned} 0 &= \tilde{\mathbf{w}} \cdot \frac{1}{\det(\mathbf{F}^e)} \mathbf{F}^e \mathbf{S}^{0e} \mathbf{F}^{e\top} \cdot \frac{\alpha \det(\mathbf{F}^e) \, dA}{da} \mathbf{F}^{e-\top} \mathbf{N}, & \frac{\alpha \, dA}{da} &\neq 0 \\ 0 &= \tilde{\mathbf{w}} \cdot \boldsymbol{\sigma}^{0e} \cdot \mathbf{n} & \forall \tilde{\mathbf{w}} \\ \Leftrightarrow 0 &= \boldsymbol{\sigma}^{0e} \cdot \mathbf{n} , \end{aligned} \quad (2.50)$$

where $\boldsymbol{\sigma}^{0e}$ is the Cauchy stress related to $\psi_{e0}(\mathbf{C}^e)$ in the current configuration. This means that the traction in the crack vanishes, which is an important property that arises from the model assumptions and is not assumed itself. This is an advantage over spectral tension-compression split approaches which are prone to violating the requirement of traction-free crack surfaces, see Strobl and Seelig [75].

2.4.3 Linearization of residual for internal variables \underline{c}

In order to update γ_i ($i = 1, 2$) and ε , we need to solve Eqs. (2.46) and (2.47). Since $\boldsymbol{\Sigma}^e$ is a nonlinear function of ε and γ_i , we cannot solve these equations directly. Instead, we use a Newton-Raphson scheme to compute iterative updates on the internal variables \underline{c} , see Section 2.5. We choose the residual for the Newton-Raphson scheme as follows

$$r^{\gamma_i} = \frac{\mathbf{d}_i \cdot \boldsymbol{\Sigma}^e \cdot \mathbf{N}}{1 + \varepsilon} - k \gamma_i, \quad i = 1, 2 \quad (2.51)$$

$$r^\varepsilon = \frac{\mathbf{N} \cdot \boldsymbol{\Sigma}^e \cdot \mathbf{N}}{1 + \varepsilon} - k \varepsilon \quad (2.52)$$

$$\underline{r} = [r^{\gamma_1}, r^{\gamma_2}, r^\varepsilon]^\top = -\frac{\partial \tilde{\psi}}{\partial \underline{c}} = -\tilde{\psi}_c . \quad (2.53)$$

The linearization of the residual r^{γ_i} in Eq. (2.51) with respect to the internal variables \underline{c} reads

$$\begin{aligned} d_c r^{\gamma_i} &= \frac{\partial r^{\gamma_i}}{\partial \varepsilon} d\varepsilon + \sum_{j=1}^2 \frac{\partial r^{\gamma_i}}{\partial \gamma_j} d\gamma_j, \quad i = 1, 2 \\ d_c r^{\gamma_i} &= d\varepsilon \left[-\frac{2}{(1 + \varepsilon)^2} \left(\mathbf{A}_{d_i}^S : \mathbf{A}_N^C + \mathbf{A}_{d_i}^C : \frac{d\mathbf{S}^{0e}}{d\mathbf{C}^e} : \mathbf{A}_N^C + \frac{1}{2} \mathbf{d}_i \cdot \boldsymbol{\Sigma}^e \cdot \mathbf{N} \right) \right] \end{aligned}$$

$$+ \sum_{j=1}^2 d\gamma_j \left[-\frac{2}{(1+\varepsilon)^2} \left(\mathbf{A}_{d_i}^S : \mathbf{A}_{d_j}^C + \mathbf{A}_{d_i}^C : \frac{d\mathbf{S}^{0e}}{d\mathbf{C}^e} : \mathbf{A}_{d_j}^C \right) - k\delta_{ij} \right], \quad (2.54)$$

where

$$\mathbf{A}_{d_i}^S = \text{sym}(\mathbf{d}_i \otimes \mathbf{S}^{0e} \cdot \mathbf{N}), \quad \mathbf{A}_{d_i}^C = \text{sym}(\mathbf{C}^e \cdot \mathbf{d}_i \otimes \mathbf{N}), \quad \text{and} \quad \mathbf{A}_N^C = \text{sym}(\mathbf{C}^e \cdot \mathbf{N} \otimes \mathbf{N}). \quad (2.55)$$

The linearization of the residual r^ε in Eq. (2.52) with respect to the internal variables \underline{c} reads

$$\begin{aligned} d_c r^\varepsilon &= \frac{\partial r^\varepsilon}{\partial \varepsilon} d\varepsilon + \sum_{j=1}^2 \frac{\partial r^\varepsilon}{\partial \gamma_j} d\gamma_j \\ d_c r^\varepsilon &= d\varepsilon \left[-\frac{2}{(1+\varepsilon)^2} \left(\mathbf{A}_N^S : \mathbf{A}_N^C + \mathbf{A}_N^C : \frac{d\mathbf{S}^{0e}}{d\mathbf{C}^e} : \mathbf{A}_N^C + \frac{1}{2} \mathbf{N} \cdot \boldsymbol{\Sigma}^e \cdot \mathbf{N} \right) - k \right] \\ &\quad + \sum_{j=1}^2 d\gamma_j \left[-\frac{2}{(1+\varepsilon)^2} \left(\mathbf{A}_N^S : \mathbf{A}_{d_j}^C + \mathbf{A}_N^C : \frac{d\mathbf{S}^{0e}}{d\mathbf{C}^e} : \mathbf{A}_{d_j}^C \right) \right], \end{aligned} \quad (2.56)$$

where

$$\mathbf{A}_N^S = \text{sym}(\mathbf{N} \otimes \mathbf{S}^{0e} \cdot \mathbf{N}). \quad (2.57)$$

The full derivations of Eqs. (2.54) and (2.56) are given in appendix 2.F. We summarize the linearization with respect to the internal variables \underline{c} as follows

$$d_c \underline{r} = \frac{\partial \underline{r}}{\partial \underline{c}} \cdot d\underline{c} = \begin{bmatrix} \partial r^{\gamma_1} / \partial \gamma_1 & \partial r^{\gamma_1} / \partial \gamma_2 & \partial r^{\gamma_1} / \partial \varepsilon \\ \partial r^{\gamma_2} / \partial \gamma_1 & \partial r^{\gamma_2} / \partial \gamma_2 & \partial r^{\gamma_2} / \partial \varepsilon \\ \partial r^\varepsilon / \partial \gamma_1 & \partial r^\varepsilon / \partial \gamma_2 & \partial r^\varepsilon / \partial \varepsilon \end{bmatrix} \cdot \begin{bmatrix} d\gamma_1 \\ d\gamma_2 \\ d\varepsilon \end{bmatrix}. \quad (2.58)$$

We do not only need the linearization of the residual \underline{r} , Eq. (2.53), with respect to the internal variables \underline{c} but also with respect to the degrees of freedom \mathbf{u} and \mathbf{N} (or rather \mathbf{d} and $\boldsymbol{\omega}$). The latter two linearizations are crucial to express the differential $d\underline{c}$ in terms of \mathbf{d}_d and $\boldsymbol{\omega}_d$ (see Eqs. (2.72), (2.75), (2.79) and (2.82) and cf. Eqs. (2.121) and (2.161)). In order to find $d\underline{c}$, we consider the equilibrium state where $\underline{r} = \underline{0}$. In the equilibrium state $\underline{r} = \underline{0}$, we do not want \underline{r} to change anymore which is reflected in the condition $d\underline{r} = \underline{0}$. This condition yields the desired expression of the differential $d\underline{c}$

$$\begin{aligned} \underline{0} = d\underline{r} \quad \Leftrightarrow \quad \underline{0} &= \frac{\partial \underline{r}}{\partial \underline{c}} \cdot d\underline{c} + \underline{r}_\omega \cdot \boldsymbol{\omega}_d + \underline{r}_d : \mathbf{d}_d \\ d\underline{c} &= -\left(\frac{\partial \underline{r}}{\partial \underline{c}} \right)^{-1} (\underline{r}_\omega \cdot \boldsymbol{\omega}_d + \underline{r}_d : \mathbf{d}_d) \end{aligned} \quad (2.59)$$

in terms of \mathbf{d}_d and $\boldsymbol{\omega}_d$. The linearization of the residual r^{γ_i} in Eq. (2.51) with respect to the degrees of freedom \mathbf{u} and \mathbf{N} (or rather \mathbf{d} and $\boldsymbol{\omega}$, i.e., for fixed \underline{c}) reads

$$\begin{aligned} \left. dr^{\gamma_i} \right|_{\underline{c}} &= r_{\omega}^{\gamma_i} \cdot \boldsymbol{\omega}_d + r_d^{\gamma_i} : \mathbf{d}_d \\ \left. dr^{\gamma_i} \right|_{\underline{c}} &= \frac{1}{1+\varepsilon} \left(\mathbf{d}_i \times (\boldsymbol{\Sigma}^e \cdot \mathbf{N}) + \mathbf{N} \times (\boldsymbol{\Sigma}^{e\top} \cdot \mathbf{d}_i) + \left(\mathbf{A}_{d_i}^S + \mathbf{A}_{d_i}^C : \frac{d\mathbf{S}^{0e}}{d\mathbf{C}^e} \right) : \mathbf{C}_{\omega}^e \right) \cdot \boldsymbol{\omega}_d \\ &\quad + \frac{1}{1+\varepsilon} \left(\mathbf{A}_{d_i}^S + \mathbf{A}_{d_i}^C : \frac{d\mathbf{S}^{0e}}{d\mathbf{C}^e} \right) \mathbf{C}_d^e : \mathbf{d}_d, \end{aligned} \quad (2.60)$$

where

$$\mathbf{C}_{\omega}^e = -2\mathbf{C}^e \square_{\mathbb{S}} \mathbf{I} : \mathbf{L}_{\omega}^c, \quad \mathbf{L}_{\omega}^c = -\left(\mathbb{I} - \mathbf{F}^c \square \mathbf{F}^{c-1} \right) : \boldsymbol{\epsilon} \quad \text{and} \quad \mathbf{C}_d^e = 2\mathbf{F}^{e\top} \square_{\mathbb{S}} \mathbf{F}^e. \quad (2.61)$$

The linearization of the residual r^{ε} in Eq. (2.52) with respect to the degrees of freedom \mathbf{u} and \mathbf{N} (\mathbf{d} and $\boldsymbol{\omega}$) reads

$$\begin{aligned} \left. dr^{\varepsilon} \right|_{\underline{c}} &= r_{\omega}^{\varepsilon} \cdot \boldsymbol{\omega}_d + r_d^{\varepsilon} : \mathbf{d}_d \\ \left. dr^{\varepsilon} \right|_{\underline{c}} &= \frac{1}{1+\varepsilon} \left(\mathbf{N} \times (2 \operatorname{sym}(\boldsymbol{\Sigma}^e) \cdot \mathbf{N}) + \left(\mathbf{A}_N^S + \mathbf{A}_N^C : \frac{d\mathbf{S}^{0e}}{d\mathbf{C}^e} \right) : \mathbf{C}_{\omega}^e \right) \cdot \boldsymbol{\omega}_d \\ &\quad + \frac{1}{1+\varepsilon} \left(\mathbf{A}_N^S + \mathbf{A}_N^C : \frac{d\mathbf{S}^{0e}}{d\mathbf{C}^e} \right) : \mathbf{C}_d^e : \mathbf{d}_d. \end{aligned} \quad (2.62)$$

The full derivations of Eqs. (2.60) and (2.62) are given in appendix 2.F. We summarize the full linearization as follows

$$\begin{aligned} \underline{dr} &= \begin{bmatrix} \partial r^{\gamma_1} / \partial \gamma_1 & \partial r^{\gamma_1} / \partial \gamma_2 & \partial r^{\gamma_1} / \partial \varepsilon \\ \partial r^{\gamma_2} / \partial \gamma_1 & \partial r^{\gamma_2} / \partial \gamma_2 & \partial r^{\gamma_2} / \partial \varepsilon \\ \partial r^{\varepsilon} / \partial \gamma_1 & \partial r^{\varepsilon} / \partial \gamma_2 & \partial r^{\varepsilon} / \partial \varepsilon \end{bmatrix} \cdot \begin{bmatrix} d\gamma_1 \\ d\gamma_2 \\ d\varepsilon \end{bmatrix} + \begin{bmatrix} r_{\omega}^{\gamma_1} \\ r_{\omega}^{\gamma_2} \\ r_{\omega}^{\varepsilon} \end{bmatrix} \cdot \boldsymbol{\omega}_d + \begin{bmatrix} r_d^{\gamma_1} \\ r_d^{\gamma_2} \\ r_d^{\varepsilon} \end{bmatrix} : \mathbf{d}_d \\ \underline{r}_{\omega} &= -\tilde{\psi}_{c\omega} = [r_{\omega}^{\gamma_1}, r_{\omega}^{\gamma_2}, r_{\omega}^{\varepsilon}]^{\top} \\ \underline{r}_d &= -\tilde{\psi}_{cd} = [r_d^{\gamma_1}, r_d^{\gamma_2}, r_d^{\varepsilon}]^{\top}. \end{aligned} \quad (2.63)$$

$$\underline{r}_d = -\tilde{\psi}_{cd} = [r_d^{\gamma_1}, r_d^{\gamma_2}, r_d^{\varepsilon}]^{\top}. \quad (2.64)$$

2.4.4 Stationarity condition for damage D

Next, we treat the last condition, $\delta_D \Pi_{\Delta} = 0$, which we obtained from the stationarity of the incremental potential in Eq. (2.31). As mentioned before in Section 2.3, the condition

$$\delta_D \Pi_{\Delta} = \int_{\Omega_0} \delta_D \pi_{\Delta} d\Omega \stackrel{!}{=} 0 \quad (2.65)$$

serves as the residual for a Newton–Raphson scheme which computes updates of D . The condition in Eq. (2.65) is fulfilled if the integrand is zero

$$\begin{aligned} 0 &= \delta_D \pi_\Delta = \delta_D \left(g(D) \psi_{e0}(\mathbf{C}) + \psi_h(D) + \psi_\chi(D_\chi - D) + \phi_\Delta \right) \\ &= \left(g'(D) \psi_{e0}(\mathbf{C}) + \frac{\partial \psi_h}{\partial D} + \frac{\partial \psi_\chi}{\partial D} + \frac{\partial \phi_\Delta}{\partial D} \right) \delta D = \frac{\partial \pi_\Delta}{\partial D} \delta D . \end{aligned}$$

Using our choices for ψ and ϕ_Δ , the variation with respect to D reads

$$\delta_D \pi_\Delta = \frac{\partial \pi_\Delta}{\partial D} \delta D = \left(g'(D) \psi_{e0}(\mathbf{C}) + HD - H_\chi(D_\chi - D) + \frac{\eta_D}{\Delta t} (D - D_n) \right) \delta D .$$

We finally obtain the following residual for the Newton–Raphson scheme

$$\begin{aligned} r(D) &= -\frac{\partial \pi_\Delta}{\partial D} = -g'(D) \psi_{e0}(\mathbf{C}) - \frac{\partial \psi_h}{\partial D} - \frac{\partial \psi_\chi}{\partial D} - \frac{\partial \phi_\Delta}{\partial D} \\ &= -g'(D) \psi_{e0}(\mathbf{C}) - HD + H_\chi(D_\chi - D) - \frac{\eta_D}{\Delta t} (D - D_n) . \end{aligned} \quad (2.66)$$

The case $r(D) < 0$, which implies $\partial \pi_\Delta / \partial D > 0$, indicates that the potential π_Δ increases with increasing D . Thus, the material is not degrading (i.e., not losing energy) with increasing D , which means that $r(D) < 0$ denotes the non-damage case. Conversely, $r(D) > 0$ indicates the damage case. $r(D) = 0$, which implies $\partial \pi_\Delta / \partial D = 0$, indicates a stationary point of the rate potential π_Δ which we are ultimately searching for.

The usual procedure would be to only update the damage variable D in case $r(D) > 0$. This implies that D is monotonically increasing, i.e., that any increase in damage is irreversible. However, there are indications to suggest that damage should only be irreversible once it has crossed a threshold close to 1, see Linse et al. [86]. In order to account for this phenomenon, we update D irrespective of whether $r(D)$ is greater or less than zero. This allows for positive and negative increments of D . Relaxed irreversibility of damage only ceases once the threshold $D = 1 - \epsilon$ is reached where $\epsilon > 0$ is small. Only complete damage is irreversible. The update of D is performed until a stationary point of π_Δ with respect to D , indicated by $r(D) = 0$, is found.

For the linearization, we require $r(D)$ to remain zero upon perturbations in the degrees of freedom, i.e., we require

$$0 = dr = \frac{\partial r}{\partial D} dD + \frac{\partial r}{\partial \mathbf{C}} : d\mathbf{C} + \frac{\partial r}{\partial D_\chi} dD_\chi$$

which can be reformulated to yield

$$dD = -\frac{1}{\partial r / \partial D} \left(\frac{\partial r}{\partial \mathbf{C}} : d\mathbf{C} + \frac{\partial r}{\partial D_\chi} dD_\chi \right)$$

$$dD = \frac{1}{-g''(D)\psi_{e0}(\mathbf{C}) - \frac{\partial^2 \psi_h}{\partial D^2} - \frac{\partial^2 \psi_\chi}{\partial D^2} - \frac{\partial^2 \phi_\Delta}{\partial D^2}} \left(g'(D)\boldsymbol{\tau}^v : \mathbf{d}_d + \frac{\partial^2 \psi_\chi}{\partial D \partial D_\chi} dD_\chi \right), \quad (2.67)$$

where we used $\partial \psi_{e0}(\mathbf{C})/\partial \mathbf{C} : d\mathbf{C} = \boldsymbol{\tau}^v : \mathbf{d}_d$, cf. appendix 2.C. To shorten the notation of Eq. (2.67), we write

$$dD = \frac{1}{\partial r/\partial D} \left(g'(D)\boldsymbol{\tau}^v : \mathbf{d}_d + \frac{\partial^2 \psi_\chi}{\partial D \partial D_\chi} dD_\chi \right). \quad (2.68)$$

Using our choice of ψ and ϕ_Δ , this expression reads

$$dD = \frac{1}{-g''(D)\psi_{e0}(\mathbf{C}) - H - H_\chi - \frac{\eta_D}{\Delta t}} \left(g'(D)\boldsymbol{\tau}^v : \mathbf{d}_d - H_\chi dD_\chi \right)$$

or again in short notation

$$dD = \frac{1}{\partial r/\partial D} \left(g'(D)\boldsymbol{\tau}^v : \mathbf{d}_d - H_\chi dD_\chi \right). \quad (2.69)$$

2.4.5 Linearization of residuals G_u , G_N and G_{D_χ}

Besides the residuals which we derived in Section 2.3, we also need the linearization of the residuals for the FEM implementation. The linearization of G_u , Eq. (2.32), reads

$$\begin{aligned} dG_u = \int_{\Omega_0} & \left((\mathbf{l}_d \cdot [g(D)\boldsymbol{\tau}^v + (1 - g(D_\chi))\boldsymbol{\tau}^0] \cdot \mathbf{l}_\delta^\top) : \mathbf{I} \right. \\ & + \mathbf{d}_\delta : \left[g(D)\mathbb{C}_v^e + (1 - g(D_\chi))\mathbb{C}_{dd} + \frac{(g'(D))^2}{\partial r/\partial D} \boldsymbol{\tau}^v \otimes \boldsymbol{\tau}^v \right] : \mathbf{d}_d \\ & + \mathbf{d}_\delta : [(1 - g(D_\chi))\mathbb{C}_{d\omega}] \cdot \boldsymbol{\omega}_d \\ & \left. + \mathbf{d}_\delta : \left[\frac{g'(D)}{\partial r/\partial D} \frac{\partial^2 \psi_\chi}{\partial D \partial D_\chi} \boldsymbol{\tau}^v - g'(D_\chi)\boldsymbol{\tau}^0 \right] dD_\chi \right) d\Omega, \end{aligned} \quad (2.70)$$

where $\mathbf{l}_d = d\mathbf{F}\mathbf{F}^{-1}$ (similar \mathbf{l}_δ), \mathbb{C}_{dd} denotes the spatial algorithmic moduli related to $\boldsymbol{\tau}^0$ and \mathbf{d}_d , \mathbb{C}_v^e denotes the spatial algorithmic moduli related to $\boldsymbol{\tau}^v$ and \mathbf{d}_d and $\mathbb{C}_{d\omega}$ denotes the spatial algorithmic moduli related to $\boldsymbol{\tau}^0$ and $\boldsymbol{\omega}_d$. It is again important to note that $d \neq \delta$. With our choice for ψ and ϕ_Δ , we obtain

$$\begin{aligned} dG_u = \int_{\Omega_0} & \left((\mathbf{l}_d \cdot [g(D)\boldsymbol{\tau}^v + (1 - g(D_\chi))\boldsymbol{\tau}^0] \cdot \mathbf{l}_\delta^\top) : \mathbf{I} \right. \\ & + \mathbf{d}_\delta : \left[g(D)\mathbb{C}_v^e + (1 - g(D_\chi))\mathbb{C}_{dd} + \frac{(g'(D))^2}{\partial r/\partial D} \boldsymbol{\tau}^v \otimes \boldsymbol{\tau}^v \right] : \mathbf{d}_d \\ & \left. + \mathbf{d}_\delta : [(1 - g(D_\chi))\mathbb{C}_{d\omega}] \cdot \boldsymbol{\omega}_d \right) \end{aligned}$$

$$+\mathbf{d}_\delta : \left[-\frac{g'(D)H_\chi}{\partial r/\partial D} \boldsymbol{\tau}^v - g'(D_\chi) \boldsymbol{\tau}^0 \right] dD_\chi \Big) d\Omega , \quad (2.71)$$

where

$$\mathbb{C}_{dd} = \mathbb{C}_0^e + \underline{r}_d^\top \left(\frac{\partial \underline{r}}{\partial \underline{c}} \right)^{-1} \underline{r}_d \quad (2.72)$$

$$\mathbb{C}_0^e = \mathbf{F}^e \stackrel{s}{\square} \mathbf{F}^{e\top} : 2 \frac{d\mathbf{S}^{0e}}{d\mathbf{C}^e} : \mathbf{F}^{e\top} \stackrel{s}{\square} \mathbf{F}^e \quad (2.73)$$

$$\mathbb{C}_v^e = \mathbf{F} \stackrel{s}{\square} \mathbf{F}^\top : 2 \frac{d\mathbf{S}^v}{d\mathbf{C}} : \mathbf{F}^\top \stackrel{s}{\square} \mathbf{F} \quad (2.74)$$

$$\mathbb{C}_{d\omega} = \tilde{\psi}_{d\omega} + \underline{r}_d^\top \left(\frac{\partial \underline{r}}{\partial \underline{c}} \right)^{-1} \underline{r}_\omega \quad (2.75)$$

$$\tilde{\psi}_{d\omega} = \mathbf{F}^e \stackrel{s}{\square} \mathbf{F}^{e\top} : \left(-2 \mathbf{I} \stackrel{s}{\square} \mathbf{S}^{0e} - \frac{d\mathbf{S}^{0e}}{d\mathbf{C}^e} : 2\mathbf{C}^e \stackrel{s}{\square} \mathbf{I} \right) : \mathbf{L}_\omega^c . \quad (2.76)$$

See appendix 2.C for the full derivation and Eqs. (2.58), (2.63) and (2.64) for $\partial \underline{r}/\partial \underline{c}$, \underline{r}_ω and \underline{r}_d . Note that r represents the stationarity condition for D and \underline{r} reflects the stationarity condition for \underline{c} . Next, the linearization of G_N , Eq. (2.35), reads

$$\begin{aligned} dG_N = \int_{\Omega_0} & \left(\boldsymbol{\omega}_\delta \cdot \left[(1 - g(D_\chi)) \mathbb{C}_{\omega\omega} - \left(\mathbf{N} \cdot \frac{\partial}{\partial \mathbf{N}} (\psi_{\text{pin}} + \psi_{\text{aniso}} + \phi_\Delta) \right) \mathbf{I} \right. \right. \\ & \quad \left. \left. - \boldsymbol{\epsilon} : \mathbf{N} \otimes \frac{\partial^2}{\partial \mathbf{N}^2} (\psi_{\text{pin}} + \psi_{\text{aniso}} + \phi_\Delta) \otimes \mathbf{N} : \boldsymbol{\epsilon} \right] \cdot \boldsymbol{\omega}_d \right. \\ & + \boldsymbol{\omega}_\delta \cdot \left[(1 - g(D_\chi)) \mathbb{C}_{\omega d} \right] : \mathbf{d}_d \\ & + \boldsymbol{\omega}_\delta \cdot \left[-g'(D_\chi) \mathbf{M}_0 \right] dD_\chi \\ & \left. + \text{Grad}(\delta \mathbf{N}) : \frac{\partial \boldsymbol{\xi}_N}{\partial \text{Grad}(\mathbf{N})} : \text{Grad}(d\mathbf{N}) - \boldsymbol{\xi}_N : \text{Grad}((\boldsymbol{\omega}_\delta \cdot \boldsymbol{\omega}_d) \mathbf{N}) \right) d\Omega , \end{aligned} \quad (2.77)$$

where $\mathbb{C}_{\omega\omega}$ and $\mathbb{C}_{\omega d}$ denote the spatial algorithmic moduli related to \mathbf{M}_0 and $\boldsymbol{\omega}_d$, and \mathbf{M}_0 and \mathbf{d}_d , respectively. Using our choices for ψ and ϕ_Δ from above, we write the linearization of G_N , Eq. (2.36), as follows

$$\begin{aligned} dG_N = \int_{\Omega_0} & \left(\boldsymbol{\omega}_\delta \cdot \left[(1 - g(D_\chi)) \mathbb{C}_{\omega\omega} + \begin{cases} H_N(\mathbf{N}^* \cdot \mathbf{N}) \mathbf{I}, & D \text{ or } D_\chi \geq 1 - \epsilon \\ 0, & \text{else} \end{cases} + \frac{\eta_N}{\Delta t} (\mathbf{N}_n \cdot \mathbf{N}) \mathbf{I} \right. \right. \\ & \quad \left. \left. + \sum_{m=1}^3 \beta_m \left((\mathbf{N} \times \mathbf{p}_m) \otimes (\mathbf{N} \times \mathbf{p}_m) - (\mathbf{N} \cdot \mathbf{p}_m)^2 \mathbf{I} \right) \right] \cdot \boldsymbol{\omega}_d \right. \\ & + \boldsymbol{\omega}_\delta \cdot \left[(1 - g(D_\chi)) \mathbb{C}_{\omega d} \right] : \mathbf{d}_d \\ & \left. + \boldsymbol{\omega}_\delta \cdot \left[-g'(D_\chi) \mathbf{M}_0 \right] dD_\chi \right) \end{aligned}$$

$$+\text{Grad}(\delta \mathbf{N}) : \frac{\partial \boldsymbol{\xi}_N}{\partial \text{Grad}(\mathbf{N})} : \text{Grad}(\text{d}\mathbf{N}) - \boldsymbol{\xi}_N : \text{Grad}((\boldsymbol{\omega}_\delta \cdot \boldsymbol{\omega}_d) \mathbf{N}) \Big) \text{d}\Omega, \quad (2.78)$$

where

$$\mathbb{C}_{\omega\omega} = \mathbb{C}_{\omega\omega}^e + \underline{r}_\omega^\top \left(\frac{\partial \underline{r}}{\partial \underline{c}} \right)^{-1} \underline{r}_\omega \quad (2.79)$$

$$\begin{aligned} \mathbb{C}_{\omega\omega}^e = & \mathbf{L}_\omega^c{}^\top : \left(\mathbf{C}^e \square \mathbf{S}^{0e} + \mathbf{C}^e \square_{\underline{s}} \mathbf{I} : 2 \frac{\text{d}\mathbf{S}^{0e}}{\text{d}\mathbf{C}^e} : \mathbf{C}^e \square_{\underline{s}} \mathbf{I} \right) : \mathbf{L}_\omega^c \\ & - 2 \text{tr}(\boldsymbol{\Sigma}^e) \mathbf{I} + 2 \text{sym}(\boldsymbol{\Sigma}^e) - k\boldsymbol{\gamma} + 2 \text{sym}(\boldsymbol{\epsilon} : \mathbf{F}^{c-\top} \square \mathbf{F}^c{}^\top \boldsymbol{\Sigma}^e : \boldsymbol{\epsilon}) \end{aligned} \quad (2.80)$$

$$\boldsymbol{\gamma} = \sum_{m=1}^2 \sum_{n=1}^2 \gamma_m \gamma_n \mathbf{d}_m \otimes \mathbf{d}_n \quad (2.81)$$

$$\mathbb{C}_{\omega d} = \tilde{\psi}_{\omega d} + \underline{r}_\omega^\top \left(\frac{\partial \underline{r}}{\partial \underline{c}} \right)^{-1} \underline{r}_d \quad (2.82)$$

$$\tilde{\psi}_{\omega d} = -\mathbf{L}_\omega^c{}^\top : \left(\mathbf{I} \square_{\underline{s}} \mathbf{S}^{0e} + \mathbf{C}^e \square_{\underline{s}} \mathbf{I} : \frac{\text{d}\mathbf{S}^{0e}}{\text{d}\mathbf{C}^e} \right) : \mathbf{C}_d^e \quad (2.83)$$

$$\frac{\partial \boldsymbol{\xi}_N}{\partial \text{Grad}(\mathbf{N})} = K_{gN} \mathbb{I}. \quad (2.84)$$

We present the full derivation in appendix 2.D. Moreover, we refer to Eqs. (2.58), (2.63) and (2.64) for $\partial \underline{r}/\partial \underline{c}$, \underline{r}_ω and \underline{r}_d . The linearization of the last residual G_{D_χ} , Eq. (2.40), reads

$$\begin{aligned} \text{d}G_{D_\chi} = & \int_{\Omega_0} \left(\delta D_\chi \left[-g''(D_\chi)(\psi_{e0}(\mathbf{C}^e) + \psi_k(\underline{c})) + \frac{\partial^2 \psi_\chi}{\partial D_\chi^2} + \frac{1}{\partial r/\partial D} \left(\frac{\partial^2 \psi_\chi}{\partial D \partial D_\chi} \right)^2 \right] \text{d}D_\chi \right. \\ & + \delta D_\chi \left[-g'(D_\chi) \boldsymbol{\tau}^0 + \frac{g'(D)}{\partial r/\partial D} \frac{\partial^2 \psi_\chi}{\partial D \partial D_\chi} \boldsymbol{\tau}^v \right] : \mathbf{d}_d \\ & + \delta D_\chi [-g'(D_\chi) \mathbf{M}_0] \cdot \boldsymbol{\omega}_d \\ & \left. + \text{Grad}(\delta D_\chi) \cdot \frac{\partial \boldsymbol{\xi}_{D_\chi}}{\partial \text{Grad}(D_\chi)} \cdot \text{Grad}(\text{d}D_\chi) \right) \text{d}\Omega. \end{aligned} \quad (2.85)$$

With our choices for ψ , we obtain the following form of the linearization of G_{D_χ} , Eq. (2.41),

$$\begin{aligned} \text{d}G_{D_\chi} = & \int_{\Omega_0} \left(\delta D_\chi \left[-g''(D_\chi)(\psi_{e0}(\mathbf{C}^e) + \psi_k(\underline{c})) + H_\chi + \frac{H_\chi^2}{\partial r/\partial D} \right] \text{d}D_\chi \right. \\ & + \delta D_\chi \left[-g'(D_\chi) \boldsymbol{\tau}^0 - \frac{g'(D)}{\partial r/\partial D} H_\chi \boldsymbol{\tau}^v \right] : \mathbf{d}_d \\ & + \delta D_\chi [-g'(D_\chi) \mathbf{M}_0] \cdot \boldsymbol{\omega}_d \\ & \left. + \text{Grad}(\delta D_\chi) \cdot \frac{\partial \boldsymbol{\xi}_{D_\chi}}{\partial \text{Grad}(D_\chi)} \cdot \text{Grad}(\text{d}D_\chi) \right) \text{d}\Omega, \end{aligned} \quad (2.86)$$

where $\partial \boldsymbol{\xi}_{D_\chi} / \partial \text{Grad}(D_\chi) = K_{g\chi} \mathbf{I}$. The full derivation of the linearization of G_{D_χ} is given in appendix 2.E.

2.5 Implementation and finite element method

Within the framework of the finite element method (FEM), the quantities \mathbf{u} , \mathbf{N} and D_χ serve as degrees of freedom, which means that they are updated as part of the global FEM system of linear equations. More specifically, we use the angular velocity vector $\boldsymbol{\omega}$ instead of the crack surface normal \mathbf{N} as a degree of freedom, see Section 2.3. Furthermore, we formulate the residuals G_u , G_N and G_{D_χ} such that they contain \mathbf{d}_δ instead of $\delta \mathbf{F}$ because in the FEM context it is possible to use the same sparse matrix \underline{B} to get \mathbf{d}_δ from $\delta \mathbf{F}$ that would be used to get $\boldsymbol{\varepsilon}$ from $\delta \mathbf{u}$ in the small strain setting, see Wriggers [85].

The quantities D and \underline{c} are treated as internal variables. Thus, they are updated on integration point level. In order to update the damage variable D , we rely on the Newton–Raphson scheme using the residual given in Eq. (2.66). The residual and its derivative read

$$\begin{aligned} r(D) &= -g'(D)\psi_{e0}(\mathbf{C}) - HD + H_\chi(D_\chi - D) - \frac{\eta D}{\Delta t}(D - D_n) \\ r'(D) &= -g''(D)\psi_{e0}(\mathbf{C}) - H - H_\chi - \frac{\eta D}{\Delta t}. \end{aligned}$$

In the first step, we assume that no further damage occurs, i.e., that the new damage variable D is equal to the previous one D_n . We update the damage variable D using the Newton–Raphson scheme as summarized in Algo. 2.1. Note that we only allow updates of D if

Algo. 2.1: Newton–Raphson scheme for updating the damage variable D .

```

D ← Dn
if D < 1 − told then
  do
    iter ← iter + 1
    if iter ≥ maxiter then
      ⊥ exit
    r(D) ← −g'(D)ψe0(C) − HD + Hχ(Dχ − D) −  $\frac{\eta D}{\Delta t}(D - D_n)$ 
    r'(D) ← −g''(D)ψe0(C) − H − Hχ −  $\frac{\eta D}{\Delta t}$ 
    if |r| ≤ tol then
      ⊥ exit
    D ← D −  $\frac{r(D)}{r'(D)}$ 
if D > 1 − told then
  ⊥ D = 1 − told
if D < −told then
  ⊥ D = told

```

$D < 1 - \text{told}$, where told is the computational equivalent of a small number $\epsilon > 0$. As soon as D is close or equal to 1, no further evolution is allowed. Moreover, we enforce that

$-\text{tolD} \leq D \leq 1 - \text{tolD}$ after the update of D . We allow slightly negative D because in our experience, the Newton scheme of the next time step often fixes negative D by itself and makes them positive again. If D becomes negative beyond the tolerance $-\text{tolD}$, we set it to $+\text{tolD}$ to avoid going to the negative range immediately again. Allowing slightly negative D is acceptable since the monotony of $g(D)$ does not change at $D = 0$. Thus this relaxed policy does not greatly affect physical plausibility. However, at $D = 1$ the monotony does change and $D > 1$ must be avoided.

In order to update the internal variables \underline{c} , we rely again on a Newton–Raphson scheme. As indicated in Section 2.4, we choose $\underline{r} = [r^{\gamma_1}, r^{\gamma_2}, r^\varepsilon]^\top$ given in Eqs. (2.51), (2.52) and (2.53) as the residual for the Newton–Raphson method. The derivative $\partial \underline{r} / \partial \underline{c}$ of the residual \underline{r} with respect to the internal variables \underline{c} is given in Eqs. (2.54), (2.56) and (2.58). The procedure for updating the internal variables \underline{c} is summarized in Algo. 2.2. Note that we use the Neo–

Algo. 2.2: Newton–Raphson scheme for updating the internal variables \underline{c} .

```

 $\underline{c} \leftarrow \underline{c}_n$ 
do
  iter  $\leftarrow$  iter + 1
  if iter  $\geq$  maxiter then
     $\perp$  exit
   $\mathbf{C}^e \leftarrow \text{updateCe}(\underline{c}, \mathbf{d}_1, \mathbf{d}_2, \mathbf{N}, \mathbf{F})$ 
   $\frac{d\mathbf{S}^{0e}}{d\mathbf{C}^e}, \mathbf{S}^{0e}, \psi_{e0}(\mathbf{C}^e) \leftarrow \text{neoHooke}(\mathbf{C}^e)$ 
   $k_\varepsilon \leftarrow k$ 
  if  $\varepsilon < 0$  then
     $\perp k_\varepsilon \leftarrow k_{<0}$ 
   $\underline{r} \leftarrow [r^{\gamma_1}, r^{\gamma_2}, r^\varepsilon]^\top$ 
   $\frac{\partial \underline{r}}{\partial \underline{c}} \leftarrow \begin{bmatrix} \partial r^{\gamma_1} / \partial \gamma_1 & \partial r^{\gamma_1} / \partial \gamma_2 & \partial r^{\gamma_1} / \partial \varepsilon \\ \partial r^{\gamma_2} / \partial \gamma_1 & \partial r^{\gamma_2} / \partial \gamma_2 & \partial r^{\gamma_2} / \partial \varepsilon \\ \partial r^\varepsilon / \partial \gamma_1 & \partial r^\varepsilon / \partial \gamma_2 & \partial r^\varepsilon / \partial \varepsilon \end{bmatrix}$ 
  if  $\|\underline{r}\| \leq \text{tol}$  then
     $\perp$  exit
   $\underline{c} \leftarrow \underline{c} - \left( \frac{\partial \underline{r}}{\partial \underline{c}} \right)^{-1} \underline{r}$ 

```

Hookean law, see, e.g., [87] as the underlying elastic law. Further, note how we implemented the energy contribution ψ_k which prevents interpenetration for fracture mode I

$$\psi_k = \frac{1}{2} \left(k_\varepsilon \varepsilon^2 + \sum_{i=1}^2 k \gamma_i^2 \right) \quad \text{with} \quad k_\varepsilon = \begin{cases} k_{<0}, & \varepsilon < 0 \\ k, & \text{else} \end{cases}. \quad (2.87)$$

The parameter $k_{<0}$ is significantly larger than k in order to represent $\psi_k \rightarrow \infty$ in a regularized way.

The novelty of our work lies in the proposed material model. Thus, the focus of implementation and numerical experiments must be on understanding all the model’s features and characteristics. The three-dimensional case is too complicated for that. Hence, our im-

plementation is two-dimensional with the added benefit of less computational effort. For the two-dimensional implementation we use $\{\mathbf{d}_1, \mathbf{N}\}$ and $\{\gamma_1, \varepsilon\}$ instead of $\{\mathbf{d}_1, \mathbf{d}_2, \mathbf{N}\}$ and $\{\gamma_1, \gamma_2, \varepsilon\}$. This means that we retain fracture modes *I* and *II* but omit fracture mode *III*. We implemented the material model and associated custom element within the commercially available software FEAP (version 8.5) [88]. The bi-linear quadrilateral element features selective reduced integration, where full integration is based on four Gauss points and reduced integration is based on one central integration point. We use the integration point subroutine which represents the undamaged elastic energy contribution $\psi_{e0}(\mathbf{C})$ for the four full integration Gauss points while the integration point subroutine which describes the damaged elastic energy contribution $\psi_{e0}(\mathbf{C}^e)$ is applied to the reduced integration point.

In the full integration subroutine (undamaged material $\psi_{e0}(\mathbf{C})$), we use the damage variable D as the damage indicator because it is easier to handle than four separate interpolated values D_χ . The degradation function $g(D)$ is evaluated accordingly. Moreover, the update of the damage variable D according to Algo. 2.1 is computed in the full integration subroutine. In the reduced integration subroutine (damaged material $\psi_{e0}(\mathbf{C}^e)$), we use the single interpolated value D_χ as the damage indicator and evaluate the degradation function $g(D_\chi)$ correspondingly. The evaluation of the damaged elastic energy contribution $\psi_{e0}(\mathbf{C}^e)$ requires the elastic right Cauchy–Green tensor \mathbf{C}^e and therefore the internal variables \underline{c} . Thus, we use the reduced integration subroutine to perform the update of the internal variables \underline{c} according to Algo. 2.2.

Not all quantities are computed in both integration point subroutines because by design we want to compute a linear combination of contributions corresponding to $g\psi_{e0}(\mathbf{C}) + (1 - g)\psi_{e0}(\mathbf{C}^e)$. For the residual G_u in Eq. (2.32), we compute $(1 - g(D_\chi))\boldsymbol{\tau}^0$ in the reduced integration subroutine and the remaining contributions in the full integration subroutine. For the residual G_N in Eq. (2.36), we compute $(1 - g(D_\chi))\mathbf{M}_0$ in the reduced integration subroutine, the gradient term in the full integration subroutine and the remaining contributions in equal shares in both integration point subroutines. The last point is motivated by the equal weights of the integration point subroutines and experience with the numerical experiments. For the residual G_{D_χ} in Eq. (2.41), we compute $-g'(D_\chi)\tilde{\psi}$ in the reduced integration subroutine and the remaining contributions in the full integration subroutine. These allocations carry over to the linearizations in Eqs. (2.71), (2.78) and (2.86).

2.6 Numerical experiments

The numerical experiments presented in this section were conducted on conventional desktop hardware (Intel® Core™ i7-8850H CPU @ 2.60GHz \times 12 with 32 GB RAM). We used FEAP 8.5 [88] together with the PARDISO solver package. The meshes were created with Gmsh 4.4.1 [89] and the visualization of results was done with Paraview 5.8.1 [90] and gnuplot 5.2 [91].

The choice of parameters is given in Tab. 2.1. Special attention must be paid when choosing

Tab. 2.1: Choice of parameters for the numerical experiments.

tol	10^{-9}	$[-]$	$K_{\text{g}\chi}$	21	$[\text{N}]$
tolD	$5 \cdot 10^{-3}$	$[-]$	$K_{\text{g}N}$	0.21	$[\text{N}]$
k	10	$[\text{MPa}]$	β_1	0 or 10^3	$[\text{MPa}]$
$k_{<0}$	$\frac{210 \cdot 10^3}{2(1+0.3)}$	$[\text{MPa}]$	β_2	0 or 10^2	$[\text{MPa}]$
H_χ	10^4	$[\text{MPa}]$	\mathbf{p}_1	$(\sqrt{2}, \sqrt{2})^\top$	$[-]$
H_N	10^2	$[\text{MPa}]$	\mathbf{p}_2	$(\sqrt{2}, -\sqrt{2})^\top$	$[-]$
H	1	$[\text{MPa}]$	E	$210 \cdot 10^3$	$[\text{MPa}]$
η_N	10^{-6}	$[\text{MPa} \cdot \text{s}]$	ν	0.3	$[-]$
η_D	10^{-2}	$[\text{MPa} \cdot \text{s}]$			

the parameter H and the gradient related parameter $K_{\text{g}\chi}$ because they influence the internal length scale. For illustration, let us consider the contributions to ψ in Eq. (2.18) that depend on D and D_χ and compare them with the energy density of the classic phase-field functional of fracture, see, e.g., Miehe et al. [73]. The contribution $H_\chi(D_\chi - D)^2/2$ ties D and D_χ together which means we can assume $D_\chi \approx D$. Comparing the two approaches

$$\frac{1}{2}g_c \left(\frac{D^2}{l} + l \|\nabla D\|^2 \right) = \frac{1}{2}HD^2 + \frac{1}{2}K_{\text{g}\chi} \|\nabla D\|^2, \quad (2.88)$$

we conclude

$$g_c = \sqrt{HK_{\text{g}\chi}} = \sqrt{21} \frac{\text{N}}{\text{mm}} \quad \text{and} \quad l = \sqrt{\frac{K_{\text{g}\chi}}{H}} = \sqrt{21} \text{ mm}. \quad (2.89)$$

Unless otherwise stated, we use the Neo-Hookean law characterized by E and ν (or μ and λ) and isotropic damage behavior ($\beta_1 = \beta_2 = 0$).

2.6.1 Single notched edge test (SNET)

2.6.1.1 Tensile loading

In this section, we want to investigate the model behavior for the single notched edge test (SNET) sample displayed in Fig. 2.7. At the top edge, we prescribe a vertical displacement u which generates tensile loading and we leave the horizontal displacement unrestricted. The boundary conditions at the bottom and right edge eliminate one displacement degree of freedom allowing for lateral contraction of the sample.

The mesh with 11834 elements and a refined section for the expected crack path is illustrated in Fig. 2.8 on the left. A mesh with more elements in the refined section (39086 elements in

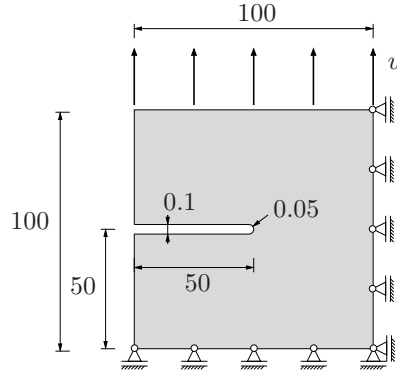


Fig. 2.7: Geometry of SNET sample (dimensions in mm) and boundary conditions.

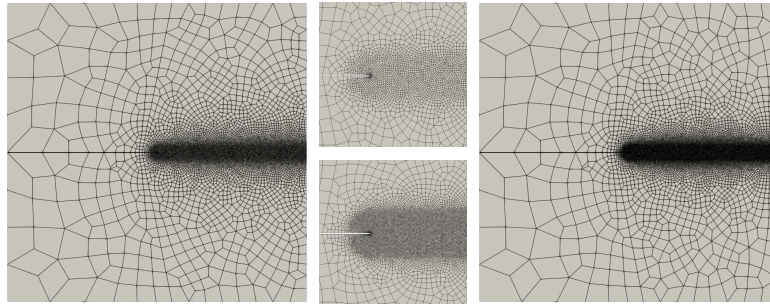


Fig. 2.8: Left: mesh with 11834 elements, right: mesh with 39086 elements, center top: close-up of refined section of coarse mesh, center bottom: close-up of refined section of fine mesh.

total) is displayed in Fig. 2.8 on the right. We use the fine mesh for comparison in Fig. 2.11. In Fig. 2.9, the damage variable D is shown. The plotted geometry is distorted according to the displacement field and exaggerated by a factor of 10. A magnified section of the field plot for the damage D is displayed in the background of Fig. 2.10. In this case, the plotted geometry is not distorted. On top of the damage D , the orientation vectors \mathbf{d}_1 , which are orthogonal to the crack surface normals \mathbf{N} , are indicated by black arrows. The force-displacement curves for the two meshes are illustrated in Fig. 2.11. Displacement is measured at the center of the top edge of the sample and force refers to the sum of all reaction forces at the top edge.

The crack path is horizontal and constitutes a straight connection between the center of the sample and the right edge. The orientation vectors \mathbf{d}_1 are aligned with the crack path. These results are in accordance with our expectation, which is physically motivated by the load case. The force-displacement curves exhibit a soft decline after the maximum force was reached. The results for both meshes align well with each other, which suggests mesh convergence.

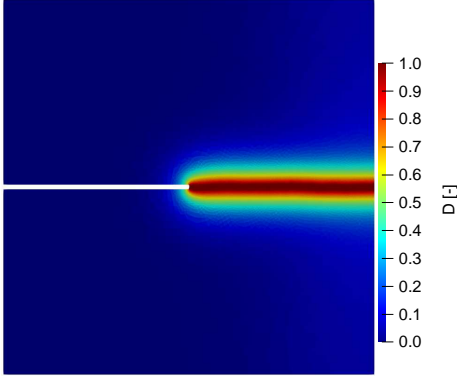


Fig. 2.9: D , warp factor 10.

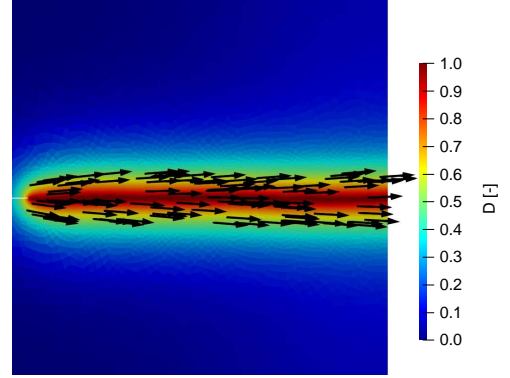


Fig. 2.10: D in background, black arrows for crack orientation $\mathbf{d}_1 \perp \mathbf{N}$, magnified.

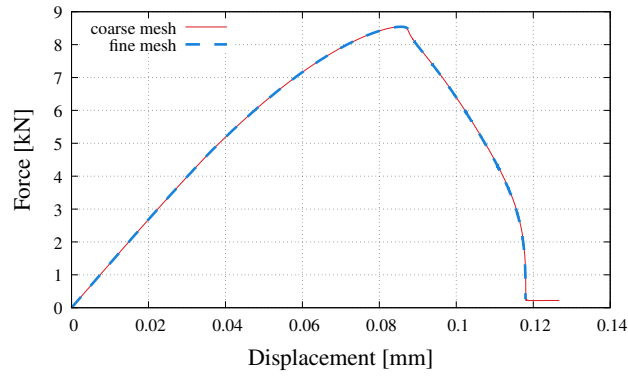


Fig. 2.11: Force–displacement curves for coarse mesh (11834 elements) and fine mesh (39086 elements).

2.6.1.2 Shear loading

Next, we want to discuss the model behavior for the same SNET sample under shear loading (mode II) instead of tensile loading. The geometry and boundary conditions are shown in Fig. 2.12. The dimensions of the sample are the same but in this case, we prescribe a horizontal displacement u of the upper half of the sample and keep the lower half fixed. This is implemented via the conditions at the left edge according to mode II loading. The boundary condition at the top edge eliminates the vertical degree of freedom ensuring pure horizontal displacement. In Fig. 2.13, the mesh with 13702 elements is visualized. In preliminary simulations with a coarse mesh, we determined the crack path and refined the section where the crack propagates through. Fig. 2.14 represents the damage D where the plotted geometry is again warped according to the displacement field exaggerated by a factor of 5. As before, a magnified section of the the damage field D is also shown in the background of Fig. 2.15 which is not warped. In the foreground, the black arrows indicate the orientation $\mathbf{d}_1 \perp \mathbf{N}$. In contrast to Section 2.6.1.1, the crack does not propagate horizontally anymore but is angled downwards. This behavior is also reflected by the orientation arrows \mathbf{d}_1 , which are

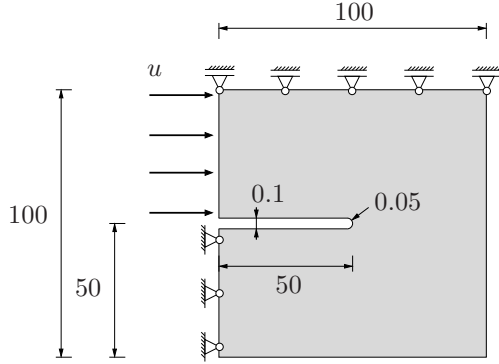


Fig. 2.12: Geometry of SNET sample (dimensions in mm) and boundary conditions.

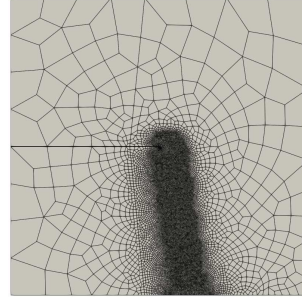


Fig. 2.13: Mesh with 13702 elements and refined section in the expected crack path.

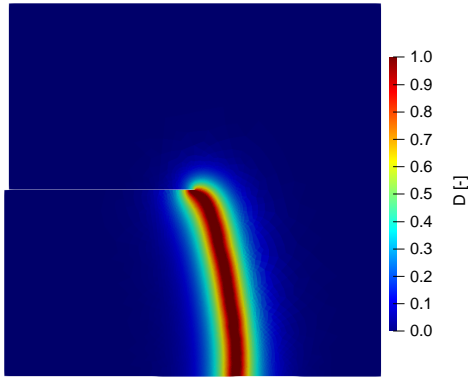


Fig. 2.14: D , warp factor 5.

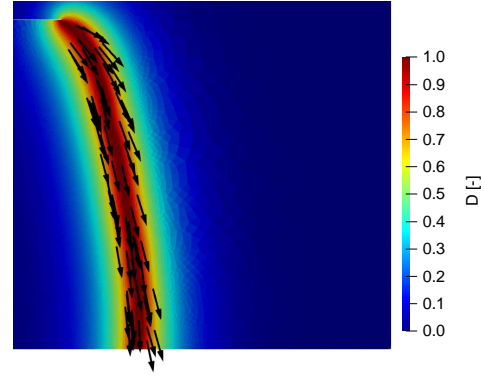


Fig. 2.15: D in the background, black arrows for crack orientation $\mathbf{d}_1 \perp \mathbf{N}$, magnified.

again aligned with the crack path. Both these observations are in correspondence with our expectations according to the loading case and the compressive regime in the upper half of the sample. With tension–compression split models, other authors have obtained similar angles, see Miehe et al. [73] and Ambati et al. [92]. According to linear elastic fracture mechanics, angles of 70° to 80° (depending on the crack path criterion) can be expected for pure mode II , see, e.g., Gross and Seelig [93] and Maiti [94].

2.6.1.3 Anisotropic damage behavior

In this section, we are interested in the performance of the free energy contribution

$$\psi_{\text{aniso}} = \sum_{i=1}^2 \frac{1}{2} \beta_m (\mathbf{N} \cdot \mathbf{p}_m)^2$$

which models anisotropic damage behavior. In order to investigate the effect of the free energy contribution ψ_{aniso} , we consider the SNET sample displayed in Fig. 2.16. The geometry and the tensile displacement condition at the top edge are the same as in Section 2.6.1.1. At the left and bottom edge there are boundary conditions which eliminate one displacement degree of freedom. In order to allow this special combination of anisotropic material behavior and displacement boundary conditions at the edge to take effect freely, we had to shift the displacement boundary condition from the right edge to the left edge. The eigenvectors $\{\mathbf{p}_1, \mathbf{p}_2\}$ and eigenvalues $\{\beta_1, \beta_2\}$ are chosen as follows

$$\mathbf{p}_1 = \frac{1}{\sqrt{2}}(\mathbf{e}_1 + \mathbf{e}_2), \quad \beta_1 = 10^3 \text{ MPa}, \quad \mathbf{p}_2 = \frac{1}{\sqrt{2}}(\mathbf{e}_1 - \mathbf{e}_2), \quad \beta_2 = 10^2 \text{ MPa}$$

and are illustrated in Fig. 2.16. Since the energy contribution β_1 is larger than β_2 , it is energetically favorable for the crack surface normal \mathbf{N} to align with \mathbf{p}_2 . The favorable and unfavorable configurations are displayed in Fig. 2.17. Note that in the present two-dimensional case, only the difference between the eigenvalues β_1 and β_2 is relevant for the anisotropic behavior:

$$\begin{aligned} \psi_{\text{aniso}} &= \frac{1}{2} \mathbf{N} \cdot \left(\beta_1 \mathbf{p}_1 \otimes \mathbf{p}_1 + \beta_2 \mathbf{p}_2 \otimes \mathbf{p}_2 \right) \cdot \mathbf{N} = \frac{1}{2} \mathbf{N} \cdot \left(\beta_1 \mathbf{p}_1 \otimes \mathbf{p}_1 + \beta_2 (\mathbf{I} - \mathbf{p}_1 \otimes \mathbf{p}_1) \right) \cdot \mathbf{N} \\ &= \frac{1}{2} (\beta_1 - \beta_2) (\mathbf{N} \cdot \mathbf{p}_1)^2 + \frac{1}{2} \beta_2. \end{aligned}$$

The geometry is discretized by 12614 elements, where more elements are located in the region of the crack path, see Fig. 2.18. We determined the crack path in preliminary simulations with a coarse mesh and refined the mesh accordingly. In Fig. 2.19, the damage field D is

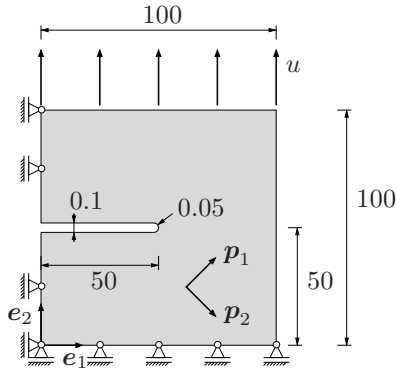


Fig. 2.16: Geometry of SNET sample (dimensions in mm), boundary conditions and preferential directions \mathbf{p}_1 and \mathbf{p}_2 .

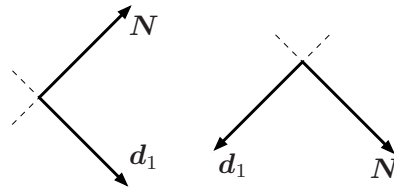


Fig. 2.17: Left: energetically unfavorable configuration, right: energetically favorable configuration.

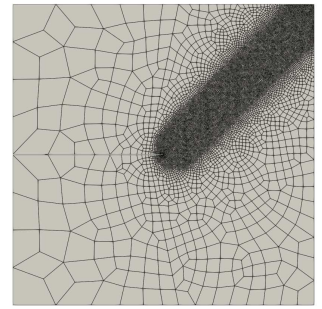


Fig. 2.18: Mesh with 12614 elements and refined section in the expected crack path.

illustrated and the plotted geometry is distorted corresponding to the displacement field. Fig. 2.20 displays the crack orientation $\mathbf{d}_1 \perp \mathbf{N}$ as black arrows in front of a magnified

section of the damage field D . No warp is applied to Fig. 2.20. The crack propagates, beginning in the center, towards the upper right corner of the sample. The resulting crack

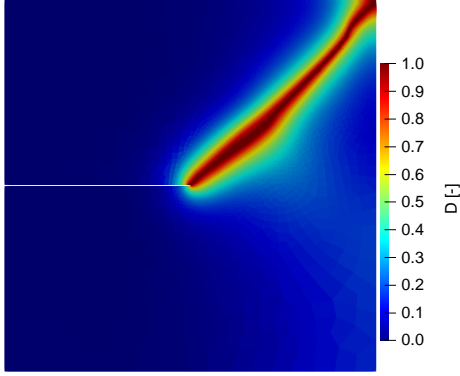


Fig. 2.19: D , warp factor 1.

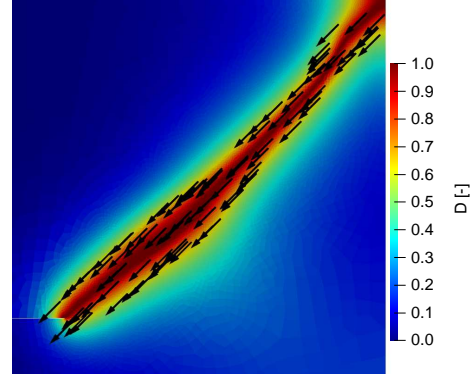


Fig. 2.20: D in the background, black arrows for crack orientation $\mathbf{d}_1 \perp \mathbf{N}$, magnified.

path and the orientation vectors \mathbf{d}_1 are in line with each other. Both results are in accordance with our expectation due to the anisotropic damage behavior. These findings show that the modeling of damage anisotropy via the energy contribution ψ_{aniso} is working correctly and effectively.

2.6.2 Double notched edge test (DNET)

2.6.2.1 Tensile loading

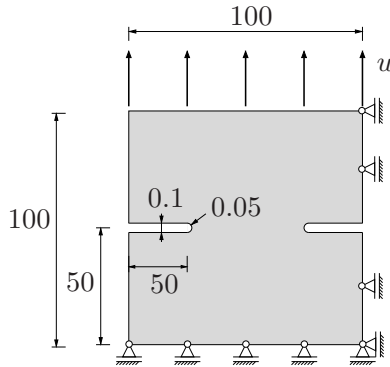


Fig. 2.21: Geometry of DNET sample (dimensions in mm) and boundary conditions.

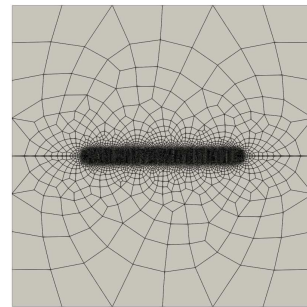


Fig. 2.22: Mesh with 13128 elements and refined section in the expected crack path.

So far, we have solely considered single notched edge tests where the crack starts in the center and propagates to an outer edge. This is certainly an important behavior for a damage model to represent. Another mechanism is merging of cracks. In order to investigate the model response for this mechanism, we consider the double notched edge test (DNET).

Geometry and boundary conditions are given in Fig. 2.21. At the top edge, a displacement u in vertical direction is prescribed which results in tensile loading. The displacement of the top edge in horizontal direction is free. Similar to Section 2.6.1.1, the boundary conditions at the right and bottom edge fix one displacement degree of freedom, thus allowing lateral contraction of the sample. However, since the sample is symmetric and the boundary conditions are non-symmetric, a slightly non-symmetric model response may occur. In Fig. 2.22, the mesh with 13128 elements and a refined section for the anticipated crack path is visualized. The damage D is illustrated in Fig. 2.23 at the time steps 200, 450, 540 and at the final step 772. The geometry is warped according to the displacement field and scaled by the factor 10. A magnified section of the damage field D is shown in the background of Fig. 2.24, where the geometry is not warped. In front of the respective damage fields D , the orientation vectors $\mathbf{d}_1 \perp \mathbf{N}$ are plotted as black arrows at the time steps 200, 450, 540 and 772 (final step). At

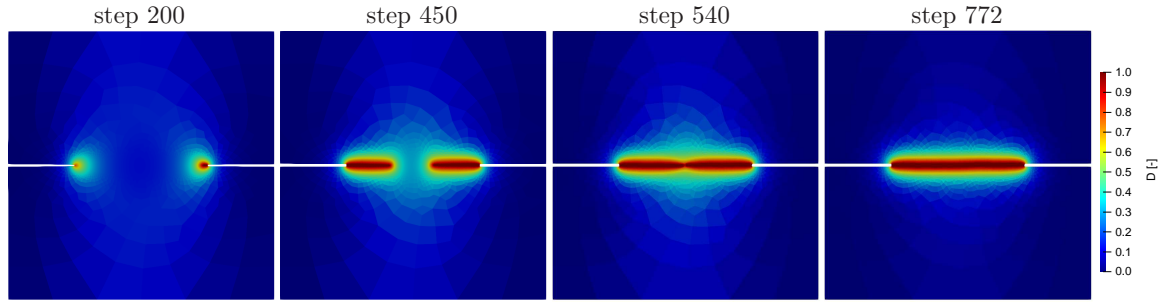


Fig. 2.23: D at different time steps, warp factor 10.

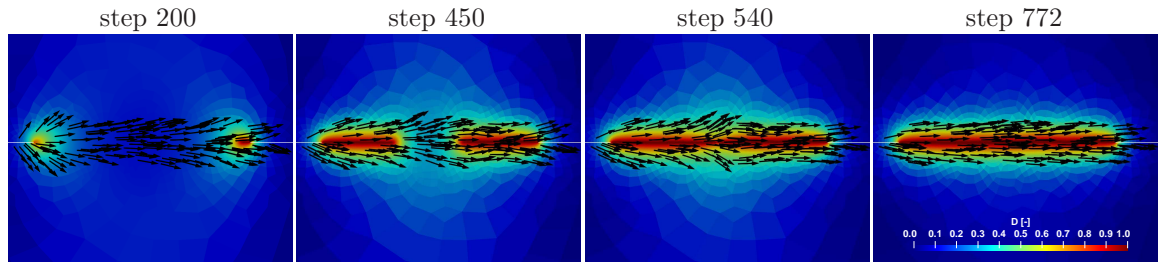


Fig. 2.24: D in the background, black arrows for orientation $\mathbf{d}_1 \perp \mathbf{N}$ at different time steps, magnified.

the first displayed time step a slightly non-symmetric model response at the two notch tips is noticeable. Since at the later time steps this asymmetry is barely observable, the choice of boundary conditions has ultimately not affected the solution excessively. The cracks start at the tips of the notches and expand towards each other. At that point, the orientation vectors \mathbf{d}_1 are relatively unstructured. Similar to the observation for the SNET sample in Section 2.6.1.1, the cracks propagate horizontally due to the load case and the isotropic damage behavior. In the later time steps, the arrows are increasingly aligned with the crack path. The crack tips meet at around step 540 and merge into one crack in the following. At that

time step, some unstructured behavior is observed in the meeting zone. At the last step 772, it is not visible that the final crack has emerged from two separate ones. The results of this section indicate that the model is able to capture merging of cracks.

2.6.2.2 Tensile loading and subsequent compression

Besides the behavior under tension, it is also interesting to investigate the model behavior under compressive loading. In Section 2.6.1.2, we have already observed that damage occurs in the tensile regime but not in the compressive regime (tension–compression asymmetry, see Fig. 2.14). To get a clearer insight into this asymmetry, we investigate pure tension and compression in this section. Geometry, boundary conditions and mesh are the same as in Section 2.6.2.1 (see Figs. 2.21 and 2.22). The loading function (displacement of upper edge) is given in Fig. 2.25. A magnified section of the resulting damage field D is displayed in Fig. 2.26.

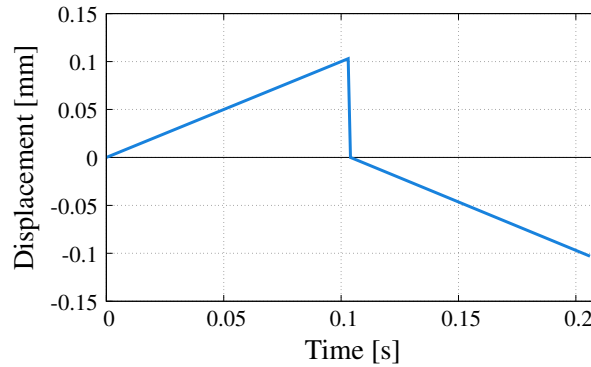


Fig. 2.25: Loading function (piecewise linear) connecting the following points (time, displacement): $(0, 0) - (0.103, 0.103) - (0.104, 0) - (0.206, -0.103)$.

The plotted geometry is warped corresponding to the displacement field. The resulting force displacement curve is given in Fig. 2.27. Force refers to the sum of all reaction forces at the top edge and displacement is measured at the center of the top edge of the sample. In Fig. 2.27, force and displacement start in the origin. With increasing displacement, the force increases until complete fracture occurs. After the force dropped to (almost) zero, the sample is rapidly unloaded. Force and displacement return to the origin. In subsequent compression, the force decreases with decreasing displacement. It can be seen that, although the sample stiffness is (almost) completely degraded in tension, in compression the sample behaves (almost) as stiff as in the undamaged case. The simulation breaks after approximately 0.15 s (not wall time) at displacement roughly -0.05 mm. We suspect the following problem. The model does not contain friction between the locally assumed layers. Thus, elements can readily be squeezed out of the crack, see Fig. 2.26. We surmise that the resulting strong mesh distortions lead to bad convergence. In addition, in the compressive regime, the damaged material behaves much stiffer in compression than in shear. This high stiffness contrast may also play a role, as the large element distortions seen in Fig. 2.26 are suspected to result mainly from shear

deformations. Thus, it is expected that a more realistic model including also friction (missing here) would also be numerically more stable in this situation. This question may be subject to further research in the future.

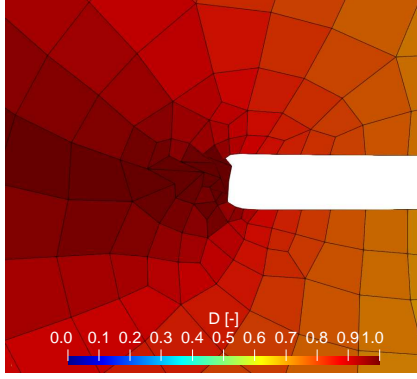


Fig. 2.26: D (warp factor 1), magnified section of right notch of DNET sample.

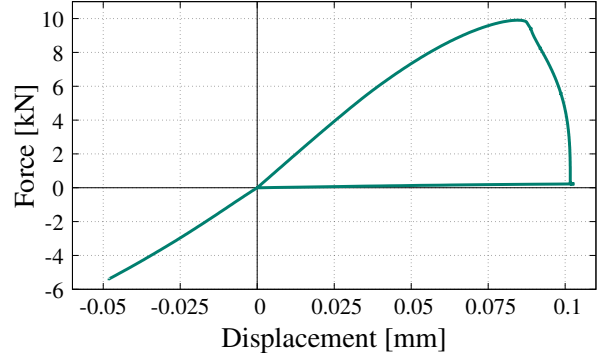


Fig. 2.27: Force–displacement curve.

2.6.3 Comparison to spectral tension–compression split

In order to remedy the symmetric tension–compression behavior of the classic phase–field model of fracture, many authors rely on a spectral tension–compression split, see, e.g., Miehe et al. [73]. However, this approach can suffer from an overly stiff model response as shown by Strobl and Seelig [76]. We want to compare our model to the spectral tension–compression approach by Fassin et al. [95] (the isotropic model in that publication). To do that, we con-

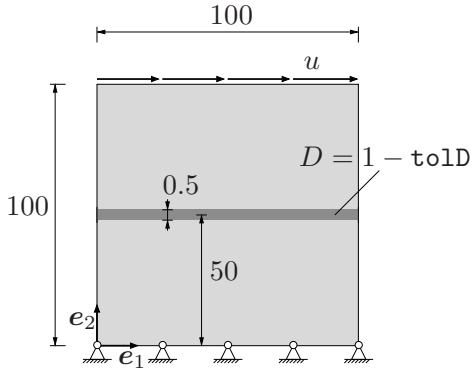


Fig. 2.28: Geometry of a simple block sample (dimensions in mm), boundary conditions and initial distribution of D .

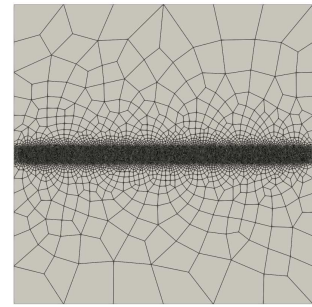


Fig. 2.29: Mesh with 11533 elements and refined section in the prescribed crack path.

sider the sample shown in Fig. 2.28. At the top edge, we prescribe the horizontal displacement u and fix the vertical displacement at zero. At the bottom edge we fix both displacement degrees of freedom. This shear loading is performed until a horizontal displacement of the upper edge of 0.1 mm is reached. As initial condition, we prescribe the distribution of the

damage D according to Fig. 2.28. This initial distribution leads to a configuration where the full block is split into two halves. We choose this example because physically we would expect the two halves of the cracked block to shear off each other without resistance. The mesh shown in Fig. 2.29 with 11533 elements features a refined section in the area of the prescribed initial distribution of D . Besides the same geometry, boundary conditions, initial

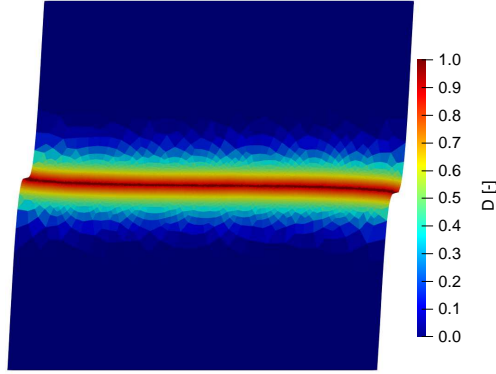


Fig. 2.30: D (warp factor 100) for model with spectral tension–compression split.

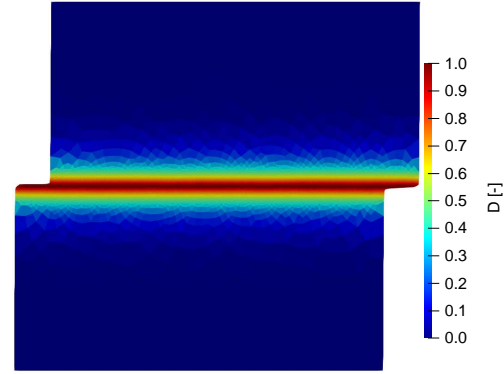


Fig. 2.31: D (warp factor 100) for gradient–extended damage model with director N .

condition and mesh, we also use the same elastic parameters for both models, see Tab. 2.1. Moreover, we tune the different damage gradient parameters of the two models such that they are equivalent. The damage variable D for the spectral tension–compression split model is displayed in Fig. 2.30 and the damage variable D for our model is illustrated in Fig. 2.31. For both figures, the shown geometry is distorted according to the displacement field and exaggerated by a factor of 100.

Fig. 2.32 illustrates the stress component σ_{12} (relevant component for the shear loading case) for the spectral tension–compression split model. Within the entire sample, σ_{12} is in the range of $[-0.593, 138.62]$ MPa and outside the crack it is approximately in the range of $[0, 65]$ MPa. The stress component σ_{12} for our model is displayed in Fig. 2.33. Overall, σ_{12} is in the range of $[-12.887, 23.419]$ MPa, whereas outside the crack, σ_{12} is roughly in the range of $[0, 5]$ MPa. For ease of comparison, both Fig. 2.32 and Fig. 2.33 are scaled to the same stress range which features as its limits the minimum and maximum stress magnitude among both figures.

When comparing the two models, it becomes apparent that the spectral tension–compression split model reveals a stiffer response. On the one hand, this is indicated by the shear angle in Fig. 2.30 compared to Fig. 2.31. Our model exhibits a significantly lower shear angle compared to the spectral tension–compression split model. Other authors have obtained comparably good shear angles for similar problems (Steinke and Kaliske [96], Wu et al. [97], Jeong et al. [98]). On the other hand, the stiffer response can be deduced from the higher stress σ_{12} in Fig. 2.32 compared to Fig. 2.33. The stress component σ_{12} outside the crack (in the homogeneous upper and lower halves) is one order of magnitude smaller for our model than for the tension–compression split model. Thus, our model comes closer to the physically

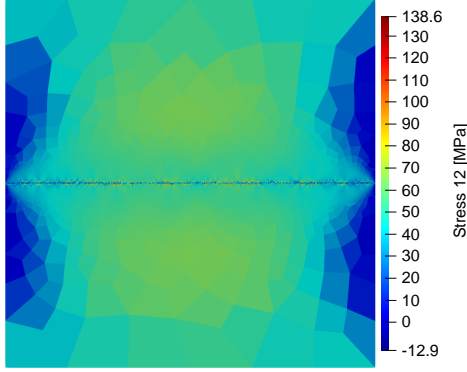


Fig. 2.32: σ_{12} for model with spectral tension-compression split, overall: $\sigma_{12} \in [-0.593, 138.62]$ MPa, outside crack: $\sigma_{12} \in [0, 65]$ MPa.

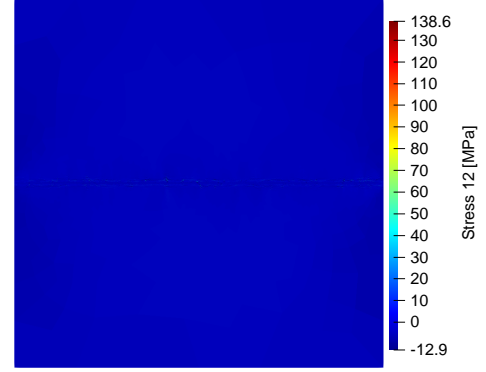


Fig. 2.33: σ_{12} for gradient-extended damage model with director \mathbf{N} , overall: $\sigma_{12} \in [-12.887, 23.419]$ MPa, outside crack: $\sigma_{12} \in [0, 5]$ MPa.

expected configuration of two homogeneous, stress free halves being sheared off each other without resistance.

2.7 Summary and outlook

In this work, we introduced a gradient-extended damage model with crack orientation director. In contrast to models of single crystal cleavage systems, the crack surface orientation is not known a priori. Thus, we treat the surface normal as a degree of freedom. Kinematically, the model represents behavior which locally corresponds to fracture modes *I*, *II* and *III*. The formulation within the generalized standard material framework ensures thermodynamic consistency. Highlights of the model formulation include the straightforward implementation of anisotropic damage behavior and the fulfillment of the traction-free condition in the crack, which arises from the model assumptions and is not assumed itself.

Numerical examples show that the introduced model exhibits a physically plausible response for different load cases as well as for isotropic and anisotropic damage behavior. Merging of cracks can be represented and advantages were observed when compared to a model featuring a spectral tension-compression split.

Future work could be devoted to the introduction of friction within the crack in order to represent the associated dissipative effects. Furthermore, a more sophisticated modeling of anisotropic damage could be approached.

Declaration of competing interest

The authors declare that they have no known competing financial interests or personal relationships that could have appeared to influence the work reported in this paper.

Acknowledgment

The authors thank Marek Fassin for providing the code for the comparison with the spectral tension–compression split.

Appendices

The appendix Sections 2.B to 2.F give exhaustive derivations of all model equations. These are given for the interested reader.

2.A Primal and dual quantities

Tab. 2.2: Primal and dual quantities (constitutive equations) in the time–continuous case.

primal quantity	dual quantity (constitutive equation)
\mathbf{C}	$\mathbf{S} = g(D)\mathbf{S}^\vee(\mathbf{C}) + (1 - g(D_\chi))\mathbf{F}^{\mathbf{c}-1}\mathbf{S}^{\mathbf{e}0}(\mathbf{C}^{\mathbf{e}})\mathbf{F}^{\mathbf{c}-\mathbf{T}}$ (Neo–Hooke: $\mathbf{S}(\mathbf{C}) = \frac{\lambda}{2}(J^2 - 1)\mathbf{C}^{-1} + \mu(\mathbf{I} - \mathbf{C}^{-1})$)
D_χ	$X = 2(1 - D_\chi)(\psi_{\mathbf{e}0}(\mathbf{C}^{\mathbf{e}}) + \psi_{\mathbf{k}}(\underline{\mathbf{c}})) + H_\chi(D_\chi - D)$ (Neo–Hooke: $\psi_{\mathbf{e}0}(\mathbf{C}) = \frac{\lambda}{4}(J^2 - 1 - 2 \ln J) + \frac{\mu}{2}(I_{\mathbf{C}} - 3 - 2 \ln J)$)
D	$Y = 2(D - 1)\psi_{\mathbf{e}0}(\mathbf{C}) + HD - H_\chi(D_\chi - D)$ $\dot{D} = -\frac{1}{\eta_D}Y$
$\underline{\mathbf{c}}$	$\underline{\mathbf{z}} = \begin{bmatrix} k\gamma_1 - \frac{1}{1+\varepsilon}\mathbf{d}_1 \cdot \boldsymbol{\Sigma}^{\mathbf{e}} \cdot \mathbf{N} \\ k\gamma_2 - \frac{1}{1+\varepsilon}\mathbf{d}_2 \cdot \boldsymbol{\Sigma}^{\mathbf{e}} \cdot \mathbf{N} \\ k\varepsilon - \frac{1}{1+\varepsilon}\mathbf{N} \cdot \boldsymbol{\Sigma}^{\mathbf{e}} \cdot \mathbf{N} \end{bmatrix} \quad (\boldsymbol{\Sigma}^{\mathbf{e}} = \mathbf{C}^{\mathbf{e}}\mathbf{S}^{\mathbf{e}0})$
$\text{Grad}(D_\chi)$	$\boldsymbol{\xi}_{D_\chi} = K_{\text{g}\chi}\text{Grad}(D_\chi)$
$\text{Grad}(\mathbf{N})$	$\boldsymbol{\xi}_{\mathbf{N}} = K_{\text{g}\mathbf{N}}\text{Grad}(\mathbf{N})$
$\boldsymbol{\omega}$	$\mathbf{M} = \left(1 - g(D_\chi)\right)\mathbf{M}_0 + \begin{cases} H_{\mathbf{N}}\mathbf{N}^* \times \mathbf{N}, & D \geq 1 - \epsilon \\ 0, & \text{else} \end{cases}$ $+ \sum_{m=1}^3 \beta_m(\mathbf{N} \cdot \mathbf{p}_m)(\mathbf{N} \times \mathbf{p}_m)$ $(\mathbf{M}_0 = -\mathbf{L}_\omega^{\mathbf{c}\mathbf{T}} : \boldsymbol{\Sigma}^{\mathbf{e}})$ $\dot{\mathbf{N}} = -\frac{1}{\eta_{\mathbf{N}}}\mathbf{M} \times \mathbf{N}$

2.B Recurring relations

In this section, we want to derive useful relations that are going to be used throughout the other sections of the appendix.

- In the following special case

$$(\mathbf{I} \square \mathbf{A}^s + \mathbf{A}^s \square^T \mathbf{I}) : \mathbf{B} = \mathbf{B} \mathbf{A}^s + \mathbf{A}^s \mathbf{B}^T = 2 \operatorname{sym}(\mathbf{B} \mathbf{A}^s) = 2 \mathbf{I} \square_s \mathbf{A}^s : \mathbf{B} , \quad (2.90)$$

where \mathbf{A}^s is a symmetric second order tensor and \mathbf{I} is the second order identity tensor, a product of the form given in Eq. (2.3) can be used to summarize two products of the form given in Eqs. (2.1) and (2.4).

- The next relation, which is frequently used, reads

$$\boldsymbol{\omega}_d \cdot \mathbf{N} = (\omega_{d1} \mathbf{d}_1 + \omega_{d2} \mathbf{d}_2) \cdot \mathbf{N} = 0 . \quad (2.91)$$

- For the derivatives of the elastic energies of the damaged and undamaged material, we use, respectively,

$$\frac{\partial \psi_{e0}(\mathbf{C}^e)}{\partial \mathbf{C}^e} = \frac{1}{2} \mathbf{S}^{0e}, \quad \frac{\partial \psi_{e0}(\mathbf{C})}{\partial \mathbf{C}} = \frac{1}{2} \mathbf{S}^v \quad (2.92)$$

and obtain for the Kirchhoff stresses according to Fig. 2.34

$$\boldsymbol{\tau}^0 = \mathbf{F} \mathbf{S}^0 \mathbf{F}^T = \mathbf{F}^e \mathbf{F}^c \mathbf{S}^0 \mathbf{F}^{cT} \mathbf{F}^{eT} = \mathbf{F}^e \mathbf{S}^{0e} \mathbf{F}^{eT} \quad (2.93)$$

$$\boldsymbol{\tau}^v = \mathbf{F} \mathbf{S}^v \mathbf{F}^T . \quad (2.94)$$

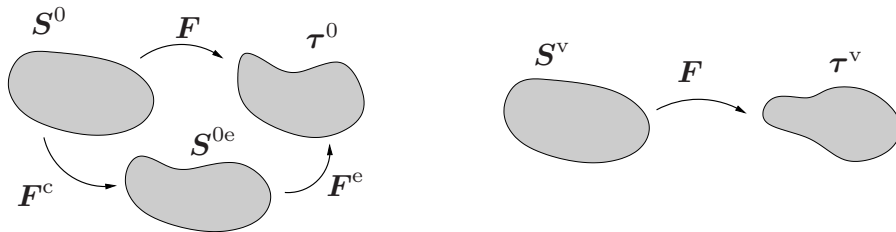


Fig. 2.34: Relation between $\boldsymbol{\tau}^0$ and \mathbf{S}^{0e} as well as $\boldsymbol{\tau}^v$ and \mathbf{S}^v .

- Another relation that we frequently use, is an expression for $\delta \mathbf{F}^{-1}$ according to

$$\begin{aligned} \delta \mathbf{I} = 0 &\Leftrightarrow 0 = \delta(\mathbf{F} \mathbf{F}^{-1}) \\ 0 &= \delta \mathbf{F} \mathbf{F}^{-1} + \mathbf{F} \delta \mathbf{F}^{-1} \\ \delta \mathbf{F}^{-1} &= -\mathbf{F}^{-1} \delta \mathbf{F} \mathbf{F}^{-1} . \end{aligned} \quad (2.95)$$

- The elastic right Cauchy–Green tensor can be expressed as

$$\mathbf{C}^e = \mathbf{F}^{e\top} \mathbf{F}^e = \mathbf{F}^{c-\top} \mathbf{F}^\top \mathbf{F} \mathbf{F}^{c-1} = \mathbf{F}^{c-\top} \mathbf{C} \mathbf{F}^{c-1} \quad (2.96)$$

from which we compute the derivative with respect to the right Cauchy–Green tensor \mathbf{C}

$$\frac{\partial \mathbf{C}^e}{\partial \mathbf{C}} = \mathbf{F}^{c-\top} \overset{\text{s}}{\square} \mathbf{F}^{c-1} . \quad (2.97)$$

- The variation of the right Cauchy–Green tensor \mathbf{C} reads

$$\delta \mathbf{C} = \delta \mathbf{F}^\top \mathbf{F} + \mathbf{F}^\top \delta \mathbf{F} = 2 \mathbf{F}^\top \overset{\text{s}}{\square} \mathbf{F} : \mathbf{d}_\delta , \quad (2.98)$$

where we used that

$$\mathbf{d}_\delta = \text{sym}(\delta \mathbf{F} \mathbf{F}^{-1}) \quad (2.99)$$

which can be thought of as the variational version of $\mathbf{d} = \text{sym}(\dot{\mathbf{F}} \mathbf{F}^{-1})$.

- In contrast to $\delta \mathbf{C}$, the variation of the elastic right Cauchy–Green tensor \mathbf{C}^e contains, for fixed internal variables \underline{c} , two contributions

$$\delta \mathbf{C}^e \Big|_{\underline{c}} = \mathbf{C}_d^e : \mathbf{d}_\delta + \mathbf{C}_\omega^e \cdot \boldsymbol{\omega}_\delta . \quad (2.100)$$

For the first contribution $\mathbf{C}_d^e : \mathbf{d}_\delta$, we freeze \mathbf{F}^c and compute the variation with respect to \mathbf{F}

$$\begin{aligned} \delta_u \mathbf{C}^e &= \mathbf{C}_d^e : \mathbf{d}_\delta = \mathbf{F}^{c-\top} \overset{\text{s}}{\square} \mathbf{F}^{c-1} : \delta \mathbf{C} \\ &= 2 \mathbf{F}^{c-\top} \overset{\text{s}}{\square} \mathbf{F}^{c-1} : \mathbf{F}^\top \overset{\text{s}}{\square} \mathbf{F} : \mathbf{d}_\delta \\ &= 2 \mathbf{F}^{e\top} \overset{\text{s}}{\square} \mathbf{F}^e : \mathbf{d}_\delta . \end{aligned} \quad (2.101)$$

For the contribution $\mathbf{C}_\omega^e \cdot \boldsymbol{\omega}_\delta$ in Eq. (2.100), we freeze \mathbf{F} and \underline{c} and compute the variation with respect to $\boldsymbol{\omega}$

$$\begin{aligned} \delta_\omega \mathbf{C}^e &= \delta_\omega \mathbf{F}^{c-\top} \mathbf{C} \mathbf{F}^{c-1} + \mathbf{F}^{c-\top} \mathbf{C} \delta_\omega \mathbf{F}^{c-1} = -(\delta_\omega \mathbf{F}^c \mathbf{F}^{c-1})^\top \mathbf{C}^e - \mathbf{C}^e (\delta_\omega \mathbf{F}^c \mathbf{F}^{c-1}) \\ &= -\left(\mathbf{I} \overset{\text{T}}{\square} \mathbf{C}^e + \mathbf{C}^e \square \mathbf{I} \right) : \delta_\omega \mathbf{F}^c \mathbf{F}^{c-1} \\ &= -2 \mathbf{C}^e \square_s \mathbf{I} : \delta_\omega \mathbf{F}^c \mathbf{F}^{c-1} , \end{aligned} \quad (2.102)$$

where we used Eqs. (2.95) and (2.90). For $\delta_\omega \mathbf{F}^c \mathbf{F}^{c-1}$, we first consider $\delta_\omega \mathbf{F}^c$ based on

Eq. (2.9)

$$\begin{aligned}
\delta_\omega \mathbf{F}^c &= \varepsilon \delta \mathbf{N} \otimes \mathbf{N} + \sum_{i=1}^2 \gamma_i \delta \mathbf{d}_i \otimes \mathbf{N} + \varepsilon \mathbf{N} \otimes \delta \mathbf{N} + \sum_{i=1}^2 \gamma_i \mathbf{d}_i \otimes \delta \mathbf{N} \\
&= \hat{\omega}_\delta \left(\varepsilon \mathbf{N} \otimes \mathbf{N} + \sum_{i=1}^2 \gamma_i \mathbf{d}_i \otimes \mathbf{N} \right) + \left(\varepsilon \mathbf{N} \otimes \mathbf{N} + \sum_{i=1}^2 \gamma_i \mathbf{d}_i \otimes \mathbf{N} \right) \hat{\omega}_\delta^\top \\
&= \hat{\omega}_\delta (\mathbf{F}^c - \mathbf{I}) - (\mathbf{F}^c - \mathbf{I}) \hat{\omega}_\delta = \hat{\omega}_\delta \mathbf{F}^c - \mathbf{F}^c \hat{\omega}_\delta
\end{aligned} \tag{2.103}$$

and obtain with \mathbf{F}^{c-1}

$$\begin{aligned}
\delta_\omega \mathbf{F}^c \mathbf{F}^{c-1} &= \mathbf{L}_\omega^c \cdot \omega_\delta = \hat{\omega}_\delta - \mathbf{F}^c \hat{\omega}_\delta \mathbf{F}^{c-1} \\
&= (\mathbb{I} - \mathbf{F}^c \square \mathbf{F}^{c-1}) : (-\epsilon \cdot \omega_\delta)
\end{aligned} \tag{2.104}$$

$$= \omega_\delta \cdot \mathbf{L}_\omega^{c\top} = \omega_\delta \cdot (-\epsilon) : (\mathbb{I} - \mathbf{F}^{c\top} \square \mathbf{F}^{c-1}) , \tag{2.105}$$

where \mathbb{I} denotes the fourth order identity tensor. Hence, for $\delta_\omega \mathbf{C}^e$, we write

$$\delta_\omega \mathbf{C}^e = \mathbf{C}_\omega^e \cdot \omega_\delta = -2\mathbf{C}^e \square \mathbf{I} : \mathbf{L}_\omega^c \cdot \omega_\delta . \tag{2.106}$$

- For the variation of the Mandel stress tensor $\Sigma^e = \mathbf{C}^e \mathbf{S}^{0e}$, we write

$$\delta \Sigma^e = \left(\delta \mathbf{C}^e \mathbf{S}^{0e} + \mathbf{C}^e \delta \mathbf{S}^{0e} \right) = \left(\mathbf{I} \square \mathbf{S}^{0e} + \mathbf{C}^e \frac{d\mathbf{S}^{0e}}{d\mathbf{C}^e} \right) : \delta \mathbf{C}^e . \tag{2.107}$$

2.C Derivation and linearization of the residual G_u

In order to find an expression for

$$\delta_u \Pi_\Delta = \int_{\Omega_0} \delta_u \pi_\Delta d\Omega - \int_{\partial\Omega_{0t}} \hat{\mathbf{t}} \cdot \delta \mathbf{u} dS - \int_{\Omega_0} \rho_0 \mathbf{b} \cdot \delta \mathbf{u} d\Omega ,$$

we look at the first summand more closely and obtain with Eqs. (2.92), (2.93), (2.94), (2.97) and (2.98)

$$\begin{aligned}
\int_{\Omega_0} \delta_u \pi_\Delta d\Omega &= \int_{\Omega_0} \left[g(D) \frac{\partial \psi_{e0}(\mathbf{C})}{\partial \mathbf{C}} + (1 - g(D_\chi)) \frac{\partial \psi_{e0}(\mathbf{C}^e)}{\partial \mathbf{C}^e} : \frac{\partial \mathbf{C}^e}{\partial \mathbf{C}} \right] : \delta \mathbf{C} d\Omega \\
&= \int_{\Omega_0} \left[g(D) \frac{1}{2} \mathbf{S}^v + (1 - g(D_\chi)) \frac{1}{2} \mathbf{S}^{0e} : \mathbf{F}^{c-1\top} \square \mathbf{F}^{c-1} \right] : 2\mathbf{F}^\top \square \mathbf{F} : \mathbf{d}_\delta d\Omega \\
&= \int_{\Omega_0} \left[g(D) \mathbf{F} \mathbf{S}^v \mathbf{F}^\top + (1 - g(D_\chi)) \mathbf{F}^e \mathbf{S}^{0e} \mathbf{F}^{e\top} \right] : \mathbf{d}_\delta d\Omega \\
&= \int_{\Omega_0} \left[g(D) \boldsymbol{\tau}^v + (1 - g(D_\chi)) \boldsymbol{\tau}^0 \right] : \mathbf{d}_\delta d\Omega .
\end{aligned} \tag{2.108}$$

Finally the full residual reads

$$G_u = \delta_u \Pi_\Delta = \int_{\Omega_0} \left[g(D) \boldsymbol{\tau}^v + (1 - g(D_\chi)) \boldsymbol{\tau}^0 \right] : \mathbf{d}_\delta \, d\Omega - \int_{\partial\Omega_{0t}} \hat{\mathbf{t}} \cdot \delta \mathbf{u} \, dS - \int_{\Omega_0} \rho_0 \mathbf{b} \cdot \delta \mathbf{u} \, d\Omega . \quad (2.109)$$

Next, we want to derive the linearization of the residual G_u and consider

$$\begin{aligned} dG_u &= \int_{\Omega_0} d \left(\left[g(D) \boldsymbol{\tau}^v + (1 - g(D_\chi)) \boldsymbol{\tau}^0 \right] : \mathbf{d}_\delta \right) d\Omega \\ &= \int_{\Omega_0} \left(\mathbf{d}_\delta : g'(D) \boldsymbol{\tau}^v dD + g(D) d(\boldsymbol{\tau}^v : \mathbf{d}_\delta) \right. \\ &\quad \left. - \mathbf{d}_\delta : g'(D_\chi) \boldsymbol{\tau}^0 dD_\chi + (1 - g(D_\chi)) d(\boldsymbol{\tau}^0 : \mathbf{d}_\delta) \right) d\Omega . \end{aligned} \quad (2.110)$$

We need an expression for $d(\boldsymbol{\tau}^v : \mathbf{d}_\delta)$ and use Eqs. (2.94), (2.98) and (2.99) to write

$$\begin{aligned} d(\boldsymbol{\tau}^v : \mathbf{d}_\delta) &= d(\mathbf{S}^v : \mathbf{F}^\top \delta \mathbf{F}) = (d\mathbf{F} \mathbf{S}^v + \mathbf{F} d\mathbf{S}^v) : \delta \mathbf{F} \\ &= d\mathbf{F} \mathbf{F}^{-1} \mathbf{F} \mathbf{S}^v \mathbf{F}^\top \mathbf{F}^{-\top} : \delta \mathbf{F} + \mathbf{F} d\mathbf{S}^v \mathbf{F}^\top \mathbf{F}^{-\top} : \delta \mathbf{F} \\ &= \mathbf{l}_d \boldsymbol{\tau}^v : \delta \mathbf{F} \mathbf{F}^{-1} + \mathbf{F} d\mathbf{S}^v \mathbf{F}^\top : \delta \mathbf{F} \mathbf{F}^{-1} \\ &= \mathbf{l}_d \boldsymbol{\tau}^v : \mathbf{l}_\delta + \mathbf{d}_\delta : \mathbf{F} \stackrel{\text{s}}{\square} \mathbf{F}^\top : \frac{d\mathbf{S}^v}{d\mathbf{C}} : d\mathbf{C} \\ &= (\mathbf{l}_d \boldsymbol{\tau}^v \mathbf{l}_\delta^\top) : \mathbf{I} + \mathbf{d}_\delta : \mathbf{F} \stackrel{\text{s}}{\square} \mathbf{F}^\top : 2 \frac{d\mathbf{S}^v}{d\mathbf{C}} : \mathbf{F}^\top \stackrel{\text{s}}{\square} \mathbf{F} : \mathbf{d}_d \\ &= (\mathbf{l}_d \boldsymbol{\tau}^v \mathbf{l}_\delta^\top) : \mathbf{I} + \mathbf{d}_\delta : \mathbb{C}_v^e : \mathbf{d}_d , \end{aligned} \quad (2.111)$$

where we used $\mathbf{d}_\delta = \text{sym}(\mathbf{l}_\delta)$ and $\mathbf{l}_\delta = \delta \mathbf{F} \mathbf{F}^{-1}$ (same for \mathbf{l}_d) as the variational version of $\mathbf{l} = \dot{\mathbf{F}} \mathbf{F}^{-1}$. In a similar way, we approach $d(\boldsymbol{\tau}^0 : \mathbf{d}_\delta)$. However, since $\boldsymbol{\tau}^0$ depends on \mathbf{C}^e , we do not only have to consider the variation with respect to \mathbf{C} (i.e., \mathbf{d}_d) but also the variations with respect to \mathbf{N} (i.e., $\boldsymbol{\omega}_d$) and \underline{c}

$$d(\boldsymbol{\tau}^0 : \mathbf{d}_\delta) = d_u(\boldsymbol{\tau}^0 : \mathbf{d}_\delta) + d_\omega(\boldsymbol{\tau}^0 : \mathbf{d}_\delta) + d_c(\boldsymbol{\tau}^0 : \mathbf{d}_\delta) . \quad (2.112)$$

We can write equivalently

$$d(\tilde{\psi}_d : \mathbf{d}_\delta) = d_u(\tilde{\psi}_d : \mathbf{d}_\delta) + d_\omega(\tilde{\psi}_d : \mathbf{d}_\delta) + d_c(\tilde{\psi}_d : \mathbf{d}_\delta) ,$$

where $\tilde{\psi} = \psi_{e0}(\mathbf{C}^e) + \psi_k$. Before we start the derivation in more detail, it is important to note that \mathbf{F} , \mathbf{F}^c and \mathbf{F}^e are connected via the relation $\mathbf{F} = \mathbf{F}^e \mathbf{F}^c$. Hence, it is only necessary to know two of the quantities because the third one follows immediately from the multiplicative connection. \mathbf{F} and \mathbf{F}^c are treated as working quantities and \mathbf{F}^e as a dependent one. This implies that, if we compute the variation with respect to \mathbf{F} , the quantity \mathbf{F}^c remains frozen.

For the first summand in Eq. (2.112), we find

$$\begin{aligned}
 d_u(\boldsymbol{\tau}^0 : \mathbf{d}_\delta) &= d_u \left(\mathbf{F}^e \mathbf{S}^{0e} \mathbf{F}^{e\top} : \delta \mathbf{F} \mathbf{F}^{-1} \right) \\
 &= d_u \left(\mathbf{S}^{0e} : \mathbf{F}^{c-\top} \overset{s}{\square} \mathbf{F}^{c-1} : \mathbf{F}^\top \delta \mathbf{F} \right) \\
 &= d_u \mathbf{S}^{0e} : \mathbf{F}^{c-\top} \overset{s}{\square} \mathbf{F}^{c-1} : \mathbf{F}^\top \delta \mathbf{F} + \mathbf{S}^{0e} : \mathbf{F}^{c-\top} \overset{s}{\square} \mathbf{F}^{c-1} : d\mathbf{F}^\top \delta \mathbf{F} \\
 &= \mathbf{F}^\top \delta \mathbf{F} : \mathbf{F}^{c-1} \overset{s}{\square} \mathbf{F}^{c-\top} : \frac{d\mathbf{S}^{0e}}{d\mathbf{C}^e} : d_u \mathbf{C}^e + \mathbf{S}^{0e} : \mathbf{F}^{c-\top} \overset{s}{\square} \mathbf{F}^{c-1} : d\mathbf{F}^\top \delta \mathbf{F} .
 \end{aligned} \tag{2.113}$$

For $\mathbf{F}^{c-1} \overset{s}{\square} \mathbf{F}^{c-\top}$ and $\mathbf{F}^{c-\top} \overset{s}{\square} \mathbf{F}^{c-1}$, we use, respectively,

$$\mathbf{F}^{c-1} \overset{s}{\square} \mathbf{F}^{c-\top} = \mathbf{F}^{-1} \overset{s}{\square} \mathbf{F}^{-\top} : \mathbf{F}^e \overset{s}{\square} \mathbf{F}^{e\top} \tag{2.114}$$

$$\mathbf{F}^{c-\top} \overset{s}{\square} \mathbf{F}^{c-1} = \mathbf{F}^{e\top} \overset{s}{\square} \mathbf{F}^e : \mathbf{F}^{-\top} \overset{s}{\square} \mathbf{F}^{-1} . \tag{2.115}$$

For $d_u \mathbf{C}^e$, we use Eq. (2.101) because \mathbf{F}^c is frozen. We obtain

$$\begin{aligned}
 d_u(\boldsymbol{\tau}^0 : \mathbf{d}_\delta) &= \mathbf{F}^\top \delta \mathbf{F} : \mathbf{F}^{-1} \overset{s}{\square} \mathbf{F}^{-\top} : \mathbf{F}^e \overset{s}{\square} \mathbf{F}^{e\top} : 2 \frac{d\mathbf{S}^{0e}}{d\mathbf{C}^e} : \mathbf{F}^{e\top} \overset{s}{\square} \mathbf{F}^e : d_d \\
 &\quad + \mathbf{S}^{0e} : \mathbf{F}^{e\top} \overset{s}{\square} \mathbf{F}^e : \mathbf{F}^{-\top} \overset{s}{\square} \mathbf{F}^{-1} : d\mathbf{F}^\top \delta \mathbf{F} \\
 &= \delta \mathbf{F} \mathbf{F}^{-1} : \mathbf{F}^e \overset{s}{\square} \mathbf{F}^{e\top} : 2 \frac{d\mathbf{S}^{0e}}{d\mathbf{C}^e} : \mathbf{F}^{e\top} \overset{s}{\square} \mathbf{F}^e : d_d + \mathbf{F}^e \mathbf{S}^{0e} \mathbf{F}^{e\top} : (d\mathbf{F} \mathbf{F}^{-1})^\top \delta \mathbf{F} \mathbf{F}^{-1} \\
 &= d_\delta : \mathbf{F}^e \overset{s}{\square} \mathbf{F}^{e\top} : 2 \frac{d\mathbf{S}^{0e}}{d\mathbf{C}^e} : \mathbf{F}^{e\top} \overset{s}{\square} \mathbf{F}^e : d_d + \boldsymbol{\tau}^0 : \mathbf{l}_d^\top \mathbf{l}_\delta \\
 &= d_\delta : \mathbb{C}_0^e : d_d + (\mathbf{l}_d \boldsymbol{\tau}^0 \mathbf{l}_\delta^\top) : \mathbf{I} .
 \end{aligned} \tag{2.116}$$

For the second summand in Eq. (2.112), \mathbf{F} is frozen and we find

$$\begin{aligned}
 d_\omega(\boldsymbol{\tau}^0 : \mathbf{d}_\delta) &= d_\delta : \mathbf{F} d_\omega(\mathbf{F}^{c-1} \mathbf{S}^{0e} \mathbf{F}^{c-\top}) \mathbf{F}^\top \\
 &= d_\delta : \mathbf{F} (d_\omega \mathbf{F}^{c-1} \mathbf{S}^{0e} \mathbf{F}^{c-\top} + \mathbf{F}^{c-1} \mathbf{S}^{0e} d_\omega \mathbf{F}^{c-\top}) \mathbf{F}^\top + d_\delta : \mathbf{F}^e d_\omega \mathbf{S}^{0e} \mathbf{F}^{e\top} .
 \end{aligned} \tag{2.117}$$

For $d_\omega \mathbf{F}^{c-1}$ and $d_\omega \mathbf{F}^{c-\top}$, we use Eq. (2.95) and obtain

$$\begin{aligned}
 d_\omega(\boldsymbol{\tau}^0 : \mathbf{d}_\delta) &= d_\delta : \mathbf{F} (-\mathbf{F}^{c-1} d_\omega \mathbf{F}^c \mathbf{F}^{c-1} \mathbf{S}^{0e} \mathbf{F}^{c-\top} - \mathbf{F}^{c-1} \mathbf{S}^{0e} \mathbf{F}^{c-\top} d_\omega \mathbf{F}^c \mathbf{F}^{c-1}) \mathbf{F}^\top \\
 &\quad + d_\delta : \mathbf{F}^e \overset{s}{\square} \mathbf{F}^{e\top} : \frac{d\mathbf{S}^{0e}}{d\mathbf{C}^e} : d_\omega \mathbf{C}^e \\
 &= -d_\delta : \mathbf{F}^e \overset{s}{\square} \mathbf{F}^{e\top} : (d_\omega \mathbf{F}^c \mathbf{F}^{c-1} \mathbf{S}^{0e} + \mathbf{S}^{0e} (d_\omega \mathbf{F}^c \mathbf{F}^{c-1})^\top) \\
 &\quad + d_\delta : \mathbf{F}^e \overset{s}{\square} \mathbf{F}^{e\top} : \frac{d\mathbf{S}^{0e}}{d\mathbf{C}^e} : d_\omega \mathbf{C}^e \\
 &= -d_\delta : \mathbf{F}^e \overset{s}{\square} \mathbf{F}^{e\top} : (\mathbf{I} \square \mathbf{S}^{0e} + \mathbf{S}^{0e} \overset{\top}{\square} \mathbf{I}) : d_\omega \mathbf{F}^c \mathbf{F}^{c-1}
 \end{aligned}$$

$$\begin{aligned}
& + \mathbf{d}_\delta : \mathbf{F}^e \stackrel{s}{\square} \mathbf{F}^{e\top} : \frac{d\mathbf{S}^{0e}}{d\mathbf{C}^e} : d_\omega \mathbf{C}^e \\
d_\omega(\boldsymbol{\tau}^0 : \mathbf{d}_\delta) &= -\mathbf{d}_\delta : \mathbf{F}^e \stackrel{s}{\square} \mathbf{F}^{e\top} : 2 \mathbf{I} \stackrel{s}{\square} \mathbf{S}^{0e} : d_\omega \mathbf{F}^c \mathbf{F}^{c-1} + \mathbf{d}_\delta : \mathbf{F}^e \stackrel{s}{\square} \mathbf{F}^{e\top} : \frac{d\mathbf{S}^{0e}}{d\mathbf{C}^e} : d_\omega \mathbf{C}^e .
\end{aligned} \tag{2.118}$$

For $d_\omega \mathbf{C}^e$, we use Eq. (2.106) because \mathbf{F} is frozen. With Eqs. (2.106) for $d_\omega \mathbf{C}^e$ and (2.104) for $d_\omega \mathbf{F}^c \mathbf{F}^{c-1}$, we finally obtain for the second summand in Eq. (2.112)

$$d_\omega(\boldsymbol{\tau}^0 : \mathbf{d}_\delta) = \mathbf{d}_\delta : \mathbf{F}^e \stackrel{s}{\square} \mathbf{F}^{e\top} : \left(-2 \mathbf{I} \stackrel{s}{\square} \mathbf{S}^{0e} - \frac{d\mathbf{S}^{0e}}{d\mathbf{C}^e} : 2\mathbf{C}^e \stackrel{s}{\square} \mathbf{I} \right) : \mathbf{L}_\omega^c \cdot \boldsymbol{\omega}_d = \mathbf{d}_\delta : \tilde{\psi}_{d\omega} \cdot \boldsymbol{\omega}_d . \tag{2.119}$$

For the third and last summand in Eq. (2.112), we write

$$d_c(\boldsymbol{\tau}^0 : \mathbf{d}_\delta) = d_c(\tilde{\psi}_d : \mathbf{d}_\delta) = \mathbf{d}_\delta : \tilde{\psi}_{dc} \cdot d_{\underline{c}} . \tag{2.120}$$

Using Eq. (2.64) ($\tilde{\psi}_{dc} = \tilde{\psi}_{cd}^\top = -\underline{r}_d^\top$) and Eq. (2.59), we obtain

$$d_c(\boldsymbol{\tau}^0 : \mathbf{d}_\delta) = \mathbf{d}_\delta : \underline{r}_d^\top \cdot \left(\frac{\partial \underline{r}}{\partial \underline{c}} \right)^{-1} (\underline{r}_\omega \cdot \boldsymbol{\omega}_d + \underline{r}_d : \mathbf{d}_d) . \tag{2.121}$$

Finally, we write for Eq. (2.112)

$$\begin{aligned}
d(\boldsymbol{\tau}^0 : \mathbf{d}_\delta) &= (\mathbf{l}_d \boldsymbol{\tau}^0 \mathbf{l}_\delta^\top) : \mathbf{I} + \mathbf{d}_\delta : \mathbb{C}_0^e : \mathbf{d}_d + \mathbf{d}_\delta : \tilde{\psi}_{d\omega} \cdot \boldsymbol{\omega}_d + \mathbf{d}_\delta : \underline{r}_d^\top \cdot \left(\frac{\partial \underline{r}}{\partial \underline{c}} \right)^{-1} (\underline{r}_\omega \cdot \boldsymbol{\omega}_d + \underline{r}_d : \mathbf{d}_d) \\
&= (\mathbf{l}_d \boldsymbol{\tau}^0 \mathbf{l}_\delta^\top) : \mathbf{I} + \mathbf{d}_\delta : \left(\mathbb{C}_0^e + \underline{r}_d^\top \left(\frac{\partial \underline{r}}{\partial \underline{c}} \right)^{-1} \underline{r}_d \right) : \mathbf{d}_d + \mathbf{d}_\delta : \left(\tilde{\psi}_{d\omega} + \underline{r}_d^\top \left(\frac{\partial \underline{r}}{\partial \underline{c}} \right)^{-1} \underline{r}_\omega \right) \cdot \boldsymbol{\omega}_d \\
&= (\mathbf{l}_d \boldsymbol{\tau}^0 \mathbf{l}_\delta^\top) : \mathbf{I} + \mathbf{d}_\delta : \mathbb{C}_{dd} : \mathbf{d}_d + \mathbf{d}_\delta : \mathbb{C}_{d\omega} \cdot \boldsymbol{\omega}_d ,
\end{aligned} \tag{2.122}$$

see Eqs. (2.116) and (2.119) for \mathbb{C}_0^e and $\tilde{\psi}_{d\omega}$. In the last step, we plug Eqs. (2.69), (2.111) and (2.122) into the linearization in Eq. (2.110) and obtain

$$\begin{aligned}
dG_u &= \int_{\Omega_0} \left(\left(\mathbf{l}_d \cdot \left[g(D) \boldsymbol{\tau}^v + (1 - g(D_\chi)) \boldsymbol{\tau}^0 \right] \cdot \mathbf{l}_\delta^\top \right) : \mathbf{I} \right. \\
&\quad + \mathbf{d}_\delta : \left[g(D) \mathbb{C}_v^e + (1 - g(D_\chi)) \mathbb{C}_{dd} + \frac{(g'(D))^2}{\partial r / \partial D} \boldsymbol{\tau}^v \otimes \boldsymbol{\tau}^v \right] : \mathbf{d}_d \\
&\quad + \mathbf{d}_\delta : [(1 - g(D_\chi)) \mathbb{C}_{d\omega}] \cdot \boldsymbol{\omega}_d \\
&\quad \left. + \mathbf{d}_\delta : \left[-\frac{g'(D) H_\chi}{\partial r / \partial D} \boldsymbol{\tau}^v - g'(D_\chi) \boldsymbol{\tau}^0 \right] dD_\chi \right) d\Omega .
\end{aligned} \tag{2.123}$$

2.D Derivation and linearization of the residual G_N

In order to find an expression for

$$\delta_\omega \Pi_\Delta = \int_{\Omega_0} \delta_\omega \pi_\Delta \, d\Omega ,$$

we consider all contributions in π_Δ that depend on the crack surface normal \mathbf{N}

$$\begin{aligned} \delta_\omega \Pi_\Delta = \int_{\Omega_0} \delta_\omega \Big((1 - g(D_\chi)) (\psi_{e0}(\mathbf{C}^e) + \psi_k) + \psi_{\text{pin}}(\mathbf{N} - \mathbf{N}^*) + \psi_{\text{aniso}}(\mathbf{N}) \\ + \psi_{gN}(\text{Grad}(\mathbf{N})) + \frac{\eta_N}{2\Delta t} \|\mathbf{N} - \mathbf{N}_n\|^2 \Big) d\Omega . \end{aligned} \quad (2.124)$$

Using $\tilde{\psi} = \psi_{e0}(\mathbf{C}^e) + \psi_k$ and Eq. (2.13) for $\delta \mathbf{N}$, we find for the first summand

$$\delta_\omega \tilde{\psi} = \frac{\partial \tilde{\psi}}{\partial \mathbf{N}} \cdot \delta \mathbf{N} = \frac{\partial \tilde{\psi}}{\partial \mathbf{N}} \cdot (\boldsymbol{\omega}_\delta \times \mathbf{N}) = \boldsymbol{\omega}_\delta \cdot \left(\mathbf{N} \times \frac{\partial \tilde{\psi}}{\partial \mathbf{N}} \right) = \tilde{\psi}_\omega \cdot \boldsymbol{\omega}_\delta . \quad (2.125)$$

In the same way that \mathbf{S}^{0e} is the conjugate force measure to \mathbf{C}^e , we assume $\tilde{\psi}_\omega$ to be the conjugate force measure to $\boldsymbol{\omega}$. Assuming that all force measures together with their respective dual quantities yield equivalent stress powers, we write

$$\frac{\partial \tilde{\psi}}{\partial \mathbf{N}} \cdot \delta \mathbf{N} = \frac{\partial \tilde{\psi}}{\partial \mathbf{C}^e} : \delta \mathbf{C}^e \quad (2.126)$$

$$\tilde{\psi}_\omega \cdot \boldsymbol{\omega}_\delta = \frac{1}{2} \mathbf{S}^{0e} : \delta \mathbf{C}^e . \quad (2.127)$$

We are interested in finding the force measure dual to $\boldsymbol{\omega}$, i.e., we do not need an \mathbf{F} contribution. Hence, we use Eqs. (2.104) and (2.106) for $\delta \mathbf{C}^e$ because \mathbf{F} is frozen. We write

$$\tilde{\psi}_\omega \cdot \boldsymbol{\omega}_\delta = -\mathbf{S}^{0e} : \mathbf{C}^e \square_{\mathbf{S}} \mathbf{I} : \mathbf{L}_\omega^c \cdot \boldsymbol{\omega}_\delta = -\boldsymbol{\Sigma}^e : \mathbf{L}_\omega^c \cdot \boldsymbol{\omega}_\delta \quad (2.128)$$

$$= \left(-\mathbf{L}_\omega^{c\top} : \boldsymbol{\Sigma}^e \right) \cdot \boldsymbol{\omega}_\delta , \quad (2.129)$$

where $\boldsymbol{\Sigma}^e = \mathbf{C}^e \mathbf{S}^{0e}$ denotes the Mandel stress tensor. Since $\tilde{\psi}_\omega$ is a frequently used stress-like quantity, we introduce the tensor notation

$$\mathbf{M}_0 := \tilde{\psi}_\omega . \quad (2.130)$$

For the variation of ψ_{pin} , we consider the active case (D or $D_\chi \geq 1 - \epsilon$)

$$\delta_\omega \psi_{\text{pin}} = H_N(\mathbf{N} - \mathbf{N}^*) \cdot \delta \mathbf{N} = H_N(\mathbf{N} - \mathbf{N}^*) \cdot (\boldsymbol{\omega}_\delta \times \mathbf{N}) = \boldsymbol{\omega}_\delta \cdot H_N(\mathbf{N}^* \times \mathbf{N}) . \quad (2.131)$$

The same derivation with \mathbf{N}_n instead of \mathbf{N}^* is valid for the contribution from the dissipation potential

$$\delta_\omega \left(\frac{\eta_N}{2\Delta t} \|\mathbf{N} - \mathbf{N}_n\|^2 \right) = \boldsymbol{\omega}_\delta \cdot \frac{\eta_N}{\Delta t} (\mathbf{N}_n \times \mathbf{N}) . \quad (2.132)$$

Next, we treat the anisotropic contribution

$$\begin{aligned} \delta_\omega \psi_{\text{aniso}} &= \sum_{m=1}^3 \beta_m (\mathbf{N} \cdot \mathbf{p}_m) (\delta \mathbf{N} \cdot \mathbf{p}_m) = \sum_{m=1}^3 \beta_m (\mathbf{N} \cdot \mathbf{p}_m) ((\boldsymbol{\omega}_\delta \times \mathbf{N}) \cdot \mathbf{p}_m) \\ &= \left[\sum_{m=1}^3 \beta_m (\mathbf{N} \cdot \mathbf{p}_m) (\mathbf{N} \times \mathbf{p}_m) \right] \cdot \boldsymbol{\omega}_\delta , \end{aligned} \quad (2.133)$$

Finally, the variation of the gradient contribution ψ_{gN} reads

$$\delta_\omega \psi_{\text{gN}} = \underbrace{\frac{\partial \psi_{\text{gN}}(\text{Grad}(\mathbf{N}))}{\partial \text{Grad}(\mathbf{N})}}_{=:\boldsymbol{\xi}_N} : \delta_\omega \text{Grad}(\mathbf{N}) = \boldsymbol{\xi}_N : \text{Grad}(\delta \mathbf{N}) . \quad (2.134)$$

In conclusion, the residual reads

$$\begin{aligned} G_N = \delta_\omega \Pi_\Delta &= \int_{\Omega_0} \left(\left[(1 - g(D_\chi)) \mathbf{M}_0 + \begin{cases} H_N \mathbf{N}^* \times \mathbf{N}, & D \text{ or } D_\chi \geq 1 - \epsilon \\ 0, & \text{else} \end{cases} + \frac{\eta_N}{\Delta t} \mathbf{N}_n \times \mathbf{N} \right. \right. \\ &\quad \left. \left. + \sum_{m=1}^3 \beta_m (\mathbf{N} \cdot \mathbf{p}_m) (\mathbf{N} \times \mathbf{p}_m) \right] \cdot \boldsymbol{\omega}_\delta + \boldsymbol{\xi}_N : \text{Grad}(\delta \mathbf{N}) \right) d\Omega . \end{aligned} \quad (2.135)$$

Next, we want to find the linearization of the residual G_N and consider all the summands in Eq. (2.135) individually. Using Eq. (2.91), the variation of $\delta_\omega \psi_{\text{pin}}$ in the active case (D or $D_\chi \geq 1 - \epsilon$) reads

$$\begin{aligned} d(H_N(\mathbf{N}^* \times \mathbf{N}) \cdot \boldsymbol{\omega}_\delta) &= H_N((\mathbf{N}^* \times d\mathbf{N}) \cdot \boldsymbol{\omega}_\delta + (\mathbf{N}^* \times \mathbf{N}) \cdot d\boldsymbol{\omega}_\delta) \\ &= H_N((\mathbf{N}^* \times (\boldsymbol{\omega}_d \times \mathbf{N})) \cdot \boldsymbol{\omega}_\delta + (\mathbf{N}^* \times \mathbf{N}) \cdot (\boldsymbol{\omega}_d \times \boldsymbol{\omega}_\delta)) \\ &= \boldsymbol{\omega}_\delta \cdot (H_N(\mathbf{N}^* \cdot \mathbf{N}) \mathbf{I}) \cdot \boldsymbol{\omega}_d . \end{aligned} \quad (2.136)$$

The same derivation with \mathbf{N}_n instead of \mathbf{N}^* holds for the contribution from the dissipation potential

$$d\left(\frac{\eta_N}{\Delta t} (\mathbf{N}_n \times \mathbf{N}) \cdot \boldsymbol{\omega}_\delta\right) = \boldsymbol{\omega}_\delta \cdot \left(\frac{\eta_N}{\Delta t} (\mathbf{N}_n \cdot \mathbf{N}) \mathbf{I}\right) \cdot \boldsymbol{\omega}_d . \quad (2.137)$$

For the gradient term, we obtain

$$\begin{aligned} d(\boldsymbol{\xi}_N : \text{Grad}(\delta \mathbf{N})) &= d(\boldsymbol{\xi}_N) : \text{Grad}(\delta \mathbf{N}) + \boldsymbol{\xi}_N : \text{Grad}(d(\boldsymbol{\omega}_\delta \times \mathbf{N})) \\ &= d(\boldsymbol{\xi}_N) : \text{Grad}(\delta \mathbf{N}) + \boldsymbol{\xi}_N : \text{Grad}((\boldsymbol{\omega}_d \times \boldsymbol{\omega}_\delta) \times \mathbf{N}) \end{aligned}$$

$$\begin{aligned}
& + \boldsymbol{\xi}_N : \text{Grad}(\boldsymbol{\omega}_\delta \times (\boldsymbol{\omega}_d \times \mathbf{N})) \\
& = \text{Grad}(\delta \mathbf{N}) : \frac{\partial \boldsymbol{\xi}_N}{\partial \text{Grad}(\mathbf{N})} : \text{Grad}(\mathbf{dN}) - \boldsymbol{\xi}_N : \text{Grad}((\boldsymbol{\omega}_\delta \cdot \boldsymbol{\omega}_d) \mathbf{N}) \\
& \quad (2.138)
\end{aligned}$$

$$= \text{Grad}(\delta \mathbf{N}) : K_{gN} \mathbb{I} : \text{Grad}(\mathbf{dN}) - \boldsymbol{\xi}_N : \text{Grad}((\boldsymbol{\omega}_\delta \cdot \boldsymbol{\omega}_d) \mathbf{N}) . \quad (2.139)$$

Next, we want to find the variation of $\delta_\omega \psi_{\text{aniso}}$ and write

$$\begin{aligned}
& \mathbf{d}(\boldsymbol{\omega}_\delta \cdot \sum_{m=1}^3 \beta_m (\mathbf{N} \cdot \mathbf{p}_m) (\mathbf{N} \times \mathbf{p}_m)) \\
& = \sum_{m=1}^3 \beta_m \left[(\mathbf{dN} \cdot \mathbf{p}_m) (\mathbf{N} \times \mathbf{p}_m) \cdot \boldsymbol{\omega}_\delta + (\mathbf{N} \cdot \mathbf{p}_m) (\mathbf{dN} \times \mathbf{p}_m) \cdot \boldsymbol{\omega}_\delta + (\mathbf{N} \cdot \mathbf{p}_m) (\mathbf{N} \times \mathbf{p}_m) \cdot \mathbf{d}\boldsymbol{\omega}_\delta \right] \\
& = \sum_{m=1}^3 \beta_m \left[((\boldsymbol{\omega}_d \times \mathbf{N}) \cdot \mathbf{p}_m) ((\mathbf{N} \times \mathbf{p}_m) \cdot \boldsymbol{\omega}_\delta) + (\mathbf{N} \cdot \mathbf{p}_m) ((\boldsymbol{\omega}_d \times \mathbf{N}) \times \mathbf{p}_m) \cdot \boldsymbol{\omega}_\delta \right. \\
& \quad \left. + ((\mathbf{N} \cdot \mathbf{p}_m) (\mathbf{N} \times \mathbf{p}_m) \cdot (\boldsymbol{\omega}_d \times \boldsymbol{\omega}_\delta)) \right] \\
& = \boldsymbol{\omega}_\delta \cdot \left[\sum_{m=1}^3 \beta_m \left((\mathbf{N} \times \mathbf{p}_m) \otimes (\mathbf{N} \times \mathbf{p}_m) - (\mathbf{N} \cdot \mathbf{p}_m)^2 \mathbf{I} \right) \right] \cdot \boldsymbol{\omega}_d . \quad (2.140)
\end{aligned}$$

The variation of $(1 - g(D_\chi)) \mathbf{M}_0 \cdot \boldsymbol{\omega}_\delta$ consists of multiple contributions

$$\begin{aligned}
& \mathbf{d}((1 - g(D_\chi)) \mathbf{M}_0 \cdot \boldsymbol{\omega}_\delta) = \boldsymbol{\omega}_\delta \cdot (-g'(D_\chi) \mathbf{M}_0) \mathbf{d}D_\chi \\
& \quad + (1 - g(D_\chi)) \left[\mathbf{d}_u(\mathbf{M}_0 \cdot \boldsymbol{\omega}_\delta) + \mathbf{d}_\omega(\mathbf{M}_0 \cdot \boldsymbol{\omega}_\delta) + \mathbf{d}_c(\mathbf{M}_0 \cdot \boldsymbol{\omega}_\delta) \right] \\
& = \boldsymbol{\omega}_\delta \cdot (-g'(D_\chi) \mathbf{M}_0) \mathbf{d}D_\chi \\
& \quad + (1 - g(D_\chi)) \left[\mathbf{d}_u(\tilde{\psi}_\omega \cdot \boldsymbol{\omega}_\delta) + \mathbf{d}_\omega(\tilde{\psi}_\omega \cdot \boldsymbol{\omega}_\delta) + \mathbf{d}_c(\tilde{\psi}_\omega \cdot \boldsymbol{\omega}_\delta) \right] . \quad (2.141)
\end{aligned}$$

For the contribution $\mathbf{d}_u(\tilde{\psi}_\omega \cdot \boldsymbol{\omega}_\delta)$, we compute the variation with respect to quantities that depend on \mathbf{F} (or rather \mathbf{d}). In particular, $\boldsymbol{\omega}_\delta$ and \mathbf{F}^c do not depend on the listed quantities. For $\mathbf{d}_u \boldsymbol{\Sigma}^e$, we use Eq. (2.107) and write

$$\mathbf{d}_u(\tilde{\psi}_\omega \cdot \boldsymbol{\omega}_\delta) = -\boldsymbol{\omega}_\delta \cdot \mathbf{L}_\omega^c : \left(\mathbf{I} \stackrel{s}{\square} \mathbf{S}^{0e} + \mathbf{C}^e \frac{\mathbf{d}\mathbf{S}^{0e}}{\mathbf{d}\mathbf{C}^e} \right) : \mathbf{d}_u \mathbf{C}^e . \quad (2.142)$$

For $\mathbf{d}_u \mathbf{C}^e$, we use Eq. (2.101) with frozen \mathbf{F}^c and obtain

$$\mathbf{d}_u(\tilde{\psi}_\omega \cdot \boldsymbol{\omega}_\delta) = \boldsymbol{\omega}_\delta \cdot \left[-\mathbf{L}_\omega^c : \left(\mathbf{I} \stackrel{s}{\square} \mathbf{S}^{0e} + \mathbf{C}^e \stackrel{s}{\square} \mathbf{I} : \frac{\mathbf{d}\mathbf{S}^{0e}}{\mathbf{d}\mathbf{C}^e} \right) : \mathbf{C}_d^e \right] : \mathbf{d}_d = \boldsymbol{\omega}_\delta \cdot \tilde{\psi}_{\omega d} : \mathbf{d}_d . \quad (2.143)$$

Next, we want to investigate the contribution $d_\omega(\tilde{\psi}_\omega \cdot \omega_\delta)$. Note that, in contrast to the previous contribution, we are now considering variations with respect to ω . Thus, we write

$$d_\omega(\tilde{\psi}_\omega \cdot \omega_\delta) = \omega_\delta \cdot d_\omega \tilde{\psi}_\omega + \tilde{\psi}_\omega \cdot d\omega_\delta \quad (2.144)$$

$$= \omega_\delta \cdot \tilde{\psi}_{\omega\omega} \cdot \omega_d + \tilde{\psi}_\omega \cdot (\omega_d \times \omega_\delta) . \quad (2.145)$$

First, we want to find $\tilde{\psi}_{\omega\omega}$ and use Eqs. (2.107) and (2.95) to write

$$\begin{aligned} \omega_\delta \cdot d_\omega \tilde{\psi}_\omega &= \omega_\delta \cdot d_\omega \left(-L_\omega^{c\top} : \Sigma^e \right) \\ &= -\omega_\delta \cdot L_\omega^{c\top} : \left(I \stackrel{s}{\square} S^{0e} + C^e \frac{dS^{0e}}{dC^e} \right) : d_\omega C^e \\ &\quad - \omega_\delta \cdot \epsilon : \left(d_\omega F^{c\top} \square F^{c-\top} + F^{c\top} \square d_\omega F^{c-\top} \right) : \Sigma^e \\ &= -\omega_\delta \cdot L_\omega^{c\top} : \left(I \stackrel{s}{\square} S^{0e} + C^e \frac{dS^{0e}}{dC^e} \right) : d_\omega C^e \\ &\quad - \omega_\delta \cdot \epsilon : \left(F^{c\top} (d_\omega F^c F^{c-1})^\top \square F^{c-\top} - F^{c\top} \square (d_\omega F^c F^{c-1})^\top F^{c-\top} \right) : \Sigma^e \\ &= -\omega_\delta \cdot L_\omega^{c\top} : \left(I \stackrel{s}{\square} S^{0e} + C^e \frac{dS^{0e}}{dC^e} \right) : d_\omega C^e \\ &\quad - \omega_\delta \cdot \epsilon : F^{c\top} \square F^{c-\top} : \left((d_\omega F^c F^{c-1})^\top \square I - I \square (d_\omega F^c F^{c-1})^\top \right) : \Sigma^e \\ &= -\omega_\delta \cdot L_\omega^{c\top} \left(I \stackrel{s}{\square} S^{0e} + C^e \frac{dS^{0e}}{dC^e} \right) : d_\omega C^e \\ &\quad - \omega_\delta \cdot \epsilon : F^{c\top} \square F^{c-\top} : (I \square \Sigma^e - \Sigma^e \square I) : (d_\omega F^c F^{c-1})^\top . \end{aligned} \quad (2.146)$$

For $d_\omega C^e$, we use Eq. (2.106) and for $d_\omega F^c F^{c-1}$, we refer to Eq. (2.104) the transpose of which is given by

$$\begin{aligned} (d_\omega F^c F^{c-1})^\top &= -(\mathbb{I} - F^c \square F^{c-1}) : \epsilon \cdot \omega_d^\top = -((\epsilon \cdot \omega_d)^\top - F^{c-\top} (\epsilon \cdot \omega_d)^\top F^{c\top}) \\ &= (\mathbb{I} - F^{c-\top} \square F^{c\top}) : \epsilon \cdot \omega_d . \end{aligned} \quad (2.147)$$

In Eq. (2.146), we obtain

$$\begin{aligned} \omega_\delta \cdot d_\omega \tilde{\psi}_\omega &= \omega_\delta \cdot L_\omega^{c\top} : \left(I \stackrel{s}{\square} S^{0e} + C^e \frac{dS^{0e}}{dC^e} \right) : 2C^e \stackrel{s}{\square} I : L_\omega^c \cdot \omega_d \\ &\quad - \omega_\delta \cdot \epsilon : F^{c\top} \square F^{c-\top} : (I \square \Sigma^e - \Sigma^e \square I) : (\mathbb{I} - F^{c-\top} \square F^{c\top}) : \epsilon \cdot \omega_d \\ &= \omega_\delta \cdot L_\omega^{c\top} : \left(2 I \stackrel{s}{\square} S^{0e} : C^e \stackrel{s}{\square} I + C^e \stackrel{s}{\square} I : 2 \frac{dS^{0e}}{dC^e} : C^e \stackrel{s}{\square} I \right) : L_\omega^c \cdot \omega_d \\ &\quad - \omega_\delta \cdot \epsilon : F^{c\top} \square F^{c-\top} : (I \square \Sigma^e - \Sigma^e \square I) : (\mathbb{I} - F^{c-\top} \square F^{c\top}) : \epsilon \cdot \omega_d . \end{aligned} \quad (2.148)$$

The following relation for $\mathbf{I} \stackrel{s}{\square} \mathbf{S}^{0e} : \mathbf{C}^e \stackrel{s}{\square} \mathbf{I}$ holds, where we used symmetry in the indices kl

$$\begin{aligned} \mathbf{I} \stackrel{s}{\square} \mathbf{S}^{0e} : \mathbf{C}^e \stackrel{s}{\square} \mathbf{I} &= \delta_{ik} S_{lj}^{0e} \frac{1}{2} (C_{km}^e \delta_{nl} + C_{lm}^e \delta_{nk}) \mathbf{e}_i \otimes \mathbf{e}_j \otimes \mathbf{e}_m \otimes \mathbf{e}_n \\ &= \frac{1}{2} (C_{im}^e S_{nj}^{0e} + \delta_{in} C_{ml}^e S_{lj}^{0e}) \mathbf{e}_i \otimes \mathbf{e}_j \otimes \mathbf{e}_m \otimes \mathbf{e}_n \\ &= \frac{1}{2} \left(\mathbf{C}^e \stackrel{s}{\square} \mathbf{S}^{0e} + \mathbf{I} \stackrel{T}{\square} \boldsymbol{\Sigma}^e \right). \end{aligned} \quad (2.149)$$

Furthermore, we use the following relation

$$\begin{aligned} \mathbf{I} \stackrel{s}{\square} \boldsymbol{\Sigma}^e : (\mathbb{I} - \mathbf{F}^{c-T} \stackrel{s}{\square} \mathbf{F}^{cT}) : \boldsymbol{\epsilon} \cdot \boldsymbol{\omega}_d &= \delta_{ik} \Sigma_{lj}^e (\delta_{km} \delta_{nl} - F_{km}^{c-T} F_{nl}^{cT}) \epsilon_{mno} \omega_o^d \mathbf{e}_i \otimes \mathbf{e}_j \\ &= -\delta_{ik} \Sigma_{lj}^e (\delta_{ln} \delta_{mk} - F_{ln}^c F_{mk}^{c-1}) \epsilon_{nmo} \omega_o^d \mathbf{e}_i \otimes \mathbf{e}_j \\ &= -\mathbf{I} \stackrel{T}{\square} \boldsymbol{\Sigma}^e : (\mathbb{I} - \mathbf{F}^c \stackrel{s}{\square} \mathbf{F}^{c-1}) : \boldsymbol{\epsilon} \cdot \boldsymbol{\omega}_d \end{aligned} \quad (2.150)$$

which holds for $\boldsymbol{\Sigma}^e \stackrel{s}{\square} \mathbf{I} : (\mathbb{I} - \mathbf{F}^{c-T} \stackrel{s}{\square} \mathbf{F}^{cT})$ analogously. Eqs. (2.149) and (2.150) yield in Eq. (2.148)

$$\boldsymbol{\omega}_\delta \cdot d_\omega \tilde{\psi}_\omega = \boldsymbol{\omega}_\delta \cdot \mathbf{L}_\omega^c : \left(\mathbf{C}^e \stackrel{s}{\square} \mathbf{S}^{0e} + \mathbf{C}^e \stackrel{s}{\square} \mathbf{I} : 2 \frac{d\mathbf{S}^{0e}}{d\mathbf{C}^e} : \mathbf{C}^e \stackrel{s}{\square} \mathbf{I} \right) : \mathbf{L}_\omega^c \cdot \boldsymbol{\omega}_d \quad (2.151)$$

$$\begin{aligned} &+ \boldsymbol{\omega}_\delta \cdot \boldsymbol{\epsilon} : (\mathbb{I} - \mathbf{F}^{cT} \stackrel{s}{\square} \mathbf{F}^{c-T}) : \mathbf{I} \stackrel{T}{\square} \boldsymbol{\Sigma}^e : (\mathbb{I} - \mathbf{F}^c \stackrel{s}{\square} \mathbf{F}^{c-1}) : \boldsymbol{\epsilon} \cdot \boldsymbol{\omega}_d \\ &+ \boldsymbol{\omega}_\delta \cdot \boldsymbol{\epsilon} : \mathbf{F}^{cT} \stackrel{s}{\square} \mathbf{F}^{c-T} : \left(\mathbf{I} \stackrel{T}{\square} \boldsymbol{\Sigma}^e - \boldsymbol{\Sigma}^e \stackrel{T}{\square} \mathbf{I} \right) : (\mathbb{I} - \mathbf{F}^c \stackrel{s}{\square} \mathbf{F}^{c-1}) : \boldsymbol{\epsilon} \cdot \boldsymbol{\omega}_d \\ &= \boldsymbol{\omega}_\delta \cdot \mathbf{L}_\omega^c : \left(\mathbf{C}^e \stackrel{s}{\square} \mathbf{S}^{0e} + \mathbf{C}^e \stackrel{s}{\square} \mathbf{I} : 2 \frac{d\mathbf{S}^{0e}}{d\mathbf{C}^e} : \mathbf{C}^e \stackrel{s}{\square} \mathbf{I} \right) : \mathbf{L}_\omega^c \cdot \boldsymbol{\omega}_d \quad (2.152) \\ &+ \boldsymbol{\omega}_\delta \cdot \boldsymbol{\epsilon} : \left(-\mathbf{I} \stackrel{T}{\square} \boldsymbol{\Sigma}^e : \mathbf{F}^c \stackrel{s}{\square} \mathbf{F}^{c-1} - \mathbf{F}^{cT} \stackrel{s}{\square} \mathbf{F}^{c-T} : \boldsymbol{\Sigma}^e \stackrel{T}{\square} \mathbf{I} \right. \\ &\quad \left. + \mathbf{I} \stackrel{T}{\square} \boldsymbol{\Sigma}^e + \mathbf{F}^{cT} \stackrel{s}{\square} \mathbf{F}^{c-T} : \boldsymbol{\Sigma}^e \stackrel{T}{\square} \mathbf{I} : \mathbf{F}^c \stackrel{s}{\square} \mathbf{F}^{c-1} \right) : \boldsymbol{\epsilon} \cdot \boldsymbol{\omega}_d. \end{aligned}$$

In order to simplify the notation, we rewrite the last line of Eq. (2.152) as follows

$$\begin{aligned} \boldsymbol{\omega}_\delta \cdot \boldsymbol{\epsilon} : \left(\mathbf{I} \stackrel{T}{\square} \boldsymbol{\Sigma}^e + \mathbf{F}^{cT} \stackrel{s}{\square} \mathbf{F}^{c-T} : \boldsymbol{\Sigma}^e \stackrel{T}{\square} \mathbf{I} : \mathbf{F}^c \stackrel{s}{\square} \mathbf{F}^{c-1} \right) : \boldsymbol{\epsilon} \cdot \boldsymbol{\omega}_d \\ &= \boldsymbol{\omega}_\delta \cdot \boldsymbol{\epsilon} : \left((-\boldsymbol{\epsilon} \cdot \boldsymbol{\omega}_d) \cdot \boldsymbol{\Sigma}^e + \mathbf{F}^{cT} \boldsymbol{\Sigma}^e \mathbf{F}^{c-T} \cdot (-\boldsymbol{\epsilon} \cdot \boldsymbol{\omega}_d) \right) \\ &= -\omega_i^\delta \epsilon_{ijk} \epsilon_{jlm} \omega_m^d \Sigma_{lk}^e - \omega_i^\delta \epsilon_{ijk} F_{jo}^{cT} \Sigma_{op}^e F_{pq}^{c-T} \epsilon_{qkm} \omega_m^d \\ &= -(\delta_{kl} \delta_{im} - \delta_{km} \delta_{il}) \omega_i^\delta \omega_m^d \Sigma_{lk}^e - (\delta_{im} \delta_{jq} - \delta_{iq} \delta_{jm}) \omega_i^\delta F_{jo}^{cT} \Sigma_{op}^e F_{pq}^{c-T} \omega_m^d \\ &= \boldsymbol{\omega}_\delta \cdot \left(\boldsymbol{\Sigma}^e + (\mathbf{F}^{cT} \boldsymbol{\Sigma}^e \mathbf{F}^{c-T})^T - 2 \operatorname{tr}(\boldsymbol{\Sigma}^e) \mathbf{I} \right) \cdot \boldsymbol{\omega}_d. \end{aligned} \quad (2.153)$$

Next, we want to incorporate the contribution $\tilde{\psi}_\omega \cdot (\omega_d \times \omega_\delta)$ from Eq. (2.145) and write

$$\begin{aligned}
\tilde{\psi}_\omega \cdot (\omega_d \times \omega_\delta) &= -\tilde{\psi}_\omega \cdot (\omega_\delta \times \omega_d) \\
&= -(\epsilon : (\Sigma^e - \mathbf{F}^{c\top} \Sigma^e \mathbf{F}^{c-\top})) \cdot \epsilon : \omega_\delta \otimes \omega_d \\
&= -(\epsilon \cdot \epsilon : (\Sigma^e - \mathbf{F}^{c\top} \Sigma^e \mathbf{F}^{c-\top})) : \omega_\delta \otimes \omega_d \\
&= \omega_\delta \cdot \left(-2 \operatorname{skw}(\Sigma^e - \mathbf{F}^{c\top} \Sigma^e \mathbf{F}^{c-\top}) \right) \cdot \omega_d \\
&= \omega_\delta \cdot \left(-2 \operatorname{skw}(\Sigma^e + (\mathbf{F}^{c\top} \Sigma^e \mathbf{F}^{c-\top})^\top) \right) \cdot \omega_d . \tag{2.154}
\end{aligned}$$

We bring Eqs. (2.152), (2.153) and (2.154) together and apply $\mathbf{A} - 2 \operatorname{skw}(\mathbf{A}) = \mathbf{A}^\top$ to $\Sigma^e + (\mathbf{F}^{c\top} \Sigma^e \mathbf{F}^{c-\top})^\top$. Hence, for the entire variation $d_\omega(\tilde{\psi}_\omega \cdot \omega_\delta)$, we obtain

$$\begin{aligned}
d_\omega(\tilde{\psi}_\omega \cdot \omega_\delta) &= \omega_\delta \cdot d_\omega \tilde{\psi}_\omega + \tilde{\psi}_\omega \cdot (\omega_d \times \omega_\delta) \\
&= \omega_\delta \cdot \left[\mathbf{L}_\omega^c : \left(\mathbf{C}^e \square \mathbf{S}^{0e} + \mathbf{C}^e \square \mathbf{I} : 2 \frac{d\mathbf{S}^{0e}}{d\mathbf{C}^e} : \mathbf{C}^e \square \mathbf{I} \right) : \mathbf{L}_\omega^c \right. \\
&\quad \left. + \epsilon : \left(-\mathbf{I} \square \Sigma^e : \mathbf{F}^c \square \mathbf{F}^{c-1} - \mathbf{F}^{c\top} \square \mathbf{F}^{c-\top} : \Sigma^e \square \mathbf{I} \right) : \epsilon \right. \\
&\quad \left. + \Sigma^{e\top} + \mathbf{F}^{c\top} \Sigma^e \mathbf{F}^{c-\top} - 2 \operatorname{tr}(\Sigma^e) \mathbf{I} \right] \cdot \omega_d . \tag{2.155}
\end{aligned}$$

Since the variation $d_\omega(\tilde{\psi}_\omega \cdot \omega_\delta)$ is the second variation, it is supposed to be symmetric. In order to make the symmetry of the contribution $\omega_\delta \cdot (\Sigma^{e\top} + \mathbf{F}^{c\top} \Sigma^e \mathbf{F}^{c-\top}) \cdot \omega_d$ easily visible, we investigate it more closely. Using Eq. (2.9), we first find

$$\omega_\delta \cdot \mathbf{F}^{c\top} = \left(\sum_{i=1}^2 \delta\omega_i \mathbf{d}_i \right) \cdot \left(\mathbf{I} + \varepsilon \mathbf{N} \otimes \mathbf{N} + \sum_{i=1}^2 \gamma_i \mathbf{N} \otimes \mathbf{d}_i \right) = \omega_\delta .$$

Using Eq. (2.10), we find

$$\mathbf{F}^{c-\top} \cdot \omega_d = \left(\mathbf{I} - \frac{\varepsilon}{1+\varepsilon} \mathbf{N} \otimes \mathbf{N} - \sum_{j=1}^2 \frac{\gamma_j}{1+\varepsilon} \mathbf{N} \otimes \mathbf{d}_j \right) \cdot \left(\sum_{k=1}^2 d\omega_k \mathbf{d}_k \right) = \left(\omega_d - \sum_{j=1}^2 \frac{\gamma_j}{1+\varepsilon} d\omega_j \mathbf{N} \right) .$$

Thus, we obtain for $\omega_\delta \cdot (\Sigma^{e\top} + \mathbf{F}^{c\top} \Sigma^e \mathbf{F}^{c-\top}) \cdot \omega_d$ the following relation

$$\begin{aligned}
\omega_\delta \cdot (\Sigma^{e\top} + \mathbf{F}^{c\top} \Sigma^e \mathbf{F}^{c-\top}) \cdot \omega_d &= \omega_\delta \cdot \Sigma^{e\top} \cdot \omega_d + \omega_\delta \cdot \Sigma^e \cdot \left(\omega_d - \sum_{j=1}^2 \frac{\gamma_j}{1+\varepsilon} d\omega_j \mathbf{N} \right) \\
&= \omega_\delta \cdot 2 \operatorname{sym}(\Sigma^e) \cdot \omega_d - \sum_{i=1}^2 \delta\omega_i \mathbf{d}_i \cdot \Sigma^e \cdot \mathbf{N} \sum_{j=1}^2 \frac{\gamma_j}{1+\varepsilon} d\omega_j .
\end{aligned}$$

From Eq. (2.47), we use that $\mathbf{d}_i \cdot \boldsymbol{\Sigma}^e \cdot \mathbf{N} = k\gamma_i(1 + \varepsilon)$ which yields

$$\begin{aligned} \boldsymbol{\omega}_\delta \cdot (\boldsymbol{\Sigma}^{e\top} + \mathbf{F}^{c\top} \boldsymbol{\Sigma}^e \mathbf{F}^{c-\top}) \cdot \boldsymbol{\omega}_d &= \boldsymbol{\omega}_\delta \cdot 2 \operatorname{sym}(\boldsymbol{\Sigma}^e) \cdot \boldsymbol{\omega}_d - \sum_{i=1}^2 \sum_{j=1}^2 k \delta \omega_i \gamma_i \gamma_j d\omega_j \\ &= \boldsymbol{\omega}_\delta \cdot 2 \operatorname{sym}(\boldsymbol{\Sigma}^e) \cdot \boldsymbol{\omega}_d \\ &\quad - \sum_{i=1}^2 \delta \omega_i \mathbf{d}_i \cdot k \sum_{m=1}^2 \sum_{n=1}^2 \gamma_m \gamma_n \mathbf{d}_m \otimes \mathbf{d}_n \cdot \sum_{j=1}^2 d\omega_j \mathbf{d}_j \\ &= \boldsymbol{\omega}_\delta \cdot (2 \operatorname{sym}(\boldsymbol{\Sigma}^e) - k\boldsymbol{\gamma}) \cdot \boldsymbol{\omega}_d \end{aligned}$$

and finally the symmetry of $\boldsymbol{\omega}_\delta \cdot (\boldsymbol{\Sigma}^{e\top} + \mathbf{F}^{c\top} \boldsymbol{\Sigma}^e \mathbf{F}^{c-\top}) \cdot \boldsymbol{\omega}_d$. We define the symmetric second order tensor $\boldsymbol{\gamma}$ as follows

$$\boldsymbol{\gamma} = \sum_{m=1}^2 \sum_{n=1}^2 \gamma_m \gamma_n \mathbf{d}_m \otimes \mathbf{d}_n . \quad (2.156)$$

For the variation of interest, $d_\omega(\tilde{\psi}_\omega \cdot \boldsymbol{\omega}_\delta)$ in Eq. (2.155), this yields

$$\begin{aligned} d_\omega(\tilde{\psi}_\omega \cdot \boldsymbol{\omega}_\delta) &= \boldsymbol{\omega}_\delta \cdot \left[\mathbf{L}_\omega^c{}^\top : \left(\mathbf{C}^e \square \mathbf{S}^{0e} + \mathbf{C}^e \square_s \mathbf{I} : 2 \frac{d\mathbf{S}^{0e}}{d\mathbf{C}^e} : \mathbf{C}^e \square_s \mathbf{I} \right) : \mathbf{L}_\omega^c \right. \\ &\quad - 2 \operatorname{tr}(\boldsymbol{\Sigma}^e) \mathbf{I} + 2 \operatorname{sym}(\boldsymbol{\Sigma}^e) - k\boldsymbol{\gamma} \\ &\quad \left. + \boldsymbol{\epsilon} : \mathbf{F}^{c-\top} \square \mathbf{F}^{c\top} \boldsymbol{\Sigma}^e : \boldsymbol{\epsilon} + \boldsymbol{\epsilon} : \mathbf{F}^{c\top} \boldsymbol{\Sigma}^e \square \mathbf{F}^{c-\top} : \boldsymbol{\epsilon} \right] \cdot \boldsymbol{\omega}_d \quad (2.157) \end{aligned}$$

$$\begin{aligned} &= \boldsymbol{\omega}_\delta \cdot \left[\mathbf{L}_\omega^c{}^\top : \left(\mathbf{C}^e \square \mathbf{S}^{0e} + \mathbf{C}^e \square_s \mathbf{I} : 2 \frac{d\mathbf{S}^{0e}}{d\mathbf{C}^e} : \mathbf{C}^e \square_s \mathbf{I} \right) : \mathbf{L}_\omega^c \right. \\ &\quad - 2 \operatorname{tr}(\boldsymbol{\Sigma}^e) \mathbf{I} + 2 \operatorname{sym}(\boldsymbol{\Sigma}^e) - k\boldsymbol{\gamma} \\ &\quad \left. + 2 \operatorname{sym}(\boldsymbol{\epsilon} : \mathbf{F}^{c-\top} \square \mathbf{F}^{c\top} \boldsymbol{\Sigma}^e : \boldsymbol{\epsilon}) \right] \cdot \boldsymbol{\omega}_d \quad (2.158) \end{aligned}$$

$$= \boldsymbol{\omega}_\delta \cdot \mathbb{C}_{\omega\omega}^e \cdot \boldsymbol{\omega}_d . \quad (2.159)$$

The last contribution in Eq. (2.141), $d_c(\tilde{\psi}_\omega \cdot \boldsymbol{\omega}_\delta)$, is approached similarly to $d_c(\boldsymbol{\tau}^0 : \mathbf{d}_\delta)$ in Eq. (2.112)

$$d_c(\tilde{\psi}_\omega \cdot \boldsymbol{\omega}_\delta) = \boldsymbol{\omega}_\delta \cdot \tilde{\psi}_{\omega c} \cdot d\mathbf{c} . \quad (2.160)$$

In this instance, we use Eq. (2.63) ($\tilde{\psi}_{\omega c} = \tilde{\psi}_{\omega c}^\top = -\mathbf{r}_\omega^\top$) and Eq. (2.59) and obtain

$$d_c(\tilde{\psi}_\omega \cdot \boldsymbol{\omega}_\delta) = \boldsymbol{\omega}_\delta \cdot \mathbf{r}_\omega^\top \left(\frac{\partial \mathbf{r}}{\partial \mathbf{c}} \right)^{-1} (\mathbf{r}_\omega \cdot \boldsymbol{\omega}_d + \mathbf{r}_d : \mathbf{d}_d) . \quad (2.161)$$

Finally, we derived all contributions in Eq. (2.141) and write

$$\begin{aligned}
& d\left((1 - g(D_\chi))\mathbf{M}_0 \cdot \boldsymbol{\omega}_\delta\right) \\
&= \boldsymbol{\omega}_\delta \cdot (-g'(D_\chi)\mathbf{M}_0) dD_\chi + (1 - g(D_\chi)) d_u(\tilde{\psi}_\omega \cdot \boldsymbol{\omega}_\delta) + (1 - g(D_\chi)) d_\omega(\tilde{\psi}_\omega \cdot \boldsymbol{\omega}_\delta) \\
&\quad + (1 - g(D_\chi)) d_c(\tilde{\psi}_\omega \cdot \boldsymbol{\omega}_\delta) \\
&= \boldsymbol{\omega}_\delta \cdot (-g'(D_\chi)\mathbf{M}_0) dD_\chi + (1 - g(D_\chi)) \boldsymbol{\omega}_\delta \cdot \tilde{\psi}_{\omega d} : \mathbf{d}_d + (1 - g(D_\chi)) \boldsymbol{\omega}_\delta \cdot \mathbb{C}_{\omega\omega}^e \cdot \boldsymbol{\omega}_d \\
&\quad + (1 - g(D_\chi)) \boldsymbol{\omega}_\delta \cdot \underline{r}_\omega^\top \left(\frac{\partial \underline{r}}{\partial \underline{c}}\right)^{-1} (\underline{r}_\omega \cdot \boldsymbol{\omega}_d + \underline{r}_d : \mathbf{d}_d) \\
&= \boldsymbol{\omega}_\delta \cdot (-g'(D_\chi)\mathbf{M}_0) dD_\chi \\
&\quad + (1 - g(D_\chi)) \boldsymbol{\omega}_\delta \cdot \left(\tilde{\psi}_{\omega d} + \underline{r}_\omega^\top \left(\frac{\partial \underline{r}}{\partial \underline{c}}\right)^{-1} \underline{r}_d\right) : \mathbf{d}_d \\
&\quad + (1 - g(D_\chi)) \boldsymbol{\omega}_\delta \cdot \left(\mathbb{C}_{\omega\omega}^e + \underline{r}_\omega^\top \left(\frac{\partial \underline{r}}{\partial \underline{c}}\right)^{-1} \underline{r}_\omega\right) \cdot \boldsymbol{\omega}_d \\
&= \boldsymbol{\omega}_\delta \cdot (-g'(D_\chi)\mathbf{M}_0) dD_\chi + (1 - g(D_\chi)) \boldsymbol{\omega}_\delta \cdot \mathbb{C}_{\omega d} : \mathbf{d}_d + (1 - g(D_\chi)) \boldsymbol{\omega}_\delta \cdot \mathbb{C}_{\omega\omega} \cdot \boldsymbol{\omega}_d .
\end{aligned} \tag{2.162}$$

The linearization of the residual G_N is constituted by the contributions of Eqs. (2.136), (2.137), (2.138), (2.140) and (2.162) and reads

$$\begin{aligned}
dG_N = \int_{\Omega_0} & \left(\boldsymbol{\omega}_\delta \cdot \left[(1 - g(D_\chi))\mathbb{C}_{\omega\omega} + \begin{cases} H_N(\mathbf{N}^* \cdot \mathbf{N})\mathbf{I}, & D \text{ or } D_\chi \geq 1 - \epsilon \\ 0, & \text{else} \end{cases} \right. \right. \\
& \left. + \frac{\eta_N}{\Delta t} (\mathbf{N}_n \cdot \mathbf{N})\mathbf{I} + \sum_{m=1}^3 \beta_m \left((\mathbf{N} \times \mathbf{p}_m) \otimes (\mathbf{N} \times \mathbf{p}_m) - (\mathbf{N} \cdot \mathbf{p}_m)^2 \mathbf{I} \right) \right] \cdot \boldsymbol{\omega}_d \\
& + \boldsymbol{\omega}_\delta \cdot \left[(1 - g(D_\chi))\mathbb{C}_{\omega d} \right] : \mathbf{d}_d \\
& + \boldsymbol{\omega}_\delta \cdot \left[-g'(D_\chi)\mathbf{M}_0 \right] dD_\chi \\
& \left. + \text{Grad}(\delta \mathbf{N}) : \frac{\partial \boldsymbol{\xi}_N}{\partial \text{Grad}(\mathbf{N})} : \text{Grad}(\mathbf{dN}) - \boldsymbol{\xi}_N : \text{Grad}((\boldsymbol{\omega}_\delta \cdot \boldsymbol{\omega}_d)\mathbf{N}) \right) d\Omega .
\end{aligned} \tag{2.163}$$

2.E Derivation and linearization of the residual G_{D_χ}

To find the variation with respect to D_χ

$$\delta_{D_\chi} \Pi_\Delta = \int_{\Omega_0} \delta_{D_\chi} \pi_\Delta d\Omega ,$$

we consider the contributions of the rate potential π_Δ that depend on D_χ

$$\delta_{D_\chi} \Pi_\Delta = \int_{\Omega_0} \delta_{D_\chi} \left((1 - g(D_\chi))(\psi_{e0}(\mathbf{C}^e) + \psi_k(\underline{c})) + \psi_\chi(D_\chi - D) + \psi_{g\chi}(\text{Grad}(D_\chi)) \right) d\Omega . \tag{2.164}$$

With the following auxiliary calculations for $(1 - g)(\psi_{e0} + \psi_k) = (1 - g)\tilde{\psi}$

$$\delta_{D_\chi} \left((1 - g(D_\chi))(\psi_{e0}(\mathbf{C}^e) + \psi_k(\underline{c})) \right) = -g'(D_\chi)(\psi_{e0}(\mathbf{C}^e) + \psi_k(\underline{c}))\delta D_\chi, \quad (2.165)$$

for ψ_χ

$$\delta_{D_\chi} \psi_\chi = \delta_{D_\chi} \left(\frac{1}{2} H_\chi (D_\chi - D)^2 \right) = H_\chi (D_\chi - D) \delta D_\chi, \quad (2.166)$$

and for $\psi_{g\chi}$

$$\delta_{D_\chi} \psi_{g\chi} = \underbrace{\frac{\partial \psi_{g\chi}(\text{Grad}(D_\chi))}{\partial \text{Grad}(D_\chi)}}_{=:\boldsymbol{\xi}_{D_\chi}} \cdot \text{Grad}(\delta D_\chi) = \boldsymbol{\xi}_{D_\chi} \cdot \text{Grad}(\delta D_\chi), \quad (2.167)$$

we find

$$\begin{aligned} G_{D_\chi} &= \delta_{D_\chi} \Pi_\Delta \\ &= \int_{\Omega_0} \left(\left[-g'(D_\chi)(\psi_{e0}(\mathbf{C}^e) + \psi_k(\underline{c})) + H_\chi (D_\chi - D) \right] \delta D_\chi + \boldsymbol{\xi}_{D_\chi} \cdot \text{Grad}(\delta D_\chi) \right) d\Omega. \end{aligned} \quad (2.168)$$

In the following, we want to derive the linearization of the residual G_{D_χ} and consider

$$dG_{D_\chi} = \int_{\Omega_0} d \left(\left[-g'(D_\chi)(\psi_{e0}(\mathbf{C}^e) + \psi_k(\underline{c})) + H_\chi (D_\chi - D) \right] \delta D_\chi + \boldsymbol{\xi}_{D_\chi} \cdot \text{Grad}(\delta D_\chi) \right) d\Omega. \quad (2.169)$$

For the gradient contribution, we find

$$d(\boldsymbol{\xi}_{D_\chi} \cdot \text{Grad}(\delta D_\chi)) = \text{Grad}(\delta D_\chi) \cdot \frac{\partial \boldsymbol{\xi}_{D_\chi}}{\partial \text{Grad}(D_\chi)} \cdot \text{Grad}(dD_\chi) \quad (2.170)$$

$$= \text{Grad}(\delta D_\chi) \cdot K_{g\chi} \mathbf{I} \cdot \text{Grad}(dD_\chi) \quad (2.171)$$

and using Eq. (2.69), we find for $d(H_\chi(D_\chi - D)\delta D_\chi)$

$$\begin{aligned} d(H_\chi(D_\chi - D)\delta D_\chi) &= \delta D_\chi H_\chi dD_\chi - \delta D_\chi H_\chi dD \\ &= \delta D_\chi H_\chi dD_\chi - \delta D_\chi H_\chi \frac{1}{\partial r / \partial D} \left(g'(D) \boldsymbol{\tau}^v : \mathbf{d}_d - H_\chi dD_\chi \right) \\ &= \delta D_\chi \left(H_\chi + \frac{H_\chi^2}{\partial r / \partial D} \right) dD_\chi + \delta D_\chi \left(-\frac{g'(D)}{\partial r / \partial D} H_\chi \boldsymbol{\tau}^v \right) : \mathbf{d}_d. \end{aligned} \quad (2.172)$$

The variation of $-g'(D_\chi) \tilde{\psi} \delta D_\chi$ reads

$$d(-g'(D_\chi) \tilde{\psi} \delta D_\chi) = \delta D_\chi \left(-g''(D_\chi) \tilde{\psi} \right) dD_\chi + \delta D_\chi \left(-g'(D_\chi) \frac{\partial \tilde{\psi}}{\partial \mathbf{C}^e} \right) : d\mathbf{C}^e. \quad (2.173)$$

We do not consider the derivative of $\tilde{\psi}$ with respect to \underline{c} since $\partial\tilde{\psi}/\partial\underline{c} = \mathbf{0}$ constitutes the stationarity conditions for internal variables, see Eq. (2.44), and is therefore zero. Using Eqs. (2.92), (2.101), (2.104) and (2.106), we rewrite Eq. (2.173) as follows

$$\begin{aligned} & d(-g'(D_\chi) \tilde{\psi} \delta D_\chi) \\ &= \delta D_\chi \left(-g''(D_\chi) \tilde{\psi} \right) dD_\chi + \delta D_\chi \left(-g'(D_\chi) \frac{1}{2} \mathbf{S}^{0e} \right) : \left(2\mathbf{F}^{e\top} \boxdot \mathbf{F}^e : \mathbf{d}_d - 2\mathbf{C}^e \boxdot \mathbf{I} : \mathbf{L}_\omega^c \cdot \boldsymbol{\omega}_d \right) \\ &= \delta D_\chi \left(-g''(D_\chi) \tilde{\psi} \right) dD_\chi + \delta D_\chi \left(-g'(D_\chi) \boldsymbol{\tau}^0 \right) : \mathbf{d}_d + \delta D_\chi \left(-g'(D_\chi) \mathbf{M}_0 \right) \cdot \boldsymbol{\omega}_d . \end{aligned} \quad (2.174)$$

The linearization of G_{D_χ} finally reads

$$\begin{aligned} dG_{D_\chi} = \int_{\Omega_0} & \left(\delta D_\chi \left[-g''(D_\chi) (\psi_{e0}(\mathbf{C}^e) + \psi_k(\underline{c})) + H_\chi + \frac{H_\chi^2}{\partial r / \partial D} \right] dD_\chi \right. \\ & + \delta D_\chi \left[-g'(D_\chi) \boldsymbol{\tau}^0 - \frac{g'(D)}{\partial r / \partial D} H_\chi \boldsymbol{\tau}^v \right] : \mathbf{d}_d \\ & + \delta D_\chi [-g'(D_\chi) \mathbf{M}_0] \cdot \boldsymbol{\omega}_d \\ & \left. + \text{Grad}(\delta D_\chi) \cdot \frac{\partial \boldsymbol{\xi}_{D_\chi}}{\partial \text{Grad}(D_\chi)} \cdot \text{Grad}(dD_\chi) \right) d\Omega , \end{aligned} \quad (2.175)$$

where $\partial \boldsymbol{\xi}_{D_\chi} / \partial \text{Grad}(D_\chi) = K_{g\chi} \mathbf{I}$.

2.F Linearization of the stationarity conditions for internal variables

In order to find the linearization of the residual r^{γ_i} in Eq. (2.51),

$$r^{\gamma_i} = \frac{1}{1+\varepsilon} \mathbf{d}_i \cdot \boldsymbol{\Sigma}^e \cdot \mathbf{N} - k\gamma_i, \quad i = 1, 2, \quad (2.176)$$

with respect to the internal variables \underline{c} , we use Eq. (2.107) and write

$$\begin{aligned} d_c r^{\gamma_i} &= \frac{1}{1+\varepsilon} \mathbf{d}_i \cdot d_c \boldsymbol{\Sigma}^e \cdot \mathbf{N} - \frac{d\varepsilon}{(1+\varepsilon)^2} \mathbf{d}_i \cdot \boldsymbol{\Sigma}^e \cdot \mathbf{N} - k d\gamma_i \\ &= \frac{1}{1+\varepsilon} \mathbf{d}_i \otimes \mathbf{N} : \left(\mathbf{I} \boxdot \mathbf{S}^{0e} + \mathbf{C}^e \frac{d\mathbf{S}^{0e}}{d\mathbf{C}^e} \right) : d_c \mathbf{C}^e - \frac{d\varepsilon}{(1+\varepsilon)^2} \mathbf{d}_i \cdot \boldsymbol{\Sigma}^e \cdot \mathbf{N} - k d\gamma_i . \end{aligned} \quad (2.177)$$

Among \mathbf{F} and \mathbf{F}^c , only \mathbf{F}^c depends on \underline{c} . Hence, we use Eq. (2.102), where \mathbf{F} is frozen, to express $d_c \mathbf{C}^e$. Together with the definition of the product in Eq. (2.3), we obtain in Eq. (2.177)

$$d_c r^{\gamma_i} = \frac{-2}{1+\varepsilon} \left(\mathbf{d}_i \otimes \mathbf{S}^{0e} \cdot \mathbf{N} + (\mathbf{C}^e \cdot \mathbf{d}_i \otimes \mathbf{N}) : \frac{d\mathbf{S}^{0e}}{d\mathbf{C}^e} \right) : \text{sym}(\mathbf{C}^e d_c \mathbf{F}^c \mathbf{F}^{c-1})$$

$$- \frac{d\varepsilon}{(1+\varepsilon)^2} \mathbf{d}_i \cdot \boldsymbol{\Sigma}^e \cdot \mathbf{N} - k d\gamma_i .$$

The double contraction of the terms $\mathbf{d}_i \otimes \mathbf{S}^{0e} \cdot \mathbf{N}$ and $\mathbf{C}^e \cdot \mathbf{d}_i \otimes \mathbf{N}$ with symmetric terms projects onto their symmetric part and we write

$$\begin{aligned} d_c r^{\gamma_i} = & - \frac{2}{1+\varepsilon} \left(\underbrace{\text{sym}(\mathbf{d}_i \otimes \mathbf{S}^{0e} \cdot \mathbf{N})}_{=: \mathbf{A}_{d_i}^S} + \underbrace{\text{sym}(\mathbf{C}^e \cdot \mathbf{d}_i \otimes \mathbf{N})}_{=: \mathbf{A}_{d_i}^C} : \frac{d\mathbf{S}^{0e}}{d\mathbf{C}^e} \right) : \text{sym}(\mathbf{C}^e d_c \mathbf{F}^c \mathbf{F}^{c-1}) \\ & - \frac{d\varepsilon}{(1+\varepsilon)^2} \mathbf{d}_i \cdot \boldsymbol{\Sigma}^e \cdot \mathbf{N} - k d\gamma_i . \end{aligned} \quad (2.178)$$

Replacing $d_c \mathbf{F}^c \mathbf{F}^{c-1}$ in Eq. (2.178) with Eq. (2.45) yields

$$\begin{aligned} d_c r^{\gamma_i} = & - \frac{2}{1+\varepsilon} \left(\mathbf{A}_{d_i}^S + \mathbf{A}_{d_i}^C : \frac{d\mathbf{S}^{0e}}{d\mathbf{C}^e} \right) : \left(\frac{d\varepsilon}{1+\varepsilon} \underbrace{\text{sym}(\mathbf{C}^e \cdot \mathbf{N} \otimes \mathbf{N})}_{=: \mathbf{A}_N^C} + \sum_{j=1}^2 \frac{d\gamma_j}{1+\varepsilon} \underbrace{\text{sym}(\mathbf{C}^e \cdot \mathbf{d}_j \otimes \mathbf{N})}_{\mathbf{A}_{d_j}^C} \right) \\ & - \frac{d\varepsilon}{(1+\varepsilon)^2} \mathbf{d}_i \cdot \boldsymbol{\Sigma}^e \cdot \mathbf{N} - k d\gamma_i \end{aligned} \quad (2.179)$$

$$\begin{aligned} d_c r^{\gamma_i} = & d\varepsilon \left[- \frac{2}{(1+\varepsilon)^2} \left(\mathbf{A}_{d_i}^S : \mathbf{A}_N^C + \mathbf{A}_{d_i}^C : \frac{d\mathbf{S}^{0e}}{d\mathbf{C}^e} : \mathbf{A}_N^C + \frac{1}{2} \mathbf{d}_i \cdot \boldsymbol{\Sigma}^e \cdot \mathbf{N} \right) \right] \\ & + \sum_{j=1}^2 d\gamma_j \left[- \frac{2}{(1+\varepsilon)^2} \left(\mathbf{A}_{d_i}^S : \mathbf{A}_{d_j}^C + \mathbf{A}_{d_i}^C : \frac{d\mathbf{S}^{0e}}{d\mathbf{C}^e} : \mathbf{A}_{d_j}^C \right) - k \delta_{ij} \right] . \end{aligned} \quad (2.180)$$

Next, we want to derive the linearization of the residual r^{γ_i} in Eq. (2.51) with respect to the the degrees of freedom \mathbf{u} and \mathbf{N} (\mathbf{d} and $\boldsymbol{\omega}$, i.e., for fixed \underline{c}) and consider

$$\begin{aligned} dr^{\gamma_i} \Big|_{\underline{c}} &= \frac{1}{1+\varepsilon} (d\mathbf{d}_i \cdot \boldsymbol{\Sigma}^e \cdot \mathbf{N} + \mathbf{d}_i \cdot \boldsymbol{\Sigma}^e \cdot d\mathbf{N} + \mathbf{d}_i \cdot d\boldsymbol{\Sigma}^e \Big|_{\underline{c}} \cdot \mathbf{N}) \\ &= \frac{1}{1+\varepsilon} ((\boldsymbol{\omega}_d \times \mathbf{d}_i) \cdot \boldsymbol{\Sigma}^e \cdot \mathbf{N} + \mathbf{d}_i \cdot \boldsymbol{\Sigma}^e \cdot (\boldsymbol{\omega}_d \times \mathbf{N}) + \mathbf{d}_i \cdot d\boldsymbol{\Sigma}^e \Big|_{\underline{c}} \cdot \mathbf{N}) \\ &= \frac{1}{1+\varepsilon} (\boldsymbol{\omega}_d \cdot (\mathbf{d}_i \times (\boldsymbol{\Sigma}^e \cdot \mathbf{N}) + \mathbf{N} \times (\boldsymbol{\Sigma}^{eT} \cdot \mathbf{d}_i)) + \mathbf{d}_i \otimes \mathbf{N} : d\boldsymbol{\Sigma}^e \Big|_{\underline{c}}) . \end{aligned} \quad (2.181)$$

We express $d\boldsymbol{\Sigma}^e \Big|_{\underline{c}}$ using Eq. (2.107) and $d\mathbf{C}^e \Big|_{\underline{c}}$ using Eqs. (2.100), (2.101), (2.104) and (2.106) which yields

$$\begin{aligned} dr^{\gamma_i} \Big|_{\underline{c}} &= \frac{1}{1+\varepsilon} \left(\boldsymbol{\omega}_d \cdot (\mathbf{d}_i \times (\boldsymbol{\Sigma}^e \cdot \mathbf{N}) + \mathbf{N} \times (\boldsymbol{\Sigma}^{eT} \cdot \mathbf{d}_i)) \right. \\ &\quad \left. + \mathbf{d}_i \otimes \mathbf{N} : \left(\mathbf{I} \stackrel{s}{\square} \mathbf{S}^{0e} + \mathbf{C}^e \frac{d\mathbf{S}^{0e}}{d\mathbf{C}^e} \right) : d\mathbf{C}^e \Big|_{\underline{c}} \right) \\ &= \frac{1}{1+\varepsilon} \left(\boldsymbol{\omega}_d \cdot (\mathbf{d}_i \times (\boldsymbol{\Sigma}^e \cdot \mathbf{N}) + \mathbf{N} \times (\boldsymbol{\Sigma}^{eT} \cdot \mathbf{d}_i)) \right. \end{aligned}$$

$$\begin{aligned}
& + \left(\underbrace{\text{sym}(\mathbf{d}_i \otimes \mathbf{S}^{0e} \cdot \mathbf{N})}_{\mathbf{A}_{d_i}^S} + \underbrace{\text{sym}(\mathbf{C}^e \cdot \mathbf{d}_i \otimes \mathbf{N})}_{\mathbf{A}_{d_i}^C} : \frac{d\mathbf{S}^{0e}}{d\mathbf{C}^e} \right) : d\mathbf{C}^e \Big|_{\underline{c}} \Big) \\
& = \frac{1}{1+\varepsilon} \left(\mathbf{d}_i \times (\boldsymbol{\Sigma}^e \cdot \mathbf{N}) + \mathbf{N} \times (\boldsymbol{\Sigma}^{eT} \cdot \mathbf{d}_i) + \left(\mathbf{A}_{d_i}^S + \mathbf{A}_{d_i}^C : \frac{d\mathbf{S}^{0e}}{d\mathbf{C}^e} \right) : \mathbf{C}_\omega^e \right) \cdot \boldsymbol{\omega}_d \\
& + \frac{1}{1+\varepsilon} \left(\mathbf{A}_{d_i}^S + \mathbf{A}_{d_i}^C : \frac{d\mathbf{S}^{0e}}{d\mathbf{C}^e} \right) \mathbf{C}_d^e : \mathbf{d}_d . \tag{2.182}
\end{aligned}$$

In order to linearize the residual r^ε in Eq. (2.52),

$$r^\varepsilon = \frac{1}{1+\varepsilon} \mathbf{N} \cdot \boldsymbol{\Sigma}^e \cdot \mathbf{N} - k\varepsilon , \tag{2.183}$$

with respect to the internal variables \underline{c} , we follow the same steps as for $d_c r^{\gamma_i}$ in Eqs. (2.177) – (2.180)

$$\begin{aligned}
d_c r^\varepsilon & = -\frac{2}{1+\varepsilon} \left(\underbrace{\text{sym}(\mathbf{N} \otimes \mathbf{S}^{0e} \cdot \mathbf{N})}_{=: \mathbf{A}_N^S} + \underbrace{\text{sym}(\mathbf{C}^e \cdot \mathbf{N} \otimes \mathbf{N})}_{\mathbf{A}_N^C} : \frac{d\mathbf{S}^{0e}}{d\mathbf{C}^e} \right) : \text{sym}(\mathbf{C}^e d_c \mathbf{F}^c \mathbf{F}^{c-1}) \\
& - \frac{d\varepsilon}{(1+\varepsilon)^2} \mathbf{N} \cdot \boldsymbol{\Sigma}^e \cdot \mathbf{N} - k d\varepsilon \\
d_c r^\varepsilon & = -\frac{2}{1+\varepsilon} \left(\mathbf{A}_N^S + \mathbf{A}_N^C : \frac{d\mathbf{S}^{0e}}{d\mathbf{C}^e} \right) : \left(\frac{d\varepsilon}{1+\varepsilon} \underbrace{\text{sym}(\mathbf{C}^e \cdot \mathbf{N} \otimes \mathbf{N})}_{\mathbf{A}_N^C} + \sum_{j=1}^2 \frac{d\gamma_j}{1+\varepsilon} \underbrace{\text{sym}(\mathbf{C}^e \cdot \mathbf{d}_j \otimes \mathbf{N})}_{\mathbf{A}_{d_j}^C} \right) \\
& - \frac{d\varepsilon}{(1+\varepsilon)^2} \mathbf{N} \cdot \boldsymbol{\Sigma}^e \cdot \mathbf{N} - k d\varepsilon
\end{aligned}$$

and obtain

$$\begin{aligned}
d_c r^\varepsilon & = d\varepsilon \left[-\frac{2}{(1+\varepsilon)^2} \left(\mathbf{A}_N^S : \mathbf{A}_N^C + \mathbf{A}_N^C : \frac{d\mathbf{S}^{0e}}{d\mathbf{C}^e} : \mathbf{A}_N^C + \frac{1}{2} \mathbf{N} \cdot \boldsymbol{\Sigma}^e \cdot \mathbf{N} \right) - k \right] \\
& + \sum_{j=1}^2 d\gamma_j \left[-\frac{2}{(1+\varepsilon)^2} \left(\mathbf{A}_N^S : \mathbf{A}_{d_j}^C + \mathbf{A}_N^C : \frac{d\mathbf{S}^{0e}}{d\mathbf{C}^e} : \mathbf{A}_{d_j}^C \right) \right] . \tag{2.184}
\end{aligned}$$

Next, we want to derive the linearization of the residual r^ε in Eq. (2.52) with respect to the the degrees of freedom \mathbf{u} and \mathbf{N} (\mathbf{d} and $\boldsymbol{\omega}$, i.e., for fixed \underline{c}) and follow the same approach as for $dr^{\gamma_i} \Big|_{\underline{c}}$ in Eqs. (2.181) – (2.182)

$$dr^\varepsilon \Big|_{\underline{c}} = \frac{1}{1+\varepsilon} \left(\boldsymbol{\omega}_d \cdot \mathbf{N} \times (2 \text{sym}(\boldsymbol{\Sigma}^e) \cdot \mathbf{N}) + \mathbf{N} \otimes \mathbf{N} : d\boldsymbol{\Sigma}^e \Big|_{\underline{c}} \right) . \tag{2.185}$$




We express $d\boldsymbol{\Sigma}^e|_{\underline{c}}$ according to Eq. (2.107) and $d\mathbf{C}^e|_{\underline{c}}$ according to Eqs. (2.100), (2.101), (2.104) and (2.106) and obtain

$$\begin{aligned}
dr^\varepsilon|_{\underline{c}} &= \frac{1}{1+\varepsilon} \left(\boldsymbol{\omega}_d \cdot \mathbf{N} \times (2 \operatorname{sym}(\boldsymbol{\Sigma}^e) \cdot \mathbf{N}) + \mathbf{N} \otimes \mathbf{N} : \left(\mathbf{I} \stackrel{s}{\square} \mathbf{S}^{0e} + \mathbf{C}^e \frac{d\mathbf{S}^{0e}}{d\mathbf{C}^e} \right) : d\mathbf{C}^e|_{\underline{c}} \right) \\
&= \frac{1}{1+\varepsilon} \left(\boldsymbol{\omega}_d \cdot \mathbf{N} \times (2 \operatorname{sym}(\boldsymbol{\Sigma}^e) \cdot \mathbf{N}) \right. \\
&\quad \left. + \left(\underbrace{\operatorname{sym}(\mathbf{N} \otimes \mathbf{S}^{0e} \cdot \mathbf{N})}_{\mathbf{A}_N^S} + \underbrace{\operatorname{sym}(\mathbf{C}^e \cdot \mathbf{N} \otimes \mathbf{N})}_{\mathbf{A}_N^C} : \frac{d\mathbf{S}^{0e}}{d\mathbf{C}^e} \right) : d\mathbf{C}^e|_{\underline{c}} \right) \\
&= \frac{1}{1+\varepsilon} \left(\mathbf{N} \times (2 \operatorname{sym}(\boldsymbol{\Sigma}^e) \cdot \mathbf{N}) + \left(\mathbf{A}_N^S + \mathbf{A}_N^C : \frac{d\mathbf{S}^{0e}}{d\mathbf{C}^e} \right) : \mathbf{C}_\omega^e \right) \cdot \boldsymbol{\omega}_d \\
&\quad + \frac{1}{1+\varepsilon} \left(\mathbf{A}_N^S + \mathbf{A}_N^C : \frac{d\mathbf{S}^{0e}}{d\mathbf{C}^e} \right) : \mathbf{C}_d^e : \mathbf{d}_d . \tag{2.186}
\end{aligned}$$

CHAPTER 3

Publication 2: Computing Barkhausen noise spectra for magnetostrictive thin film composites using efficient magnetization–magnitude preserving simulation techniques

This work was published as:

Dorn, C. , Hörsting, M.  and Wulfinghoff, S.  [2023], 'Computing Barkhausen noise spectra for magnetostrictive thin film composites using efficient magnetization–magnitude preserving simulation techniques', *Journal of Applied Physics* **134**(13), 133901.

Reproduced from [99], with the permission of AIP Publishing.

Own contributions to the following article:

- Conceptualization (large contribution)
- Planning (large contribution)
- Methodology (large contribution)
- Software implementation and validation (large contribution)
- Investigation (large contribution)
- Interpretation of results (large contribution)
- Manuscript writing (large contribution)

Abstract

Barkhausen noise is a type of magnetic noise that occurs due to interaction of domain walls with defects. In magnetic sensor applications, this can be a detrimental phenomenon since it disturbs the signal. We study this noise using coupled micro-magneto-mechanical finite element simulations. To this end, we consider in the first step a thermodynamically consistent material model within the generalized standard material approach. In our material model, we include exchange, anisotropy, demagnetizing, Zeeman and elastic energy. The coupling between mechanics and micromagnetics is implemented via a magnetostrictive strain contribution. In the following step, we extend the material model to represent the full Landau-Lifshitz-Gilbert magnetization dynamics. For the model extension, we give a detailed exposition of the finite element implementation. In particular, we use a new modified leapfrog/Crank-Nicolson time integration scheme, which preserves the magnetization magnitude exactly. Furthermore, we showcase in detail the scheme for applying our material model to noise computation (based on ensemble averaging). Finally, we investigate various numerical examples based on the magnetostrictive material FeCoSiB to illustrate the different features of our approach.

Keywords: Magnetic noise, Landau-Lifshitz-Gilbert equation, Larmor precession, Finite element method, Ensemble averaging, Modified Crank-Nicolson scheme

3.1 Introduction

Biomagnetic fields of heart and brain exhibit magnitudes in the range of 10fT to 100pT [100]. Detecting these small magnetic fields requires high-performance sensors such as SQUIDs (superconducting quantum interference devices) or OPMs (optically pumped magnetometers). The aforementioned magnetometers typically entail cumbersome measuring setups, high operating expenses and great technical complexity (e.g., for cooling or shielding). Hence, inexpensive, easy-to-use and possibly handheld diagnostic devices have the potential to facilitate the detection of heart and brain signals. To this end, robust sensors with strong signal and low noise are required. One sensor concept, which could fulfill these criteria, are composite magnetoelectric thin film sensors [101]. We aim to investigate, understand and quantify magnetic noise in magnetostrictive thin film composites.

We are particularly interested in Barkhausen noise, i.e., magnetic noise that arises due to the interaction of domain walls with defects [102, 103]. Barkhausen noise occurs in different situations and is influenced by various factors, e.g., material [104], plastic deformation [105] and grain size [106]. In addition to the experimental studies referenced before, there is a wide variety of works on the modeling of Barkhausen noise, which employ various different methods.

Earlier studies on the modeling of Barkhausen noise [102, 107] typically dealt with ana-

lytical models and used simplifying assumptions in terms of elementary processes causing Barkhausen noise. These models were derived using stochastic arguments and were often used to predict Barkhausen noise spectral densities. Alessandro et al. [108] used the Langevin description of Barkhausen noise and computed approximate analytical solutions of the associated Fokker–Planck equation (named ABBM model after the authors). Around the same time, Cote et al. [109] studied Barkhausen noise using the concept of self-organized criticality. Another approach to model Barkhausen noise was devised by Yamaguchi et al. [110] and pivots on the concept of the pseudo-nonequilibrium Monte Carlo method. Pérez-Benitez et al. [111] used a random field Ising model with magnetic long-range interaction to compute (among other quantities of interest) power spectral densities and avalanche size distributions. Furthermore, the Jiles–Atherton model of hysteresis was extended by Jiles et al. [112] to include Barkhausen noise and the magnetomechanical effect.

However, despite this wide variety of models, Santa-aho et al. [113] pointed out that modeling approaches for Barkhausen noise in the sense of full-field micromagnetic simulations were missing. To our knowledge, Herranen et al. [114] and Kaappa et al. [115] performed the first studies on Barkhausen noise using micromagnetic simulations. The two aforementioned works extracted hysteresis loops and Barkhausen jump size distributions from the simulations but did not consider noise spectra. The latter is most significant when dealing with Barkhausen noise in the context of sensor applications. Dorn et al. [116] also used micromagnetic simulations to investigate Barkhausen noise. In their approach, based on the finite element method (FEM), micromagnetics is coupled to mechanics and the model was applied to compute Barkhausen noise spectra using ensemble averaging. However, in the aforementioned work, some features such as precession and realistic numerical examples are missing. In particular, while presenting a coupled magneto–mechanical framework, no numerical examples focusing on magneto–mechanics were discussed. With the present work, we intend to address these shortcomings.

We consider the coupled micro–magneto–mechanical problem, the solution of which we obtain using the FEM. Typically, the micromagnetic problem is determined by the Landau–Lifshitz–Gilbert equation [117]. For solution with the FEM, authors often work with the weak form of the Landau–Lifshitz–Gilbert equation as part of the Galerkin method [118, 56, 37]. In essence, we follow the same route but we start with the thermodynamically consistent generalized standard material formulation [11, 10]. To overcome the known caveat of missing precession, we introduce an additional term to represent the former. In contrast to works focusing on the quasi-static case (without precession) [35, 119], the efficient treatment of precession requires higher order accurate time integration, cf. [48, 47, 49]. Hence, we adopt a generalized time discretization approach, which includes a modified version of the Crank–Nicolson method [120]. To rectify the norm of the magnetization vector, we use the exponential map. We apply our material model to simulate the interaction of domain walls with defects and to extract Barkhausen noise. We give a detailed exposition of our noise computation scheme, which is based on ensemble averaging [121]. Our numerical examples

showcase the importance of precession in noise computation. Furthermore, we demonstrate the influence of different types of defects and irregularities that can cause Barkhausen noise including surface roughness, inhomogeneous material properties and eigenstrain.

3.2 Geometry, kinematics and boundary conditions

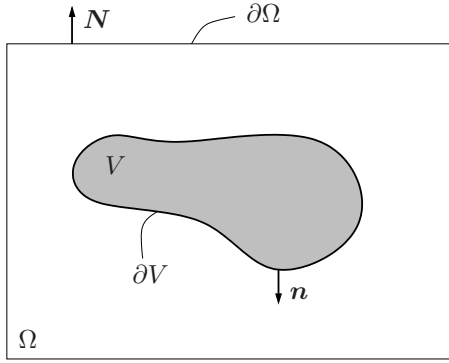


Fig. 3.1: Free space Ω with exterior normal \mathbf{N} and material volume V with exterior normal \mathbf{n} .

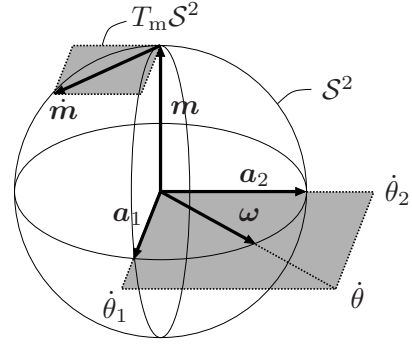


Fig. 3.2: Magnetization \mathbf{m} on unit sphere \mathcal{S}^2 , $\dot{\mathbf{m}}$ in tangent space $T_m \mathcal{S}^2$.

We consider the free space box $\Omega \subset \mathbb{R}^3$ with embedded magneto–mechanical material volume $V \subset \Omega$, see Fig. 3.1. Note that we assume the free space box Ω to be substantially larger than the material volume V such that the demagnetizing field can form freely. The two domains Ω and V are endowed with outward facing normal vectors \mathbf{N} and \mathbf{n} . We characterize the coupled micro–magneto–mechanical problem by displacement \mathbf{u} , magnetization \mathbf{m} and scalar magnetic potential φ

$$\mathbf{u} : V \times [0, T] \rightarrow \mathbb{R}^3 \quad (\mathbf{x}, t) \mapsto \mathbf{u}(\mathbf{x}, t) \quad (3.1)$$

$$\varphi : \Omega \times [0, T] \rightarrow \mathbb{R} \quad (\mathbf{x}, t) \mapsto \varphi(\mathbf{x}, t) \quad (3.2)$$

$$\mathbf{m} : V \times [0, T] \rightarrow \mathcal{S}^2 \quad (\mathbf{x}, t) \mapsto \mathbf{m}(\mathbf{x}, t) \quad \text{with} \quad \|\mathbf{m}\| = 1, \quad (3.3)$$

where $[0, T] \subset \mathbb{R}$ denotes the time range and \mathcal{S}^2 describes the unit sphere in \mathbb{R}^3 , see Fig. 3.2. Within the small strain setting, we use the symmetrized displacement gradient (strain tensor)

$$\boldsymbol{\varepsilon} = \frac{1}{2} (\nabla \mathbf{u} + \nabla \mathbf{u}^\top) \quad (3.4)$$

to quantify the local deformation of the body V . We assume the total strain $\boldsymbol{\varepsilon}$ to be composed of an elastic part $\boldsymbol{\varepsilon}^e$, a magnetostrictive contribution $\boldsymbol{\varepsilon}^m$ and an eigenstrain $\boldsymbol{\varepsilon}^*$ in an additive

fashion

$$\boldsymbol{\varepsilon} = \boldsymbol{\varepsilon}^e + \boldsymbol{\varepsilon}^m + \boldsymbol{\varepsilon}^* . \quad (3.5)$$

Often, eigenstrains are used to model the influence of thermal strains, plastic strains, and phase transformation strains. In the magnetic problem, the kinematic constraint $\|\mathbf{m}\| = 1$ arises. The magnetization \mathbf{m} (and associated vectors \mathbf{a}_1 and \mathbf{a}_2) is restricted to the unit sphere \mathcal{S}^2 , as expressed by the following equation

$$\{\dot{\mathbf{a}}_1, \dot{\mathbf{a}}_2, \dot{\mathbf{m}}\} = \dot{\boldsymbol{\omega}} \times \{\mathbf{a}_1, \mathbf{a}_2, \mathbf{m}\} \quad (3.6)$$

$$\dot{\boldsymbol{\omega}} = \dot{\theta}_1 \mathbf{a}_1 + \dot{\theta}_2 \mathbf{a}_2 \quad (3.7)$$

$$\|\boldsymbol{\omega}\| = 1 , \quad (3.8)$$

see Fig. 3.2. Note that, with a little abuse of notation, we write $\dot{\boldsymbol{\omega}}$ for the angular velocity vector, even though the angle θ (strictly speaking) does not exist. We implement the kinematic constraint in Eq. (3.6) by means of the exponential map algorithm (see Sec. 3.5.1), which is widely used in a variety of problems such as shell theory [24, 65], micromagnetics [44, 35], and damage mechanics [67].

The boundary conditions for the mechanical problem are visualized in Fig. 3.3. For the mechanical problem, the boundary ∂V is decomposed according to $\partial V = \partial V_u \cup \partial V_t$. On the Dirichlet boundary ∂V_u , we prescribe a displacement \mathbf{u} and on the Neumann boundary ∂V_t , we prescribe a traction vector \mathbf{t} being work-conjugate to \mathbf{u} (see below)

$$\mathbf{u} = \tilde{\mathbf{u}} \quad \text{on } \partial V_u \quad (3.9)$$

$$\mathbf{t} = \bar{\mathbf{t}} \quad \text{on } \partial V_t . \quad (3.10)$$

Furthermore, we include a body force density $\rho \mathbf{b}$ in the volume V . The boundary conditions for the material part of the magnetic problem are displayed in Fig. 3.4. We decompose the boundary $\partial V = \partial V_m \cup \partial V_\xi$ into a Dirichlet boundary ∂V_m and a Neumann boundary ∂V_ξ . We prescribe a magnetization \mathbf{m} on the Dirichlet boundary and a generalized traction $\boldsymbol{\Xi}$, being work-conjugate to \mathbf{m} , on the Neumann boundary

$$\mathbf{m} = \tilde{\mathbf{m}} \quad \text{on } \partial V_m \quad (3.11)$$

$$\boldsymbol{\Xi} = \bar{\boldsymbol{\Xi}} = \mathbf{0} \quad \text{on } \partial V_\xi . \quad (3.12)$$

The vacuum part of the magnetic problem is shown in Fig. 3.5. On the boundary of the material volume ∂V we prescribe

$$[\![\varphi]\!] = \varphi^+ - \varphi^- = 0 \quad \text{on } \partial V , \quad (3.13)$$

which implies continuity of the demagnetizing field $-\nabla \varphi$ in the tangential direction (perpen-

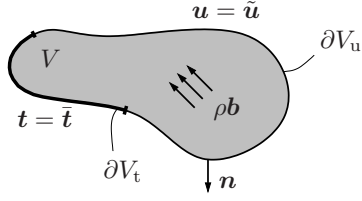


Fig. 3.3: Boundary conditions for the mechanical problem (displacement \mathbf{u}).

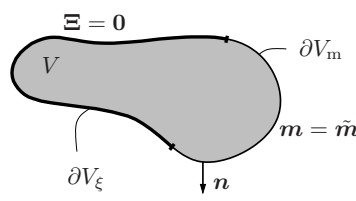


Fig. 3.4: Boundary conditions for the material part of the magnetic problem (magnetization \mathbf{m}).

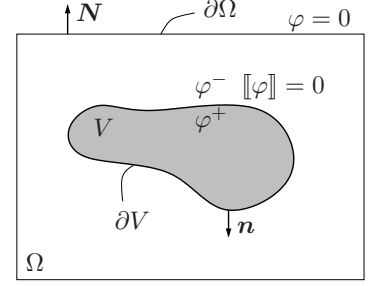


Fig. 3.5: Boundary conditions for the vacuum part of the magnetic problem (magnetic potential φ).

dicular to \mathbf{n}). On the boundary of the free space volume $\partial\Omega$ we prescribe

$$\varphi = 0 \quad \text{on } \partial\Omega . \quad (3.14)$$

3.3 Generalized standard material formulation

For the modeling of the material behavior, we adopt the framework of generalized standard materials (GSM) [11, 10]. This approach describes the material behavior by means of two ingredients: a conservative contribution (mixed energy–enthalpy) Ψ and a dissipative contribution (dissipation potential) Φ . The structure of the GSM approach ensures that the second law of thermodynamics is automatically fulfilled (if the potentials are chosen properly).

In the conservative part Ψ , we incorporate the exchange energy

$$\Psi_{\text{ex}}(\nabla \mathbf{m}) = \int_V A \|\nabla \mathbf{m}\|^2 dv , \quad (3.15)$$

with exchange stiffness constant A ; the anisotropy energy

$$\Psi_a(\mathbf{m}) = \int_V K(1 - (\mathbf{m} \cdot \mathbf{e}_a)^2) dv , \quad (3.16)$$

with uniaxial anisotropy constant K and easy axis (preferred direction) \mathbf{e}_a ; the demagnetizing energy

$$\Psi_d(\mathbf{m}, \nabla \varphi) = \int_V \mu_0 \nabla \varphi \cdot M_s \mathbf{m} dv - \frac{1}{2} \int_\Omega \mu_0 \|\nabla \varphi\|^2 dv , \quad (3.17)$$

with vacuum permeability μ_0 , spontaneous magnetization M_s , and demagnetizing field $\mathbf{H}_d = -\nabla \varphi$; the Zeeman energy

$$\Psi_z(\mathbf{m}) = \int_V -\mu_0 M_s \mathbf{m} \cdot \mathbf{H}' dv , \quad (3.18)$$

with externally applied field \mathbf{H}' ; and the elastic energy

$$\Psi_{\text{el}}(\boldsymbol{\varepsilon}, \mathbf{m}) = \int_V \frac{1}{2} \boldsymbol{\varepsilon}^e : \mathbb{C} : \boldsymbol{\varepsilon}^e \, dv, \quad (3.19)$$

with fourth order stiffness tensor \mathbb{C} (here isotropic) and magnetostrictive strain

$$\boldsymbol{\varepsilon}^m = \frac{3}{2} \lambda_s \left(\mathbf{m} \otimes \mathbf{m} - \frac{1}{3} \mathbf{I} \right), \quad (3.20)$$

where λ_s denotes the saturation magnetostriction. For a detailed explanation of the individual energies, we refer to textbooks [28, 122, 123]. In accordance with other authors [35, 43, 124], we choose the following quadratic form for the dissipation potential

$$\Phi(\dot{\mathbf{m}}) = \int_V \frac{\eta}{2} \dot{\mathbf{m}} \cdot \dot{\mathbf{m}} \, dv, \quad (3.21)$$

where η denotes the viscosity parameter (related to Gilbert damping, see Sections 3.4 and 3.7.1). In the following, we assume that energy is minimized or maximized w.r.t. the fields φ , \mathbf{u} and \mathbf{m} . Hence, we search for the following supremum w.r.t. the magnetic potential φ

$$\Psi = \Psi_{\text{ex}} + \Psi_{\text{a}} + \Psi_{\text{d}} + \Psi_{\text{z}} + \Psi_{\text{el}} \rightarrow \sup_{\varphi \in \kappa_\varphi}, \quad (3.22)$$

and the following infimum w.r.t. the displacement \mathbf{u}

$$\Psi - \int_{\partial V_t} \bar{\mathbf{t}} \cdot \mathbf{u} \, da - \int_V \rho \mathbf{b} \cdot \mathbf{u} \, dv \rightarrow \inf_{\mathbf{u} \in \kappa_{\mathbf{u}}}, \quad (3.23)$$

where we include traction loading by $\bar{\mathbf{t}}$ and body force $\rho \mathbf{b}$. Furthermore, we search for the following infimum w.r.t. $\dot{\mathbf{m}}$

$$\Pi = \dot{\Psi} + \Phi - \int_{\partial V_\xi} \bar{\boldsymbol{\Xi}} \cdot \dot{\mathbf{m}} \, da \quad (3.24)$$

$$= \int_\Omega \pi \, dv - \int_{\partial V_\xi} \bar{\boldsymbol{\Xi}} \cdot \dot{\mathbf{m}} \, da \rightarrow \inf_{\dot{\mathbf{m}} \in \kappa_{\dot{\mathbf{m}}}}, \quad (3.25)$$

where we include traction loading by $\bar{\boldsymbol{\Xi}}$. κ_φ , $\kappa_{\mathbf{u}}$ and $\kappa_{\dot{\mathbf{m}}}$ are appropriate sets of functions satisfying the boundary conditions. In the GSM context, Π is referred to as *rate potential*. For details on the saddle point formulation (sup in φ , inf in \mathbf{u} and \mathbf{m}) see [125]. Note that the volume integral in Eq. (3.25) is computed over the entire domain Ω even though \mathbf{u} and \mathbf{m} are only defined in V . We introduce this notation to conveniently summarize all energy contributions (some are computed in V , some in Ω) into one expression. To rectify the definitions of \mathbf{u} and \mathbf{m} , we continue these fields to Ω via

$$\mathbf{m}(\mathbf{x}, t) = \begin{cases} \mathbf{m}(\mathbf{x}, t), & \mathbf{x} \in V \\ \mathbf{0}, & \text{else} \end{cases} \quad \mathbf{u}(\mathbf{x}, t) = \begin{cases} \mathbf{u}(\mathbf{x}, t), & \mathbf{x} \in V \\ \mathbf{0}, & \text{else} \end{cases}. \quad (3.26)$$

This introduces a singular surface ∂V in the new domain Ω of \mathbf{u} and \mathbf{m} , which we need to consider, in particular, for the divergence theorem, see Appendix 3.A.

We find the sought infima and supremum by setting the variations to zero. From the first variation w.r.t. the magnetic potential φ , we obtain

$$0 \stackrel{!}{=} G_\varphi = \delta_\varphi \Psi = \int_\Omega \nabla \delta \varphi \cdot \mu_0 (M_s \mathbf{m} - \nabla \varphi) \, dv, \quad (3.27)$$

the strong form of which reads

$$\operatorname{div} (M_s \mathbf{m} - \nabla \varphi) = 0 \quad \text{in } V \quad (3.28)$$

$$[[M_s \mathbf{m} - \nabla \varphi]] \cdot \mathbf{n} = 0 \quad \text{on } \partial V \quad (3.29)$$

$$\operatorname{div} (\nabla \varphi) = 0 \quad \text{in } \Omega \setminus V \quad (3.30)$$

$$\varphi = 0 \quad \text{on } \partial \Omega, \quad (3.31)$$

where we used the divergence theorem for singular surfaces, see Eq. (3.80). Eqs. (3.28) and (3.30) correspond to Gauss's law. For the stationary point w.r.t. the displacement \mathbf{u} , we obtain

$$0 \stackrel{!}{=} G_u = \delta_u \Psi - \int_{\partial V_t} \bar{\mathbf{t}} \cdot \delta \mathbf{u} \, da - \int_V \rho \mathbf{b} \cdot \delta \mathbf{u} \, dv \quad (3.32)$$

$$= \int_V \boldsymbol{\sigma} : \delta \boldsymbol{\varepsilon} \, dv - \int_{\partial V_t} \bar{\mathbf{t}} \cdot \delta \mathbf{u} \, da - \int_V \rho \mathbf{b} \cdot \delta \mathbf{u} \, dv, \quad (3.33)$$

where we write $\boldsymbol{\sigma} = \mathbb{C} : (\boldsymbol{\varepsilon} - \boldsymbol{\varepsilon}^m - \boldsymbol{\varepsilon}^*)$ for the Cauchy stress. The strong form of the stationarity condition above reads

$$\operatorname{div} (\boldsymbol{\sigma}) + \rho \mathbf{b} = \mathbf{0} \quad \text{in } V \quad (3.34)$$

$$\boldsymbol{\sigma} \mathbf{n} - \bar{\mathbf{t}} = \mathbf{0} \quad \text{on } \partial V_t \quad (3.35)$$

$$\mathbf{u} = \tilde{\mathbf{u}} \quad \text{on } \partial V_u. \quad (3.36)$$

The variation of the rate potential Π w.r.t. $\dot{\mathbf{m}}$ reads

$$0 \stackrel{!}{=} \delta_{\dot{\mathbf{m}}} \Pi = \int_V \left(\frac{\partial \pi}{\partial \nabla \dot{\mathbf{m}}} : \nabla \delta \dot{\mathbf{m}} + \frac{\partial \pi}{\partial \dot{\mathbf{m}}} \cdot \delta \dot{\mathbf{m}} \right) \, dv - \int_{\partial V_\xi} \bar{\boldsymbol{\Xi}} \cdot \delta \dot{\mathbf{m}} \, da \quad (3.37)$$

$$= \int_V (\boldsymbol{\xi} : \nabla \delta \dot{\mathbf{m}} + \mathbf{S} \cdot \delta \dot{\mathbf{m}}) \, dv - \int_{\partial V_\xi} \bar{\boldsymbol{\Xi}} \cdot \delta \dot{\mathbf{m}} \, da, \quad (3.38)$$

where we introduced the force-type quantity

$$\mathbf{S} = \frac{\partial \pi}{\partial \dot{\mathbf{m}}} = \mu_0 M_s \nabla \varphi - 2K(\mathbf{m} \cdot \mathbf{e}_a) \mathbf{e}_a - \mu_0 M_s \mathbf{H}' - 3\lambda_s \boldsymbol{\sigma} \mathbf{m} + \eta \dot{\mathbf{m}} \quad (3.39)$$

work-conjugate to \mathbf{m} and the microstress

$$\boldsymbol{\xi} = \frac{\partial \pi}{\partial \nabla \dot{\mathbf{m}}} = 2A \nabla \mathbf{m} . \quad (3.40)$$

To obtain the strong form, we use $\delta \dot{\mathbf{m}} = \delta \dot{\boldsymbol{\theta}} \boldsymbol{\omega} \times \mathbf{m}$, which we understand as the variational version of Eq. (3.6). The strong form reads

$$\mathbf{m} \times (-\operatorname{div}(\boldsymbol{\xi}) + \mathbf{S}) = \mathbf{0} \quad \text{in } V \quad (3.41)$$

$$\mathbf{m} \times (\boldsymbol{\xi} \mathbf{n} - \overline{\boldsymbol{\Xi}}) = \mathbf{m} \times (\boldsymbol{\xi} \mathbf{n}) = \mathbf{0} \quad \text{on } \partial V_{\boldsymbol{\xi}} \quad (3.42)$$

$$\mathbf{m} = \tilde{\mathbf{m}} \quad \text{on } \partial V_{\mathbf{m}} . \quad (3.43)$$

Eq. (3.41) corresponds to the Landau–Lifshitz–Gilbert (LLG) equation [33, 117] (without precession).

3.4 Departure from the GSM framework to include precession

The GSM approach yields, as one of the stationary equations, the LLG equation without precession, see Eq. (3.41). To realize the latter, we rewrite Eq. (3.41) according to

$$\mathbf{0} = \mathbf{m} \times (-\operatorname{div}(\boldsymbol{\xi}) + \mu_0 M_s \nabla \varphi - 2K(\mathbf{m} \cdot \mathbf{e}_a) \mathbf{e}_a - \mu_0 M_s \mathbf{H}' - 3\lambda_s \boldsymbol{\sigma} \mathbf{m} + \eta \dot{\mathbf{m}}) \quad (3.44)$$

$$= \mathbf{m} \times (-\mu_0 M_s \mathbf{H}_{\text{eff}} + \eta \dot{\mathbf{m}}) \quad (3.45)$$

$$\dot{\mathbf{m}} = \frac{-\mu_0 M_s}{\eta} \mathbf{m} \times (\mathbf{m} \times \mathbf{H}_{\text{eff}}) . \quad (3.46)$$

We observe the lack of a precession term of the form $\mathbf{m} \times \mathbf{H}_{\text{eff}}$. This lack of a precession term may be a problem for the intended investigation of Barkhausen noise since the dynamics of domain wall motion are determined by the underlying magnetization dynamics. To obtain the LLG equation with precession, we need the following additional term

$$\mathbf{P} = -\beta \dot{\boldsymbol{\theta}} \boldsymbol{\omega} \quad (3.47)$$

in Eq. (3.41) such that

$$\mathbf{0} = \mathbf{m} \times (-\operatorname{div}(\boldsymbol{\xi}) + \mathbf{S} + \mathbf{P}) \quad (3.48)$$

$$= \mathbf{m} \times \left(-\mu_0 M_s \mathbf{H}_{\text{eff}} + \eta \dot{\mathbf{m}} - \beta \dot{\boldsymbol{\theta}} \boldsymbol{\omega} \right) \quad (3.49)$$

$$\Leftrightarrow \dot{\mathbf{m}} = \frac{\mu_0 M_s}{\beta} \mathbf{m} \times \mathbf{H}_{\text{eff}} - \frac{\eta}{\beta} \mathbf{m} \times \dot{\mathbf{m}} \quad (3.50)$$

(recall $\dot{\boldsymbol{\theta}} \boldsymbol{\omega} \times \mathbf{m} = \dot{\mathbf{m}}$ from Eq. (3.6)). With the gyromagnetic ratio $\gamma = \mu_0 M_s / \beta$ and Gilbert damping $\alpha = -\eta / \beta$ ($\beta < 0$), this is the full LLG equation. Note that the additional term \mathbf{P} is not the result of a variational principle and represents a departure from the GSM approach.

Thermodynamic consistency is retained nevertheless since the dissipative part of the GSM model remains untouched and precession is energy conservative. The showcased approach starting from a GSM model is not imperative since other options to show thermodynamic consistency are available. However, we prefer the GSM-based approach and find this detour instructive.

In Section 3.5.2, we discuss a modified Crank–Nicolson time integration scheme for Eq. (3.48). To this end, we rewrite Eq. (3.48) using

$$\mathbf{T} := \mu_0 M_s \nabla \varphi - 2K(\mathbf{m} \cdot \mathbf{e}_a) \mathbf{e}_a - \mu_0 M_s \mathbf{H}' - 3\lambda_s \boldsymbol{\sigma} \mathbf{m} \quad (3.51)$$

according to

$$-\beta \dot{\mathbf{m}} - \eta \mathbf{m} \times \dot{\mathbf{m}} = \mathbf{m} \times (-\operatorname{div}(\boldsymbol{\xi}) + \mathbf{T}) \quad (3.52)$$

$$\dot{\mathbf{m}} = (-\beta \mathbf{I} + \eta \boldsymbol{\epsilon} \cdot \mathbf{m})^{-1} (\mathbf{m} \times (-\operatorname{div}(\boldsymbol{\xi}) + \mathbf{T})) , \quad (3.53)$$

where $\boldsymbol{\epsilon}$ denotes the third order permutation tensor. With

$$(-\beta \mathbf{I} + \eta \boldsymbol{\epsilon} \cdot \mathbf{m})^{-1} = \frac{1}{\eta^2 + \beta^2} \left(-\beta \mathbf{I} - \eta \boldsymbol{\epsilon} \cdot \mathbf{m} - \frac{\eta^2}{\beta} \mathbf{m} \otimes \mathbf{m} \right) , \quad (3.54)$$

we finally obtain the following differential equation governing the evolution of the magnetization \mathbf{m}

$$\dot{\mathbf{m}} = \frac{1}{\eta^2 + \beta^2} (\beta \boldsymbol{\epsilon} \cdot \mathbf{m} - \eta (\mathbf{I} - \mathbf{m} \otimes \mathbf{m})) (-\operatorname{div}(\boldsymbol{\xi}) + \mathbf{T}) . \quad (3.55)$$

3.5 Implementation and finite element method

3.5.1 Overview

For the FEM, we use G_u , G_φ (Eqs. (3.27) and (3.33)) and the weak form of Eq. (3.55), denoted by G_m , as residuals of the global Newton–Raphson scheme. We choose displacement \mathbf{u} , magnetization \mathbf{m} and magnetic potential φ as nodal degrees of freedom because we need gradients of all three quantities (easily realized using shape functions). To be specific, after time discretization, we use the angle increments $\Delta\theta_1$ and $\Delta\theta_2$ from the exponential map in terms of Rodrigues’s rotation formula

$$\{\mathbf{a}_1, \mathbf{a}_2, \mathbf{m}\} \leftarrow \exp(\Delta\theta \hat{\boldsymbol{\omega}}_\Delta) \{\mathbf{a}_1, \mathbf{a}_2, \mathbf{m}\} \quad (3.56)$$

$$\exp(\Delta\theta \hat{\boldsymbol{\omega}}_\Delta) = \boldsymbol{\omega}_\Delta \otimes \boldsymbol{\omega}_\Delta + \cos(\Delta\theta) (\mathbf{I} - \boldsymbol{\omega}_\Delta \otimes \boldsymbol{\omega}_\Delta) + \sin(\Delta\theta) \hat{\boldsymbol{\omega}}_\Delta \quad (3.57)$$

$$\hat{\boldsymbol{\omega}}_\Delta = -\boldsymbol{\epsilon} \cdot \boldsymbol{\omega}_\Delta = -\epsilon_{ijk} \omega_k^\Delta \mathbf{e}_i \otimes \mathbf{e}_j \quad (3.58)$$

$$\Delta\theta \boldsymbol{\omega}_\Delta = \Delta\theta_1 \mathbf{a}_1 + \Delta\theta_2 \mathbf{a}_2 \quad (3.59)$$

as degrees of freedom instead of the magnetization vector \mathbf{m} . Here, the vectors $\{\mathbf{a}_1, \mathbf{a}_2, \mathbf{m}\}$ form an orthonormal basis, being continuously updated during the simulation, i.e., the update (3.56) is done after each global Newton step. The parametrization by the exponential map reduces the number of nodal unknowns by one and ensures $\|\mathbf{m}\| = 1$. To discretize space, we use tetrahedral elements ($N = 4$ nodes) with linear shape functions N_I ($I = 1, \dots, N$) to approximate the fields of interest.

In the following sections, we focus on implementation details regarding the residual G_m . For treatment of the remaining residuals G_φ and G_u , we refer to [35].

3.5.2 Time discretization

We seek the time and space discrete weak form of Eq. (3.55), which we can subsequently use as an FEM residual. The spatial discretization follows the standard FEM approach (see Appendix 3.C). For the time discretization, we use a modified Crank–Nicolson scheme. To simplify the exposition, we abbreviate Eq. (3.55) as follows

$$\dot{\mathbf{m}} = \mathbf{f} . \quad (3.60)$$

In order to obtain the weak form, we need a test function \mathbf{v} which suits the structure of Eq. (3.60)

$$\dot{\mathbf{m}} \cdot \mathbf{v} = \mathbf{f} \cdot \mathbf{v} . \quad (3.61)$$

The aforementioned equation only has two components (in \mathbf{a}_1 – and \mathbf{a}_2 –directions) and it vanishes in the \mathbf{m} –direction ($\mathbf{m} \cdot \dot{\mathbf{m}} = \mathbf{m} \cdot \mathbf{f} = 0$). Hence, a general test function $\tilde{\mathbf{v}} = \delta\theta_1 \mathbf{a}_1 + \delta\theta_2 \mathbf{a}_2 + \delta\vartheta \mathbf{m}$ only yields two non–vanishing scalar–valued weak forms related to $\delta\theta_1$ and $\delta\theta_2$. In other words, for Eq. (3.60), equality is only required in the two–dimensional subspace perpendicular to \mathbf{m} . Thus, for the test function, we can choose the projected form $\mathbf{v} = (\mathbf{I} - \mathbf{m} \otimes \mathbf{m})\tilde{\mathbf{v}} = \delta\theta_1 \mathbf{a}_1 + \delta\theta_2 \mathbf{a}_2$. Later on, we carry this test function over to the time–discrete case as well. The two–dimensional nature of Eq. (3.60) also manifests itself via any parametrization of \mathbf{m} by two scalars. We have two equations to determine two unknowns. For time discretization, the time range $[0, T]$ is divided into discrete points $t_0, \dots, t_n, t_{n+1}, \dots, T$ with time step $\Delta t = t_{n+1} - t_n$. We use the following generalized time discretization scheme for Eq. (3.61)

$$\frac{\mathbf{m}_{n+1} - \mathbf{m}_n}{\Delta t} \cdot \mathbf{v} = (c\mathbf{f}_{n+1} + (1-c)\mathbf{f}_n) \cdot \mathbf{v} \quad \text{with test function} \quad \mathbf{v} \perp \mathbf{m}_{n+1} , \quad (3.62)$$

or equivalently

$$(\mathbf{I} - \mathbf{m}_{n+1} \otimes \mathbf{m}_{n+1}) \frac{\mathbf{m}_{n+1} - \mathbf{m}_n}{\Delta t} = (\mathbf{I} - \mathbf{m}_{n+1} \otimes \mathbf{m}_{n+1}) (c\mathbf{f}_{n+1} + (1-c)\mathbf{f}_n) , \quad (3.63)$$

where $c = 0$ represents the explicit case, $c = 1$ represents the implicit case and $c = 0.5$ yields the modified Crank–Nicolson scheme. In Appendix 3.B, we show that the modified (i.e., projected) Crank–Nicolson scheme is second order accurate. In the following, we drop the index $(\bullet)_{n+1}$, which previously indicated quantities at the current time step.

The derivations of the space- and time-discrete residual G_m as well as the consistent linearization are given in Appendices 3.C and 3.D.

3.5.3 Magnetization magnitude in the Gauss points

We need to address the constraint $\|\mathbf{m}\| = 1$ one more time. In the nodes, this constraint is always fulfilled due to the design of the exponential map. Thus, coming from a finished Newton iteration, we get an updated \mathbf{m} with $\|\mathbf{m}\| = 1$ at each node. However, to evaluate the residuals within a certain element, we have to interpolate the nodal \mathbf{m} onto the integration points. As a result, in the integration points, $\|\mathbf{m}\| = 1$ is not ensured (instead $\|\mathbf{m}\| \leq 1$). Our approach to overcome this problem is to renormalize $\bar{\mathbf{m}} \leftarrow \mathbf{m}/\|\mathbf{m}\|$. Further, it is noted that the angles $\Delta\theta_1$ and $\Delta\theta_2$ (see Eqs. (3.56) to (3.59)) are evaluated exclusively on the nodes. For alternatives to renormalization, see [65]. In the residuals, we simply use $\bar{\mathbf{m}}$ instead of \mathbf{m} . However, for the variation of $\bar{\mathbf{m}}$ and in the linearization of residuals, we need to carefully consider the changes that $\bar{\mathbf{m}}$ implies. We approach the variation of $\bar{\mathbf{m}}$ as follows

$$\bar{\mathbf{m}} = \frac{\mathbf{m}}{\|\mathbf{m}\|} \quad (3.64)$$

$$\delta\bar{\mathbf{m}} = \frac{1}{\|\mathbf{m}\|} \left(\mathbf{I} - \frac{\mathbf{m}}{\|\mathbf{m}\|} \otimes \frac{\mathbf{m}}{\|\mathbf{m}\|} \right) \delta\mathbf{m} = \frac{1}{\|\mathbf{m}\|} \mathcal{P}_{\bar{\mathbf{m}}} \delta\mathbf{m} = \hat{\mathcal{P}}_{\bar{\mathbf{m}}} \delta\mathbf{m} , \quad (3.65)$$

where we introduced the symmetric projector $\mathcal{P}_{\bar{\mathbf{m}}}$. Note that $\delta\mathbf{m} \cdot \mathbf{m} \neq 0$ since the interpolated $\mathbf{m} \notin \mathcal{S}^2$. However, $\delta\bar{\mathbf{m}} \cdot \bar{\mathbf{m}} = 0$ does hold in general.

3.5.4 Remarks on quadrature

To compute the discretized integrals, we rely on Gauss quadrature. For the abovementioned tetrahedral elements with linear shape functions, it would be sufficient to employ a single Gauss point in most cases. However, in the present case, for interpolation of magnetization vectors, this approach can raise the following problem. We can construct a (non-artificial) scenario in which the interpolated magnetization vanishes, see Fig. 3.6 (two-dimensional illustration). Since all shape functions assume the same value in the single central Gauss point, the magnetizations add up close to zero. In this state, small perturbations (e.g., from round-off errors) in the interpolation of the magnetizations from the nodes can lead to severe changes of the magnetization in the Gauss point. Since this behavior is extremely erratic and nonlinear, it is expected to lead to poor conditioning of the underlying linear systems and we observe bad convergence in this case. To remedy this pitfall, we use four Gauss points, which

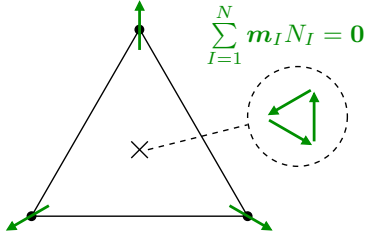


Fig. 3.6: Two-dimensional illustration of the triangular element with single Gauss point, interpolated magnetization vanishes.

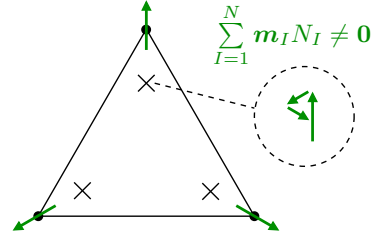


Fig. 3.7: Two-dimensional illustration of the triangular element with three Gauss points, interpolated magnetization is non-zero.

are placed away from the center and close to the nodes, see Tab. 3.1. A two-dimensional illustration is given in Fig. 3.7. Each Gauss point is strongly influenced by the closest node and weakly influenced by the remaining nodes. Hence, magnetizations cannot add up to zero anymore, which improves convergence greatly.

Tab. 3.1: Gauss point positions (reference coordinates ξ_i , η_i , ζ_i) and weights w_i , see [126].

i	ξ_i	η_i	ζ_i	w_i
1	$\frac{1}{4} - \frac{1}{4\sqrt{5}}$	$\frac{1}{4} - \frac{1}{4\sqrt{5}}$	$\frac{1}{4} - \frac{1}{4\sqrt{5}}$	$\frac{1}{4}$
2	$\frac{1}{4} + \frac{3}{4\sqrt{5}}$	$\frac{1}{4} - \frac{1}{4\sqrt{5}}$	$\frac{1}{4} - \frac{1}{4\sqrt{5}}$	$\frac{1}{4}$
3	$\frac{1}{4} - \frac{1}{4\sqrt{5}}$	$\frac{1}{4} + \frac{3}{4\sqrt{5}}$	$\frac{1}{4} - \frac{1}{4\sqrt{5}}$	$\frac{1}{4}$
4	$\frac{1}{4} - \frac{1}{4\sqrt{5}}$	$\frac{1}{4} - \frac{1}{4\sqrt{5}}$	$\frac{1}{4} + \frac{3}{4\sqrt{5}}$	$\frac{1}{4}$

3.6 Computing magnetic noise by ensemble averaging

We apply the previously outlined material model and FEM scheme to investigate magnetic noise. In particular, we are interested in noise that originates from the interaction of domain walls with defects (Barkhausen noise). In the following, we give a detailed exposition of our noise computation scheme¹.

We consider the voltage induced by the magnetic material in a surrounding coil, see Fig. 3.8. This voltage serves as the signal whose noise characteristics we want to study. The signal is inspired by a magnetoelectric sensor structure presented in [127, 128]. We refer to the signal as *loop voltage* by which we mean the *average induced electromotive force per loop*. A discrete coil composed of k loops at positions x_{1i} with areas $A(x_{1i})$ and normal \mathbf{e}_1 exhibits the following loop voltage \mathcal{V}

$$\mathcal{V} = \frac{1}{k} \sum_{i=1}^k \left[- \int_{A(x_{1i})} \frac{d\mathbf{B}}{dt} \cdot \mathbf{e}_1 da \right]. \quad (3.66)$$

¹We previously suggested this scheme at a conference [116].

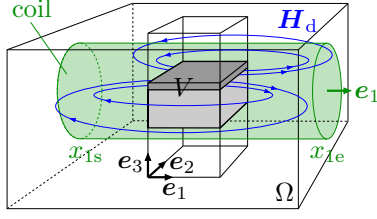


Fig. 3.8: Geometrical setting for noise computation, coil radius $0.3\mu\text{m}$, coil length $2.5\mu\text{m}$.

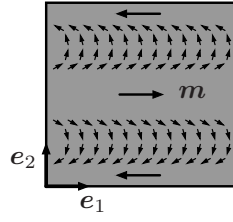


Fig. 3.9: Schematic of initial condition $\mathbf{m}(\mathbf{x}, 0)$.

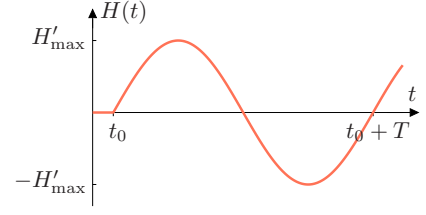


Fig. 3.10: Applied field magnitude $H(t)$.

For $k \rightarrow \infty$, we obtain the following integral over the coil volume

$$\mathcal{V} = -\frac{1}{L} \int_{x_{1s}}^{x_{1e}} \int_A \frac{d\mathbf{B}}{dt} \cdot \mathbf{e}_1 da dx_1 = -\frac{1}{L} \int_{V_{\text{coil}}} \frac{d\mathbf{B}}{dt} \cdot \mathbf{e}_1 dv. \quad (3.67)$$

This is the signal we compute using the presented FEM scheme and investigate in the following.

The aim is to study sensor-like structures composed of a magneto-mechanical thin film deposited on a mechanical substrate, see Fig. 3.8. Since these sensor structures exhibit dimensions in the μm to mm range, they are much too large for numerical resolution (FEM element size in nm range). To alleviate the issue, we use periodic boundary conditions. Our implementation of periodic boundary conditions relies on the idea to modify the FEM mesh such that periodically repeated nodes receive the same node number [129]. With periodic boundary conditions, we obtain the material response of an infinitely extended film and substrate, i.e., boundary effects such as closure domains are eliminated. However, due to periodic boundary conditions in \mathbf{e}_1 - and \mathbf{e}_2 -directions, the embedding of the stack *free space-substrate-film-free space* (center column in Fig. 3.8) in the surrounding free space poses the following issue. Due to periodic boundary conditions, no information can enter or leave the center column (by information, we mean, e.g., the state of a field variable). Inbound information is passed to the opposite face by virtue of periodic boundary conditions and skips the center column (vice versa for outbound information). Thus, the center column and the surrounding free space would be, in a sense, disconnected. To work around this problem, we devised the following two-step simulation process. In the first step, we solve the fully coupled problem only for the center column in Fig. 3.8 with periodic boundary conditions in \mathbf{e}_1 - and \mathbf{e}_2 -direction. The magnetization history $\mathbf{m}(\mathbf{x}, t)$ is recorded. In the following step, we use the recorded history $\mathbf{m}(\mathbf{x}, t)$ to *prescribe* the magnetization of the thin film and only solve for the scalar magnetic potential φ ; but this time in the entire domain (center column and embedding in Fig. 3.8). Using this two-step process, we obtain the behavior of an infinitely extended film and substrate which still emits a stray field into free space. In particular, we get the flux density $\mathbf{B} = \mu_0(M_s \mathbf{m} + \mathbf{H}_d)$ within the coil volume which surrounds the film and substrate, see Fig. 3.8.

In order to study the interaction of domain walls with defects, we first need to introduce domain walls into the magnetic material. We use the initial condition $\mathbf{m}(\mathbf{x}, 0)$ to establish two repulsive domain walls (similar to Néel walls) which are compatible with the periodic boundary conditions, see Fig. 3.9. To make the walls move in a reciprocating fashion, we apply a sinusoidal external field $\mathbf{H}' = H(t)\mathbf{e}_1$ with period T after a relaxation stage $[0, t_0]$, see Fig. 3.10.

So far, we specified the initial distribution (domain wall setting), applied field (source of domain wall motion) and signal (affected by noise). The final ingredient for studying Barkhausen noise is a defect which the domain walls can interact with. For illustration in the present section, we consider three cylindrical holes (radius 10nm) in the magnetic film as prototypical defects, see Fig. 3.12. In Sec. 3.7, we investigate more realistic defects.

A domain wall can reduce its energy by attaching to one of the cylindrical holes since

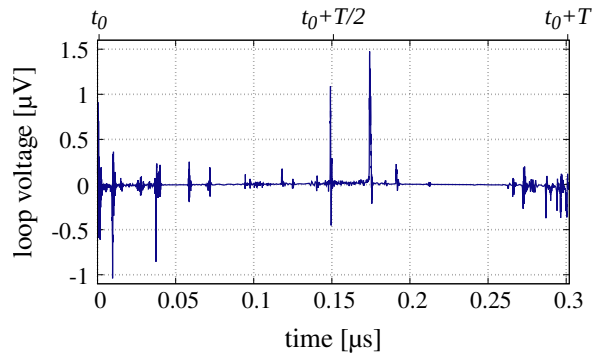


Fig. 3.11: Loop voltage for realization 4.

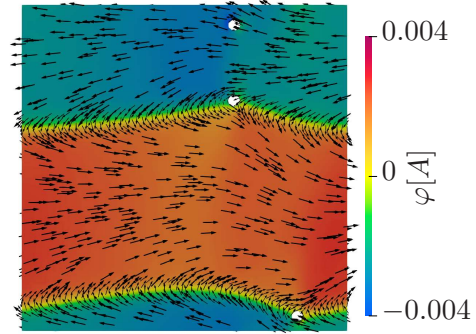


Fig. 3.12: Scalar magnetic potential φ and magnetization \mathbf{m} at time $t > t_0$ for realization 4.

anisotropy and exchange energy vanish in the defect volume. Hence, attaching to a defect is energetically favorable for the domain wall. In a situation where a domain wall enters the vicinity of one of the cylindrical holes, it leaps toward it in order to attach. This results in a peak of loop voltage, see Fig. 3.11. Subsequently, the domain wall exhibits the propensity to remain attached to the cylindrical hole. Under the influence of applied magnetic field \mathbf{H}' , the domain wall bulges out and ultimately detaches from the defect (under sufficiently large field), see Fig. 3.12. This leap away from the defect causes another loop voltage peak.

The loop voltage signal displayed in Fig. 3.11 is valid for one microstructure (i.e., the one placement of defects shown in Fig. 3.12). Hence, so far, we discussed a purely deterministic signal. Performing the same simulation for the same microstructure (same placement of defects) would yield the same loop voltage signal again. For another placement of defects, the number of peaks is different, and voltage peaks occur at different times and exhibit different heights. Yet the signal is still deterministic. In order to introduce randomness, we perform a large set of simulations (see Fig. 3.13) for varying microstructures whose defects are chosen randomly. In the particular example of cylindrical holes, we choose cylinder positions ran-

domly (all positions have the same probability). We call the microstructures *realizations* and the set of microstructures an *ensemble*. This allows us to obtain a pseudo-stochastic signal. By considering many different microstructures (realizations), we go from one tangible microstructure (with one specific set of defects) to an abstract microstructure (with a statistical distribution of defects). In terms of the loop voltage, this means that we go from a single, deterministic signal to a stochastic signal with mean (see Fig. 3.14) and fluctuation (noise). The latter is our quantity of interest.

To compute noise, we study M realizations. Each realization i is accompanied by one loop

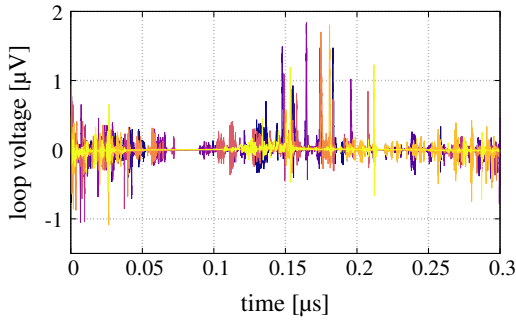


Fig. 3.13: Ensemble of eight loop voltages.

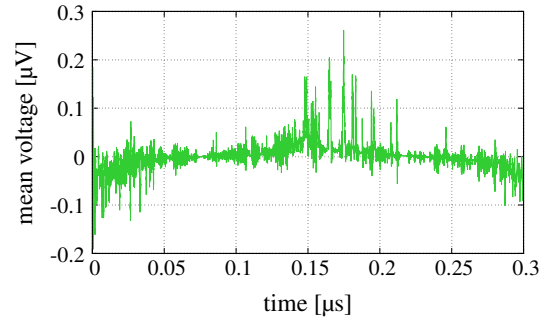


Fig. 3.14: Mean voltage (ensemble average).

voltage array $\tilde{\mathbf{v}}^i$ and time array \mathbf{t}^i (realizations $i=0, \dots, M-1$). Time points in \mathbf{t}^i result from the automatic time step control of the FEM program and are in general not equidistant. Moreover, different realizations can exhibit different numbers of time steps (\mathbf{n}_i steps for realization i). Hence, we introduce the unified time array \mathbf{t} (length \mathbf{n}) with equidistant time points and time step size

$$\Delta \mathbf{t} = \min_{i,j} \left\{ \mathbf{t}^i[j+1] - \mathbf{t}^i[j] \right\}, \quad (3.68)$$

where we indicate by $\mathbf{a}[j]$ the computer array \mathbf{a} at index j . Furthermore, we choose the maximum starting time

$$\mathbf{t}[0] = \max_i \left\{ \mathbf{t}^i[0] \right\} \quad (3.69)$$

and minimum final time

$$\mathbf{t}[\mathbf{n}-1] = \min_i \left\{ \mathbf{t}^i[\mathbf{n}_i - 1] \right\} \quad (3.70)$$

to avoid extrapolation. We interpolate all loop voltage arrays $\tilde{\mathbf{v}}^i$ to the new unified time vector \mathbf{t} and obtain the interpolated loop voltage arrays \mathbf{v}^i . Interpolated arrays in the time- and frequency-domain have the length \mathbf{n} .

Computation of noise voltage power spectral density $S_{\delta v}$ is based on

$$S_{\delta v}(f) = \lim_{T \rightarrow \infty} \left\langle \frac{|\widehat{\delta v_T}(f)|^2}{T} \right\rangle, \quad (3.71)$$

see [130, 131]. In Eq.(3.71), δv denotes the fluctuation of loop voltage around the mean value, see Eq. (3.73). Furthermore, f denotes frequency, T is the size of time range, $\langle \bullet \rangle$ reflects the ensemble average, index T indicates truncated quantities and we use $\widehat{(\bullet)}$ to denote the Fourier transform. The algorithmic implementation of Eq. (3.71) is illustrated in Algo.3.1. Note that we are limited to a finite time range. Hence, we omit the limit $T \rightarrow \infty$ and drop the index T .

Algo. 3.1: Noise computation

1. Loop voltage mean (ensemble average)

$$\langle \underline{v} \rangle[j] = \frac{1}{M} \sum_{i=0}^{M-1} \underline{v}^i[j], \quad j = 0, \dots, n-1. \quad (3.72)$$

2. Loop voltage fluctuation for each realization

$$\delta \underline{v}^i = \underline{v}^i - \langle \underline{v} \rangle, \quad i = 0, \dots, M-1. \quad (3.73)$$

3. Fourier transform of fluctuations for each realization

$$\widehat{\delta \underline{v}^i} = \mathcal{FFT}(\delta \underline{v}^i), \quad i = 0, \dots, M-1, \quad (3.74)$$

cf. Appendix 3.E.

4. Two-sided noise voltage power spectral density

$$\underline{S}_{\delta v}[j] = \Delta t^2 \frac{1}{M} \sum_{i=0}^{M-1} \frac{|\widehat{\delta \underline{v}^i}[j]|^2}{T}, \quad j = 0, \dots, n-1, \quad (3.75)$$

with Δt^2 for consistency with the time-continuous case.

5. One-sided noise voltage spectral density (nvsvd)

$$\underline{nvsvd}[j] = \sqrt{2\underline{S}_{\delta v}[j]}, \quad j = 0, \dots, \frac{n-1}{2}. \quad (3.76)$$

3.7 Numerical examples

3.7.1 Software details and material parameters

We implement our material model as a user element in the finite element program ParFEAP 8.6.1j (MPI parallel version of FEAP [132] with PETSc 3.13.2 [133]). For mesh generation, we

rely on Gmsh 4.4.1 [89]². We implement the noise computation algorithm with Python 3.8.10 and use NumPy 1.23.5 [135] to compute the fast Fourier transform (FFT). For visualization, we use Paraview 5.10.0 [90], Gnuplot 5.2 [91] and Matplotlib 3.6.2 [136]. For structure generation in Sec. 3.7.5, we use Scipy 1.6.1 (Delaunay triangulation) [137].

In our numerical examples, we focus on FeCoSiB [138, 139] as thin film material and silicon as substrate. Unless otherwise stated, we use the (estimated) parameter set displayed in Tab. 3.2. With the precession parameter β as chosen in Tab. 3.2, we obtain for the Gilbert damping

Tab. 3.2: Estimated material parameters.

		FeCoSiB	substrate
A	Exchange stiffness constant	$1.5 \cdot 10^{-11} \frac{\text{J}}{\text{m}}$	–
M_s	Spontaneous magnetization	$1.5 \cdot 10^6 \frac{\text{A}}{\text{m}}$	–
K	Anisotropy constant	$3 \cdot 10^2 \frac{\text{J}}{\text{m}^3}$	–
\mathbf{e}_a	Easy axis	\mathbf{e}_1	–
η	Viscosity parameter	$8.528 \cdot 10^{-8} \frac{\text{J}\cdot\text{s}}{\text{m}^3}$	–
β	Precession parameter	$-8.528 \cdot 10^{-6} \frac{\text{J}\cdot\text{s}}{\text{m}^3}$	–
λ_s	Saturation magnetostriction	$30 \cdot 10^{-6}$	–
λ	First Lamé parameter	172GPa	150GPa
μ	Second Lamé parameter	54GPa	50GPa

$\alpha = -\eta/\beta = 0.01$. For the gyromagnetic ratio, we obtain $\gamma = \mu_0 M_s / \beta \approx -2.2 \cdot 10^5 \text{m}/(\text{As})$, cf. [28, 123].

The loop voltage data for the numerical experiments in Secs. 3.7.3 to 3.7.6 as well as the noise computation script are available [140].

3.7.2 Single element

In this first numerical example, we show that our implementation of precession works according to expectation. To this end, we compare the following two cases: *full LLG* and *pure precession*. We consider a single tetrahedral element, see Fig. 3.15. The initial condition for the magnetization reads

$$\mathbf{m}(t=0) = \frac{\sqrt{2}}{2} \mathbf{e}_1 + \frac{\sqrt{2}}{2} \mathbf{e}_2. \quad (3.77)$$

We deactivate the mechanical and vacuum magnetic problem. Furthermore, we use a constant applied field $\mathbf{H}' = H' \mathbf{e}_1$ with $H' = 10^{-2} \text{A}/\mu\text{m}$ starting at $t = 0$ instead of the previously mentioned sinusoidal field. The described setup establishes an initial angle of $\pi/4$ between

²The mesh size for micromagnetic simulations must be in the range of the exchange length $l_{\text{ex}} = \sqrt{2A/(\mu_0 M_s^2)}$ [134] to properly resolve the exchange interaction between neighboring magnetization vectors \mathbf{m} . For noise computation, we can even use a slightly coarser mesh, see [116]. In the present case, this entails a mesh size around 10nm.

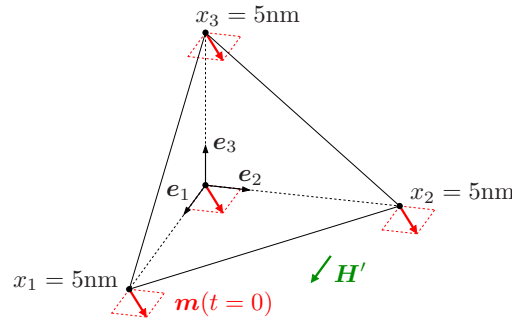


Fig. 3.15: Single element with dimensions $5 \times 5 \times 5 \text{ nm}^3$, initial condition $\mathbf{m}(t = 0)$ and applied field \mathbf{H}' .

magnetization \mathbf{m} and field \mathbf{H}' . Depending on the active contributions, we expect the magnetization to either spin around \mathbf{H}' (pure precession) or to spin around while gradually aligning with \mathbf{H}' (precession and damping). For this numerical example, we increase the viscosity parameter by a factor of ten compared to Tab. 3.2 to make damping effects easily visible (viscosity parameter $\eta = 8.528 \cdot 10^{-7} \text{ Js/m}^3$, Gilbert damping $\alpha = 0.1$). The quantity of interest in this example is the average magnetization \mathbf{m}_{avg} (computed as volume average over magnetization in the Gauss points).

We illustrate the results in Fig. 3.16. We display the three components $(\mathbf{m}_{\text{avg}})_i$ ($i = 1, 2, 3$)

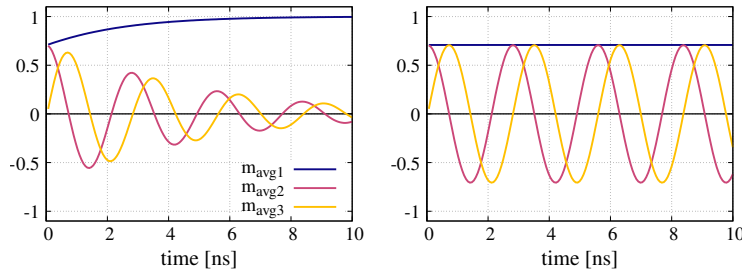


Fig. 3.16: Average magnetization components, left: full LLG, right: pure precession.

of the average magnetization over time for the two considered cases. In all cases, the magnetization components are in line with our expectations.

Furthermore, we demonstrate the behavior of our model for different time step sizes in Fig. 3.17. The displayed case is the full LLG case. We observe that large time steps are possible and that the model rapidly converges with decreasing time step size (i.e., time convergence is ensured). In our experience, such large time steps are not possible with a first order accurate time integration scheme (requires time steps in the order of 30 to $50 \cdot 10^{-12} \text{ s}$).

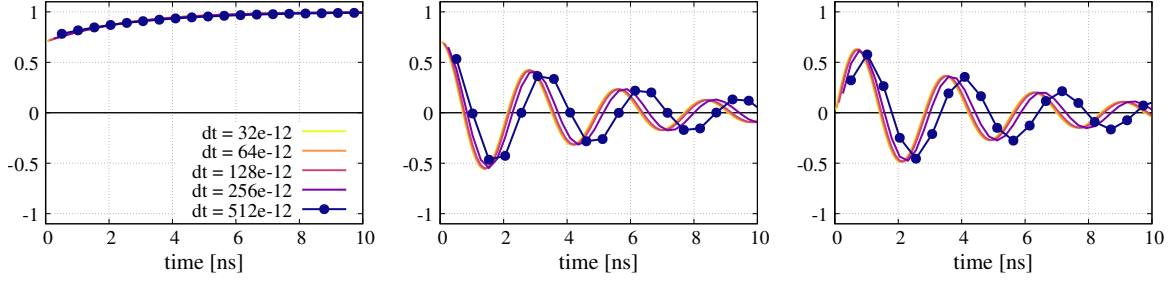


Fig. 3.17: Average magnetization components for different time step sizes, left: $(\mathbf{m}_{\text{avg}})_1$, center: $(\mathbf{m}_{\text{avg}})_2$, right: $(\mathbf{m}_{\text{avg}})_3$.

3.7.3 Influence of precession on noise

We convinced ourselves in Sec. 3.7.2 that the implementation of precession conforms with our expectations. Next, we determine the influence of precession on the noise spectrum. To this end, we compare the full LLG case with the pure damping case. The latter is based on the pure GSM model without the additional precession term, see Section 3.3. It must be noted, that the pure damping case is based on a first order time integration scheme.

We apply the noise computation scheme outlined in Sec. 3.6. In contrast to Sec. 3.6, we do not

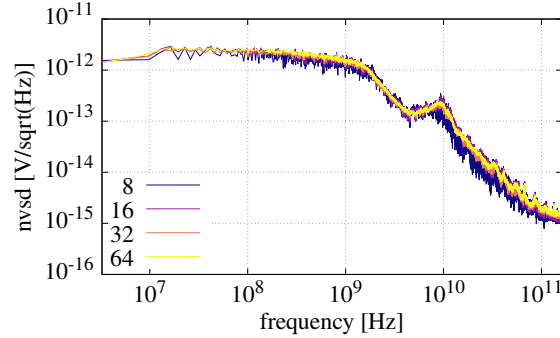


Fig. 3.18: One-sided noise voltage spectral density (nvsd) with precession for different ensemble sizes.

consider cylindrical holes as defects. Instead, we study a magnetic film with surface roughness, see Figs. 3.19 and 3.22. For details on the generation of the surface roughness microstructures, we refer to Sec. 3.7.4. We use the medium height ensemble from the aforementioned section for both cases (with and without precession). Hence, the two resulting noise spectra are based on exactly the same microstructure ensemble (ensemble size 64). A short remark on ensemble size is in order. In Fig. 3.18, we illustrate the noise spectrum for the case with precession for different ensemble sizes. We observe convergence with increasing ensemble size, see [116] for a detailed discussion.

The geometrical dimensions of film, substrate, and surrounding free space box are illustrated in Fig. 3.19. The film features the following dimensions $0.5 \times 0.5 \times 0.01 \mu\text{m}^3$. Note that, due to the uneven surface, the value of $0.01 \mu\text{m}$ is an average thickness. The substrate measures

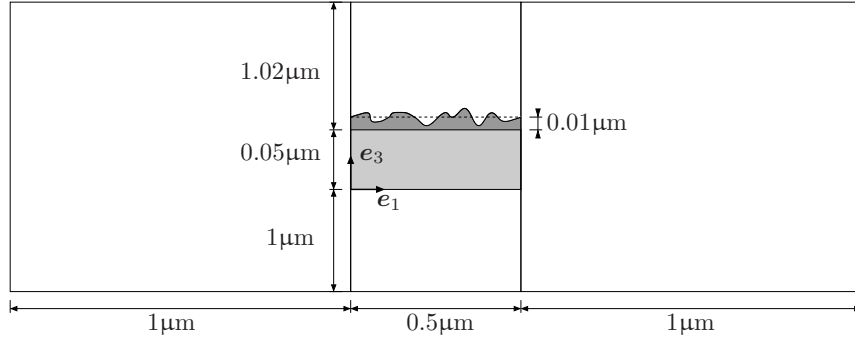


Fig. 3.19: Two-dimensional illustration of measurements: film and substrate embedded in free space box.

$0.5 \times 0.5 \times 0.05 \mu\text{m}^3$ and the surrounding free space box has the dimensions $2.5 \times 2.5 \times 2.07 \mu\text{m}^3$. In terms of the loading by the applied field, we use $t_0 = 10^{-9}\text{s}$, $T = 3 \cdot 10^{-7}\text{s}$ and $H'_{\text{max}} = 5 \cdot 10^{-3}\text{A}/\mu\text{m}$, cf. Fig. 3.10.

We showcase the induced loop voltage for a single domain wall jump event (with and without precession) in Fig. 3.20 (for dimensions of the coil, see caption of Fig. 3.8). Note that the displayed time range is only a small subset of the full time range $[0, t_0 + T]$. We observe

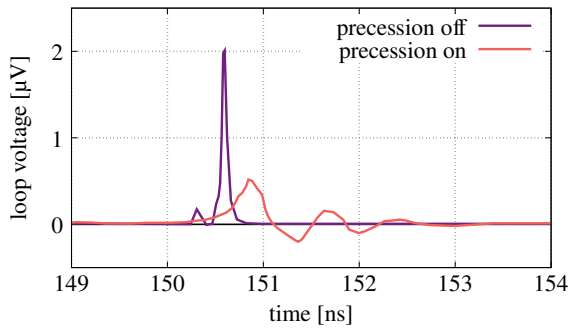


Fig. 3.20: Loop voltage for single domain wall jump event with and without precession (realization 1).

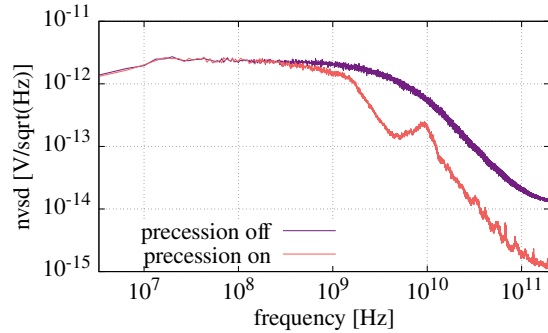


Fig. 3.21: One-sided noise voltage spectral density (nvsvd) with and without precession.

that the loop voltage with precession exhibits a smaller peak height, a longer peak duration and an overshooting behavior. These differences are reflected in the noise spectra as well, see Fig. 3.21. With precession, the noise voltage spectral density is smaller for medium to large frequencies compared to the case without precession. Moreover, with precession, we observe a more pronounced kink in the noise spectrum around 10^9Hz and a peak at 10^{10}Hz . A rough estimation using Kittel's formula [141] suggests that the latter peak occurs at a frequency in the range of the ferromagnetic resonance frequency.

Since the difference between the cases with and without precession is so striking, we always include precession in the following.

3.7.4 Influence of surface roughness height on noise

In Sec. 3.7.3, we used an ensemble of magnetic films with surface roughness to study the influence of precession on noise. In the present section, we study the influence of the aforementioned surface roughness on noise. We keep precession active in all cases and vary the surface roughness height. The geometrical dimensions and applied field characteristics (t_0 , T and H'_{\max}) remain as in Sec. 3.7.3.

To generate the microstructures, we express the height $h(x_1, x_2)$ of the surface as a Fourier series ($x_i \in [0, l_i]$, $i = 1, 2$). We discretize the continuous domain $[0, l_1] \times [0, l_2]$ with $N_1 \times N_2$ grid points. The height at grid location (n_1, n_2) in real space reads

$$h_{n_1 n_2} = \frac{1}{N_1 \cdot N_2} \sum_{k_1=1}^{M_1} \sum_{k_2=-M_2}^{M_2} 2\hat{h}_{k_1 k_2} \cos\left(2\pi\left(\frac{k_1 n_1}{N_1} + \frac{k_2 n_2}{N_2}\right) - \phi_{k_1 k_2}\right) \quad (3.78)$$

with $n_i = 0, \dots, N_i - 1$ and $N_i = 2M_i + 1$ ($i = 1, 2$). We choose for the real-valued Fourier coefficients $\hat{h}_{k_1 k_2} = 1$. Furthermore, we draw $\phi_{k_1 k_2} \in [0, 2\pi)$ from a uniform distribution. As a result, we obtain what we call a *white surface* (by analogy with white noise). To avoid surfaces that are too jagged, we set Fourier coefficients $\hat{h}_{k_1 k_2}$ with $\sqrt{k_1^2 + k_2^2} > k_{\text{cut}}$ to zero (we use $N_i = 31$ and $k_{\text{cut}} = 5$).

We consider three ensembles of surface roughness: small, medium and large surface rough-

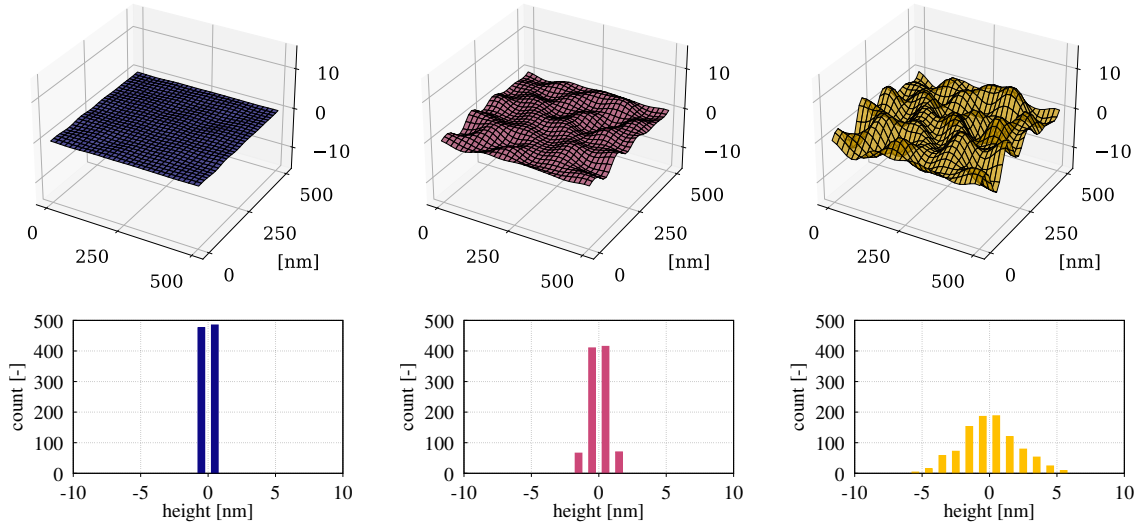


Fig. 3.22: Same single realization of surface roughness, left: small height, center: medium height, right: large height, top: surface plot, bottom: height histogram.

ness height, see Fig. 3.22. Each ensemble comprises 64 realizations. Note that, occasionally, a realization is not usable in the sense that during the simulation, the magnetic structure of two domain walls is lost (e.g., vortex formation, homogeneous magnetization). In this case, the realization is replaced. Hence, the ensembles only contain realizations that retain the two

domain walls.

The corresponding one-sided noise voltage spectral densities are summarized in Fig. 3.23.

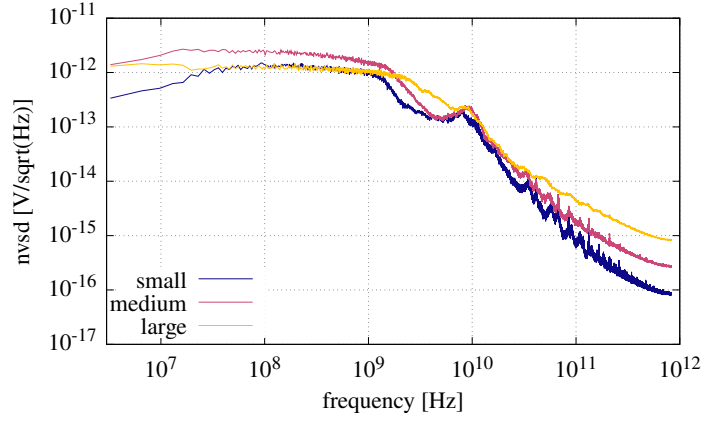


Fig. 3.23: One-sided noise voltage spectral density (nvsd) for three different surface roughness heights.

We observe that a larger surface roughness height causes stronger noise at medium to large frequencies. At lower frequencies, the medium surface roughness height causes the strongest noise. A rough surface exhibits peaks and valleys which inhibit domain wall motion (analogous to cylindrical holes in Sec. 3.6). A larger surface roughness height constitutes more difficult obstacles to overcome. If, for a given applied field magnitude, a domain wall can overcome such obstacles then the result is a domain wall jump. In this case, a larger surface roughness height causes greater domain wall jumps and stronger noise (as displayed in Fig. 3.23 at medium to large frequencies). However, if the applied field magnitude is not large

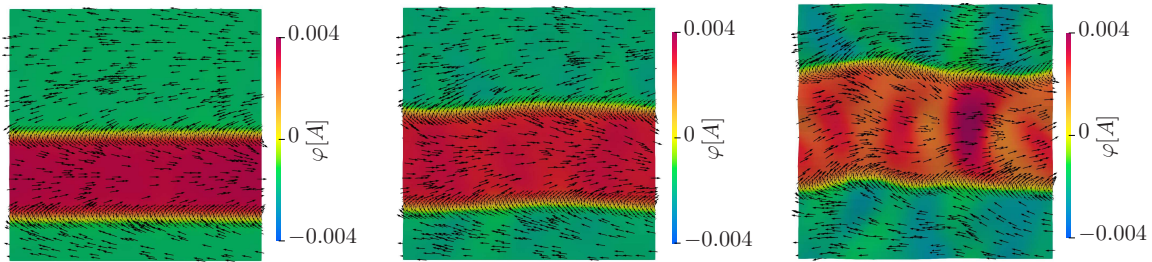


Fig. 3.24: Scalar magnetic potential φ and magnetization \mathbf{m} at $t \approx 2 \cdot 10^{-7}$ s for same single realization of surface roughness, left: small height, center: medium height, right: large height.

enough for a domain wall to overcome the obstacles, then noise is decreased. We also expect low noise for small surface roughness height since domain wall motion is possible with little obstruction. Thus, for a given applied field magnitude, both very rough and very smooth surfaces can cause low noise. The largest noise can be expected at medium surface roughness height (as displayed in Fig. 3.23 at small to medium frequencies). Why the two different lines of reasoning apply to different frequency regions remains an open question.

In Fig. 3.24, we showcase the scalar magnetic potential φ and magnetization \mathbf{m} for the same realization at the three considered heights. We observe that small surface roughness does not have a profound effect on the domain walls. In turn, large roughness leads to curly, non-straight domain walls.

3.7.5 Influence of inhomogeneous material properties on noise

In this numerical example, we study the influence of inhomogeneous material properties (material contrast) on noise. To this end, we need a microstructure in which we can assign different materials (with different properties) to different regions of the structure. The structure itself is not of major interest as we want to focus on the material contrast. The idea is to decompose the magnetic film into cells of non-uniform shape. For simplicity, we start by using a Delaunay triangulation of the magnetic film to generate triangular cells (we simply use the existing routines in Scipy). Note that this is not the triangulation which generates the finite element mesh. After cell generation, we assign the cells to two different materials in such a way that we obtain approximately 50% volume fraction for each material. Hence, in terms of the material composition, all generated microstructures are stochastically equivalent. Furthermore, note that the cell assignment also entails that two neighboring cells of the same material merge to form a non-triangular cell. One realization is illustrated in Fig. 3.25. We

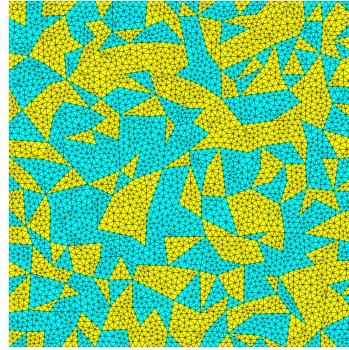


Fig. 3.25: Single realization of the microstructure consisting of two materials (displayed in different colors), finite element mesh indicated with black lines.

use the same ensemble of 64 realizations for all considered material combinations. Hence, all spectra result from the same microstructure ensemble. The exterior geometrical dimensions are similar to the ones in the Secs. 3.7.3 and 3.7.4. However, since the magnetic film does not exhibit a surface roughness, its thickness of $0.01\mu\text{m}$ is not an average thickness in this case. This also means that the free space box is slightly shallower ($2.5 \times 2.5 \times 2.06\mu\text{m}$). The applied field characteristics are similar to the ones in Secs. 3.7.3 and 3.7.4 as well, except that the field magnitude is $H'_{\text{max}} = 1 \cdot 10^{-2} \text{A}/\mu\text{m}$, cf. Fig. 3.10. The larger applied magnetic field is necessary in order to make the domain walls move. We interpret this required increase in magnetic field as follows. As discussed in Sec. 3.7.4, defect and applied magnetic field must

be balanced. For a specific type of defect, a certain field strength is necessary to overcome the defect. Below this field strength, domain wall motion is restricted resulting in no (few) domain wall jumps. On the other hand, excessively large applied magnetic field forces the two domain walls together and often results in a breakdown of the two-domain-wall setup. It turns out that the inhomogeneous material properties considered in the present section are more difficult to overcome than the surface roughness considered in Secs. 3.7.3 and 3.7.4 and, hence, require a stronger applied magnetic field.

The material parameters, for which we investigate inhomogeneous material properties, are the exchange stiffness constant A and the spontaneous magnetization M_s . For each property, we compute three spectra at three different material contrasts. In the first set of examples, we keep the exchange constant of the first magnetic material at $A = 15$ pJ/m and assign the second magnetic material either 30 pJ/m, 45 pJ/m or 60 pJ/m (i.e., three spectra). The exchange stiffness of 30 pJ/m is physically still plausible (e.g., Cobalt [123]) while we choose the other two options to try out the limits of our material model and noise computation scheme. The resulting noise spectra are illustrated in Fig. 3.26, where we also display the spectrum for the medium surface roughness (with precession) for comparison. We observe

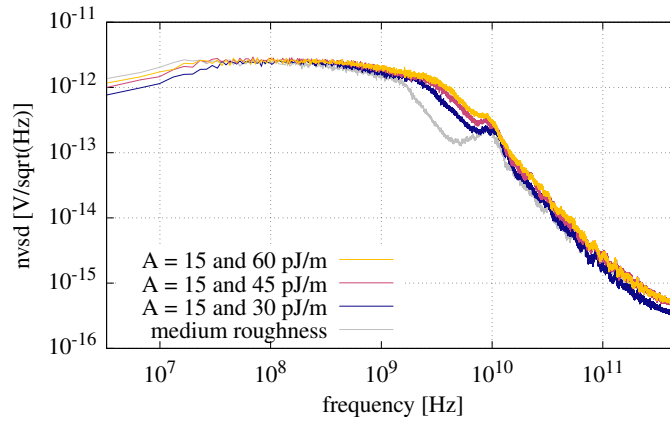


Fig. 3.26: One-sided noise voltage spectral density (nvsvd) for three different material contrasts of exchange stiffness constant A .

that a larger material contrast causes stronger noise at medium to large frequencies. At small frequencies, it is difficult to distinguish between the spectra. Furthermore, we notice that the noise due to inhomogeneous material properties is larger than the noise due to surface roughness for medium frequencies and approximately the same for low and very high frequencies. This comparison should be considered under the caveat that the applied field magnitude for the surface roughness spectrum is half as large as for the spectra involving inhomogeneous materials.

In the second set of spectra, we fix the spontaneous magnetization of the first magnetic material at $M_s = 1.5$ A/ μ m. For the second magnetic material, we choose either 1.25 A/ μ m, 1.0 A/ μ m or 0.75 A/ μ m (again three spectra). In this case, all considered spontaneous magne-

tizations M_s are physically plausible, cf. [123]. We display the three noise spectra in Fig. 3.27 (including comparison to the medium surface roughness spectrum). In this case, we observe

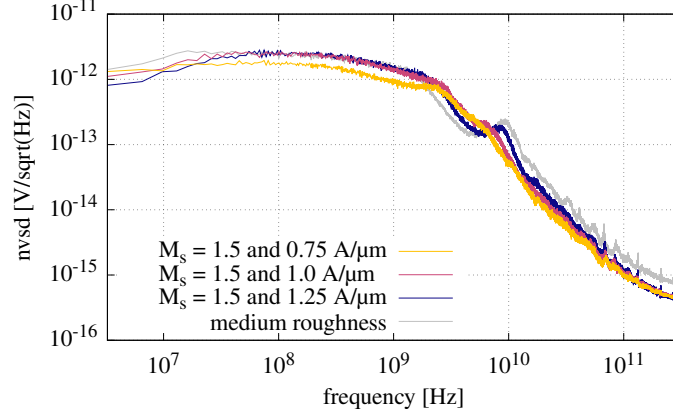


Fig. 3.27: One-sided noise voltage spectral density (nvsd) for three different material contrasts of spontaneous magnetization M_s .

that, at higher frequencies, small material contrast leads to stronger noise (i.e., the opposite trend compared to Fig. 3.26). In this frequency range, all M_s -contrasts lead to smaller noise than the medium surface roughness. Our second observation relates to the peak around 10^{10} Hz. It is apparent that larger material contrast leads to a shift of the peak to smaller frequencies. We propose the following explanation. In the considered cases, the M_s -contrast means a decrease of the effective spontaneous magnetization M_s . We essentially mix 50% original material ($M_s = 1.5\text{A}/\mu\text{m}$) and 50% material with $M_s < 1.5\text{A}/\mu\text{m}$. The larger the M_s -contrast is, the smaller the effective M_s becomes. In Kittel's formula, the ferromagnetic resonance frequency depends on $\sqrt{M_s}$, thus shifting the peak to smaller frequencies. The same line of reasoning also explains larger noise for smaller material contrast. Smaller contrast is accompanied by larger effective M_s , larger loop voltage (see Eq. (3.67)), and, consequently, stronger noise.

Finally, note that our choices of investigated material property ranges (increased A , decreased M_s) both increase the exchange length $l_{\text{ex}} = \sqrt{2A/(\mu_0 M_s^2)}$. Hence, the mesh resolution of 10nm remains appropriate in all cases.

3.7.6 Influence of inhomogeneous eigenstrain on noise

The last type of defect (obstacle) we want to study is inhomogeneous eigenstrain. Here we have volumetric eigenstrain in mind which could occur after, e.g., (local) phase transformation or an imperfect production process. We consider the same microstructure ensemble and applied field characteristics as in Sec. 3.7.5. Thus, the microstructure consists of a magnetic film with two phases, see Fig. 3.25, on top of a substrate, see Fig. 3.8. In the present case, we assign the same material parameters to the two phases but we prescribe different eigenstrains

according to

$$\epsilon^* = \begin{cases} \mathbf{0} & \text{phase 1} \\ a\mathbf{I} & \text{phase 2} \end{cases}. \quad (3.79)$$

For the eigenstrain magnitude values, we consider $a \in \{0.5\%, 1\%, 2\%\}$. The resulting noise spectra are illustrated in Fig. 3.28 along with the spectrum for medium surface roughness (with precession) for comparison. The difference between the three spectra (for eigenstrain)

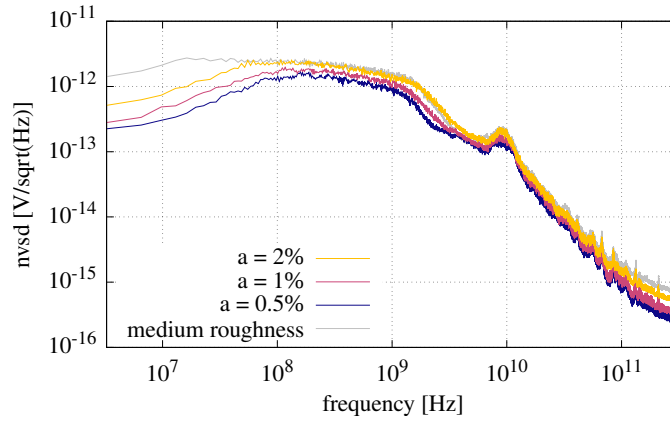


Fig. 3.28: One-sided noise voltage spectral density (nvsvd) for three different eigenstrain magnitudes a .

is mainly observable at small to medium frequencies where they are clearly spaced apart. We observe a monotonous behavior w.r.t. eigenstrain at (almost) all frequencies. Larger volumetric eigenstrain magnitude causes stronger noise. Furthermore, we observe that noise due to inhomogeneous eigenstrain is smaller than noise due to the medium surface roughness at (almost) all frequencies. Particularly noteworthy is the relatively small noise caused by inhomogeneous eigenstrain at small frequencies (compared to all previous examples).

Finally, we compare the results to experimental studies [105, 142, 143]. The referenced studies must be considered under the caveat that they do not focus on thin films but rather on bulk material. Furthermore, the considered plastic deformation is deviatoric and not spherical (volumetric). Nevertheless, we can deduce that higher mechanical deformation causes stronger Barkhausen noise (in the high-frequency regime, for moderate deformation). This is in line with Fig. 3.28.

3.7.7 Remark on comparison with experiments

We want to comment on the comparison of noise levels with experimental data. Experimentally determined noise spectra for thin films [107, 144] and magnetostrictive materials [145, 146, 147] are readily available, while works on magnetostrictive thin films [148] are scarce. Furthermore, experimental studies typically consider macroscopic samples which are much

larger than the small material sections investigated here. The frequency ranges in the referenced experimental works do not exceed 100kHz (while ours start at approximately 3MHz) and, often, we do not know if the domain structures are comparable to the structure in the present work.

Higher frequency spectra for thin film structures are typically considered for hard disk read heads (giant magnetoresistance structures) [149, 150]. However, for these structures, Barkhausen noise is typically not of foremost interest, the domain structure is unknown or not comparable, and the readout is not based on a coil as in our case.

The magnetoelectric composite sensor by Hayes et al. [128] features magnetostrictive material, frequency range, domain structure, and coil readout which are close to the present work (since it inspired our setup of numerical experiments). Unfortunately, the considered composite is again much larger than the small material sections investigated here. A comparison of absolute noise values is a complicated scale transition problem and it is planned to be investigated in future works.

3.8 Summary and Outlook

With the present work, we aimed to quantify Barkhausen noise in magnetostrictive thin film composites. For this purpose, we formulated a micro-magneto-mechanical material model within the GSM approach. As a result of the GSM formulation, our material model is thermodynamically consistent. In order to include precession, we introduced an additional contribution into the model formulation. Particularly noteworthy is the modified Crank-Nicolson time integration scheme in combination with the exponential map (to retain the magnetization magnitude). Furthermore, we devised a scheme to extract noise from a set of simulations based on ensemble averaging. With this approach, we were able to gain valuable insights into magnetic noise.

First, we observed that precession is an essential part for Barkhausen noise. Without including precession, we omit part of the magnetization dynamics and as a result also part of the domain wall dynamics. The noise computed from an ensemble without precession exceeds the noise of its counterpart with precession by orders of magnitude. Second, we were able to illustrate the influence of surface roughness on the noise spectrum. In particular, at higher frequencies, larger roughness yields stronger noise. Furthermore, we noticed that different material parameters (or rather their respective contrasts) affect the noise spectrum in different ways. Finally, it was observed that eigenstrain has a distinct influence on Barkhausen noise.

Investigating the relation between noise and the applied field magnitude as well as between noise and the applied field frequency is beyond the scope of this work. The same applies to an investigation of the relation between noise and the periodic composite size. Additional future work could be devoted to studying surface roughness with a bias, i.e., structured surfaces. Further, more sophisticated microstructures (e.g., Voronoi tessellation) for investigating in-

homogeneous material properties and microstructure influence could be considered.

Acknowledgment

This research was supported by the Deutsche Forschungsgemeinschaft (DFG, German Research Foundation) under project 286471992 (Collaborative Research Center 1261). This research was supported in part through high-performance computing resources available at the Kiel University Computing Center.

Appendices

3.A Divergence theorem for a domain with singular surface

Divergence theorem for a vector \mathbf{g} in a volume Ω with singular surface S , as illustrated in Fig. 3.29, reads [151]

$$\int_{\Omega} \operatorname{div}(\mathbf{g}) \, dv = \int_{\partial\Omega} \mathbf{g} \cdot \mathbf{n} \, da + \int_S \llbracket \mathbf{g} \rrbracket \cdot \mathbf{p} \, da \quad (3.80)$$

$$\llbracket \mathbf{g} \rrbracket = \mathbf{g}^+ - \mathbf{g}^- . \quad (3.81)$$

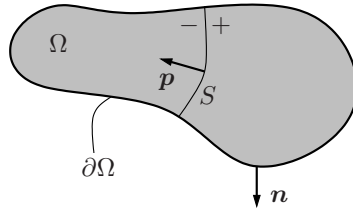


Fig. 3.29: Volume Ω with external normal \mathbf{n} including singular surface S with normal \mathbf{p} (pointing from S^+ to S^-).

3.B Accuracy of modified Crank–Nicolson scheme

We investigate Eq. (3.63) to derive the order of accuracy of the modified (i.e., projected) Crank–Nicolson scheme. To this end, we consider the projection to a general plane perpendicular to \mathbf{a} with $\|\mathbf{a}\| = 1$. In this case, the modified Crank–Nicolson scheme reads

$$(\mathbf{I} - \mathbf{a} \otimes \mathbf{a}) \frac{\mathbf{m}_{n+1} - \mathbf{m}_n}{\Delta t} = (\mathbf{I} - \mathbf{a} \otimes \mathbf{a}) \frac{1}{2} (\mathbf{f}_{n+1} + \mathbf{f}_n) \quad (3.82)$$

or equivalently with projector $\mathcal{A}(\mathbf{a}) = (\mathbf{I} - \mathbf{a} \otimes \mathbf{a})$,

$$\mathcal{A}(\mathbf{a})\mathbf{m}_{n+1} = \mathcal{A}(\mathbf{a}) \left(\mathbf{m}_n + \frac{1}{2}\Delta t (\mathbf{f}_{n+1} + \mathbf{f}_n) \right). \quad (3.83)$$

In the following, we understand all vectors in the above equation as global degree-of-freedom vectors in the sense of FEM (with condensed-out displacement and magnetic potential degrees of freedom). In a strict sense, this is possible if the integration points for the weak form of (at least) the left hand-side of Eq. (3.82) are placed in the nodes, while \mathbf{f}_n is the related global residual vector at time t_n . The vector \mathbf{m}_{n+1} is the time-discrete magnetization direction in the new time step t_{n+1} , \mathbf{m}_n is the corresponding version in the old time step t_n and we further introduce the vector \mathbf{m}_{n+1}^* , which denotes the exact, time-continuous magnetization update at the new time t_{n+1} . We seek to investigate the error $\|\mathbf{m}_{n+1}^* - \mathbf{m}_{n+1}\|$. The associated right hand sides are \mathbf{f}_{n+1} , \mathbf{f}_n and \mathbf{f}_{n+1}^* . To assess accuracy, we consider the difference between the time-discrete update and the exact update, assuming that $\mathbf{m}_n = \mathbf{m}_n^*$,

$$\left\| \mathcal{A}(\mathbf{a}) \frac{\mathbf{m}_{n+1} - \mathbf{m}_n}{\Delta t} - \mathcal{A}(\mathbf{a}) \frac{\mathbf{m}_{n+1}^* - \mathbf{m}_n}{\Delta t} \right\| = \frac{\|\mathcal{A}(\mathbf{a})(\mathbf{m}_{n+1}^* - \mathbf{m}_{n+1})\|}{\Delta t}. \quad (3.84)$$

For a general vector \mathbf{y} , we obtain (where the dyadic product is evaluated node-wise)

$$\|\mathcal{A}(\mathbf{a})\mathbf{y}\| = \|(\mathbf{I} - \mathbf{a} \otimes \mathbf{a})\mathbf{y}\| \leq \|\mathbf{y}\| \quad (3.85)$$

(which also makes sense geometrically). In particular, we find for the difference between exact and time-discrete solution,

$$\|\mathcal{A}(\mathbf{a})(\mathbf{m}_{n+1}^* - \mathbf{m}_{n+1})\| \leq \|\mathbf{m}_{n+1}^* - \mathbf{m}_{n+1}\| \quad (3.86)$$

$$= \|(\mathbf{I} - \mathbf{a} \otimes \mathbf{a} + \mathbf{a} \otimes \mathbf{a})(\mathbf{m}_{n+1}^* - \mathbf{m}_{n+1})\| \quad (3.87)$$

$$\leq \|\mathcal{A}(\mathbf{a})(\mathbf{m}_{n+1}^* - \mathbf{m}_{n+1})\| + \|\mathbf{a} \otimes \mathbf{a}(\mathbf{m}_{n+1}^* - \mathbf{m}_{n+1})\|, \quad (3.88)$$

where the last step holds due to triangle inequality. In the following, to simplify the geometrical interpretation, we choose $\mathbf{a} = \mathbf{m}_{n+1}$. Note that the original Crank–Nicolson scheme without projector \mathcal{A} is not norm-preserving. To rectify the norm, we employ the parametrization of \mathbf{m}_{n+1} via the exponential map (see Eqs. (3.56) to (3.59)). From the conceptual Fig. 3.30, we deduce

$$\|\mathcal{A}(\mathbf{m}_{n+1})(\mathbf{m}_{n+1}^* - \mathbf{m}_{n+1})\| = \sin \gamma \quad (3.89)$$

$$\|\mathbf{m}_{n+1} \otimes \mathbf{m}_{n+1}(\mathbf{m}_{n+1}^* - \mathbf{m}_{n+1})\| = 1 - \cos \gamma \leq \sin \gamma \quad \text{if } \gamma \in \left[0, \frac{\pi}{2}\right] \quad (3.90)$$

which implies

$$\|\mathbf{m}_{n+1} \otimes \mathbf{m}_{n+1}(\mathbf{m}_{n+1}^* - \mathbf{m}_{n+1})\| \leq \sin \gamma = \|\mathcal{A}(\mathbf{m}_{n+1})(\mathbf{m}_{n+1}^* - \mathbf{m}_{n+1})\|. \quad (3.91)$$

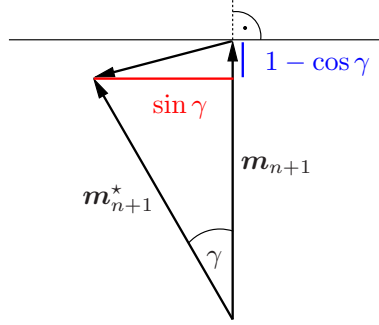


Fig. 3.30: Schematic geometrical relation between time-discrete update \mathbf{m}_{n+1} and exact solution \mathbf{m}_{n+1}^* (actually holds node-wise); the Crank–Nicolson scheme is projected to subspace perpendicular to \mathbf{m}_{n+1} .

This geometrical relation is valid for three-dimensional vectors as well as node-wise in the sense of high-dimensional FEM degree-of-freedom vectors

$$\|\mathcal{A}(\mathbf{m}_{n+1})(\mathbf{m}_{n+1}^* - \mathbf{m}_{n+1})\| = \sqrt{\sum_i \|\mathcal{A}_i(\mathbf{m}_i^* - \mathbf{m}_i)\|^2} = \sqrt{\sum_i \sin^2 \gamma_i} \quad (3.92)$$

$$\geq \sqrt{\sum_i (1 - \cos \gamma_i)^2} = \sqrt{\sum_i \|\mathbf{m}_i \otimes \mathbf{m}_i (\mathbf{m}_i^* - \mathbf{m}_i)\|^2} \quad (3.93)$$

$$= \|\mathbf{m}_{n+1} \otimes \mathbf{m}_{n+1}(\mathbf{m}_{n+1}^* - \mathbf{m}_{n+1})\|, \quad (3.94)$$

where i denotes the node index and we occasionally drop the index $(\bullet)_{n+1}$ for readability. With this geometrical relation at hand, we obtain with Eqs. (3.86) and (3.88)

$$\|\mathcal{A}(\mathbf{m}_{n+1})(\mathbf{m}_{n+1}^* - \mathbf{m}_{n+1})\| \leq \|\mathbf{m}_{n+1}^* - \mathbf{m}_{n+1}\| \quad (3.95)$$

$$\leq \|\mathcal{A}(\mathbf{m}_{n+1})(\mathbf{m}_{n+1}^* - \mathbf{m}_{n+1})\| + \|\mathbf{m}_{n+1} \otimes \mathbf{m}_{n+1}(\mathbf{m}_{n+1}^* - \mathbf{m}_{n+1})\| \quad (3.96)$$

$$\leq 2 \|\mathcal{A}(\mathbf{m}_{n+1})(\mathbf{m}_{n+1}^* - \mathbf{m}_{n+1})\|. \quad (3.97)$$

To proceed from here, we express the exact magnetization in the new time step \mathbf{m}_{n+1}^* using a *forward* Taylor series

$$\mathbf{m}_{n+1}^* = \mathbf{m}_n + \mathbf{f}_n \Delta t + \frac{1}{2} \ddot{\mathbf{m}}(t_n) \Delta t^2 + \mathcal{O}(\Delta t^3) \quad (3.98)$$

as well as a *backward* Taylor series

$$\mathbf{m}_{n+1}^* = \mathbf{m}_n - \mathbf{f}_{n+1}^*(-\Delta t) - \frac{1}{2} \ddot{\mathbf{m}}(t_{n+1})(-\Delta t)^2 + \mathcal{O}(\Delta t^3) \quad (3.99)$$

and combine the two as follows

$$\mathbf{m}_{n+1}^* = \frac{1}{2}(\mathbf{m}_{n+1}^* + \mathbf{m}_{n+1}^*) \quad (3.100)$$

$$= \mathbf{m}_n + \frac{1}{2}\Delta t(\mathbf{f}_{n+1}^* + \mathbf{f}_n) + \frac{1}{4}\Delta t^2(\ddot{\mathbf{m}}(t_n) - \ddot{\mathbf{m}}(t_{n+1})) + \mathcal{O}(\Delta t^3) \quad (3.101)$$

and, hence, obtain

$$\mathcal{A}(\mathbf{m}_{n+1})\mathbf{m}_{n+1}^* = \mathcal{A}(\mathbf{m}_{n+1})\left(\mathbf{m}_n + \frac{1}{2}\Delta t(\mathbf{f}_{n+1}^* + \mathbf{f}_n) + \frac{1}{4}\Delta t^2(\ddot{\mathbf{m}}(t_n) - \ddot{\mathbf{m}}(t_{n+1}))\right) + \mathcal{O}(\Delta t^3). \quad (3.102)$$

Combining Eqs. (3.83) and (3.102) yields

$$\begin{aligned} & \|\mathcal{A}(\mathbf{m}_{n+1})(\mathbf{m}_{n+1}^* - \mathbf{m}_{n+1})\| \\ &= \left\| \mathcal{A}\left(\frac{1}{2}\Delta t(\mathbf{f}_{n+1}^* - \mathbf{f}_{n+1}) + \frac{1}{4}\Delta t^2(\ddot{\mathbf{m}}(t_n) - \ddot{\mathbf{m}}(t_{n+1}))\right) + \mathcal{O}(\Delta t^3) \right\| \end{aligned} \quad (3.103)$$

$$\leq \frac{\Delta t}{2} \|\mathcal{A}(\mathbf{f}_{n+1}^* - \mathbf{f}_{n+1})\| + \frac{\Delta t^2}{4} \|\mathcal{A}(\ddot{\mathbf{m}}(t_n) - \ddot{\mathbf{m}}(t_{n+1}))\| + \mathcal{O}(\Delta t^3), \quad (3.104)$$

where the last step holds due to triangle inequality. Using a Taylor series, we write for $\ddot{\mathbf{m}}(t_{n+1})$

$$\ddot{\mathbf{m}}(t_{n+1}) = \ddot{\mathbf{m}}(t_n) + \dddot{\mathbf{m}}(t_n)\Delta t + \mathcal{O}(\Delta t^2) \quad (3.105)$$

which yields with Eq. (3.85) and triangle inequality

$$\|\mathcal{A}(\mathbf{m}_{n+1})(\ddot{\mathbf{m}}(t_n) - \ddot{\mathbf{m}}(t_{n+1}))\| \leq \|\ddot{\mathbf{m}}(t_n)\|\Delta t + \mathcal{O}(\Delta t^2). \quad (3.106)$$

Assuming \mathbf{f} to be a Lipschitz continuous function of \mathbf{m} with Lipschitz constant L and using Eq. (3.85) again, we write

$$\|\mathcal{A}(\mathbf{f}_{n+1}^* - \mathbf{f}_{n+1})\| \leq L\|\mathbf{m}_{n+1}^* - \mathbf{m}_{n+1}\|. \quad (3.107)$$

Together with Eq. (3.104), we obtain the following estimate

$$\|\mathcal{A}(\mathbf{m}_{n+1})(\mathbf{m}_{n+1}^* - \mathbf{m}_{n+1})\| \leq \frac{\Delta t L}{2} \|\mathbf{m}_{n+1}^* - \mathbf{m}_{n+1}\| + \frac{\Delta t^3}{4} \|\ddot{\mathbf{m}}(t_n)\| + \mathcal{O}(\Delta t^3) \quad (3.108)$$

$$= \frac{\Delta t L}{2} \|\mathbf{m}_{n+1}^* - \mathbf{m}_{n+1}\| + \mathcal{O}(\Delta t^3) \quad (3.109)$$

which yields with Eq. (3.97),

$$\|\mathbf{m}_{n+1}^* - \mathbf{m}_{n+1}\| \leq 2\|\mathcal{A}(\mathbf{m}_{n+1})(\mathbf{m}_{n+1}^* - \mathbf{m}_{n+1})\| \quad (3.110)$$

$$\leq \Delta t L \|\mathbf{m}_{n+1}^* - \mathbf{m}_{n+1}\| + \mathcal{O}(\Delta t^3) \quad (3.111)$$

$$\Leftrightarrow (1 - \Delta t L) \|\mathbf{m}_{n+1}^* - \mathbf{m}_{n+1}\| \leq \mathcal{O}(\Delta t^3) . \quad (3.112)$$

Requiring $\Delta t < 1/L$, we deduce

$$\|\mathbf{m}_{n+1}^* - \mathbf{m}_{n+1}\| \leq \frac{1}{1 - \Delta t L} \mathcal{O}(\Delta t^3) \hat{=} \mathcal{O}(\Delta t^3) \quad (3.113)$$

which proves second order accuracy.

3.C Time and space discrete magnetization residual

In the following derivations, we usually start from tensor notation with bold faced letters and transition to matrix notation with underlined letters.

As mentioned above, we use tetrahedral elements ($N = 4$ nodes) with linear shape functions N_I ($I = 1, \dots, N$) to approximate the fields of interest. As an example, the magnetization \mathbf{m} in one element is interpolated according to

$$\mathbf{m} = \sum_{I=1}^N \mathbf{m}_I N_I(\underline{x}) , \quad (3.114)$$

where \mathbf{m}_I are the nodal values of \mathbf{m} in the element. The matrix version of the interpolant reads

$$\underline{\mathbf{m}} = \underline{N}_{\mathbf{m}} \underline{\mathbf{m}}^e \quad \text{with} \quad \underline{\mathbf{m}} \in \mathbb{R}^{3 \times 1}, \quad \underline{N}_{\mathbf{m}} \in \mathbb{R}^{3 \times 3N}, \quad \underline{\mathbf{m}}^e \in \mathbb{R}^{3N \times 1} , \quad (3.115)$$

where $\underline{\mathbf{m}}^e$ denotes the nodal magnetization direction vector. The same shape function $\underline{N}_{\mathbf{m}}$ is used for $\delta \mathbf{m}$ and $d\mathbf{m}$ (or $\delta \underline{\mathbf{m}}$ and $d\underline{\mathbf{m}}$, respectively). The gradient of the magnetization is interpolated according to

$$\widehat{\underline{\nabla \mathbf{m}}} = \underline{B}_{\mathbf{m}} \underline{\mathbf{m}}^e \quad \text{with} \quad \widehat{\underline{\nabla \mathbf{m}}} \in \mathbb{R}^{9 \times 1}, \quad \underline{B}_{\mathbf{m}} \in \mathbb{R}^{9 \times 3N} , \quad (3.116)$$

where $(\widehat{\bullet})$ indicates Voigt notation (here: for the non-symmetric matrix $\underline{\nabla \mathbf{m}}$). For the displacement \mathbf{u} , the interpolant reads

$$\underline{\mathbf{u}} = \underline{N}_{\mathbf{u}} \underline{\mathbf{u}}^e \quad \text{with} \quad \underline{\mathbf{u}} \in \mathbb{R}^{3 \times 1}, \quad \underline{N}_{\mathbf{u}} \in \mathbb{R}^{3 \times 3N}, \quad \underline{\mathbf{u}}^e \in \mathbb{R}^{3N \times 1} . \quad (3.117)$$

We use $\underline{\mathbf{u}}^e$ to denote the nodal displacement vector. For the strain $\boldsymbol{\varepsilon}$ (symmetric matrix) we use Mandel notation $\widehat{\underline{\varepsilon}}$ and interpolate according to

$$\widehat{\underline{\varepsilon}} = \underline{B}_{\varepsilon} \underline{\mathbf{u}}^e \quad \text{with} \quad \widehat{\underline{\varepsilon}} \in \mathbb{R}^{6 \times 1}, \quad \underline{B}_{\varepsilon} \in \mathbb{R}^{6 \times 3N} . \quad (3.118)$$

Note that, while \underline{N}_m and \underline{N}_u are identical, \underline{B}_m and $\underline{B}_\varepsilon$ are distinct. For the interpolation of the magnetic potential φ , we write

$$\varphi = \underline{N}_\varphi \underline{\varphi}^e \quad \text{with} \quad \varphi \in \mathbb{R}, \quad \underline{N}_\varphi \in \mathbb{R}^{1 \times N}, \quad \underline{\varphi}^e \in \mathbb{R}^{N \times 1}. \quad (3.119)$$

Again, $\underline{\varphi}^e$ is the nodal degree of freedom vector of the scalar magnetic potential. The gradient of the magnetic potential is interpolated according to

$$\nabla \varphi = \underline{B}_\varphi \underline{\varphi}^e \quad \text{with} \quad \nabla \varphi \in \mathbb{R}^{3 \times 1}, \quad \underline{B}_\varphi \in \mathbb{R}^{3 \times N}. \quad (3.120)$$

We seek the weak form of the time discrete Eq. (3.63), which in expanded form reads

$$\begin{aligned} \mathbf{0} = & (\mathbf{I} - \mathbf{m} \otimes \mathbf{m}) \left[(\eta^2 + \beta^2) \frac{\mathbf{m} - \mathbf{m}_n}{\Delta t} - c(\beta \boldsymbol{\epsilon} \cdot \mathbf{m} - \eta(\mathbf{I} - \mathbf{m} \otimes \mathbf{m}))(-\operatorname{div}(\boldsymbol{\xi}) + \mathbf{T}) \right. \\ & \left. - (1 - c)(\beta \boldsymbol{\epsilon} \cdot \mathbf{m}_n - \eta(\mathbf{I} - \mathbf{m}_n \otimes \mathbf{m}_n))(-\operatorname{div}(\boldsymbol{\xi}_n) + \mathbf{T}_n) \right]. \end{aligned} \quad (3.121)$$

To this end, we multiply the equation with the test function $\mathbf{v} = \delta\theta_1 \mathbf{a}_1 + \delta\theta_2 \mathbf{a}_2 = \delta\theta \boldsymbol{\omega}_\delta$ (for discussion, see Section 3.5.2) and integrate over the element volume V^e . Note that, upon multiplication with \mathbf{v} , we obtain $(\mathbf{I} - \mathbf{m} \otimes \mathbf{m})\mathbf{v} = \mathbf{v}$ and, hence, the projector does not occur in the following anymore. Note that, in the integral, we use the renormalized version $\bar{\mathbf{m}}$ instead of \mathbf{m} . For the first term in Eq. (3.121), we obtain (with $\mathbf{m} \cdot \delta\theta \boldsymbol{\omega}_\delta = 0$)

$$\int_{V^e} (\eta^2 + \beta^2) \frac{\bar{\mathbf{m}} - \bar{\mathbf{m}}_n}{\Delta t} \cdot \delta\theta \boldsymbol{\omega}_\delta \, dv = \int_{V^e} -\frac{\eta^2 + \beta^2}{\Delta t} \delta\theta \boldsymbol{\omega}_\delta \cdot \bar{\mathbf{m}}_n \, dv \quad (3.122)$$

$$= \int_{V^e} -\frac{\eta^2 + \beta^2}{\Delta t} \sum_{I=1}^N N_I (\delta\theta_{1I} \mathbf{a}_{1I} + \delta\theta_{2I} \mathbf{a}_{2I}) \cdot \bar{\mathbf{m}}_n \, dv \quad (3.123)$$

$$= \sum_{I=1}^N \begin{bmatrix} \delta\theta_{1I} \\ \delta\theta_{2I} \end{bmatrix}^\top \int_{V^e} -\frac{\eta^2 + \beta^2}{\Delta t} \begin{bmatrix} \bar{\mathbf{m}}_n \cdot \mathbf{a}_{1I} N_I \\ \bar{\mathbf{m}}_n \cdot \mathbf{a}_{2I} N_I \end{bmatrix} \, dv \quad (3.124)$$

$$= \sum_{I=1}^N \delta\theta_I^e \int_{V^e} -\frac{\eta^2 + \beta^2}{\Delta t} \begin{bmatrix} \bar{\mathbf{m}}_n \cdot \mathbf{a}_{1I} N_I \\ \bar{\mathbf{m}}_n \cdot \mathbf{a}_{2I} N_I \end{bmatrix} \, dv, \quad (3.125)$$

where we use $\delta\theta_I^e$ to denote the two angle variations in element e associated with node I . For the second term in Eq. (3.121), we find

$$\int_{V^e} \delta\theta \boldsymbol{\omega}_\delta \cdot \left[-c(\beta \boldsymbol{\epsilon} \cdot \bar{\mathbf{m}} - \eta(\mathbf{I} - \bar{\mathbf{m}} \otimes \bar{\mathbf{m}}))(-\operatorname{div}(\boldsymbol{\xi}) + \mathbf{T}) \right] \, dv \quad (3.126)$$

$$= \int_{V^e} c\beta(-\operatorname{div}(\boldsymbol{\xi}) + \mathbf{T}) \cdot \delta\bar{\mathbf{m}} \, dv + \int_{V^e} c\eta \mathbf{T} \cdot \delta\theta \boldsymbol{\omega}_\delta + c\eta \boldsymbol{\xi} : \nabla(\delta\theta \boldsymbol{\omega}_\delta) \, dv \quad (3.127)$$

$$= \int_{V^e} (c\beta \boldsymbol{\xi} : \nabla \delta\bar{\mathbf{m}} + c\beta \mathbf{T} \cdot \delta\bar{\mathbf{m}}) \, dv \quad (3.128)$$

$$+ \sum_{I=1}^N \delta\theta_I^e \int_{V^e} c\eta \begin{bmatrix} \mathbf{T} \cdot \mathbf{a}_{1I} N_I \\ \mathbf{T} \cdot \mathbf{a}_{2I} N_I \end{bmatrix} \, dv \quad (3.129)$$

$$+ \int_{V^e} c\eta \boldsymbol{\xi} : \sum_{I=1}^N (\delta\theta_{1I} \underline{\mathbf{a}}_{1I} + \delta\theta_{2I} \underline{\mathbf{a}}_{2I}) \otimes \nabla N_I \, dv \quad (3.130)$$

$$= \delta \underline{\mathbf{m}}^{e\top} \int_{V^e} \left(\underline{\mathbf{B}}_{\mathbf{m}}^\top c\beta \hat{\underline{\xi}} + \underline{\mathbf{N}}_{\mathbf{m}}^\top \hat{\underline{\mathcal{P}}}_{\bar{\mathbf{m}}} c\beta \underline{\mathbf{T}} \right) dv \quad (3.131)$$

$$+ \sum_{I=1}^N \delta \theta_I^{e\top} \int_{V^e} c\eta \begin{bmatrix} \underline{\mathbf{T}} \cdot \underline{\mathbf{a}}_{1I} N_I \\ \underline{\mathbf{T}} \cdot \underline{\mathbf{a}}_{2I} N_I \end{bmatrix} dv \quad (3.132)$$

$$+ \sum_{I=1}^N \delta \theta_I^{e\top} \int_{V^e} c\eta \begin{bmatrix} \underline{\xi} : \underline{\mathbf{a}}_{1I} \otimes \nabla N_I \\ \underline{\xi} : \underline{\mathbf{a}}_{2I} \otimes \nabla N_I \end{bmatrix} dv . \quad (3.133)$$

Note that $\delta \bar{\mathbf{m}}$ does not occur in the gradient terms. We assume that the renormalization does not have extensive influence on the gradient terms and, thus, can be omitted. As mentioned before, the degree of freedom is not actually \mathbf{m} but $\triangle\theta_1$ and $\triangle\theta_2$. Hence, we intend to replace $\delta \underline{\mathbf{m}}^{e\top}$. At node I , the magnetization variation reads

$$\delta \mathbf{m}_I = \delta\theta_{1I} \boldsymbol{\omega}_{\delta I} \times \mathbf{m}_I = (\delta\theta_{1I} \underline{\mathbf{a}}_{1I} + \delta\theta_{2I} \underline{\mathbf{a}}_{2I}) \times \mathbf{m}_I \quad (3.134)$$

$$= \delta\theta_{2I} \underline{\mathbf{a}}_{1I} - \delta\theta_{1I} \underline{\mathbf{a}}_{2I} . \quad (3.135)$$

For element e with nodes $I = 1, \dots, N$, this yields in matrix notation, see [35],

$$\delta \underline{\mathbf{m}}^e = \begin{bmatrix} -\underline{a}_{21} & \underline{a}_{11} & \underline{0} & \underline{0} & \dots & \underline{0} & \underline{0} \\ \underline{0} & \underline{0} & -\underline{a}_{22} & \underline{a}_{12} & \dots & \underline{0} & \underline{0} \\ \vdots & & & & & & \\ \underline{0} & \underline{0} & \underline{0} & \underline{0} & \dots & -\underline{a}_{2N} & \underline{a}_{1N} \end{bmatrix} \begin{bmatrix} \delta\theta_{11} \\ \delta\theta_{21} \\ \vdots \\ \delta\theta_{1N} \\ \delta\theta_{2N} \end{bmatrix} , \quad (3.136)$$

$$\delta \underline{\mathbf{m}}^e = \underline{\mathbf{G}} \delta \underline{\theta}^e \quad \text{with} \quad \underline{\mathbf{G}} \in \mathbb{R}^{3N \times 2N}, \quad \delta \underline{\theta}^e \in \mathbb{R}^{2N \times 1} , \quad (3.137)$$

where $\underline{a}_{kI} \in \mathbb{R}^3$ ($k = 1, 2; I = 1, \dots, N$) are the matrix equivalents of the orientation vectors \mathbf{a}_{kI} at node I and $\delta \underline{\theta}^e$ is the variation of the element degree of freedom vector of orientation angles.

For the third term in Eq. (3.121), we treat three contributions separately

$$\int_{V^e} \delta\theta \boldsymbol{\omega}_\delta \cdot \left[-(1-c)(\beta \boldsymbol{\epsilon} \cdot \bar{\mathbf{m}}_n - \eta (\mathbf{I} - \bar{\mathbf{m}}_n \otimes \bar{\mathbf{m}}_n)) (-\operatorname{div}(\boldsymbol{\xi}_n) + \mathbf{T}_n) \right] dv \quad (3.138)$$

$$= \int_{V^e} (1-c)\beta \delta\theta \boldsymbol{\omega}_\delta \times \bar{\mathbf{m}}_n \cdot (-\operatorname{div}(\boldsymbol{\xi}_n) + \mathbf{T}_n) dv \quad (3.139)$$

$$+ \int_{V^e} (1-c)\eta (-\operatorname{div}(\boldsymbol{\xi}_n) + \mathbf{T}_n) \cdot \delta\theta \boldsymbol{\omega}_\delta dv \quad (3.140)$$

$$+ \int_{V^e} -(1-c)\eta (\bar{\mathbf{m}}_n \cdot (-\operatorname{div}(\boldsymbol{\xi}_n) + \mathbf{T}_n)) \bar{\mathbf{m}}_n \cdot \delta\theta \boldsymbol{\omega}_\delta dv . \quad (3.141)$$

The first contribution in Eq. (3.139) reads

$$\int_{V^e} (1-c)\beta\delta\theta\omega_\delta \times \bar{\mathbf{m}}_n \cdot (-\operatorname{div}(\boldsymbol{\xi}_n) + \mathbf{T}_n) dv \quad (3.142)$$

$$= \int_{V^e} (1-c)\beta\boldsymbol{\xi}_n : \sum_{I=1}^N (\delta\theta_{1I}\underline{\mathbf{a}}_{1I} + \delta\theta_{2I}\underline{\mathbf{a}}_{2I}) \times \underline{\mathbf{m}}_n \otimes \nabla N_I dv \quad (3.143)$$

$$+ \sum_{I=1}^N \delta\theta_I^e \int_{V^e} (1-c)\beta \left[\frac{\bar{\mathbf{m}}_n \times \underline{\mathbf{T}}_n N_I \cdot \underline{\mathbf{a}}_{1I}}{\bar{\mathbf{m}}_n \times \underline{\mathbf{T}}_n N_I \cdot \underline{\mathbf{a}}_{2I}} \right] dv \quad (3.144)$$

$$= \sum_{I=1}^N \delta\theta_I^e (1-c)\beta \int_{V^e} \left(\left[\frac{\underline{\mathbf{m}}_n \times (\boldsymbol{\xi}_n \nabla N_I) \cdot \underline{\mathbf{a}}_{1I}}{\underline{\mathbf{m}}_n \times (\boldsymbol{\xi}_n \nabla N_I) \cdot \underline{\mathbf{a}}_{2I}} \right] + \left[\frac{\bar{\mathbf{m}}_n \times \underline{\mathbf{T}}_n N_I \cdot \underline{\mathbf{a}}_{1I}}{\bar{\mathbf{m}}_n \times \underline{\mathbf{T}}_n N_I \cdot \underline{\mathbf{a}}_{2I}} \right] \right) dv . \quad (3.145)$$

The second contribution in Eq. (3.140) yields

$$\int_{V^e} (1-c)\eta(-\operatorname{div}(\boldsymbol{\xi}_n) + \mathbf{T}_n) \cdot \delta\theta\omega_\delta dv \quad (3.146)$$

$$= \int_{V^e} (1-c)\eta\boldsymbol{\xi}_n : \nabla(\delta\theta\omega_\delta) dv + \int_{V^e} (1-c)\eta\mathbf{T}_n \cdot \delta\theta\omega_\delta dv \quad (3.147)$$

$$= \sum_{I=1}^N \delta\theta_I^e (1-c)\eta \int_{V^e} \left(\left[\frac{\boldsymbol{\xi}_n : \underline{\mathbf{a}}_{1I} \otimes \nabla N_I}{\boldsymbol{\xi}_n : \underline{\mathbf{a}}_{2I} \otimes \nabla N_I} \right] + \left[\frac{\underline{\mathbf{T}}_n \cdot \underline{\mathbf{a}}_{1I} N_I}{\underline{\mathbf{T}}_n \cdot \underline{\mathbf{a}}_{2I} N_I} \right] \right) dv . \quad (3.148)$$

The third contribution in Eq. (3.141) is treated according to

$$\int_{V^e} -(1-c)\eta(\bar{\mathbf{m}}_n \cdot (-\operatorname{div}(\boldsymbol{\xi}_n) + \mathbf{T}_n))(\bar{\mathbf{m}}_n \cdot \delta\theta\omega_\delta) dv \quad (3.149)$$

$$= \int_{V^e} -(1-c)\eta\boldsymbol{\xi}_n : \nabla(\bar{\mathbf{m}}_n \otimes \bar{\mathbf{m}}_n \delta\theta\omega_\delta) dv + \int_{V^e} -(1-c)\eta(\bar{\mathbf{m}}_n \cdot \mathbf{T}_n)(\bar{\mathbf{m}}_n \cdot \delta\theta\omega_\delta) dv \quad (3.150)$$

$$= \int_{V^e} -(1-c)\eta(\boldsymbol{\xi}_n : \boldsymbol{\xi}_n)(\bar{\mathbf{m}}_n \cdot \delta\theta\omega_\delta) dv \quad (3.151)$$

$$+ \int_{V^e} -(1-c)\eta \frac{1}{2A} (\boldsymbol{\xi}_n \boldsymbol{\xi}_n^T \mathbf{m}_n) \cdot \delta\theta\omega_\delta dv \quad (3.152)$$

$$+ \int_{V^e} -(1-c)\eta\boldsymbol{\xi}_n : \mathbf{m}_n \otimes (\nabla\delta\theta\omega_\delta)^T \mathbf{m}_n dv \quad (3.153)$$

$$+ \int_{V^e} -(1-c)\eta(\bar{\mathbf{m}}_n \cdot \mathbf{T}_n)(\bar{\mathbf{m}}_n \cdot \delta\theta\omega_\delta) dv . \quad (3.154)$$

Similar steps as before yield

$$\int_{V^e} -(1-c)\eta(\bar{\mathbf{m}}_n \cdot (-\operatorname{div}(\boldsymbol{\xi}_n) + \mathbf{T}_n))(\bar{\mathbf{m}}_n \cdot \delta\theta\omega_\delta) dv \quad (3.155)$$

$$= \sum_{I=1}^N \delta\theta_I^e \int_{V^e} -(1-c)\eta \left[\frac{\|\boldsymbol{\xi}_n\|^2 \underline{\mathbf{m}}_n \cdot \underline{\mathbf{a}}_{1I} N_I}{\|\boldsymbol{\xi}_n\|^2 \underline{\mathbf{m}}_n \cdot \underline{\mathbf{a}}_{2I} N_I} \right] dv \quad (3.156)$$

$$+ \sum_{I=1}^N \delta\theta_I^e \int_{V^e} -(1-c)\eta \left[\frac{1}{2A} \left(\boldsymbol{\xi}_n \boldsymbol{\xi}_n^T \underline{\mathbf{m}}_n \right) \cdot \underline{\mathbf{a}}_{1I} N_I \right. \\ \left. + \frac{1}{2A} \left(\boldsymbol{\xi}_n \boldsymbol{\xi}_n^T \underline{\mathbf{m}}_n \right) \cdot \underline{\mathbf{a}}_{2I} N_I \right] dv \quad (3.157)$$

$$+ \sum_{I=1}^N \delta \theta_I^e \int_{V^e} -(1-c)\eta \left[\begin{array}{l} (\underline{\xi}_n : \underline{m}_n \otimes \nabla N_I) \underline{m}_n \cdot \underline{a}_{1I} \\ (\underline{\xi}_n : \underline{m}_n \otimes \nabla N_I) \underline{m}_n \cdot \underline{a}_{2I} \end{array} \right] dv \quad (3.158)$$

$$+ \sum_{I=1}^N \delta \theta_I^e \int_{V^e} -(1-c)\eta \left[\begin{array}{l} (\bar{\underline{m}}_n \cdot \underline{T}_n) N_I \bar{\underline{m}}_n \cdot \underline{a}_{1I} \\ (\bar{\underline{m}}_n \cdot \underline{T}_n) N_I \bar{\underline{m}}_n \cdot \underline{a}_{2I} \end{array} \right] dv . \quad (3.159)$$

Taking all previous contributions into account, we obtain the full weak form, which is summarized in Eq. (3.160) for the convenience of the reader

$$\begin{aligned} G_m^e &= \delta \underline{\theta}^e \underline{G}^T \int_{V^e} \left(\underline{B}_m^T c \beta \hat{\underline{\xi}} + \underline{N}_m^T \hat{\underline{\mathcal{P}}}_m c \beta \underline{T} \right) dv \\ &+ \sum_{I=1}^N \delta \theta_I^e \int_{V^e} \left\{ - \frac{\eta^2 + \beta^2}{\Delta t} \left[\begin{array}{l} \bar{\underline{m}}_n \cdot \underline{a}_{1I} N_I \\ \bar{\underline{m}}_n \cdot \underline{a}_{2I} N_I \end{array} \right] + \eta \left[\begin{array}{l} (c \underline{T} + (1-c) \underline{T}_n) \cdot \underline{a}_{1I} N_I \\ (c \underline{T} + (1-c) \underline{T}_n) \cdot \underline{a}_{2I} N_I \end{array} \right] \right. \\ &\quad + \eta \left[\begin{array}{l} (c \underline{\xi} + (1-c) \underline{\xi}_n) : \underline{a}_{1I} \otimes \nabla N_I \\ (c \underline{\xi} + (1-c) \underline{\xi}_n) : \underline{a}_{2I} \otimes \nabla N_I \end{array} \right] \\ &\quad + (1-c) \beta \left[\begin{array}{l} (\bar{\underline{m}}_n \times \underline{T}_n N_I + \underline{m}_n \times (\underline{\xi}_n \nabla N_I)) \cdot \underline{a}_{1I} \\ (\bar{\underline{m}}_n \times \underline{T}_n N_I + \underline{m}_n \times (\underline{\xi}_n \nabla N_I)) \cdot \underline{a}_{2I} \end{array} \right] \\ &\quad - (1-c) \eta \left[\begin{array}{l} ((\bar{\underline{m}}_n \cdot \underline{T}_n) N_I \bar{\underline{m}}_n + (\underline{\xi}_n : \underline{m}_n \otimes \nabla N_I) \underline{m}_n) \cdot \underline{a}_{1I} \\ ((\bar{\underline{m}}_n \cdot \underline{T}_n) N_I \bar{\underline{m}}_n + (\underline{\xi}_n : \underline{m}_n \otimes \nabla N_I) \underline{m}_n) \cdot \underline{a}_{2I} \end{array} \right] \\ &\quad \left. - (1-c) \eta \left[\begin{array}{l} (\|\underline{\xi}_n\|^2 \underline{m}_n + \frac{1}{2A} \underline{\xi}_n \underline{\xi}_n^T \underline{m}_n) \cdot \underline{a}_{1I} N_I \\ (\|\underline{\xi}_n\|^2 \underline{m}_n + \frac{1}{2A} \underline{\xi}_n \underline{\xi}_n^T \underline{m}_n) \cdot \underline{a}_{2I} N_I \end{array} \right] \right\} dv . \quad (3.160) \end{aligned}$$

Note that in some cases, we do not use Voigt notation $\hat{\underline{\xi}}_{(n)}$ for the second order tensor $\underline{\xi}_{(n)}$ but we keep it as a 3×3 matrix $\underline{\xi}_{(n)}$. This is necessary to evaluate the corresponding tensor operations.

3.D Linearization of the time and space discrete magnetization residual

In this section, we compute the consistent linearization of the residual G_m derived in Appendix 3.C. As illustrated by the following example

$$d(\underline{T} \cdot \delta \bar{\underline{m}}) = d\underline{T} \cdot \delta \bar{\underline{m}} + \underline{T} \cdot d(\delta \bar{\underline{m}}) , \quad (3.161)$$

we first need an expression for $d(\delta \bar{\underline{m}})$. Note that we use $\delta(\bullet)$ for the first variation, $d(\bullet)$ for the differential and $\Delta(\bullet)$ for time-discrete quantities. We obtain the desired expression via

$$d(\delta \bar{\underline{m}}) = d \left(\frac{\delta \underline{m}}{\|\underline{m}\|} - \frac{\underline{m}(\underline{m} \cdot \delta \underline{m})}{\|\underline{m}\|^3} \right) \quad (3.162)$$

$$= \hat{\underline{\mathcal{P}}}_{\bar{\underline{m}}} d(\delta \underline{m}) - \frac{\bar{\underline{m}} \cdot d\underline{m}}{\|\underline{m}\|} \delta \bar{\underline{m}} - \frac{\bar{\underline{m}} \otimes \delta \underline{m}}{\|\underline{m}\|} d\bar{\underline{m}} - \frac{\bar{\underline{m}} \cdot \delta \underline{m}}{\|\underline{m}\|} d\bar{\underline{m}} . \quad (3.163)$$

For the term of interest, $c\beta \mathbf{T} \cdot d(\delta \bar{\mathbf{m}})$, this yields

$$c\beta \mathbf{T} \cdot d(\delta \bar{\mathbf{m}}) = (c\beta \hat{\mathbf{P}}_{\bar{\mathbf{m}}} \mathbf{T}) \cdot d(\delta \mathbf{m}) \quad (3.164)$$

$$\begin{aligned} & + \delta \mathbf{m} \cdot c\beta \left(-\frac{(\hat{\mathbf{P}}_{\bar{\mathbf{m}}} \mathbf{T}) \otimes \bar{\mathbf{m}}}{\|\mathbf{m}\|} - \frac{(\mathbf{T} \cdot \bar{\mathbf{m}})}{\|\mathbf{m}\|} \hat{\mathbf{P}}_{\bar{\mathbf{m}}} - \frac{\bar{\mathbf{m}} \otimes (\hat{\mathbf{P}}_{\bar{\mathbf{m}}} \mathbf{T})}{\|\mathbf{m}\|} \right) d\mathbf{m} \\ & = (c\beta \hat{\mathbf{P}}_{\bar{\mathbf{m}}} \mathbf{T}) \cdot d(\delta \mathbf{m}) + \delta \mathbf{m} \cdot \mathbf{A} d\mathbf{m} , \end{aligned} \quad (3.165)$$

where we introduced the second order tensor \mathbf{A} as short notation. Note that $d(\delta \mathbf{m}) \neq \mathbf{0}$. Usually, we would expect this type of variation to vanish. However, \mathbf{m} is a *dependent* quantity which is given in terms of the *independent* angle increments $\Delta\theta_1$ and $\Delta\theta_2$ (see Eqs. (3.56) to (3.59)), such that $\delta \mathbf{m} = (\delta\theta_1 \mathbf{a}_1 + \delta\theta_2 \mathbf{a}_2) \times \mathbf{m} = \delta\theta_2 \mathbf{a}_1 - \delta\theta_1 \mathbf{a}_2$ (being evaluated at the nodes). In the differential of $\delta \mathbf{m}$, the terms $d(\delta\theta_i) = 0$ vanish while the differentials of \mathbf{a}_i read $d\mathbf{a}_i = (d\theta_1 \mathbf{a}_1 + d\theta_2 \mathbf{a}_2) \times \mathbf{a}_i$ ($i = 1, 2$).

The first contribution for the linearization originates from Eq. (3.122) and reads

$$d\left(\int_{V^e} (\eta^2 + \beta^2) \frac{\bar{\mathbf{m}} - \bar{\mathbf{m}}_n}{\Delta t} \cdot \delta \theta \boldsymbol{\omega}_\delta dv \right) \quad (3.166)$$

$$= \int_{V^e} -\frac{\eta^2 + \beta^2}{\Delta t} \bar{\mathbf{m}}_n \cdot d(\delta \theta \boldsymbol{\omega}_\delta) dv \quad (3.167)$$

$$= \int_{V^e} -\frac{\eta^2 + \beta^2}{\Delta t} \bar{\mathbf{m}}_n \cdot \sum_{I=1}^N (\delta\theta_{1I} d\mathbf{a}_{1I} + \delta\theta_{2I} d\mathbf{a}_{2I}) N_I dv \quad (3.168)$$

$$= \int_{V^e} -\frac{\eta^2 + \beta^2}{\Delta t} \bar{\mathbf{m}}_n \cdot \sum_{I=1}^N (-\delta\theta_{1I} d\theta_{2I} + \delta\theta_{2I} d\theta_{1I}) \underline{\mathbf{m}}_I N_I dv \quad (3.169)$$

$$= \int_{V^e} -\frac{\eta^2 + \beta^2}{\Delta t} \bar{\mathbf{m}}_n \cdot \sum_{I=1}^N -\begin{bmatrix} \delta\theta_{1I} \\ \delta\theta_{2I} \end{bmatrix}^\top \begin{bmatrix} 0 & 1 \\ -1 & 0 \end{bmatrix} \begin{bmatrix} d\theta_{1I} \\ d\theta_{2I} \end{bmatrix} \underline{\mathbf{m}}_I N_I dv \quad (3.170)$$

$$= \sum_{I=1}^N \delta \underline{\theta}_I^e \left[-\underline{\mathbf{m}}_I \cdot \int_{V^e} -\frac{\eta^2 + \beta^2}{\Delta t} \bar{\mathbf{m}}_n N_I dv \right] \underline{\epsilon}_2 d\underline{\theta}_I^e , \quad (3.171)$$

where we use $\underline{\epsilon}_2$ to denote the matrix equivalent of the two-dimensional permutation symbol.

The next part of the linearization originates from Eq. (3.127) (first term) and reads

$$d\left(\int_{V^e} \left\{ c\beta \boldsymbol{\xi} : \nabla \delta \mathbf{m} + c\beta \mathbf{T} \cdot \delta \bar{\mathbf{m}} \right\} dv \right) \quad (3.172)$$

$$= \int_{V^e} \left\{ c\beta d\boldsymbol{\xi} : \nabla \delta \mathbf{m} + c\beta \boldsymbol{\xi} : d(\nabla \delta \mathbf{m}) + c\beta d\mathbf{T} \cdot \delta \bar{\mathbf{m}} + c\beta \mathbf{T} \cdot d(\delta \bar{\mathbf{m}}) \right\} dv \quad (3.173)$$

$$= \int_{V^e} \left\{ \nabla \delta \mathbf{m} : c\beta \frac{\partial \boldsymbol{\xi}}{\partial \nabla \mathbf{m}} : \nabla d\mathbf{m} + c\beta \boldsymbol{\xi} : d(\nabla \delta \mathbf{m}) \right. \quad (3.174)$$

$$\left. + \delta \bar{\mathbf{m}} \cdot \left(c\beta \frac{\partial \mathbf{T}}{\partial \bar{\mathbf{m}}} d\bar{\mathbf{m}} + c\beta \frac{\partial \mathbf{T}}{\partial \boldsymbol{\varepsilon}} : d\boldsymbol{\varepsilon} + c\beta \frac{\partial \mathbf{T}}{\partial \nabla \varphi} d\nabla \varphi \right) + c\beta \mathbf{T} \cdot d(\delta \bar{\mathbf{m}}) \right\} dv . \quad (3.175)$$

For the individual terms in the preceding equation, we find

$$c\beta \frac{\partial \underline{\xi}}{\partial \nabla \underline{\mathbf{m}}} = c\beta 2A\mathbb{I} \quad (3.176)$$

$$\int_{V^e} c\beta \underline{\xi} : d(\nabla \delta \underline{\mathbf{m}}) dv = \int_{V^e} c\beta \underline{\xi} : d \left(\nabla \sum_{I=1}^N (\delta \theta_{2I} \underline{\mathbf{a}}_{1I} - \delta \theta_{1I} \underline{\mathbf{a}}_{2I}) N_I \right) dv \quad (3.177)$$

$$= \int_{V^e} c\beta \underline{\xi} : \sum_{I=1}^N (-\delta \theta_{2I} d\theta_{1I} - \delta \theta_{1I} d\theta_{2I}) \underline{\mathbf{m}}_I \otimes \nabla N_I dv \quad (3.178)$$

$$= \sum_{I=1}^N \delta \theta_I^e \left[-\underline{\mathbf{m}}_I \cdot \int_{V^e} c\beta \underline{\xi} \nabla N_I dv \right] \underline{\mathbf{I}}_2 d\theta_I^e \quad (3.179)$$

$$c\beta \frac{\partial \underline{\mathbf{T}}}{\partial \underline{\bar{\mathbf{m}}}} = c\beta \left[-2K \underline{\mathbf{e}}_a \otimes \underline{\mathbf{e}}_a - 3\lambda_s \left(\underline{\boldsymbol{\sigma}} - \frac{3}{2} \lambda_s (2\underline{\bar{\mathbf{m}}} \cdot \underline{\mathbb{C}} \cdot \underline{\bar{\mathbf{m}}}) \right) \right] \quad (3.180)$$

$$c\beta \frac{\partial \underline{\mathbf{T}}}{\partial \underline{\boldsymbol{\varepsilon}}} = c\beta \frac{\partial^2 \psi_{\text{el}}}{\partial \underline{\boldsymbol{\varepsilon}} \partial \underline{\bar{\mathbf{m}}}} \quad (3.181)$$

$$= c\beta \left(\frac{\partial^2 \psi_{\text{el}}}{\partial \underline{\bar{\mathbf{m}}} \partial \underline{\boldsymbol{\varepsilon}}} \right)^T \quad (3.182)$$

$$= -c\beta \frac{3}{2} \lambda_s (\underline{\mathbb{C}} : (\underline{\bar{\mathbf{m}}} \otimes \underline{\mathbf{e}}_i + \underline{\mathbf{e}}_i \otimes \underline{\bar{\mathbf{m}}}) \otimes \underline{\mathbf{e}}_i)^T \quad (3.183)$$

$$c\beta \frac{\partial \underline{\mathbf{T}}}{\partial \nabla \varphi} = c\beta \mu_0 M_s \underline{\mathbf{I}} \quad (3.184)$$

$$c\beta \underline{\mathbf{T}} \cdot d(\delta \underline{\bar{\mathbf{m}}}) = (c\beta \hat{\underline{\mathcal{P}}}_{\underline{\bar{\mathbf{m}}}} \underline{\mathbf{T}}) \cdot d(\delta \underline{\mathbf{m}}) + \delta \underline{\mathbf{m}} \cdot \underline{\mathbf{A}} d\underline{\mathbf{m}} \quad (3.185)$$

$$\int_{V^e} (c\beta \hat{\underline{\mathcal{P}}}_{\underline{\bar{\mathbf{m}}}} \underline{\mathbf{T}}) \cdot d(\delta \underline{\mathbf{m}}) dv = \int_{V^e} (c\beta \hat{\underline{\mathcal{P}}}_{\underline{\bar{\mathbf{m}}}} \underline{\mathbf{T}}) \cdot d \left(\sum_{I=1}^N (\delta \theta_{2I} \underline{\mathbf{a}}_{1I} - \delta \theta_{1I} \underline{\mathbf{a}}_{2I}) N_I \right) dv \quad (3.186)$$

$$= \int_{V^e} (c\beta \hat{\underline{\mathcal{P}}}_{\underline{\bar{\mathbf{m}}}} \underline{\mathbf{T}}) \cdot \sum_{I=1}^N (-\delta \theta_{2I} d\theta_{1I} - \delta \theta_{1I} d\theta_{2I}) \underline{\mathbf{m}}_I N_I dv \quad (3.187)$$

$$= \sum_{I=1}^N \delta \theta_I^e \left[-\underline{\mathbf{m}}_I \cdot \int_{V^e} (c\beta \hat{\underline{\mathcal{P}}}_{\underline{\bar{\mathbf{m}}}} \underline{\mathbf{T}}) N_I dv \right] \underline{\mathbf{I}}_2 d\theta_I^e, \quad (3.188)$$

where \mathbb{I} denotes the fourth order identity tensor. In total, we obtain for the linearization in Eq. (3.172)

$$\begin{aligned} & d \left(\int_{V^e} \left\{ c\beta \underline{\xi} : \nabla \delta \underline{\mathbf{m}} + c\beta \underline{\mathbf{T}} \cdot \delta \underline{\mathbf{m}} \right\} dv \right) \\ &= \delta \theta^e \underline{\mathbf{G}}^T \int_{V^e} \left[\underline{\mathbf{B}}_{\underline{\mathbf{m}}}^T c\beta \frac{\partial \hat{\underline{\xi}}}{\partial \nabla \underline{\mathbf{m}}} \underline{\mathbf{B}}_{\underline{\mathbf{m}}} + \underline{\mathbf{N}}_{\underline{\mathbf{m}}}^T \left(\hat{\underline{\mathcal{P}}}_{\underline{\bar{\mathbf{m}}}} c\beta \frac{\partial \underline{\mathbf{T}}}{\partial \underline{\bar{\mathbf{m}}}} \hat{\underline{\mathcal{P}}}_{\underline{\bar{\mathbf{m}}}} + \underline{\mathbf{A}} \right) \underline{\mathbf{N}}_{\underline{\mathbf{m}}} \right] dv \underline{\mathbf{G}} d\theta^e \\ &+ \delta \theta^e \underline{\mathbf{G}}^T \int_{V^e} \underline{\mathbf{N}}_{\underline{\mathbf{m}}}^T \hat{\underline{\mathcal{P}}}_{\underline{\bar{\mathbf{m}}}} c\beta \frac{\partial \underline{\mathbf{T}}}{\partial \underline{\boldsymbol{\varepsilon}}} \underline{\mathbf{B}}_{\underline{\boldsymbol{\varepsilon}}} dv d\underline{\boldsymbol{\varepsilon}}^e + \delta \theta^e \underline{\mathbf{G}}^T \int_{V^e} \underline{\mathbf{N}}_{\underline{\mathbf{m}}}^T \hat{\underline{\mathcal{P}}}_{\underline{\bar{\mathbf{m}}}} c\beta \frac{\partial \underline{\mathbf{T}}}{\partial \nabla \varphi} \underline{\mathbf{B}} dv d\varphi^e \\ &+ \sum_{I=1}^N \delta \theta_I^e \left[-\underline{\mathbf{m}}_I \cdot \int_{V^e} c\beta (\hat{\underline{\mathcal{P}}}_{\underline{\bar{\mathbf{m}}}} \underline{\mathbf{T}} N_I + \underline{\xi} \nabla N_I) dv \right] \underline{\mathbf{I}}_2 d\theta_I^e. \end{aligned} \quad (3.189)$$

The linearization for the second term in Eq. (3.127) is treated as follows

$$d\left(\int_{V^e} c\eta \underline{\xi} : \nabla(\delta\theta\omega_\delta) + c\eta \underline{T} \cdot \delta\theta\omega_\delta dv\right) \quad (3.190)$$

$$= \int_{V^e} c\eta d\underline{\xi} : \nabla(\delta\theta\omega_\delta) + c\eta \underline{\xi} : d(\nabla(\delta\theta\omega_\delta)) + c\eta d\underline{T} \cdot \delta\theta\omega_\delta + c\eta \underline{T} \cdot d(\delta\theta\omega_\delta) dv \quad (3.191)$$

$$= \int_{V^e} c\eta \nabla(\delta\theta\omega_\delta) : \frac{\partial \underline{\xi}}{\partial \nabla \underline{m}} : \nabla d\underline{m} + c\eta \underline{\xi} : d(\nabla(\delta\theta\omega_\delta)) \quad (3.192)$$

$$+ \delta\theta\omega_\delta \cdot c\eta \left(\frac{\partial \underline{T}}{\partial \underline{m}} d\underline{m} + \frac{\partial \underline{T}}{\partial \underline{\varepsilon}} : d\underline{\varepsilon} + \frac{\partial \underline{T}}{\partial \nabla \varphi} d\nabla \varphi \right) + c\eta \underline{T} \cdot d(\delta\theta\omega_\delta) dv . \quad (3.193)$$

The different contributions in the equation above read

$$\int_{V^e} c\eta \nabla(\delta\theta\omega_\delta) : \frac{\partial \underline{\xi}}{\partial \nabla \underline{m}} : \nabla d\underline{m} dv = \int_{V^e} \sum_{I=1}^N (\delta\theta_{1I} \underline{a}_{1I} + \delta\theta_{2I} \underline{a}_{2I}) \otimes \nabla N_I : c\eta \frac{\partial \underline{\xi}}{\partial \nabla \underline{m}} : \nabla d\underline{m} dv \quad (3.194)$$

$$= \sum_{I=1}^N \delta\theta_I^e \int_{V^e} \begin{bmatrix} (\underline{a}_{1I} \widehat{\otimes} \nabla N_I)^\top \\ (\underline{a}_{2I} \widehat{\otimes} \nabla N_I)^\top \end{bmatrix} c\eta \frac{\partial \underline{\xi}}{\partial \nabla \underline{m}} \underline{B}_m dv \underline{G} d\theta^e , \quad (3.195)$$

$$\int_{V^e} c\eta \underline{\xi} : d(\nabla(\delta\theta\omega_\delta)) dv = \int_{V^e} c\eta \underline{\xi} : \sum_{I=1}^N (\delta\theta_{1I} d\underline{a}_{1I} + \delta\theta_{2I} d\underline{a}_{2I}) \otimes \nabla N_I dv \quad (3.196)$$

$$= \sum_{I=1}^N \int_{V^e} c\eta \underline{\xi} : \underline{m}_I \otimes \nabla N_I dv (-\delta\theta_{1I} d\theta_{2I} + \delta\theta_{2I} d\theta_{1I}) \quad (3.197)$$

$$= \sum_{I=1}^N \delta\theta_I^e \int_{V^e} \left[-\underline{m}_I \cdot \int_{V^e} c\eta \underline{\xi} \nabla N_I dv \right] \underline{\varepsilon}_2 d\theta_I^e , \quad (3.198)$$

$$\int_{V^e} \delta\theta\omega_\delta \cdot c\eta \frac{\partial \underline{T}}{\partial \underline{m}} d\underline{m} dv = \sum_{I=1}^N \delta\theta_I^e \int_{V^e} \begin{bmatrix} \underline{a}_{1I}^\top N_I \\ \underline{a}_{2I}^\top N_I \end{bmatrix} c\eta \frac{\partial \underline{T}}{\partial \underline{m}} \widehat{\underline{\mathcal{P}}}_{\underline{m}} \underline{N}_m dv \underline{G} d\theta^e , \quad (3.199)$$

$$\int_{V^e} \delta\theta\omega_\delta \cdot c\eta \frac{\partial \underline{T}}{\partial \underline{\varepsilon}} : d\underline{\varepsilon} dv = \sum_{I=1}^N \delta\theta_I^e \int_{V^e} \begin{bmatrix} \underline{a}_{1I}^\top N_I \\ \underline{a}_{2I}^\top N_I \end{bmatrix} c\eta \frac{\partial \underline{T}}{\partial \underline{\varepsilon}} \underline{B}_\varepsilon dv d\underline{u}^e , \quad (3.200)$$

$$\int_{V^e} \delta\theta\omega_\delta \cdot c\eta \frac{\partial \underline{T}}{\partial \nabla \varphi} d\nabla \varphi dv = \sum_{I=1}^N \delta\theta_I^e \int_{V^e} \begin{bmatrix} \underline{a}_{1I}^\top N_I \\ \underline{a}_{2I}^\top N_I \end{bmatrix} c\eta \frac{\partial \underline{T}}{\partial \nabla \varphi} \underline{B} dv d\underline{\varphi}^e , \quad (3.201)$$

$$\int_{V^e} c\eta \underline{T} \cdot d(\delta\theta\omega_\delta) dv = \sum_{I=1}^N \delta\theta_I^e \int_{V^e} \left[-\underline{m}_I \cdot \int_{V^e} c\eta \underline{T} N_I dv \right] \underline{\varepsilon}_2 d\theta_I^e . \quad (3.202)$$

Note that we use the same ordering for the Voigt notations $\underline{a}_{kI} \widehat{\otimes} \nabla N_I$ and $\widehat{\underline{\xi}}$ (here: row-wise). In conclusion, the linearization in Eq. (3.190) reads

$$d\left(\int_{V^e} c\eta \underline{\xi} : \nabla(\delta\theta\omega_\delta) + c\eta \underline{T} \cdot \delta\theta\omega_\delta dv\right) \quad (3.203)$$

$$= \sum_{I=1}^N \delta \underline{\theta}_I^e \int_{V^e} \left(\left[\begin{array}{c} (\underline{a}_{1I} \otimes \nabla N_I)^\top \\ (\underline{a}_{2I} \otimes \nabla N_I)^\top \end{array} \right] c\eta \frac{\partial \hat{\underline{\xi}}}{\partial \nabla \underline{m}} \underline{B}_m + \left[\begin{array}{c} \underline{a}_{1I}^\top N_I \\ \underline{a}_{2I}^\top N_I \end{array} \right] c\eta \frac{\partial \underline{T}}{\partial \nabla \underline{m}} \hat{\underline{\mathcal{P}}}_{\underline{m} N_m} \right) dv \underline{G} d\theta^e \quad (3.204)$$

$$+ \sum_{I=1}^N \delta \underline{\theta}_I^e \int_{V^e} \left[-\underline{m}_I \cdot \int_{V^e} c\eta (\underline{\xi} \nabla N_I + \underline{T} N_I) dv \right] \epsilon_2 d\theta_I^e \quad (3.205)$$

$$+ \sum_{I=1}^N \delta \underline{\theta}_I^e \int_{V^e} \left[\begin{array}{c} \underline{a}_{1I}^\top N_I \\ \underline{a}_{2I}^\top N_I \end{array} \right] c\eta \frac{\partial \underline{T}}{\partial \underline{\epsilon}} \underline{B}_\epsilon dv d\theta^e \quad (3.206)$$

$$+ \sum_{I=1}^N \delta \underline{\theta}_I^e \int_{V^e} \left[\begin{array}{c} \underline{a}_{1I}^\top N_I \\ \underline{a}_{2I}^\top N_I \end{array} \right] c\eta \frac{\partial \underline{T}}{\partial \nabla \varphi} \underline{B} dv d\varphi^e. \quad (3.207)$$

The last three parts of the linearization originate from Eq. (3.138). As before, we treat the three terms separately. The linearization of Eq. (3.139) yields

$$d \left(\int_{V^e} (1-c) \beta \delta \theta \omega_\delta \times \bar{\underline{m}}_n \cdot (-\operatorname{div}(\underline{\xi}_n) + \underline{T}_n) dv \right) \quad (3.208)$$

$$= \sum_{I=1}^N \delta \underline{\theta}_I^e \int_{V^e} (1-c) \beta \left(\left[\begin{array}{c} \underline{m}_n \times (\underline{\xi}_n \nabla N_I) \cdot d\underline{a}_{1I} \\ \underline{m}_n \times (\underline{\xi}_n \nabla N_I) \cdot d\underline{a}_{2I} \end{array} \right] + \left[\begin{array}{c} \bar{\underline{m}}_n \times \underline{T}_n N_I \cdot d\underline{a}_{1I} \\ \bar{\underline{m}}_n \times \underline{T}_n N_I \cdot d\underline{a}_{2I} \end{array} \right] \right) dv \quad (3.209)$$

$$= \sum_{I=1}^N \delta \underline{\theta}_I^e \int_{V^e} (1-c) \beta \left[\begin{array}{c} (\underline{m}_n \times (\underline{\xi}_n \nabla N_I) + \bar{\underline{m}}_n \times \underline{T}_n N_I) \cdot (-d\theta_{2I} \underline{m}_I) \\ (\underline{m}_n \times (\underline{\xi}_n \nabla N_I) + \bar{\underline{m}}_n \times \underline{T}_n N_I) \cdot d\theta_{1I} \underline{m}_I \end{array} \right] dv \quad (3.210)$$

$$= \sum_{I=1}^N \delta \underline{\theta}_I^e \int_{V^e} \left[-\underline{m}_I \cdot \int_{V^e} (1-c) \beta (\underline{m}_n \times (\underline{\xi}_n \nabla N_I) + \bar{\underline{m}}_n \times \underline{T}_n N_I) dv \right] \epsilon_2 d\theta_I^e. \quad (3.211)$$

The linearization of Eq. (3.140) yields

$$d \left(\int_{V^e} (1-c) \eta (-\operatorname{div}(\underline{\xi}_n) + \underline{T}_n) \cdot \delta \theta \omega_\delta dv \right) \quad (3.212)$$

$$= \sum_{I=1}^N \delta \underline{\theta}_I^e \int_{V^e} (1-c) \eta \left(\left[\begin{array}{c} (\underline{\xi}_n \nabla N_I) \cdot d\underline{a}_{1I} \\ (\underline{\xi}_n \nabla N_I) \cdot d\underline{a}_{2I} \end{array} \right] + \left[\begin{array}{c} \underline{T}_n N_I \cdot d\underline{a}_{1I} \\ \underline{T}_n N_I \cdot d\underline{a}_{2I} \end{array} \right] \right) dv \quad (3.213)$$

$$= \sum_{I=1}^N \delta \underline{\theta}_I^e \int_{V^e} \left[-\underline{m}_I \cdot \int_{V^e} (1-c) \eta (\underline{\xi}_n \nabla N_I + \underline{T}_n N_I) dv \right] \epsilon_2 d\theta_I^e. \quad (3.214)$$

We obtain the following for the linearization of Eq. (3.141)

$$d \left(\int_{V^e} -(1-c) \eta (\bar{\underline{m}}_n \cdot (-\operatorname{div}(\underline{\xi}_n) + \underline{T}_n)) (\bar{\underline{m}}_n \cdot \delta \theta \omega_\delta) dv \right) \quad (3.215)$$

$$= \sum_{I=1}^N \delta \underline{\theta}_I^e \int_{V^e} -(1-c) \eta \left[\left(\left\| \underline{\xi}_n \right\|^2 \underline{m}_n + \frac{1}{2A} \left(\underline{\xi}_n \underline{\xi}_n^\top \underline{m}_n \right) + (\bar{\underline{m}}_n \cdot \underline{T}_n) \bar{\underline{m}}_n \right) N_I \cdot d\underline{a}_{1I} \right. \\ \left. \left(\left\| \underline{\xi}_n \right\|^2 \underline{m}_n + \frac{1}{2A} \left(\underline{\xi}_n \underline{\xi}_n^\top \underline{m}_n \right) + (\bar{\underline{m}}_n \cdot \underline{T}_n) \bar{\underline{m}}_n \right) N_I \cdot d\underline{a}_{2I} \right] dv \quad (3.216)$$

$$+ \sum_{I=1}^N \delta \theta_I^e \int_{V^e} -(1-c)\eta \left[\frac{(\xi_n : \underline{m}_n \otimes \nabla N_I) \underline{m}_n \cdot d\underline{a}_{1I}}{(\xi_n : \underline{m}_n \otimes \nabla N_I) \underline{m}_n \cdot d\underline{a}_{2I}} \right] dv \quad (3.217)$$

$$= \sum_{I=1}^N \delta \theta_I^e \int_{V^e} \left[-\underline{m}_I \cdot \int_{V^e} -(1-c)\eta \left\{ (\xi_n : \underline{m}_n \otimes \nabla N_I) \underline{m}_n \right. \right. \quad (3.218)$$

$$\left. + \left(\|\xi_n\|^2 \underline{m}_n + \frac{1}{2A} (\xi_n \xi_n^T \underline{m}_n) + (\bar{\underline{m}}_n \cdot \underline{T}_n) \bar{\underline{m}}_n \right) N_I \right\} dv \right] \epsilon_2 d\theta_I^e . \quad (3.219)$$

In conclusion, the linearization of the residual G_m^e reads

$$\begin{aligned} dG_m^e &= \delta \theta^e \underline{G}^T \int_{V^e} \left[\underline{B}_m^T c \beta \frac{\partial \hat{\xi}}{\partial \nabla \underline{m}} \underline{B}_m + \underline{N}_m^T \left(\hat{\underline{\mathcal{P}}}_{\bar{m}} c \beta \frac{\partial \underline{T}}{\partial \underline{m}} \hat{\underline{\mathcal{P}}}_{\bar{m}} + \underline{A} \right) \underline{N}_m \right] dv \underline{G} d\theta^e \\ &+ \delta \theta^e \underline{G}^T \int_{V^e} \underline{N}_m^T \hat{\underline{\mathcal{P}}}_{\bar{m}} c \beta \frac{\partial \underline{T}}{\partial \underline{\varepsilon}} \underline{B}_\varepsilon dv d\underline{u}^e \\ &+ \delta \theta^e \underline{G}^T \int_{V^e} \underline{N}_m^T \hat{\underline{\mathcal{P}}}_{\bar{m}} c \beta \frac{\partial \underline{T}}{\partial \nabla \varphi} \underline{B} dv d\varphi^e \\ &+ \sum_{I=1}^N \delta \theta_I^e \int_{V^e} \left(\left[\frac{(\underline{a}_{1I} \otimes \nabla N_I)^T}{(\underline{a}_{2I} \otimes \nabla N_I)^T} \right] c \eta \frac{\partial \hat{\xi}}{\partial \nabla \underline{m}} \underline{B}_m + \left[\frac{\underline{a}_{1I}^T N_I}{\underline{a}_{2I}^T N_I} \right] c \eta \frac{\partial \underline{T}}{\partial \underline{m}} \hat{\underline{\mathcal{P}}}_{\bar{m}} \underline{N}_m \right) dv \underline{G} d\theta^e \\ &+ \sum_{I=1}^N \delta \theta_I^e \int_{V^e} \left[\frac{\underline{a}_{1I}^T N_I}{\underline{a}_{2I}^T N_I} \right] c \eta \frac{\partial \underline{T}}{\partial \underline{\varepsilon}} \underline{B}_\varepsilon dv d\underline{u}^e \\ &+ \sum_{I=1}^N \delta \theta_I^e \int_{V^e} \left[\frac{\underline{a}_{1I}^T N_I}{\underline{a}_{2I}^T N_I} \right] c \eta \frac{\partial \underline{T}}{\partial \nabla \varphi} \underline{B} dv d\varphi^e \\ &+ \sum_{I=1}^N \delta \theta_I^e \int_{V^e} \left[-\underline{m}_I \cdot \int_{V^e} \left\{ -\frac{\eta^2 + \beta^2}{\Delta t} \bar{\underline{m}}_n N_I \right. \right. \\ &\quad + \eta \left((c \underline{\xi} + (1-c) \underline{\xi}_n) \nabla N_I + (c \underline{T} + (1-c) \underline{T}_n) N_I \right) \\ &\quad + (1-c) \beta \left(\underline{m}_n \times (\underline{\xi}_n \nabla N_I) + \bar{\underline{m}}_n \times \underline{T}_n N_I \right) \\ &\quad - (1-c) \eta \left(\|\underline{\xi}_n\|^2 \underline{m}_n + \frac{1}{2A} (\xi_n \xi_n^T \underline{m}_n) + (\bar{\underline{m}}_n \cdot \underline{T}_n) \bar{\underline{m}}_n \right) N_I \\ &\quad \left. \left. - (1-c) \eta (\xi_n : \underline{m}_n \otimes \nabla N_I) \underline{m}_n \right\} dv \right] \epsilon_2 d\theta_I^e \\ &+ \sum_{I=1}^N \delta \theta_I^e \int_{V^e} \left[-\underline{m}_I \cdot \int_{V^e} c \beta (\hat{\underline{\mathcal{P}}}_{\bar{m}} \underline{T} N_I + \underline{\xi} \nabla N_I) dv \right] \underline{I}_2 d\theta_I^e . \quad (3.220) \end{aligned}$$

3.E Fourier transform

As mentioned before, we use NumPy 1.23.5 [135] to compute the Fourier transform. We denote by $\hat{\mathbf{a}}$ the Fourier transform of the computer array \mathbf{a}

$$\hat{\mathbf{a}} = \mathcal{FFT}(\mathbf{a}) \quad (3.221)$$


which is computed according to

$$\hat{\mathbf{a}}[k] = \sum_{m=0}^{n-1} \mathbf{a}[m] \exp\left(-2\pi i \frac{mk}{n}\right), \quad k = 0, \dots, n-1. \quad (3.222)$$

CHAPTER 4

Manuscript 3: Stability analysis of the coupled micro–magneto–mechanical problem involving undulating magnetization states in thin films

This work was prepared for publication:

Dorn, C. , Hörsting, M. , Schmalz, J. , McCord, J.  and Wulfinghoff, S.  'Stability analysis of the coupled micro–magneto–mechanical problem involving undulating magnetization states in thin films'.

Own contributions to the following article:

- Conceptualization (small contribution)
- Planning (large contribution)
- Methodology (large contribution)
- Investigation (large contribution)
- Interpretation of results (large contribution)
- Manuscript writing (large contribution)

Abstract

We present a stability theory which allows to assess the emergence of an undulating domain (sub-)structure. Other authors experimentally observe this domain structure in regions of small or vanishing anisotropy of magnetostrictive thin films. The structure is characterized by spatially oscillating magnetization with wavelengths in the micrometer range. To derive the related stability criterion, we set up a model system with simplified kinematics consisting of substrate and thin film. We obtain the coupled micro-magneto-mechanical equations by optimizing the related potential. Governing equations include a linearized form of the Landau-Lifshitz-Gilbert equation and the balance of linear momentum. We propose a solution ansatz for the system of equations and perform a stability analysis which yields the aforementioned criterion. To illustrate our findings, we conduct parameter studies including stability maps for realistic sets of model parameters. We find good agreement with experimental results.

Keywords: Micro-magneto-mechanics, Domain theory, Magnetic thin film, Stability analysis, Landau-Lifshitz-Gilbert equation

4.1 Introduction

In the present work, we consider a pronounced type of domain (sub-)structure. Magneto-optic Kerr effect (MOKE) microscopy experiments by Urs et al. [138] showcase the characteristic, spatially modulated magnetization orientation, which we refer to as *undulations*, see Fig. 4.1. Undulations are a micro-magneto-mechanical domain phenomenon specific to magnetostrictive thin films on elastic substrates. Two important factors for the emergence of undulations are, firstly, magneto-mechanical coupling (non-vanishing magnetostriction) and, secondly, presence of areas with small or vanishing magnetic anisotropy (e.g., at film edges, see [152, 138]). The importance of elastic energies for domain wall phenomena was previously discussed in [122, 153].

However, while qualitative influence factors for undulations are known, we still strive for a deep understanding of the underlying mechanisms as well as a quantitative treatment. Furthermore, the influence of undulations on the performance of magnetoelectric sensor devices (e.g., [128, 154]) is not fully understood. We are interested in modeling the aforementioned undulations since we anticipate new insights into smarter sensor design and the micromagnetic effects occurring inside the thin magnetic films.

In the past, many different methods for solving micromagnetic problems have been applied. These include, on the one hand, numerous analytical approaches, which can solve small boundary value problems or problems with simplified assumptions, e.g., [122, 155, 156]. On the other hand, there are many numerical approaches making use of finite difference schemes [41, 157, 158, 159, 160] and finite element schemes [56, 35, 119]. While the finite difference

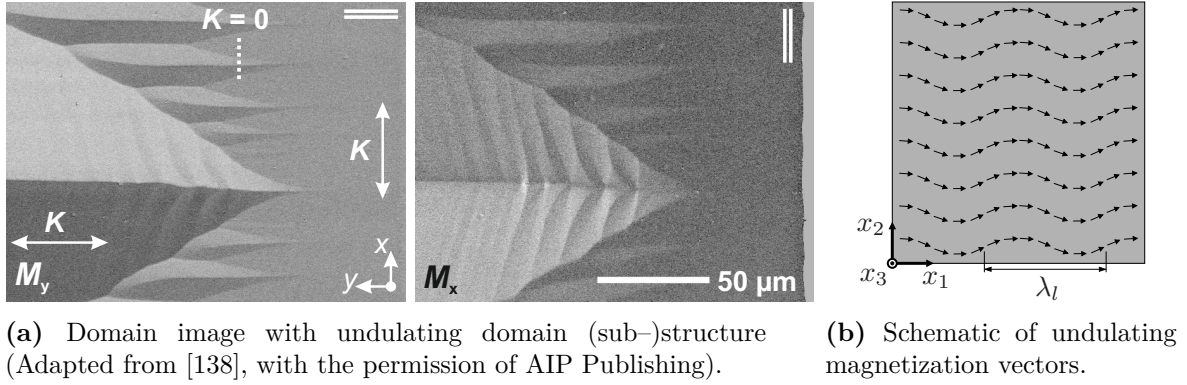


Fig. 4.1: Illustration of undulations

schemes can solve the magnetic field equations fast, they are less capable of solving problems with complicated geometries or solids moving in space.

The stability analysis for magneto-elastic thin films, which we present in this work, belongs to the first category of analytical approaches. As in the case of many analytical approaches, we focus on one specific boundary value problem (here: thin film on substrate). For this particular problem, we are able to assess which combinations of substrate parameters, thin film parameters and geometrical parameters result in undulations.

4.2 Kinematics

We consider a domain $\Omega = V^s \cup V^{\text{fm}}$ consisting of substrate (s) and thin film (fm) (see Fig. 4.2), where V^s is infinitely extended in negative x_3 -direction. The displacement field $\mathbf{u} : \Omega \times [0, T] \rightarrow \mathbb{R}^3$ associates with every point $\mathbf{x} \in \Omega \subset \mathbb{R}^3$ at every time $t \in [0, T] \subset \mathbb{R}$ a displacement vector $\mathbf{u} \in \mathbb{R}^3$. We adopt small strain theory in the following. The gradient of

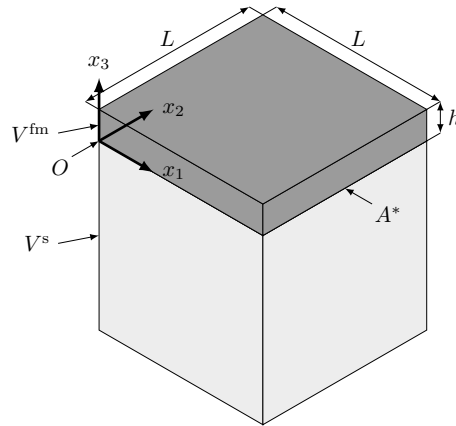


Fig. 4.2: Thin film V^{fm} on substrate V^s , interface area A^* at $x_3 = 0$.

the displacement field and its symmetric part (strain) read

$$\mathbf{h} = \text{grad}(\mathbf{u}) = \frac{\partial u_i}{\partial x_j} \mathbf{e}_i \otimes \mathbf{e}_j \quad \text{and} \quad \boldsymbol{\varepsilon} = \text{sym}(\mathbf{h}) = \frac{1}{2} (\mathbf{h} + \mathbf{h}^\top) . \quad (4.1)$$

Further, we assume an additive split of strain

$$\boldsymbol{\varepsilon} = \boldsymbol{\varepsilon}^e + \boldsymbol{\varepsilon}^m + \boldsymbol{\varepsilon}^* \quad (4.2)$$

into an elastic part $\boldsymbol{\varepsilon}^e$, a magnetostrictive part $\boldsymbol{\varepsilon}^m$ and an eigenstrain contribution $\boldsymbol{\varepsilon}^*$. The eigenstrains $\boldsymbol{\varepsilon}^*$ originate from the production process and, for simplicity, we assume the following form

$$\boldsymbol{\varepsilon}^* = \sum_{i=1}^3 \varepsilon_i^* \mathbf{e}_i \otimes \mathbf{e}_i. \quad (4.3)$$

In accordance with other authors [122, 35], we adopt the following expression

$$\boldsymbol{\varepsilon}^m = \frac{3}{2} \Lambda_s \left(\mathbf{m} \otimes \mathbf{m} - \frac{1}{3} \mathbf{I} \right) \quad (4.4)$$

for the magnetostrictive strain, where Λ_s is the saturation magnetostriction, \mathbf{I} is the second order identity tensor and $\mathbf{m} : V^{\text{fm}} \times [0, T] \rightarrow \mathcal{S}^2$ denotes the local magnetization director. The latter describes the magnetization direction $\mathbf{m} \in \mathcal{S}^2$ on the unit sphere \mathcal{S}^2 at every point $\mathbf{x} \in V^{\text{fm}}$ and every time $t \in [0, T]$. The magnetization of the material reads $M_s \mathbf{m}$, where M_s is the spontaneous magnetization and $\|\mathbf{m}\| = 1$, see, e.g., [35] for a detailed discussion. Inspired by experimental observations on sufficiently small films and for simplicity, we assume

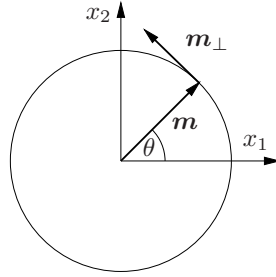


Fig. 4.3: Magnetization director $\mathbf{m}(\mathbf{x}, t)$ on unit sphere \mathcal{S}^1 and orthogonal vector $\mathbf{m}_\perp(\mathbf{x}, t)$ in tangent space $T_m \mathcal{S}^1$ in \mathbb{R}^2 , cf. [24, 35].

the magnetization director \mathbf{m} to be restricted to the x_1 - x_2 -plane which yields the form

$$\mathbf{m}(\mathbf{x}, t) = \cos(\theta(\mathbf{x}, t)) \mathbf{e}_1 + \sin(\theta(\mathbf{x}, t)) \mathbf{e}_2 , \quad (4.5)$$

where $\theta : V^{\text{fm}} \times [0, T] \rightarrow [-\pi, \pi)$ denotes the angle between the magnetization direction \mathbf{m} and \mathbf{e}_1 , see Fig. 4.3. Note that for all solution fields ξ (displacement \mathbf{u} and magnetization \mathbf{m}

or angle θ), we assume periodic boundary conditions in x_1 - and x_2 -direction, i.e.,

$$\xi(x_i) = \xi(x_i + L), \quad i = 1, 2. \quad (4.6)$$

The non-periodic case can in principle be recovered with $L \rightarrow \infty$. In the following sections, it is useful to accompany the magnetization director \mathbf{m} with the orthogonal direction

$$\mathbf{m}_\perp(\mathbf{x}, t) = \frac{\partial \mathbf{m}}{\partial \theta} = -\sin(\theta(\mathbf{x}, t))\mathbf{e}_1 + \cos(\theta(\mathbf{x}, t))\mathbf{e}_2. \quad (4.7)$$

4.3 Potential formulation and stationarity conditions

4.3.1 Magnetic equilibrium

We model the material behavior via the potential Ψ which reads

$$\Psi = \int_{\Omega} \left(\psi_{\text{ex}}(\nabla \mathbf{m}) + \psi_{\text{a}}(\mathbf{m}) + \psi_{\text{e}}(\boldsymbol{\varepsilon}^{\text{e}}) + \psi_{\text{z}}(\mathbf{m}) + \psi_{\text{d}}(\mathbf{m}, \nabla \varphi) \right) dv, \quad (4.8)$$

where ψ_{ex} is the exchange energy, ψ_{a} denotes the anisotropy energy, ψ_{e} reflects the elastic energy, $\psi_{\text{z}}(\mathbf{m})$ is the Zeeman energy and ψ_{d} represents the energy associated with the demagnetizing field. Here, φ denotes the magnetic potential which is used to compute the demagnetizing field $\mathbf{H}_{\text{d}} = -\nabla \varphi$. The exchange energy ψ_{ex} reads

$$\psi_{\text{ex}} = A \nabla \mathbf{m} : \nabla \mathbf{m} = A(\mathbf{m}_\perp \otimes \nabla \theta) : (\mathbf{m}_\perp \otimes \nabla \theta) = A \nabla \theta \cdot \nabla \theta, \quad (4.9)$$

see, e.g., [28] and reflects the propensity of neighboring magnetic moments to align with each other. A is the exchange stiffness constant. For the anisotropy energy ψ_{a} , we adopt the form

$$\psi_{\text{a}} = K \left(1 - (\mathbf{m} \cdot \mathbf{e}_{\text{a}})^2 \right), \quad (4.10)$$

where K is the uniaxial anisotropy constant. This energy contribution models the behavior of magnetic moments to preferentially align with a direction \mathbf{e}_{a} called *easy axis*. In the following, we assume the easy axis to be \mathbf{e}_1 which entails for the anisotropy energy

$$\psi_{\text{a}} = K \sin^2(\theta), \quad (4.11)$$

see, e.g., [122]. To obtain linear elastic material behavior, we prescribe the elastic energy contribution ψ_{e} as

$$\psi_{\text{e}} = \frac{\lambda}{2} \text{tr}^2(\boldsymbol{\varepsilon}^{\text{e}}) + \mu \boldsymbol{\varepsilon}^{\text{e}} : \boldsymbol{\varepsilon}^{\text{e}}, \quad (4.12)$$

see, e.g., [161], where

$$\lambda = \begin{cases} \lambda^{\text{fm}} & \text{in } V^{\text{fm}} \\ \lambda^{\text{s}} & \text{in } V^{\text{s}} \end{cases} \quad \text{and} \quad \mu = \begin{cases} \mu^{\text{fm}} & \text{in } V^{\text{fm}} \\ \mu^{\text{s}} & \text{in } V^{\text{s}} \end{cases} \quad (4.13)$$

are the Lamé parameters. μ is also referred to as *shear modulus*. Note that, while Λ_s denotes the saturation magnetostriction, we use λ^s to denote the first Lamé parameter of the substrate. The Zeeman energy reads

$$\psi_z(\mathbf{m}) = -\mu_0 M_s \mathbf{m} \cdot \mathbf{H}' , \quad (4.14)$$

see, e.g., [122], where \mathbf{H}' is the externally applied magnetic field. We assume the applied field \mathbf{H}' to be constant and parallel to the easy axis \mathbf{e}_a . Hence, we obtain

$$\mathbf{H}' = H' \mathbf{e}_1 , \quad \text{where} \quad H' = \text{const} . \quad (4.15)$$

For the demagnetizing field, we write

$$\psi_d = \mu_0 M_s \mathbf{m} \cdot \nabla \varphi - \frac{\mu_0}{2} \|\nabla \varphi\|^2 , \quad (4.16)$$

see, e.g., [28]. The stationarity condition of Ψ w.r.t. θ yields a simplified version of Brown's micromagnetic equations [28] which reads

$$0 = 2A\Delta\theta - K \sin(2\theta) + 3\Lambda_s \boldsymbol{\sigma} : \mathbf{m}_\perp \otimes \mathbf{m} - \mu_0 M_s \mathbf{m}_\perp \cdot (\nabla \varphi - \mathbf{H}') \quad \text{in } V^{\text{fm}} , \quad (4.17)$$

where we use $\boldsymbol{\sigma}$ to denote the Cauchy stress tensor

$$\boldsymbol{\sigma} = \frac{\partial \psi^e}{\partial \boldsymbol{\varepsilon}^e} = \lambda \text{tr}(\boldsymbol{\varepsilon}^e) \mathbf{I} + 2\mu \boldsymbol{\varepsilon}^e \quad (4.18)$$

and a colon to denote double contraction $\mathbf{A} : \mathbf{B} = A_{ij} B_{ij}$ of two second order tensors.

4.3.2 Magnetic non-equilibrium states

To also consider non-equilibrium states, we introduce a dissipative term with Gilbert damping constant $\eta > 0$, see [117], into the left hand side of Eq. (4.17). We neglect precession effects. With the dissipative term, we obtain the following non-equilibrium version of Eq. (4.17)

$$\eta \dot{\theta} = 2A\Delta\theta - K \sin(2\theta) + 3\Lambda_s \boldsymbol{\sigma} : \mathbf{m}_\perp \otimes \mathbf{m} - \mu_0 M_s \mathbf{m}_\perp \cdot (\nabla \varphi - \mathbf{H}') \quad \text{in } V^{\text{fm}} \quad (4.19)$$

which we consider as a simplified Landau–Lifshitz–Gilbert (LLG) equation, cf. [117]. Note that the coupling of micromagnetics and mechanics manifests itself via the contribution $3\Lambda_s \boldsymbol{\sigma} : \mathbf{m}_\perp \otimes \mathbf{m}$ in Eq. (4.19).

4.4 Linearization of the Landau–Lifshitz–Gilbert equation

Next, we linearize Eq. (4.19) for small angles θ . At time $t = 0$, we assume the magnetization to homogeneously point in x_1 -direction (i.e., $\theta = 0$) and we are interested in the *initial*

evolution of $\theta(\mathbf{x}, t)$, such that the case $|\theta| \ll 1$ applies. In Eq. (4.19), the assumption $|\theta| \ll 1$ entails

$$K \sin(2\theta) \approx 2K\theta, \quad \mathbf{m} \approx \mathbf{e}_1 + \theta \mathbf{e}_2, \quad \text{and} \quad \mathbf{m}_\perp \approx -\theta \mathbf{e}_1 + \mathbf{e}_2. \quad (4.20)$$

Moreover, for the stress term, we obtain

$$\boldsymbol{\sigma} : \mathbf{m}_\perp \otimes \mathbf{m} = \left(\lambda^{\text{fm}} \text{tr}(\boldsymbol{\varepsilon}^e) \mathbf{I} + 2\mu^{\text{fm}} \boldsymbol{\varepsilon}^e \right) : \mathbf{m}_\perp \otimes \mathbf{m} \quad (4.21)$$

$$= 2\mu^{\text{fm}} \boldsymbol{\varepsilon}^e : \mathbf{m}_\perp \otimes \mathbf{m}, \quad (4.22)$$

where we use $\mathbf{I} : \mathbf{m}_\perp \otimes \mathbf{m} = \mathbf{m}_\perp \cdot \mathbf{m} = 0$. Note that we use the Lamé parameters of the thin film since the simplified LLG equation (4.19) is only relevant for magnetic materials. Furthermore, we insert the additive decomposition of strain from Eq. (4.2) and the definition of magnetostrictive strain from Eq. (4.4) which yields

$$\boldsymbol{\sigma} : \mathbf{m}_\perp \otimes \mathbf{m} = 2\mu^{\text{fm}} \left(\boldsymbol{\varepsilon}^{\text{fm}} - \boldsymbol{\varepsilon}^* - \frac{3}{2} \Lambda_s \left(\mathbf{m} \otimes \mathbf{m} - \frac{1}{3} \mathbf{I} \right) \right) : \mathbf{m}_\perp \otimes \mathbf{m} \quad (4.23)$$

$$= 2\mu^{\text{fm}} \left(\boldsymbol{\varepsilon}^{\text{fm}} - \boldsymbol{\varepsilon}^* \right) : \mathbf{m}_\perp \otimes \mathbf{m}, \quad (4.24)$$

where we use $\mathbf{m}_\perp \cdot \mathbf{m} = 0$ again. Using Eq. (4.20) and with terms in θ^2 being small of higher order, the term $\mathbf{m}_\perp \otimes \mathbf{m}$ reads

$$\mathbf{m}_\perp \otimes \mathbf{m} \approx \mathbf{e}_2 \otimes \mathbf{e}_1 + \theta(-\mathbf{e}_1 \otimes \mathbf{e}_1 + \mathbf{e}_2 \otimes \mathbf{e}_2) \quad (4.25)$$

which yields for the stress term

$$\boldsymbol{\sigma} : \mathbf{m}_\perp \otimes \mathbf{m} = 2\mu^{\text{fm}} \left(\boldsymbol{\varepsilon}^{\text{fm}} - \boldsymbol{\varepsilon}^* \right) : (\mathbf{e}_2 \otimes \mathbf{e}_1 + \theta(-\mathbf{e}_1 \otimes \mathbf{e}_1 + \mathbf{e}_2 \otimes \mathbf{e}_2)) \quad (4.26)$$

$$= 2\mu^{\text{fm}} \left(\varepsilon_{12}^{\text{fm}} + \theta(\varepsilon_{22}^{\text{fm}} - \varepsilon_{11}^{\text{fm}}) - \theta(\varepsilon_2^* - \varepsilon_1^*) \right). \quad (4.27)$$

Since we assume angle θ , displacement \mathbf{u} and strain $\boldsymbol{\varepsilon}$ to be small in the vicinity of $t = 0$, the term $\theta(\varepsilon_{22}^{\text{fm}} - \varepsilon_{11}^{\text{fm}})$ is small of order two and vanishes approximately. Thus, the stress contribution in Eq. (4.19) finally reads

$$3\Lambda_s \boldsymbol{\sigma} : \mathbf{m}_\perp \otimes \mathbf{m} \approx 6\Lambda_s \mu^{\text{fm}} \varepsilon_{12}^{\text{fm}} - 6\Lambda_s \mu^{\text{fm}} (\varepsilon_2^* - \varepsilon_1^*) \theta. \quad (4.28)$$

In Eq. (4.19), there is one remaining term: $-\mu_0 M_s \mathbf{m}_\perp \cdot (\nabla \varphi - \mathbf{H}')$. We treat the two contributions separately. For the term including the external field, we employ Eqs. (4.15) and (4.20) and obtain

$$\mu_0 M_s \mathbf{m}_\perp \cdot \mathbf{H}' = \mu_0 M_s (-\theta \mathbf{e}_1 + \mathbf{e}_2) \cdot H' \mathbf{e}_1 \quad (4.29)$$

$$= -\mu_0 M_s H' \theta. \quad (4.30)$$

Under the presented assumptions, the term including the demagnetizing field $-\nabla\varphi$ vanishes due to vanishing magnetic potential φ , see appendix 4.A for a detailed discussion. Finally, the linearized LLG equation reads

$$\eta\dot{\theta} = 2A\Delta\theta - 2\mathcal{L}\theta + 6\Lambda_s\mu^{\text{fm}}\varepsilon_{12}^{\text{fm}} \quad \text{in } V^{\text{fm}}, \quad (4.31)$$

where we summarize all contributions which align the magnetization along \mathbf{e}_1 in the alignment constant

$$\mathcal{L} = K + 3\Lambda_s\mu^{\text{fm}}(\varepsilon_2^* - \varepsilon_1^*) + \frac{1}{2}\mu_0 M_s H'. \quad (4.32)$$

4.5 Evaluation of the linear momentum balance

The stationarity condition of the potential Ψ in Eq. (4.8) w.r.t. displacement \mathbf{u} reads

$$0 = \int_{\Omega} \boldsymbol{\sigma} : \text{sym}(\text{grad}(\delta\mathbf{u})) \, dv \quad (4.33)$$

$$= \int_{\Omega} \boldsymbol{\sigma} : \text{grad}(\delta\mathbf{u}) \, dv, \quad (4.34)$$

where $\delta\mathbf{u}$ denotes the virtual displacement and $\text{sym}(\cdot)$ can be omitted due to symmetry of stress $\boldsymbol{\sigma}$. In the following, we derive the governing equations for the mechanical sub-problem by evaluating the linear momentum balance in Eq. (4.34) for the system at hand. Recall that we assume periodic boundary conditions in x_1 - and x_2 -direction for all solutions fields, see Sec. 4.2. We presume the following structure for the displacements in the thin film \mathbf{u}^{fm} and the substrate \mathbf{u}^{s} , respectively

$$\mathbf{u}^{\text{fm}} = u_1^{\text{fm}}(x_1)\mathbf{e}_1 + u_2^{\text{fm}}(x_1)\mathbf{e}_2 + u_3^{\text{fm}}(x_1, x_3)\mathbf{e}_3 \quad (4.35)$$

$$\mathbf{u}^{\text{s}} = \mathbf{u}^{\text{s}}(x_1, x_3). \quad (4.36)$$

Since we search for a solution similar to Fig. 4.1b (solution repeated in x_2 -direction), we drop the dependence on x_2 for both displacement fields. Furthermore, we assume u_1^{fm} and u_2^{fm} to only depend on x_1 due to the small thickness h of the magnetic thin film V^{fm} . The same reasoning also leads to the assumption $\theta = \theta(x_1)$. In contrast to u_1^{fm} and u_2^{fm} , we retain the dependence of u_3^{fm} on x_3 to be able to compensate for the magnetic and eigenstrain components $\varepsilon_{33}^{\text{m}}$ and ε_3^* , see Eq. (4.69). We denote the stresses in film and substrate by $\boldsymbol{\sigma}^{\text{fm}}$ and $\boldsymbol{\sigma}^{\text{s}}$, respectively, both of which are determined by Eqs. (4.18) and (4.13). Note that we assume $\boldsymbol{\sigma} = \mathbf{0}$ as $x_3 \rightarrow -\infty$. The structure of the virtual displacements $\delta\mathbf{u}^{\text{fm}}$ and $\delta\mathbf{u}^{\text{s}}$ is equivalent to the structure of the displacements \mathbf{u}^{fm} and \mathbf{u}^{s} in Eqs. (4.35) and (4.36).

Without loss of generality, we evaluate the balance of linear momentum in Eq. (4.34) by considering the virtual displacement $\delta\mathbf{u}$ component-wise.

First component non-zero: $\delta u_1 \neq 0$ and $\delta u_2 = \delta u_3 = 0$.

First, we process the case $\delta u_1 \neq 0$, in which the gradients of virtual displacement read

$$\text{grad}(\delta \mathbf{u}^{\text{fm}}) = \frac{\partial \delta u_1^{\text{fm}}}{\partial x_1} \mathbf{e}_1 \otimes \mathbf{e}_1 \quad \text{and} \quad \text{grad}(\delta \mathbf{u}^{\text{s}}) = \frac{\partial \delta u_1^{\text{s}}}{\partial x_1} \mathbf{e}_1 \otimes \mathbf{e}_1 + \frac{\partial \delta u_1^{\text{s}}}{\partial x_3} \mathbf{e}_1 \otimes \mathbf{e}_3 . \quad (4.37)$$

We obtain in the linear momentum balance, Eq. (4.34),

$$0 = \int_{V^{\text{fm}}} \sigma_{11}^{\text{fm}} \frac{\partial \delta u_1^{\text{fm}}}{\partial x_1} dv + \int_{V^{\text{s}}} \left(\sigma_{11}^{\text{s}} \frac{\partial \delta u_1^{\text{s}}}{\partial x_1} + \sigma_{13}^{\text{s}} \frac{\partial \delta u_1^{\text{s}}}{\partial x_3} \right) dv . \quad (4.38)$$

Since none of the quantities depend on x_2 , we can compute the corresponding integrals immediately, yielding

$$0 = L \int_0^h \int_0^L \left(\frac{\partial}{\partial x_1} (\sigma_{11}^{\text{fm}} \delta u_1^{\text{fm}}) - \frac{\partial \sigma_{11}^{\text{fm}}}{\partial x_1} \delta u_1^{\text{fm}} \right) dx_1 dx_3 \quad (4.39)$$

$$+ \int_{V^{\text{s}}} \left(\frac{\partial}{\partial x_1} (\sigma_{11}^{\text{s}} \delta u_1^{\text{s}}) + \frac{\partial}{\partial x_3} (\sigma_{13}^{\text{s}} \delta u_1^{\text{s}}) - \delta u_1^{\text{s}} \left(\frac{\partial \sigma_{11}^{\text{s}}}{\partial x_1} + \frac{\partial \sigma_{13}^{\text{s}}}{\partial x_3} \right) \right) dv$$

$$= L \int_0^h \sigma_{11}^{\text{fm}} \delta u_1^{\text{fm}} \Big|_{x_1=0}^{x_1=L} dx_3 - L \int_0^h \int_0^L \frac{\partial \sigma_{11}^{\text{fm}}}{\partial x_1} \delta u_1^{\text{fm}} dx_1 dx_3 \quad (4.40)$$

$$+ L \int_0^h \sigma_{11}^{\text{s}} \delta u_1^{\text{s}} \Big|_{x_1=0}^{x_1=L} dx_3 + L \int_0^L \sigma_{13}^{\text{s}} \delta u_1^{\text{s}} \Big|_{x_3=-\infty}^{x_3=0} dx_1 - \int_{V^{\text{s}}} \delta u_1^{\text{s}} \left(\frac{\partial \sigma_{11}^{\text{s}}}{\partial x_1} + \frac{\partial \sigma_{13}^{\text{s}}}{\partial x_3} \right) dv$$

$$= -L \int_0^L \delta u_1^{\text{fm}}(x_1) \int_0^h \frac{\partial \sigma_{11}^{\text{fm}}}{\partial x_1} dx_3 dx_1 + L \int_0^L \sigma_{13}^{\text{s}}(x_1, 0) \delta u_1^{\text{s}}(x_1, 0) dx_1 \quad (4.41)$$

$$- \int_{V^{\text{s}}} \delta u_1^{\text{s}} \left(\frac{\partial \sigma_{11}^{\text{s}}}{\partial x_1} + \frac{\partial \sigma_{13}^{\text{s}}}{\partial x_3} \right) dv ,$$

where we used periodicity in x_1 and $\sigma_{13}^{\text{s}} = 0$ for $x_3 \rightarrow -\infty$. At the interface A^* ($x_3 = 0$), the virtual displacements $\delta u_1^{\text{fm}} = \delta u_1^{\text{s}} = \delta u_1$ coincide which yields

$$0 = L \int_0^L \delta u_1(x_1) \left(\sigma_{13}^{\text{s}}(x_1, 0) - \int_0^h \frac{\partial \sigma_{11}^{\text{fm}}}{\partial x_1} dx_3 \right) dx_1 - \int_{V^{\text{s}}} \delta u_1^{\text{s}} \left(\frac{\partial \sigma_{11}^{\text{s}}}{\partial x_1} + \frac{\partial \sigma_{13}^{\text{s}}}{\partial x_3} \right) dv . \quad (4.42)$$

Since Eq. (4.42) has to hold for arbitrary virtual displacements $\delta \mathbf{u}$, we obtain the following governing equations

$$\sigma_{13}^{\text{s}}(x_1, x_3 = 0) = \int_0^h \frac{\partial \sigma_{11}^{\text{fm}}}{\partial x_1} dx_3 \quad \text{and} \quad \frac{\partial \sigma_{11}^{\text{s}}}{\partial x_1} + \frac{\partial \sigma_{13}^{\text{s}}}{\partial x_3} = 0 \quad \text{in } V^{\text{s}} . \quad (4.43)$$

The same result can be obtained by considering the first component of $\text{div}(\boldsymbol{\sigma}) = \mathbf{0}$ in thin film and substrate, neglecting the dependence on x_2 and integrating $\partial \sigma_{11}/\partial x_1 + \partial \sigma_{13}/\partial x_3$ over the thin film's thickness.

Second component non-zero: $\delta u_1 = 0$, $\delta u_2 \neq 0$ and $\delta u_3 = 0$.

Proceeding to the next component of the virtual displacement, we consider $\delta u_2 \neq 0$ which

entails for the gradients of virtual displacement

$$\text{grad}(\delta \mathbf{u}^{\text{fm}}) = \frac{\partial \delta u_2^{\text{fm}}}{\partial x_1} \mathbf{e}_2 \otimes \mathbf{e}_1 \quad \text{and} \quad \text{grad}(\delta \mathbf{u}^{\text{s}}) = \frac{\partial \delta u_2^{\text{s}}}{\partial x_1} \mathbf{e}_2 \otimes \mathbf{e}_1 + \frac{\partial \delta u_2^{\text{s}}}{\partial x_3} \mathbf{e}_2 \otimes \mathbf{e}_3 . \quad (4.44)$$

In the linear momentum balance from Eq. (4.34), this yields

$$0 = \int_{V^{\text{fm}}} \sigma_{12}^{\text{fm}} \frac{\partial \delta u_2^{\text{fm}}}{\partial x_1} dv + \int_{V^{\text{s}}} \left(\sigma_{12}^{\text{s}} \frac{\partial \delta u_2^{\text{s}}}{\partial x_1} + \sigma_{23}^{\text{s}} \frac{\partial \delta u_2^{\text{s}}}{\partial x_3} \right) dv . \quad (4.45)$$

Following the same steps as before, we obtain

$$0 = L \int_0^L \delta u_2(x_1) \left(\sigma_{23}^{\text{s}}(x_1, 0) - \int_0^h \frac{\partial \sigma_{12}^{\text{fm}}}{\partial x_1} dx_3 \right) dx_1 - \int_{V^{\text{s}}} \delta u_2^{\text{s}} \left(\frac{\partial \sigma_{12}^{\text{s}}}{\partial x_1} + \frac{\partial \sigma_{23}^{\text{s}}}{\partial x_3} \right) dv . \quad (4.46)$$

To further simplify, we investigate σ_{12}^{fm}

$$\boldsymbol{\sigma}^{\text{fm}} = \lambda^{\text{fm}} \text{tr}(\boldsymbol{\varepsilon}^{\text{e}}) \mathbf{I} + 2\mu^{\text{fm}} \boldsymbol{\varepsilon}^{\text{e}} \quad \text{with} \quad \boldsymbol{\varepsilon}^{\text{e}} = \boldsymbol{\varepsilon}^{\text{fm}} - \boldsymbol{\varepsilon}^* - \boldsymbol{\varepsilon}^{\text{m}} \quad (4.47)$$

$$\sigma_{12}^{\text{fm}} = 2\mu^{\text{fm}} \varepsilon_{12}^{\text{e}} \quad (4.48)$$

$$= \mu^{\text{fm}} \frac{\partial u_2^{\text{fm}}(x_1)}{\partial x_1} - 3\mu^{\text{fm}} \Lambda_{\text{s}} \theta(x_1) , \quad (4.49)$$

where we use that $\boldsymbol{\varepsilon}^*$ has no off-diagonal components and that we can write the magnetostriuctive strain $\boldsymbol{\varepsilon}^{\text{m}}$ with Eq. (4.20) as

$$\boldsymbol{\varepsilon}^{\text{m}} = \frac{3}{2} \Lambda_{\text{s}} \left(\mathbf{e}_1 \otimes \mathbf{e}_1 + \theta(\mathbf{e}_2 \otimes \mathbf{e}_1 + \mathbf{e}_1 \otimes \mathbf{e}_2) - \frac{1}{3} \mathbf{I} \right) \quad \Rightarrow \quad \varepsilon_{12}^{\text{m}} = \frac{3}{2} \Lambda_{\text{s}} \theta . \quad (4.50)$$

Thus, σ_{12}^{fm} only depends on x_1 which means that we can compute the x_3 -integral in Eq. (4.46) immediately. Computing the integral and requiring Eq. (4.46) to hold for arbitrary virtual displacements $\delta \mathbf{u}$ yields

$$\sigma_{23}^{\text{s}}(x_1, x_3 = 0) = h \frac{\partial \sigma_{12}^{\text{fm}}}{\partial x_1} \quad \text{and} \quad \frac{\partial \sigma_{12}^{\text{s}}}{\partial x_1} + \frac{\partial \sigma_{23}^{\text{s}}}{\partial x_3} = 0 \quad \text{in } V^{\text{s}} . \quad (4.51)$$

Third component non-zero: $\delta u_1 = \delta u_2 = 0$ and $\delta u_3 \neq 0$.

Finally, we consider the last component of the virtual displacement to be non-zero, $\delta u_3 \neq 0$, in which case the gradient reads

$$\text{grad}(\delta \mathbf{u}) = \frac{\partial \delta u_3}{\partial x_1} \mathbf{e}_3 \otimes \mathbf{e}_1 + \frac{\partial \delta u_3}{\partial x_3} \mathbf{e}_3 \otimes \mathbf{e}_3 . \quad (4.52)$$

A dedicated treatment of film and substrate is not necessary in this case as will become clear in the following. With Eq. (4.52), the linear momentum balance, Eq. (4.34), reads

$$0 = \int_{\Omega} \left(\sigma_{13} \frac{\partial \delta u_3}{\partial x_1} + \sigma_{33} \frac{\partial \delta u_3}{\partial x_3} \right) dv \quad (4.53)$$

$$= \int_{\Omega} \left(\frac{\partial}{\partial x_1} (\sigma_{13} \delta u_3) + \frac{\partial}{\partial x_3} (\sigma_{33} \delta u_3) - \delta u_3 \left(\frac{\partial \sigma_{13}}{\partial x_1} + \frac{\partial \sigma_{33}}{\partial x_3} \right) \right) dv \quad (4.54)$$

$$= L \int_{-\infty}^h \sigma_{13} \delta u_3 \Big|_{x_1=0}^{x_1=L} dx_3 + L \int_0^L \sigma_{33} \delta u_3 \Big|_{x_3=-\infty}^{x_3=h} dx_1 - \int_{\Omega} \delta u_3 \left(\frac{\partial \sigma_{13}}{\partial x_1} + \frac{\partial \sigma_{33}}{\partial x_3} \right) dv \quad (4.55)$$

$$= L \int_0^L \sigma_{33}(x_1, h) \delta u_3(x_1, h) dx_1 - \int_{\Omega} \delta u_3 \left(\frac{\partial \sigma_{13}}{\partial x_1} + \frac{\partial \sigma_{33}}{\partial x_3} \right) dv. \quad (4.56)$$

As before, we use periodicity in x_1 and $\sigma_{33} = 0$ for $x_3 \rightarrow -\infty$. Requiring Eq. (4.56) to hold for arbitrary virtual displacements yields the final set of governing equations

$$\sigma_{33}^{\text{fm}}(x_1, x_3 = h) = 0, \quad \frac{\partial \sigma_{13}^{\text{fm}}}{\partial x_1} + \frac{\partial \sigma_{33}^{\text{fm}}}{\partial x_3} = 0 \quad \text{in } V^{\text{fm}}, \quad \text{and} \quad \frac{\partial \sigma_{13}^{\text{s}}}{\partial x_1} + \frac{\partial \sigma_{33}^{\text{s}}}{\partial x_3} = 0 \quad \text{in } V^{\text{s}}. \quad (4.57)$$

To summarize, the following equations govern the boundary value problem:

$$\eta \dot{\theta} = 2A\Delta\theta - 2\mathcal{L}\theta + 6\Lambda_s \mu^{\text{fm}} \varepsilon_{12}^{\text{fm}} \quad \text{in } V^{\text{fm}} \quad (4.58)$$

$$\mathcal{L} = K + 3\Lambda_s \mu^{\text{fm}} (\varepsilon_2^* - \varepsilon_1^*) + \frac{1}{2} \mu_0 M_s H' \quad (4.59)$$

$$\sigma_{13}^{\text{s}}(x_1, x_3 = 0) = \int_0^h \frac{\partial \sigma_{11}^{\text{fm}}}{\partial x_1} dx_3 \quad (4.60)$$

$$0 = \frac{\partial \sigma_{11}^{\text{s}}}{\partial x_1} + \frac{\partial \sigma_{13}^{\text{s}}}{\partial x_3} \quad \text{in } V^{\text{s}} \quad (4.61)$$

$$\sigma_{23}^{\text{s}}(x_1, x_3 = 0) = h \frac{\partial \sigma_{12}^{\text{fm}}}{\partial x_1} \quad (4.62)$$

$$0 = \frac{\partial \sigma_{12}^{\text{s}}}{\partial x_1} + \frac{\partial \sigma_{23}^{\text{s}}}{\partial x_3} \quad \text{in } V^{\text{s}} \quad (4.63)$$

$$\sigma_{33}^{\text{fm}}(x_1, x_3 = h) = 0 \quad (4.64)$$

$$0 = \frac{\partial \sigma_{13}^{\text{fm}}}{\partial x_1} + \frac{\partial \sigma_{33}^{\text{fm}}}{\partial x_3} \quad \text{in } V^{\text{fm}} \quad (4.65)$$

$$0 = \frac{\partial \sigma_{13}^{\text{s}}}{\partial x_1} + \frac{\partial \sigma_{33}^{\text{s}}}{\partial x_3} \quad \text{in } V^{\text{s}}. \quad (4.66)$$

4.6 Stability analysis of the trivial solution for the coupled micro-magneto-mechanical problem

The coupled micro-magneto-mechanical problem is characterized by the linearized LLG equation and the governing mechanical equations, see Eqs. (4.58) to (4.66). Magnetization angle θ and displacement of thin film \mathbf{u}^{fm} and substrate \mathbf{u}^{s} are the primary solution fields. The

trivial solution of Eq. (4.58) reads

$$\theta = 0 \quad \text{and} \quad u_2^{\text{fm}} = 0 \quad \Rightarrow \quad \varepsilon_{12}^{\text{fm}} = \frac{1}{2} \frac{\partial u_2^{\text{fm}}}{\partial x_1} = 0 . \quad (4.67)$$

The remaining governing equations Eqs. (4.60) to (4.66) are trivially solved by

$$\mathbf{u}^s = \mathbf{0}, \quad u_1^{\text{fm}} = u_2^{\text{fm}} = 0 \quad \text{and} \quad u_3^{\text{fm}} = h_{33}^{\text{fm}} x_3 , \quad (4.68)$$

where the constant h_{33}^{fm} follows from Eq. (4.64) together with Hooke's law from Eq. (4.18) and the additive decomposition of strain from Eq. (4.2)

$$\sigma_{33}^{\text{fm}} = \lambda^{\text{fm}} \left(\frac{\partial u_1^{\text{fm}}}{\partial x_1} + \frac{\partial u_3^{\text{fm}}}{\partial x_3} - \text{tr}(\boldsymbol{\varepsilon}^*) \right) + 2\mu^{\text{fm}} \left(\frac{\partial u_3^{\text{fm}}}{\partial x_3} + \frac{1}{2} \Lambda_s - \varepsilon_3^* \right) \quad (4.69)$$

$$= \lambda^{\text{fm}} \left(h_{33}^{\text{fm}} - \text{tr}(\boldsymbol{\varepsilon}^*) \right) + 2\mu^{\text{fm}} \left(h_{33}^{\text{fm}} + \frac{1}{2} \Lambda_s - \varepsilon_3^* \right) \quad (4.70)$$

$$\sigma_{33}^{\text{fm}}(x_1, x_3 = h) = 0 \quad \Leftrightarrow \quad h_{33}^{\text{fm}} = \frac{\lambda^{\text{fm}} \text{tr}(\boldsymbol{\varepsilon}^*) - \mu^{\text{fm}} \Lambda_s + 2\mu^{\text{fm}} \varepsilon_3^*}{\lambda^{\text{fm}} + 2\mu^{\text{fm}}} . \quad (4.71)$$

The trivial solution is only physically relevant if it is stable. To assess stability in the sense of Lyapunov, we consider small arbitrary perturbations in the initial conditions. The behavior of these perturbations (decay or self-stimulating) allows to draw conclusions concerning the stability of the trivial solution. The idea is that instabilities will invoke a behavior of the solution which corresponds to experimentally observed undulations. Since these undulations are periodic in nature, we assume the perturbations in the general form of a Fourier series (keeping in mind that the dimension L of the computational domain under consideration may be chosen arbitrarily large, thus covering also the non-periodic case, in principle). The main quantity, for which undulations are experimentally observed, is the magnetization angle θ . In the very first instance of time, $t = 0$, we introduce the perturbation of the orientation θ according to

$$\theta(x_1, t = 0) = \sum_{l \in \mathbb{Z}} \theta_l \exp(ik_l x_1) , \quad (4.72)$$

where θ_l denote the Fourier coefficients, \mathbb{Z} denotes integers and k_l is the wavenumber. The latter is related to the periodic domain size L , see Fig. 4.2, and the wavelength λ_l , see Fig. 4.1b, by

$$k_l = \frac{2\pi l}{L} = \frac{2\pi}{\lambda_l} . \quad (4.73)$$

In analogy, we can always write for the initial conditions of u_2^{fm}

$$u_2^{\text{fm}}(x_1, t = 0) = \sum_{l \in \mathbb{Z}} u_{2l}^{\text{fm}} \exp(ik_l x_1) , \quad (4.74)$$

where u_{2l}^{fm} are the Fourier coefficients of u_2^{fm} . The perturbed initial conditions of u_2^{s} at the interface (at $x_3 = 0$) read

$$u_2^{\text{s}}(x_1, x_3 = 0, t = 0) = \sum_{l \in \mathbb{Z}} u_{2l}^{\text{s}} \exp(ik_l x_1) , \quad (4.75)$$

where u_{2l}^{s} are the Fourier coefficients of u_2^{s} . No further displacement components are affected by the assumed perturbations. To model the dependence of u_2^{s} on x_3 , we consider the earlier assumption, $\boldsymbol{\sigma}^{\text{s}} = \mathbf{0}$ as $x_3 \rightarrow -\infty$, again. We can fulfill this assumption via $\mathbf{u}^{\text{s}} = \mathbf{0}$ as $x_3 \rightarrow -\infty$. To achieve the latter, we introduce the term $\exp(x_3/L_l)$ to the displacement component u_2^{s}

$$u_2^{\text{s}}(x_1, x_3, t = 0) = \sum_{l \in \mathbb{Z}} u_{2l}^{\text{s}} \exp\left(ik_l x_1 + \frac{x_3}{L_l}\right) , \quad (4.76)$$

i.e., the displacements are assumed to decay exponentially in the downside direction in the substrate. The consistency of these initial conditions with the linear momentum balance will be shown below. The quantity L_l can be thought of as a characteristic length, which can be different for each Fourier mode l . This allows each mode to decrease to zero at a different rate $1/L_l$. Note that $\exp(x_3/L_l)$ does not represent a Fourier series in the x_3 -slot and thus $u_2^{\text{s}}(x_1, x_3, t = 0)$ is not periodic in x_3 .

The two displacement components u_2^{fm} and u_2^{s} have to coincide at $x_3 = 0$. To achieve that, we assume the same Fourier coefficients $u_{2l}^{\text{fm}} = u_{2l}^{\text{s}} = u_{2l}$ for the two displacement components in film and substrate. For the stability analysis, we infer that a stable solution is equivalent to attenuated perturbations over time. Conversely, an unstable solution corresponds to amplified perturbations over time (yielding experimentally observed undulations). We represent this behavior by introducing the term $\exp(-t/\tau_l)$ to the perturbed solution. $\tau_l > 0$ reflects stable (attenuating) behavior and conversely $\tau_l \leq 0$ represents unstable (amplifying) behavior which leads to undulations. Thus, taking all the previous assumptions into consideration, the solution ansatz reads

$$\theta(x_1, t) = \sum_{l \in \mathbb{Z}} \theta_l \exp\left(ik_l x_1 - \frac{t}{\tau_l}\right) \quad (4.77)$$

$$\mathbf{u}^{\text{fm}}(x_1, x_3, t) = \left(\sum_{l \in \mathbb{Z}} u_{2l} \exp\left(ik_l x_1 - \frac{t}{\tau_l}\right) \right) \mathbf{e}_2 + h_{33}^{\text{fm}} x_3 \mathbf{e}_3 \quad (4.78)$$

$$\mathbf{u}^{\text{s}}(x_1, x_3, t) = \left(\sum_{l \in \mathbb{Z}} u_{2l} \exp\left(ik_l x_1 + \frac{x_3}{L_l} - \frac{t}{\tau_l}\right) \right) \mathbf{e}_2 . \quad (4.79)$$

In the following, the dependence of these three functions on x_1 , x_3 and t is not written explicitly anymore. The quantity τ_l is considered as a characteristic time scale which can be different for each Fourier mode l . This allows each individual mode to adopt attenuating ($\tau_l > 0$) or amplifying ($\tau_l \leq 0$) nature. Note that $\exp(-t/\tau_l)$ does not represent a Fourier

series in the time slot and thus the solution ansatz is not periodic in time t . We stress that Eqs. (4.77) to (4.79) are a solution *ansatz*. Thus, in the following, we verify that this ansatz solves the initial boundary value problem summarized in the boxed Eqs. (4.58) to (4.66). Due to the linearity of the governing equations, each Fourier mode l must satisfy the initial boundary value problem individually. From the trivial solution, we learn that for $l = 0$, we have $\theta_0 = u_{20} = 0$, thus, we concentrate on the case $l \neq 0$ in the following ($l \in \mathbb{Z} \setminus \{0\}$). Using the solution ansatz from Eqs. (4.77) to (4.79) together with Hooke's law from Eq. (4.18) and the additive decomposition of strain from Eq. (4.2), we compute strain and stress in the substrate

$$\boldsymbol{\varepsilon}^s = \begin{bmatrix} 0 & \frac{1}{2} \frac{\partial u_2^s}{\partial x_1} & 0 \\ & 0 & \frac{1}{2} \frac{\partial u_2^s}{\partial x_3} \\ \text{sym} & & 0 \end{bmatrix} \mathbf{e}_i \otimes \mathbf{e}_j, \quad \boldsymbol{\sigma}^s = \begin{bmatrix} 0 & \mu^s \frac{\partial u_2^s}{\partial x_1} & 0 \\ & 0 & \mu^s \frac{\partial u_2^s}{\partial x_3} \\ \text{sym} & & 0 \end{bmatrix} \mathbf{e}_i \otimes \mathbf{e}_j \quad (4.80)$$

and the thin film

$$\boldsymbol{\varepsilon}^{\text{fm}} = \begin{bmatrix} 0 & \frac{1}{2} \frac{\partial u_2^{\text{fm}}}{\partial x_1} & 0 \\ & 0 & 0 \\ \text{sym} & & h_{33}^{\text{fm}} \end{bmatrix} \mathbf{e}_i \otimes \mathbf{e}_j, \quad \boldsymbol{\sigma}^{\text{fm}} = \begin{bmatrix} \sigma_{11}^{\text{fm}} & \sigma_{12}^{\text{fm}} & 0 \\ & \sigma_{22}^{\text{fm}} & 0 \\ \text{sym} & & \sigma_{33}^{\text{fm}} \end{bmatrix} \mathbf{e}_i \otimes \mathbf{e}_j \quad (4.81)$$

$$\sigma_{11}^{\text{fm}} = \lambda^{\text{fm}} \left(h_{33}^{\text{fm}} - \text{tr}(\boldsymbol{\varepsilon}^*) \right) + 2\mu^{\text{fm}}(-\Lambda_s - \varepsilon_1^*) \quad (4.82)$$

$$\sigma_{12}^{\text{fm}} = \mu^{\text{fm}} \frac{\partial u_2^{\text{fm}}}{\partial x_1} - 3\mu^{\text{fm}} \Lambda_s \theta \quad (4.83)$$

$$\sigma_{22}^{\text{fm}} = \lambda^{\text{fm}} \left(h_{33}^{\text{fm}} - \text{tr}(\boldsymbol{\varepsilon}^*) \right) + 2\mu^{\text{fm}} \left(\frac{1}{2} \Lambda_s - \varepsilon_2^* \right) \quad (4.84)$$

$$\sigma_{33}^{\text{fm}} = \lambda^{\text{fm}} \left(h_{33}^{\text{fm}} - \text{tr}(\boldsymbol{\varepsilon}^*) \right) + 2\mu^{\text{fm}} \left(h_{33}^{\text{fm}} + \frac{1}{2} \Lambda_s - \varepsilon_3^* \right). \quad (4.85)$$

Governing equations Eqs. (4.61) and (4.66) are fulfilled since $\sigma_{11}^s = \sigma_{13}^s = \sigma_{33}^s = 0$. Eq. (4.60) is fulfilled since σ_{11}^{fm} is constant and $\sigma_{13}^s = 0$. The definition of h_{33}^{fm} in Eq. (4.71) satisfies Eq. (4.64) identically. Eq. (4.65) is satisfied since σ_{33}^{fm} is constant and $\sigma_{13}^{\text{fm}} = 0$. For Eq. (4.62), which reads with Eqs. (4.80) and (4.83)

$$\mu^s \frac{\partial u_2^s(x_1, x_3)}{\partial x_3} \Big|_{x_3=0} = h \frac{\partial}{\partial x_1} \left(\mu^{\text{fm}} \frac{\partial u_2^{\text{fm}}(x_1)}{\partial x_1} - 3\mu^{\text{fm}} \Lambda_s \theta(x_1) \right), \quad (4.86)$$

we compute the following derivatives of the perturbed solution

$$\frac{\partial u_2^s}{\partial x_3} \Big|_{x_3=0} = \sum_{l \in \mathbb{Z} \setminus \{0\}} \frac{1}{L_l} u_{2l} \exp \left(i k_l x_1 - \frac{t}{\tau_l} \right) \quad (4.87)$$

$$\frac{\partial^2 u_2^{\text{fm}}}{\partial x_1^2} = \sum_{l \in \mathbb{Z} \setminus \{0\}} -k_l^2 u_{2l} \exp\left(ik_l x_1 - \frac{t}{\tau_l}\right) \quad (4.88)$$

$$\frac{\partial \theta}{\partial x_1} = \sum_{l \in \mathbb{Z} \setminus \{0\}} ik_l \theta_l \exp\left(ik_l x_1 - \frac{t}{\tau_l}\right) \quad (4.89)$$

and insert them into Eq. (4.86)

$$0 = \sum_{l \in \mathbb{Z} \setminus \{0\}} \left(\frac{\mu^s}{L_l} u_{2l} + h\mu^{\text{fm}} k_l^2 u_{2l} + 3h\mu^{\text{fm}} \Lambda_s ik_l \theta_l \right) \exp\left(ik_l x_1 - \frac{t}{\tau_l}\right). \quad (4.90)$$

Since Eq. (4.90) has to hold for arbitrary locations x_1 , times t , and modes l , the Fourier coefficient has to vanish. We obtain

$$u_{2l} = -i \frac{3h\mu^{\text{fm}} \Lambda_s k_l}{\frac{\mu^s}{L_l} + h\mu^{\text{fm}} k_l^2} \theta_l. \quad (4.91)$$

The last of the governing mechanics equations, Eq. (4.63), reads with $\mu^s \neq 0$

$$0 = \frac{\partial \sigma_{12}^s}{\partial x_1} + \frac{\partial \sigma_{23}^s}{\partial x_3} \quad \Leftrightarrow \quad 0 = \frac{\partial^2 u_2^s}{\partial x_1^2} + \frac{\partial^2 u_2^s}{\partial x_3^2}. \quad (4.92)$$

We compute the following derivatives of the perturbed solution

$$\frac{\partial^2 u_2^s}{\partial x_1^2} = \sum_{l \in \mathbb{Z} \setminus \{0\}} -k_l^2 u_{2l} \exp\left(ik_l x_1 + \frac{x_3}{L_l} - \frac{t}{\tau_l}\right) \quad (4.93)$$

$$\frac{\partial^2 u_2^s}{\partial x_3^2} = \sum_{l \in \mathbb{Z} \setminus \{0\}} \frac{1}{L_l^2} u_{2l} \exp\left(ik_l x_1 + \frac{x_3}{L_l} - \frac{t}{\tau_l}\right) \quad (4.94)$$

and insert them into Eq. (4.92)

$$0 = \sum_{l \in \mathbb{Z} \setminus \{0\}} \left(\frac{1}{L_l^2} - k_l^2 \right) u_{2l} \exp\left(ik_l x_1 + \frac{x_3}{L_l} - \frac{t}{\tau_l}\right) \quad (4.95)$$

which is identically satisfied due to Eq. (4.73), if $L_l = \text{sg}(l)L/(2\pi l)$ ($l \neq 0$). That is, undulations with shorter wavelength show a faster decay within the substrate. In Eq. (4.91), we obtain with $k_l = 1/L_l \neq 0$

$$u_{2l} = -i \frac{3h\mu^{\text{fm}} \Lambda_s k_l}{\mu^s k_l + h\mu^{\text{fm}} k_l^2} \theta_l = -i \frac{3h\mu^{\text{fm}} \Lambda_s}{\mu^s + h\mu^{\text{fm}} k_l} \theta_l. \quad (4.96)$$

For the final governing equation, Eq. (4.58), which reads with $\theta = \theta(x_1, t)$

$$\eta \dot{\theta} = 2A \frac{\partial^2 \theta}{\partial x_1^2} - 2\mathcal{L}\theta + 3\Lambda_s \mu^{\text{fm}} \frac{\partial u_2^{\text{fm}}}{\partial x_1}, \quad (4.97)$$

we compute the following derivatives of the perturbed trivial solution

$$\dot{\theta} = \sum_{l \in \mathbb{Z} \setminus \{0\}} -\frac{1}{\tau_l} \theta_l \exp\left(ik_l x_1 - \frac{t}{\tau_l}\right) \quad (4.98)$$

$$\frac{\partial^2 \theta}{\partial x_1^2} = \sum_{l \in \mathbb{Z} \setminus \{0\}} -k_l^2 \theta_l \exp\left(ik_l x_1 - \frac{t}{\tau_l}\right) \quad (4.99)$$

$$\frac{\partial u_2^{\text{fm}}}{\partial x_1} = \sum_{l \in \mathbb{Z} \setminus \{0\}} ik_l u_{2l} \exp\left(ik_l x_1 - \frac{t}{\tau_l}\right) \quad (4.100)$$

and insert them into Eq. (4.97)

$$0 = \sum_{l \in \mathbb{Z} \setminus \{0\}} \left(-\frac{\eta}{\tau_l} \theta_l + 2Ak_l^2 \theta_l + 2\mathcal{L} \theta_l - 3\Lambda_s \mu^{\text{fm}} ik_l u_{2l} \right) \exp\left(ik_l x_1 - \frac{t}{\tau_l}\right). \quad (4.101)$$

With u_{2l} from Eq. (4.96), we obtain

$$0 = \sum_{l \in \mathbb{Z} \setminus \{0\}} \left(-\frac{\eta}{\tau_l} + 2Ak_l^2 + 2\mathcal{L} - 3\Lambda_s \mu^{\text{fm}} k_l \frac{3h\mu^{\text{fm}} \Lambda_s}{\mu^s + h\mu^{\text{fm}} k_l} \right) \theta_l \exp\left(ik_l x_1 - \frac{t}{\tau_l}\right) \quad (4.102)$$

which has to hold for arbitrary locations x_1 , times t , and modes l . This yields

$$\frac{\eta}{\tau_l} = 2Ak_l^2 + 2\mathcal{L} - \frac{9(\Lambda_s \mu^{\text{fm}})^2 h}{\frac{\mu^s}{k_l} + h\mu^{\text{fm}}}. \quad (4.103)$$

With Gilbert damping parameter $\eta > 0$, we expect stable behavior (attenuated perturbations, $\tau_l > 0$) if

$$\frac{\eta}{\tau_l} = 2Ak_l^2 + 2\mathcal{L} - \frac{9(\Lambda_s \mu^{\text{fm}})^2 h}{\frac{\mu^s}{k_l} + h\mu^{\text{fm}}} > 0. \quad (4.104)$$

Hence, the stability criterion f reads with Eq. (4.73)

$$f := \frac{8\pi^2 A}{\lambda_l^2} + 2\mathcal{L} - \frac{18\pi(\Lambda_s \mu^{\text{fm}})^2 h}{\mu^s \lambda_l + 2\pi h \mu^{\text{fm}}} \begin{cases} > 0 & \text{stable (no undulations)} \\ < 0 & \text{unstable (undulations possible)} \end{cases}. \quad (4.105)$$

4.7 An energetic view on stability

Our previous arguments related to stability were based exclusively on attenuation or amplification of perturbations. In this section, we briefly want to adopt the energetic point of view (energy minimum is stable, maximum is unstable).

We consider the potential $\Psi(\underline{d})$ from Eq. (4.8) with the degree of freedom vector $\underline{d} = [\mathbf{u}, \theta]^\top$. We denote the trivial solution by $\underline{d}_0 = [\mathbf{u}_0, \theta_0]^\top$ (stability to be assessed). The trivial solution is perturbed by $\epsilon \delta \underline{d} = [\epsilon \delta \mathbf{u}, \epsilon \delta \theta]^\top$ with a small number $\epsilon \in \mathbb{R}_{>0}$. The following derivative

determines stability

$$\frac{d}{d\epsilon}\Psi(\underline{d}_0 + \epsilon\delta\underline{d}) \begin{cases} > 0 & \underline{d}_0 \text{ is stable} \\ < 0 & \underline{d}_0 \text{ is unstable} \end{cases} . \quad (4.106)$$

In case the energy increases for any small deviation $\epsilon\delta\underline{d}$ from \underline{d}_0 , then \underline{d}_0 must be the minimum (stable). Vice versa, an energy decrease indicates the maximum (unstable). With vanishing φ (see appendix 4.A) and the assumptions we made in Secs. 4.3 and 4.4, we obtain

$$\begin{aligned} & \frac{d}{d\epsilon}\Psi(\underline{d}_0 + \epsilon\delta\underline{d}) \\ &= \int_{V^{\text{fm}}} \left[-2A\Delta(\theta_0 + \epsilon\delta\theta) + 2\mathcal{L}(\theta_0 + \epsilon\delta\theta) - 3\mu^{\text{fm}}\Lambda_s \frac{\partial(u_2^0 + \epsilon\delta u_2)}{\partial x_1} \right] \delta\theta \\ & \quad + \left[-\text{div}(\boldsymbol{\sigma}(\mathbf{u}_0 + \epsilon\delta\mathbf{u})) \right] \cdot \delta\mathbf{u} \, dv . \end{aligned} \quad (4.107)$$

The derivative in Eq. (4.107) expresses the following potential optimization or minimization

$$\text{stat}_{\theta} \left(\inf_{\mathbf{u}} \Psi \right) = \text{stat}_{\theta} \left(\tilde{\Psi} \right) , \quad (4.108)$$

in which we search for stationary points w.r.t. magnetization angle θ and the minimum w.r.t. displacement \mathbf{u} . While searching for stationary points w.r.t. θ , we simultaneously keep the displacement \mathbf{u} in its minimum. Essentially, we search for magnetic stationary points of a potential $\tilde{\Psi}$ which is mechanically minimized. As a result, the linear momentum balance is always fulfilled, $\text{div}(\boldsymbol{\sigma}) = \mathbf{0}$. After separating the trivial solution of the LLG equation $[\mathbf{u}_0, \theta_0]^\top$ from Eq. (4.107), we arrive at

$$\frac{d}{d\epsilon}\Psi(\underline{d}_0 + \epsilon\delta\underline{d}) = \epsilon \int_{V^{\text{fm}}} \left[-2A\Delta(\delta\theta) + 2\mathcal{L}\delta\theta - 3\mu^{\text{fm}}\Lambda_s \frac{\partial(\delta u_2)}{\partial x_1} \right] \delta\theta \, dv . \quad (4.109)$$

Next, we assume a Fourier series representation for $\delta\theta$ and $\delta\mathbf{u}$ similar to Eqs. (4.77) to (4.79) (but without the time dependence). We use Eq. (4.96), which we obtain from the linear momentum balance, to replace the Fourier coefficients of δu_2 . With the Kronecker delta property associated with Fourier series, we finally arrive at

$$\frac{d}{d\epsilon}\Psi(\underline{d}_0 + \epsilon\delta\underline{d}) = \epsilon L^2 h \sum_{l \in \mathbb{Z} \setminus \{0\}} \left(2Ak_l^2 + 2\mathcal{L} - \frac{9hk_l(\mu^{\text{fm}}\Lambda_s)^2}{\mu^s + h\mu^{\text{fm}}k_l} \right) \delta\theta_l \delta\theta_{-l} . \quad (4.110)$$

Since θ is a real-valued function, we find that the Fourier coefficient $\delta\theta_{-l}$ is equal to its complex conjugate $\delta\theta_l^*$. Hence, the expression $\delta\theta_l \delta\theta_{-l} = \delta\theta_l \delta\theta_l^* = |\delta\theta_l|^2 \geq 0$ in Eq. (4.110) is non-negative. Furthermore, the expression $\epsilon L^2 h > 0$ in Eq. (4.110) is positive. Assuming the respective Fourier mode $\delta\theta_l \neq 0$ does not vanish, the term in parenthesis in Eq. (4.110) determines whether $d\Psi(\underline{d}_0 + \epsilon\delta\underline{d})/d\epsilon$ is greater or smaller than zero and thus determines

stability. The term in parenthesis in Eq. (4.110) coincides with the stability criterion in Eq. (4.105).

To conclude, the reasoning based on attenuation or amplification of perturbations in Sec. 4.6 is completely equivalent to the energetic reasoning in this section. Undulations occur due to energetic instability.

4.8 Results

4.8.1 Qualitative conclusions from the stability criterion

In case the stability criterion in Eq. (4.105) gives $f > 0$, the trivial solution in Eqs. (4.67) and (4.68) is stable (i.e., valid). Then, the magnetization \mathbf{m} is homogeneously aligned in x_1 -direction ($\theta = 0$) and no undulations are expected. Conversely, if the stability criterion yields $f < 0$, the introduced perturbations intensify and the trivial solution is unstable (i.e., not valid). In this case, undulations can occur.

In the following, we want to discuss special cases of the stability criterion f . All discussed points pivot on our energetic interpretation that the magneto-mechanical material can reduce its elastic energy by forming undulations (elastic energy is driving force for undulations). The stability criterion in Eq. (4.105) predicts stability ($f > 0$) in the following special cases (with $A, \mathcal{L} > 0$):

- For vanishing magnetostriction $\Lambda_s \rightarrow 0$, no undulations occur. The elastic energy is not coupled to magnetic energies. Hence, *elastic* energy cannot be reduced by forming *magnetic* undulations.
- In case of a rigid substrate, $\mu^s \rightarrow \infty$, no undulations occur. To create undulations, the magnetization in the film has to rotate from its initial homogeneous state. By virtue of magnetostrictive coupling, this rotation leads to deformation of the film. Since film and substrate share a surface (see Fig. 4.2), deformation of the substrate ensues. For a rigid substrate, this deformation is thwarted and, consequently, undulations are prevented.
- A mechanically soft film $\mu^{\text{fm}} \rightarrow 0$ does not exhibit undulations. The elastic energy of the film scales with μ^{fm} . With vanishing shear modulus μ^{fm} we essentially deactivate the elastic energy associated with magnetostrictive strain. Thus, the driving energy for undulations drops out.
- For a film with vanishing thickness $h \rightarrow 0$, no undulations occur. The elastic energy of the film is computed as the volume integral of the elastic energy density. With vanishing film thickness h , we decrease the film volume and the elastic energy to zero. Again, the driving energy for undulations drops out.

4.8.2 Stability maps

The stability criterion in Eq. (4.105) depends on various film and substrate parameters. We are particularly interested in the dependence of the stability criterion f on the undulation wavelength λ_l because the latter can be observed in experiments, see Fig. 4.1a. We showcase an example of a stability criterion plot $f(\lambda_l)$ for different substrate shear moduli μ^s in Fig. 4.4 (for other parameters, see caption of the figure). Minima $(\lambda_l^{\min}, f_{\min})$ are highlighted with red dots. In case the minimum f_{\min} is smaller than or equal to zero, there is at least one unstable

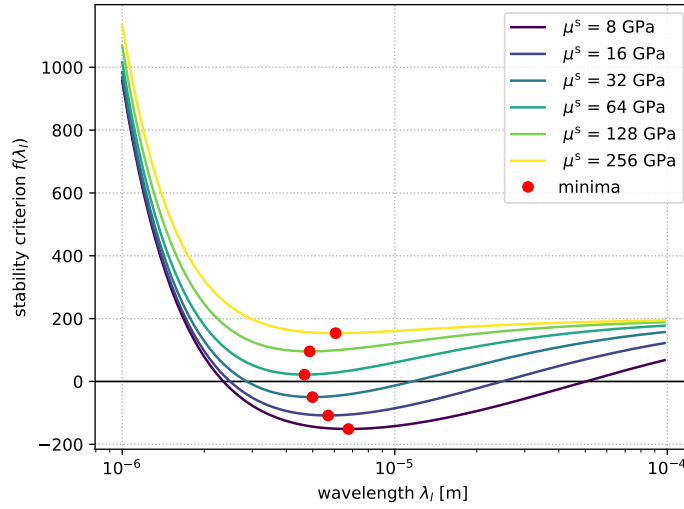


Fig. 4.4: Example of stability criterion $f(\lambda_l)$ for different substrate shear moduli μ^s , minima highlighted with red dots, remaining parameters fixed: $\mathcal{L} = 100\text{J/m}^3$, $h = 1\mu\text{m}$, $\mu^{\text{fm}} = 54\text{GPa}$, $A = 15\text{pJ/m}$, $\Lambda_s = 30 \cdot 10^{-6}$.

mode. Thus, at least one undulation wavelength occurs. To paraphrase, undulations occur if $f_{\min} < 0$.

In the following, we use the former criterion to create stability maps. To this end, we compute the wavelength λ_l^{\min} at which the minimum f_{\min} occurs

$$\lambda_l^{\min} = \arg \min_{\lambda_l} f(A, \lambda_l, \mathcal{L}, \Lambda_s, \mu^{\text{fm}}, h, \mu^s) . \quad (4.111)$$

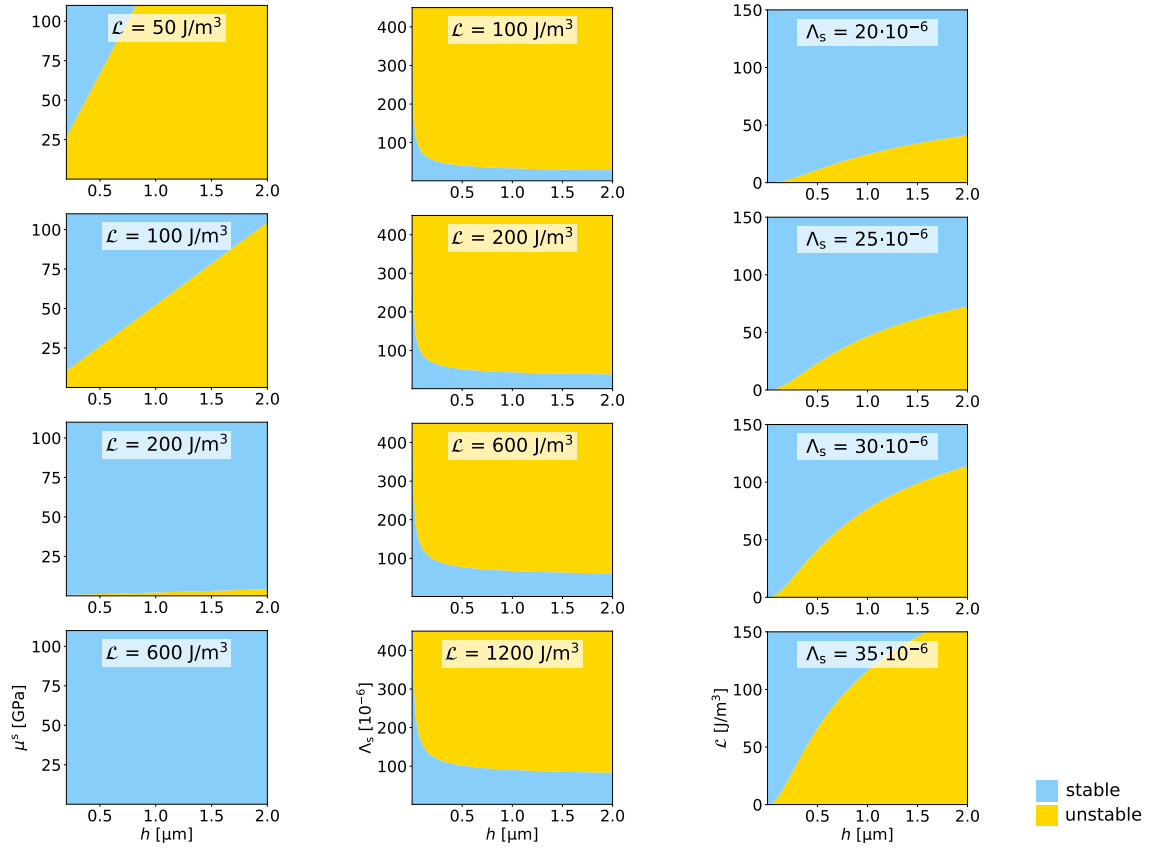
Hence, the stability limit occurs at

$$f(A, \lambda_l, \mathcal{L}, \Lambda_s, \mu^{\text{fm}}, h, \mu^s) \Big|_{\lambda_l = \lambda_l^{\min}} = 0 . \quad (4.112)$$

We rearrange Eq. (4.112) to yield one model parameter as a function of another model parameter *at the stability limit*. For example, we choose fixed A , \mathcal{L} , Λ_s and μ^{fm} and rearrange Eq. (4.112) to obtain $\mu^s(h)$ at the stability limit, see Fig. 4.5a. Values of μ^s that are larger than the obtained stability limit yield stable behavior (no undulations, blue in stability map). Smaller values of μ^s yield unstable behavior (undulations, yellow in stability map).

We showcase three examples of such stability maps in Fig. 4.5. With these stability maps, we investigate parameter ranges tailored to the parameter sets of FeCoSiB [138, 139] thin film material and silicon substrate material. The influence of the exchange stiffness constant A on the stability criterion is of small interest. Large A fosters $f > 0$ and prevents undulating magnetization structure. This behavior conforms to the physical interpretation of the exchange energy ψ_{ex} . Hence, in Fig. 4.5, we always keep the exchange stiffness constant fixed at $A = 15\text{pJ/m}$.

Fig. 4.5a illustrates a linear relation $\mu^s(h)$ at the stability limit. Large film thickness h



(a) $\mu^{\text{fm}} = 54\text{GPa}$,
 $\Lambda_s = 30 \cdot 10^{-6}$

(b) $\mu^{\text{fm}} = 54\text{GPa}$,
 $\mu^s = 80\text{GPa}$

(c) $\mu^s = 80\text{GPa}$,
 $\mu^{\text{fm}} = 54\text{GPa}$

Fig. 4.5: Examples of stability maps for (a) μ^s (b) Λ_s and (c) \mathcal{L} in dependence of film thickness h , blue indicates stable regime (no undulations), yellow indicates unstable regime (undulations possible).

introduces a large amount of elastic energy (driving force for undulations). To prevent undulations, we need a stiff substrate because it resists the magnetization rotation introduced by undulations. Hence, a large film thickness h requires a large substrate shear modulus μ^s to remain stable. Furthermore, large \mathcal{L} increases the stable regime because the alignment constant \mathcal{L} is forcing magnetization to conform with a homogeneous magnetization state.

Fig. 4.5b showcases an inversely proportional relation $\Lambda_s(h)$ at the stability limit. Again,

large film thickness h corresponds to large elastic driving force for undulations. One way to prevent undulations is to weaken the coupling between magnetics and mechanics (small Λ_s). With small Λ_s , the *elastic* energy gain from changing the *magnetization* state (creating undulations) is small and undulations become less favorable. Hence, large film thickness h requires small Λ_s to remain stable. As before, large \mathcal{L} increases the stable regime. Fig. 4.5c displays a non-linear increasing relation $\mathcal{L}(h)$ at the stability limit. Similar to Figs. 4.5a and 4.5b, we are able to observe the stabilizing effect (contra undulation) of \mathcal{L} and the destabilizing effect (pro undulation) of Λ_s .

4.8.3 Undulation wavelength and stability limit of alignment constant

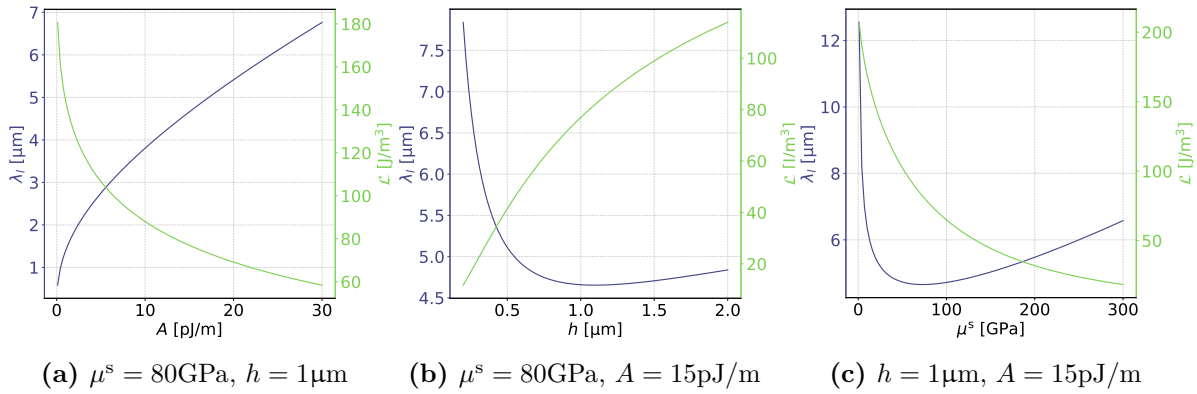


Fig. 4.6: Undulation wavelength λ_l and uniaxial alignment \mathcal{L} at stability limit as functions of (a) exchange stiffness constant A , (b) film thickness h , and (c) substrate shear modulus μ^s ; $\Lambda_s = 30 \cdot 10^{-6}$, $\mu^{\text{fm}} = 54 \text{ GPa}$.

So far, we discussed the influence of system parameters on stability. However, we did not yet relate model parameters to the experimentally observable undulation wavelength λ_l . In Fig. 4.6, we display the undulation wavelength λ_l and the uniaxial alignment \mathcal{L} as functions of model parameters. The displayed wavelength corresponds to the wavelength λ_l^{min} at which the minimum of f occurs, see Eq. (4.111). This is the undulation wavelength that would most probably be observable experimentally. The displayed alignment parameter corresponds to \mathcal{L} for which the stability limit occurs, see Eq. (4.112) (solve for \mathcal{L}). We include \mathcal{L} here because anisotropy (or lack thereof) is crucial for the emergence of undulations.

In Fig. 4.6a, we observe a monotonically increasing relation between undulation wavelength λ_l and exchange stiffness constant A . Moreover, in Fig. 4.6a, we also observe an inverse relation of \mathcal{L} w.r.t. A . Both A and \mathcal{L} prevent undulations because the associated energies align magnetization locally (either with neighbors or with easy axis). In case of a small exchange stiffness constant A , we need a high alignment constant \mathcal{L} to stay at the stability limit (to prevent undulations). \mathcal{L} compensates for missing A (and vice versa).

In Fig. 4.6b, we display the undulation wavelength λ_l and the uniaxial alignment \mathcal{L} as functions of film thickness h . The behavior of λ_l w.r.t. h is non-monotonic and appears to have a

minimum around $h \approx 1\mu\text{m}$. The behavior of \mathcal{L} as a function of h conforms with the discussion for Fig. 4.5c.

In Fig. 4.6c, we observe a non-monotonic relation between undulation wavelength λ_l and substrate shear modulus μ^s with an apparent minimum around $\mu^s = 70\text{GPa}$. This behavior is also observable by tracing the red dots (minima) in Fig. 4.4. The behavior of the alignment constant \mathcal{L} w.r.t. substrate shear modulus μ^s in Fig. 4.6c is similar to the relation between \mathcal{L} and A in Fig. 4.6a. Both \mathcal{L} and μ^s prevent undulations. Large \mathcal{L} aligns magnetization with the easy axis and large μ^s obstructs magnetization rotation by obstructing substrate deformation. In case either \mathcal{L} or μ^s is small, we need the other to compensate in order to stay at the stability limit.

Particularly noteworthy is the fact that all predicted wavelengths are in the order of 1 to $10\mu\text{m}$, which is consistent with experimentally observed structures, see Fig. 4.1a.

4.9 Conclusion

We presented a stability analysis for composites of magneto-elastic thin film and elastic substrate. We obtained a criterion which allows to predict the stability of a homogeneous magnetization state. Unstable behavior corresponds to undulations.

We investigated the stability criterion w.r.t. material and geometry parameters of thin film and substrate. To this end, we created stability maps involving relevant parameter sets. The results are in good agreement with experimental observations.

With this work, we intended to gain insights into the micromagnetic effects related to undulations and to form a basis to gather ideas for smarter sensor design. In this respect, the stability criterion can serve as a rigorous guideline to support the design process for thin film composites. By exploring and discussing the stability criterion, we were able to shed some new light upon the underpinning micromagnetic effects of the considered undulations.

Acknowledgment

This research was supported by the Deutsche Forschungsgemeinschaft (DFG, German Research Foundation) under project 286471992 (Collaborative Research Center 1261). We thank Benjamin Spetzler, Necdet Onur Urs and Matic Jovičević-Klug for helpful discussions.

Appendix

4.A Vanishing magnetic potential

Under the assumptions made in this work, the magnetic potential φ for the magnetic thin film vanishes. The magnetic potential φ can be expressed explicitly as

$$\varphi = \frac{M_s}{4\pi} \left(\int_{V^{\text{fm}}} \frac{-\text{div}'(\mathbf{m}(\mathbf{x}'))}{\|\mathbf{x} - \mathbf{x}'\|} dv' + \int_{\partial V^{\text{fm}}} \frac{\mathbf{m}(\mathbf{x}') \cdot \mathbf{n}}{\|\mathbf{x} - \mathbf{x}'\|} da' \right), \quad (4.113)$$

see [28], where \mathbf{n} denotes the outer normal of the volume V^{fm} . The divergence of $\mathbf{m}(\mathbf{x}') = \mathbf{e}_1 + \theta \mathbf{e}_2$ vanishes if the assumption $\theta = \theta(x_1)$ from Sec. 4.5 is adopted. This leaves only the surface terms

$$\varphi = \frac{M_s}{4\pi} \left(\int_{A(x'_1=0)} \frac{\mathbf{m}(\mathbf{x}') \cdot (-\mathbf{e}_1)}{\|\mathbf{x} - \mathbf{x}'\|} da' + \int_{A(x'_1=L)} \frac{\mathbf{m}(\mathbf{x}') \cdot \mathbf{e}_1}{\|\mathbf{x} - \mathbf{x}'\|} da' \right. \quad (4.114)$$

$$\left. \int_{A(x'_2=0)} \frac{\mathbf{m}(\mathbf{x}') \cdot (-\mathbf{e}_2)}{\|\mathbf{x} - \mathbf{x}'\|} da' + \int_{A(x'_2=L)} \frac{\mathbf{m}(\mathbf{x}') \cdot \mathbf{e}_2}{\|\mathbf{x} - \mathbf{x}'\|} da' \right. \quad (4.115)$$

$$\left. \int_{A(x'_3=0)} \frac{\mathbf{m}(\mathbf{x}') \cdot (-\mathbf{e}_3)}{\|\mathbf{x} - \mathbf{x}'\|} da' + \int_{A(x'_3=h)} \frac{\mathbf{m}(\mathbf{x}') \cdot \mathbf{e}_3}{\|\mathbf{x} - \mathbf{x}'\|} da' \right). \quad (4.116)$$

The integrals in Eqs. (4.114) and (4.115) vanish due to periodicity in x_1 - and x_2 -direction and the integrals in Eq. (4.116) vanish since $\mathbf{m} \cdot \mathbf{e}_3 = 0$. Thus, the magnetic potential φ vanishes altogether.

CHAPTER 5

Summary and outlook

The dissertation at hand was devoted to continuum models which describe the local material orientation using a director. Two peer-reviewed publications and one manuscript prepared for publication were presented to illustrate various facets of directors in continuum models. Throughout this work, we showed that director-based continuum models are a powerful tool to represent locally oriented material behavior.

In Publication 1, we showcased a gradient-extended phase-field damage model in the finite strain setting. The formulation as a GSM means that the model is thermodynamically consistent. The desire to capture tension-compression asymmetry and anisotropic crack behavior led us to introduce a crack orientation director. To obtain a norm conserving algorithm, we made use of the exponential map. The crack orientation director, in combination with a set of internal variables, enables the representation of fracture modes *I*, *II*, *III* in each material point. Particularly noteworthy is that the model assumptions entail a traction free crack surface.

The second publication dealt with micromagnetics and small strain linear elasticity coupled by magnetostriction. In this model, the magnetization is represented by a unit vector (director). Norm conservation is achieved by using the exponential map in conjunction with the modified Crank-Nicolson time integration scheme. In addition to being norm conservative, the latter is second order accurate and enables larger time steps compared to a first order accurate time integration scheme. We started the model formulation based on the GSM framework and later introduced an additional term to represent precession. Although this represents a departure from GSM, thermodynamic consistency was retained since precession is an energy conservative process and the dissipative properties of the model remained un-

changed. We applied the model to investigate Barkhausen noise in magnetostrictive thin film composites. Our scheme to quantify Barkhausen noise is based on ensemble averaging. Coupled micro-magneto-mechanics was also the topic of Manuscript 3. In this case, we investigated a particular domain (sub-)structure which we referred to as *undulations*. An analytical theory based on a model system with simplified geometry and kinematics was developed to assess the emergence of undulations. To this end, a homogeneously magnetized state was assumed to be subject to small (spatially) periodic perturbations. Self-amplification of these perturbations was interpreted as what is experimentally observed as undulations. Besides this perturbation approach, we also took the energetic perspective and arrived at the same conclusion. The main outcome of Manuscript 3 is a stability criterion which allows to assess the emergence of undulations. It can serve as a design guideline to support the development of thin film composites. With regard to director-based continua, the model contains the magnetization director which is expressed in polar coordinates and later linearized around a fixed orientation. Since the theory is purely analytical, no computational techniques were necessary to retain the magnetization norm.

As with most research work, there is still room for improvement. Ideas for future work include a range of technical improvements, extensions and applications.

With respect to Publication 1, for example, it could be interesting to extend the model to the three-dimensional case, introduce friction between the locally assumed layers or try out other formulations of anisotropic material behavior.

For Publication 2, further numerical studies could yield interesting results. The relation between magnetic noise and applied field (magnitude and frequency) could be quantified. Furthermore, other types of Barkhausen noise processes (other than interaction of domain walls with defects) could be investigated. This would address the question of what happens when the domain wall structure is lost (vortex formation, magnetization reversal without domain walls).

With regard to Manuscript 3, it would be insightful to apply the stability criterion as a design guideline in practice and assess the accuracy of the predictions. Moreover, we could explore the feasibility of describing other types of periodic magnetic domain phenomena in a similar way.

Other ideas are less technical and address more overarching questions. Both, Publications 1 and 2, are based on phase-field models (damage, magnetization) characterized by strong localized gradients which necessitate fine spatial resolution. In case of the damage model, this always entailed a precursory simulation with coarse mesh to determine the crack path and a subsequent local mesh refinement for the actual simulation. For the magneto-mechanical model, we were restricted to using fine mesh in the entire material domain due to the motion of the domain walls. Both these problems could benefit from techniques to reduce the number of degrees of freedom in areas with little activity (small gradients). In this respect, adaptive mesh refinement and model order reduction techniques spring to mind.

Somewhat related is the following challenge regarding scale. Due to the limitations w.r.t. spatial resolution, the noise computed in Publication 2 is valid only on the microscopic scale. Hence, a comparison with absolute noise values from experiments on the macroscopic scale is not straightforward. Further effort towards multi-scale noise computation and homogenization techniques would be necessary to bridge the scales.

The final thought is less a problem driven imperative but more an idea out of curiosity. It could be instructive to explore the relation between continuum models with directors (as used in the present dissertation) and (micro-)polar or Cosserat-type continua. Further investigation of the topic could help to identify new fields of application for continuum models with directors.

Bibliography

- [1] P. Duhem. “Le potentiel thermodynamique et la pression hydrostatique”. In: *Annales scientifiques de l’École Normale Supérieure*. Vol. 10. 1893, pp. 183–230.
- [2] E. M. P. Cosserat and F. Cosserat. *Théorie des corps déformables*. Paris, France: A. Hermann et fils, 1909.
- [3] J. Ericksen and C. Truesdell. “Exact theory of stress and strain in rods and shells”. In: *Archive for Rational Mechanics and Analysis* 1 (1957), pp. 295–323.
- [4] J. Altenbach, H. Altenbach, and V. A. Eremeyev. “On generalized Cosserat-type theories of plates and shells: a short review and bibliography”. In: *Archive of Applied Mechanics* 80.1 (2010), pp. 73–92.
- [5] M. E. Gurtin. “Generalized Ginzburg–Landau and Cahn–Hilliard equations based on a microforce balance”. In: *Physica D: Nonlinear Phenomena* 92.3-4 (1996), pp. 178–192.
- [6] B. D. Coleman and W. Noll. “The thermodynamics of elastic materials with heat conduction and viscosity”. In: *Archive for Rational Mechanics and Analysis* 13 (1963), pp. 167–178.
- [7] B. D. Coleman and M. E. Gurtin. “Thermodynamics with internal state variables”. In: *The Journal of Chemical Physics* 47.2 (1967), pp. 597–613.
- [8] A. E. Green and P. M. Naghdi. “On thermodynamics, rate of work and energy”. In: *Archive for Rational Mechanics and Analysis* 40 (1971), pp. 37–49.
- [9] A. E. Green and P. M. Naghdi. “On continuum thermodynamics”. In: *Archive for Rational Mechanics and Analysis* 48 (1972), pp. 352–378.
- [10] C. Miehe. “A multi-field incremental variational framework for gradient-extended standard dissipative solids”. In: *Journal of the Mechanics and Physics of Solids* 59.4 (2011), pp. 898–923.
- [11] B. Halphen and Q. S. Nguyen. “Sur les matériaux standard généralisés”. In: *Journal de Mécanique* 14.1 (1975), pp. 39–63.

- [12] C. Oseen. “The theory of liquid crystals”. In: *Transactions of the Faraday Society* 29.140 (1933), pp. 883–899.
- [13] F. C. Frank. “I. Liquid crystals. On the theory of liquid crystals”. In: *Discussions of the Faraday Society* 25 (1958), pp. 19–28.
- [14] F. Leslie. “Continuum theory of liquid crystals”. In: *Rheologica Acta* 10.1 (1971), pp. 91–95.
- [15] S. Singh and D. Dunmur. *Liquid Crystals: Fundamentals*. Singapore: World Scientific Publishing Company, 2002, p. 7.
- [16] J. Ericksen. “Equilibrium theory of liquid crystals”. In: *Advances in Liquid Crystals*. Vol. 2. Elsevier, 1976, pp. 233–298.
- [17] R. Bertóti and T. Böhlke. “Flow-induced anisotropic viscosity in short FRPs”. In: *Mechanics of Advanced Materials and Modern Processes* 3 (2017), pp. 1–12.
- [18] G. B. Jeffery. “The motion of ellipsoidal particles immersed in a viscous fluid”. In: *Proceedings of the Royal Society of London. Series A, containing Papers of a Mathematical and Physical Character* 102.715 (1922), pp. 161–179.
- [19] M. Junk and R. Illner. “A new derivation of Jeffery’s equation”. In: *Journal of Mathematical Fluid Mechanics* 9 (2007), pp. 455–488.
- [20] S. K. Kugler et al. “Fiber orientation predictions – a review of existing models”. In: *Journal of Composites Science* 4.2 (2020), p. 69.
- [21] S. S. Antman. “Kirchhoff’s problem for nonlinearly elastic rods”. In: *Quarterly of Applied Mathematics* 32.3 (1974), pp. 221–240.
- [22] S. S. Antman and K. B. Jordan. “5. – Qualitative Aspects of the Spatial Deformation of Non-linearly Elastic Rods”. In: *Proceedings of the Royal Society of Edinburgh Section A: Mathematics* 73 (1975), pp. 85–105.
- [23] J. C. Simo and L. Vu-Quoc. “On the dynamics in space of rods undergoing large motions – a geometrically exact approach”. In: *Computer Methods in Applied Mechanics and Engineering* 66.2 (1988), pp. 125–161.
- [24] J. C. Simo and D. D. Fox. “On a stress resultant geometrically exact shell model. Part I: Formulation and optimal parametrization”. In: *Computer Methods in Applied Mechanics and Engineering* 72.3 (1989), pp. 267–304.
- [25] A. E. Green, P. M. Naghdi, and W. L. Wainwright. “A general theory of a Cosserat surface”. In: *Archive for Rational Mechanics and Analysis* 20 (1965), pp. 287–308.
- [26] P. Betsch and N. Sängler. “On the use of geometrically exact shells in a conserving framework for flexible multibody dynamics”. In: *Computer Methods in Applied Mechanics and Engineering* 198.17-20 (2009), pp. 1609–1630.
- [27] J. Lu and C. Zheng. “Dynamic cloth simulation by isogeometric analysis”. In: *Computer Methods in Applied Mechanics and Engineering* 268 (2014), pp. 475–493.
- [28] J. M. D. Coey. *Magnetism and magnetic materials*. Cambridge, United Kingdom: Cambridge University Press, 2010.

- [29] W. F. Brown. *Magnetostatic principles in ferromagnetism*. Amsterdam: North-Holland Publ. Comp., 1962.
- [30] A. De Simone. “Energy minimizers for large ferromagnetic bodies”. In: *Archive for Rational Mechanics and Analysis* 125 (1993), pp. 99–143.
- [31] R. D. James and D. Kinderlehrer. “Frustration in ferromagnetic materials”. In: *Continuum Mechanics and Thermodynamics* 2 (1990), pp. 215–239.
- [32] P. Weiss. “L’hypothèse du champ moléculaire et la propriété ferromagnétique”. In: *Journal de Physique Théorique et Appliquée* 6.1 (1907), pp. 661–690.
- [33] L. Landau and E. Lifshitz. “On the theory of the dispersion of magnetic permeability in ferromagnetic bodies”. In: *Perspectives in Theoretical Physics*. Elsevier, 1992, pp. 51–65.
- [34] M. Kruzik and A. Prohl. “Recent developments in the modeling, analysis, and numerics of ferromagnetism”. In: *SIAM Review* 48.3 (2006), pp. 439–483.
- [35] C. Miehe and G. Ethiraj. “A geometrically consistent incremental variational formulation for phase field models in micromagnetics”. In: *Computer Methods in Applied Mechanics and Engineering* 245 (2012), pp. 331–347.
- [36] M. K. Keane and R. C. Rogers. “A finite dimensional model problem in ferromagnetism”. In: *Journal of Intelligent Material Systems and Structures* 4.4 (1993), pp. 463–468.
- [37] M. Reichel, B.-X. Xu, and J. Schröder. “A comparative study of finite element schemes for micromagnetic mechanically coupled simulations”. In: *Journal of Applied Physics* 132.18 (2022), p. 183903.
- [38] R. Cohen, S.-Y. Lin, and M. Luskin. “Relaxation and gradient methods for molecular orientation in liquid crystals”. In: *Computer Physics Communications* 53.1-3 (1989), pp. 455–465.
- [39] S.-Y. Lin and M. Luskin. “Relaxation methods for liquid crystal problems”. In: *SIAM Journal on Numerical Analysis* 26.6 (1989), pp. 1310–1324.
- [40] T. Koehler. “Hybrid FEM–BEM method for fast micromagnetic calculations”. In: *Physica B: Condensed Matter* 233.4 (1997), pp. 302–307.
- [41] D. Berkov, K. Ramstöck, and A. Hubert. “Solving micromagnetic problems. Towards an optimal numerical method”. In: *Physica Status Solidi (A)* 137.1 (1993), pp. 207–225.
- [42] A. Sridhar, M.-A. Keip, and C. Miehe. “Computational Homogenization in Micro-Magneto-Elasticity”. In: *PAMM* 15.1 (2015), pp. 363–364.
- [43] A. Sridhar, M.-A. Keip, and C. Miehe. “Homogenization in micro-magneto-mechanics”. In: *Computational Mechanics* 58.1 (2016), pp. 151–169.
- [44] D. Lewis and N. Nigam. “Geometric integration on spheres and some interesting applications”. In: *Journal of Computational and Applied Mathematics* 151.1 (2003), pp. 141–170.

- [45] P. B. Monk and O. Vacus. “Error estimates for a numerical scheme for ferromagnetic problems”. In: *SIAM Journal on Numerical Analysis* 36.3 (1999), pp. 696–718.
- [46] P. B. Monk and O. Vacus. “Accurate discretization of a non-linear micromagnetic problem”. In: *Computer Methods in Applied Mechanics and Engineering* 190.40-41 (2001), pp. 5243–5269.
- [47] A. W. Spargo, P. H. W. Ridley, and G. W. Roberts. “Geometric integration of the Gilbert equation”. In: *Journal of Applied Physics* 93.10 (2003), pp. 6805–6807.
- [48] C. Serpico, I. D. Mayergoyz, and G. Bertotti. “Numerical technique for integration of the Landau–Lifshitz equation”. In: *Journal of Applied Physics* 89.11 (2001), pp. 6991–6993.
- [49] M. d’Aquino, C. Serpico, and G. Miano. “Geometrical integration of Landau–Lifshitz–Gilbert equation based on the mid-point rule”. In: *Journal of Computational Physics* 209.2 (2005), pp. 730–753.
- [50] F. Alouges. “A new algorithm for computing liquid crystal stable configurations: the harmonic mapping case”. In: *SIAM Journal on Numerical Analysis* 34.5 (1997), pp. 1708–1726.
- [51] F. Alouges. “A new finite element scheme for Landau–Lifschitz equations”. In: *Discrete and Continuous Dynamical Systems - Series S* 1.2 (2008), pp. 187–196.
- [52] F. Alouges, E. Kritsikis, and J.-C. Toussaint. “A convergent finite element approximation for Landau–Lifschitz–Gilbert equation”. In: *Physica B: Condensed Matter* 407.9 (2012), pp. 1345–1349.
- [53] F. Alouges et al. “A convergent and precise finite element scheme for Landau–Lifschitz–Gilbert equation”. In: *Numerische Mathematik* 128.3 (2014), pp. 407–430.
- [54] I. Danaila and P. Kazemi. “A new Sobolev gradient method for direct minimization of the Gross–Pitaevskii energy with rotation”. In: *SIAM Journal on Scientific Computing* 32.5 (2010), pp. 2447–2467.
- [55] D. Suss, T. Schrefl, and J. Fidler. “Micromagnetics simulation of high energy density permanent magnets”. In: *IEEE Transactions on Magnetics* 36.5 (2000), pp. 3282–3284.
- [56] J. Fidler and T. Schrefl. “Micromagnetic modelling – the current state of the art”. In: *Journal of Physics D: Applied Physics* 33.15 (2000), R135.
- [57] W. Scholz et al. “Scalable parallel micromagnetic solvers for magnetic nanostructures”. In: *Computational Materials Science* 28.2 (2003), pp. 366–383.
- [58] M. Yi and B.-X. Xu. “A constraint-free phase field model for ferromagnetic domain evolution”. In: *Proceedings of the Royal Society A: Mathematical, Physical and Engineering Sciences* 470.2171 (2014), p. 20140517.
- [59] J. Wang and J. Zhang. “A real-space phase field model for the domain evolution of ferromagnetic materials”. In: *International Journal of Solids and Structures* 50.22-23 (2013), pp. 3597–3609.

- [60] H. Zhang, X. Zhang, and Y. Pei. “A finite element based real-space phase field model for domain evolution of ferromagnetic materials”. In: *Computational Materials Science* 118 (2016), pp. 214–223.
- [61] C. M. Landis. “A continuum thermodynamics formulation for micro-magneto-mechanics with applications to ferromagnetic shape memory alloys”. In: *Journal of the Mechanics and Physics of Solids* 56.10 (2008), pp. 3059–3076.
- [62] Y. Shi et al. “Phase field simulations on domain switching-induced toughening in ferromagnetic materials”. In: *European Journal of Mechanics-A/Solids* 65 (2017), pp. 205–211.
- [63] H. Szabolics et al. “A constrained finite element formulation for the Landau–Lifshitz–Gilbert equations”. In: *Computational Materials Science* 44.2 (2008), pp. 253–258.
- [64] D. Ohmer et al. “Phase-field modelling of paramagnetic austenite–ferromagnetic martensite transformation coupled with mechanics and micromagnetics”. In: *International Journal of Solids and Structures* 238 (2022), p. 111365.
- [65] J. C. Simo, D. D. Fox, and M. S. Rifai. “On a stress resultant geometrically exact shell model. Part III: Computational aspects of the nonlinear theory”. In: *Computer Methods in Applied Mechanics and Engineering* 79.1 (1990), pp. 21–70.
- [66] J. Faraut. *Analysis on Lie groups : An introduction*. Cambridge: Cambridge University Press, 2008, p. 19.
- [67] C. Dorn and S. Wulfinghoff. “A gradient-extended large-strain anisotropic damage model with crack orientation director”. In: *Computer Methods in Applied Mechanics and Engineering* 387 (2021), p. 114123.
- [68] A. A. Griffith. “VI. The phenomena of rupture and flow in solids”. In: *Philosophical Transactions of the Royal Society of London. Series A, containing Papers of a Mathematical or Physical Character* 221.582-593 (1921), pp. 163–198.
- [69] G. A. Francfort and J.-J. Marigo. “Revisiting brittle fracture as an energy minimization problem”. In: *Journal of the Mechanics and Physics of Solids* 46.8 (1998), pp. 1319–1342.
- [70] L. Ambrosio and V. M. Tortorelli. “Approximation of functional depending on jumps by elliptic functional via Γ -convergence”. In: *Communications on Pure and Applied Mathematics* 43.8 (1990), pp. 999–1036.
- [71] H. Amor, J.-J. Marigo, and C. Maurini. “Regularized formulation of the variational brittle fracture with unilateral contact: Numerical experiments”. In: *Journal of the Mechanics and Physics of Solids* 57.8 (2009), pp. 1209–1229.
- [72] F. Freddi and G. Royer-Carfagni. “Regularized variational theories of fracture: A unified approach”. In: *Journal of the Mechanics and Physics of Solids* 58.8 (2010), pp. 1154–1174.
- [73] C. Miehe, M. Hofacker, and F. Welschinger. “A phase field model for rate-independent crack propagation: Robust algorithmic implementation based on operator splits”. In:

- Computer Methods in Applied Mechanics and Engineering* 199.45-48 (2010), pp. 2765–2778.
- [74] C. Miehe, F. Welschinger, and M. Hofacker. “Thermodynamically consistent phase–field models of fracture: Variational principles and multi–field FE implementations”. In: *International Journal for Numerical Methods in Engineering* 83.10 (2010), pp. 1273–1311.
 - [75] M. Strobl and T. Seelig. “A novel treatment of crack boundary conditions in phase field models of fracture”. In: *PAMM* 15.1 (2015), pp. 155–156.
 - [76] M. Strobl and T. Seelig. “On constitutive assumptions in phase field approaches to brittle fracture”. In: *Procedia Structural Integrity* 2.3705-3712 (2016), 21st.
 - [77] M. Strobl and T. Seelig. “Restrictions in phase field modeling of brittle fracture”. In: *PAMM* 18.1 (2018), e201800157.
 - [78] P. Shanthraj et al. “Elasto–viscoplastic phase field modelling of anisotropic cleavage fracture”. In: *Journal of the Mechanics and Physics of Solids* 99 (2017), pp. 19–34.
 - [79] E. C. Bryant and W. Sun. “A mixed–mode phase field fracture model in anisotropic rocks with consistent kinematics”. In: *Computer Methods in Applied Mechanics and Engineering* 342 (2018), pp. 561–584.
 - [80] O. Aslan and S. Forest. “Crack growth modelling in single crystals based on higher order continua”. In: *Computational Materials Science* 45.3 (2009), pp. 756–761.
 - [81] O. Aslan and S. Forest. “The micromorphic versus phase field approach to gradient plasticity and damage with application to cracking in metal single crystals”. In: *Multiscale Methods in Computational Mechanics: Progress and Accomplishments* (2011), pp. 135–153.
 - [82] P. A. Sabnis, S. Forest, and J. Cormier. “Microdamage modelling of crack initiation and propagation in FCC single crystals under complex loading conditions”. In: *Computer Methods in Applied Mechanics and Engineering* 312 (2016), pp. 468–491.
 - [83] K. Pham et al. “Gradient damage models and their use to approximate brittle fracture”. In: *International Journal of Damage Mechanics* 20.4 (2011), pp. 618–652.
 - [84] S. Forest. “Micromorphic approach for gradient elasticity, viscoplasticity, and damage”. In: *Journal of Engineering Mechanics* 135.3 (2009), pp. 117–131.
 - [85] P. Wriggers. *Nonlinear finite element methods*. Berlin, Germany: Springer Berlin Heidelberg, 2008, pp. 22–23, 134–136.
 - [86] T. Linse et al. “A convergence study of phase–field models for brittle fracture”. In: *Engineering Fracture Mechanics* 184 (2017), pp. 307–318.
 - [87] K. S. Chavan, B. P. Lamichhane, and B. I. Wohlmuth. “Locking–free finite element methods for linear and nonlinear elasticity in 2D and 3D”. In: *Computer Methods in Applied Mechanics and Engineering* 196.41-44 (2007), pp. 4075–4086.
 - [88] R. L. Taylor. *FEAP – Finite Element Analysis Program*. <http://projects.ce.berkeley.edu/feap/>. 2017.

- [89] C. Geuzaine and J.-F. Remacle. “Gmsh: A 3-D finite element mesh generator with built-in pre- and post-processing facilities”. In: *International Journal for Numerical Methods in Engineering* 79.11 (2009), pp. 1309–1331.
- [90] J. Ahrens, B. Geveci, and C. Law. “Paraview: An end-user tool for large data visualization”. In: *The Visualization Handbook* 717 (2005).
- [91] T. Williams, C. Kelley, et al. *Gnuplot 5.2: An interactive plotting program*. <http://www.gnuplot.info>. 2017.
- [92] M. Ambati, T. Gerasimov, and L. De Lorenzis. “A review on phase-field models of brittle fracture and a new fast hybrid formulation”. In: *Computational Mechanics* 55.2 (2015), pp. 383–405.
- [93] D. Gross and T. Seelig. *Bruchmechanik*. 6th ed. Berlin, Germany: Springer Berlin Heidelberg, 2016, pp. 132–135.
- [94] S. K. Maiti. *Fracture Mechanics*. Delhi, India: Cambridge University Press, 2015, pp. 152–162.
- [95] M. Fassin et al. “Efficient algorithmic incorporation of tension compression asymmetry into an anisotropic damage model”. In: *Computer Methods in Applied Mechanics and Engineering* 354 (2019), pp. 932–962.
- [96] C. Steinke and M. Kaliske. “A phase-field crack model based on directional stress decomposition”. In: *Computational Mechanics* 63.5 (2019), pp. 1019–1046.
- [97] J.-Y. Wu et al. “A variationally consistent phase-field anisotropic damage model for fracture”. In: *Computer Methods in Applied Mechanics and Engineering* 358 (2020), p. 112629.
- [98] H. Jeong et al. “Phase field modeling of crack propagation under combined shear and tensile loading with hybrid formulation”. In: *Computational Materials Science* 155 (2018), pp. 483–492.
- [99] C. Dorn, M. Hörsting, and S. Wulfinhoff. “Computing Barkhausen noise spectra for magnetostrictive thin film composites using efficient magnetization-magnitude preserving simulation techniques”. In: *Journal of Applied Physics* 134.13 (2023).
- [100] V. Röbisch et al. “Pushing the detection limit of thin film magnetoelectric heterostructures”. In: *Journal of Materials Research* 32.6 (2017), pp. 1009–1019.
- [101] M. Fiebig. “Revival of the magnetoelectric effect”. In: *Journal of Physics D: Applied Physics* 38.8 (2005), R123.
- [102] H. Bittel. “Noise of ferromagnetic materials”. In: *IEEE Transactions on Magnetics* 5.3 (1969), pp. 359–365.
- [103] D. Spasojević et al. “Barkhausen noise: Elementary signals, power laws, and scaling relations”. In: *Physical Review E* 54.3 (1996), p. 2531.
- [104] P. Mazzetti and G. Montalenti. “Power spectrum of the Barkhausen noise of various magnetic materials”. In: *Journal of Applied Physics* 34.11 (1963), pp. 3223–3225.
- [105] M. Küpferling et al. “Barkhausen noise in plastically deformed low-carbon steels”. In: *Journal of Magnetism and Magnetic Materials* 320.20 (2008), e527–e530.

- [106] G. Bertotti and A. Montorsi. “Dependence of Barkhausen noise on grain size in ferromagnetic materials”. In: *Journal of Magnetism and Magnetic Materials* 83.1-3 (1990), pp. 214–216.
- [107] N. J. Wiegman. “Barkhausen noise in magnetic thin films”. PhD thesis. Technische Hogeschool Eindhoven, 1979.
- [108] B. Alessandro et al. “Domain-wall dynamics and Barkhausen effect in metallic ferromagnetic materials. I. Theory”. In: *Journal of Applied Physics* 68.6 (1990), pp. 2901–2907.
- [109] P. J. Cote and L. V. Meisel. “Self-organized criticality and the Barkhausen effect”. In: *Physical Review Letters* 67.10 (1991), p. 1334.
- [110] K. Yamaguchi et al. “Monte Carlo simulation of Barkhausen noise for micromagnetic clusters”. In: *IEEE Transactions on Magnetics* 41.5 (2005), pp. 1536–1539.
- [111] J. A. Pérez-Benitez, J. Capó-Sánchez, and L. R. Padovese. “Simulation of the Barkhausen Noise using random field Ising model with long-range interaction”. In: *Computational Materials Science* 44.3 (2009), pp. 850–857.
- [112] D. C. Jiles and W. Kiarie. “An integrated model of magnetic hysteresis, the magneto-mechanical effect, and the Barkhausen effect”. In: *IEEE Transactions on Magnetics* 57.2 (2020), pp. 1–11.
- [113] S. Santa-aho et al. “Barkhausen noise probes and modelling: A review”. In: *Journal of Nondestructive Evaluation* 38.4 (2019), p. 94.
- [114] T. Herranen and L. Laurson. “Barkhausen noise from precessional domain wall motion”. In: *Physical Review Letters* 122.11 (2019), p. 117205.
- [115] S. Kaappa and L. Laurson. “Barkhausen noise from formation of 360° domain walls in disordered permalloy thin films”. In: *Physical Review Research* 5.2 (2023), p. L022006.
- [116] C. Dorn and S. Wulfinhoff. “Computing magnetic noise with micro-magneto-mechanical simulations”. In: *IEEE Transactions on Magnetics* 59.2 (2022), pp. 1–4.
- [117] T. L. Gilbert. “A phenomenological theory of damping in ferromagnetic materials”. In: *IEEE Transactions on Magnetics* 40.6 (2004), pp. 3443–3449.
- [118] B. Yang and D. R. Fredkin. “Dynamical micromagnetics by the finite element method”. In: *IEEE Transactions on Magnetics* 34.6 (1998), pp. 3842–3852.
- [119] M.-A. Keip and A. Sridhar. “A variationally consistent phase-field approach for micro-magnetic domain evolution at finite deformations”. In: *Journal of the Mechanics and Physics of Solids* 125 (2019), pp. 805–824.
- [120] J. Crank and P. Nicolson. “A practical method for numerical evaluation of solutions of partial differential equations of the heat-conduction type”. In: *Mathematical Proceedings of the Cambridge Philosophical Society*. Vol. 43. 1. Cambridge University Press. 1947, pp. 50–67.
- [121] S. Kogan. *Electronic noise and fluctuations in solids*. Cambridge, UK: Cambridge University Press, 2008, p. 5.

- [122] A. Hubert and R. Schäfer. *Magnetic domains: the analysis of magnetic microstructures*. 3rd ed. Berlin, Germany: Springer Science & Business Media, 2008.
- [123] H. Kronmüller and M. Fähnle. *Micromagnetism and the microstructure of ferromagnetic solids*. Cambridge, United Kingdom: Cambridge University Press, 2003.
- [124] G. Ethiraj, A. Sridhar, and C. Miehe. “Variational modeling and homogenization in dissipative magneto–mechanics”. In: *GAMM-Mitteilungen* 38.1 (2015), pp. 75–101.
- [125] C. Miehe, D. Rosato, and B. Kiefer. “Variational principles in dissipative electro–magneto–mechanics: A framework for the macro–modeling of functional materials”. In: *International Journal for Numerical Methods in Engineering* 86.10 (2011), pp. 1225–1276.
- [126] J. Fish and T. Belytschko. *A first course in finite elements*. Vol. 1. Chichester, England: John Wiley & Sons New York, 2007, p. 185.
- [127] P. Hayes et al. “Electrically modulated magnetoelectric AlN/FeCoSiB film composites for DC magnetic field sensing”. In: *Journal of Physics D: Applied Physics* 51.35 (2018), p. 354002.
- [128] P. Hayes et al. “Converse magnetoelectric composite resonator for sensing small magnetic fields”. In: *Scientific Reports* 9.1 (2019), p. 16355.
- [129] C. Miehe. “Strain–driven homogenization of inelastic microstructures and composites based on an incremental variational formulation”. In: *International Journal for Numerical Methods in Engineering* 55.11 (2002), pp. 1285–1322.
- [130] M. A. Carlton and J. L. Devore. *Probability with applications in engineering, science, and technology*. Cham, Switzerland: Springer, 2017.
- [131] F. Bruckner et al. “Large scale finite–element simulation of micromagnetic thermal noise”. In: *Journal of Magnetism and Magnetic Materials* 475 (2019), pp. 408–414.
- [132] R. L. Taylor. *FEAP – A Finite Element Analysis Program*. <http://projects.ce.berkeley.edu/feap/>. 2020.
- [133] S. Balay et al. “Efficient Management of Parallelism in Object Oriented Numerical Software Libraries”. In: *Modern Software Tools in Scientific Computing*. Ed. by E. Arge, A. M. Bruaset, and H. P. Langtangen. Birkhäuser Press, 1997, pp. 163–202.
- [134] G. S. Abo et al. “Definition of magnetic exchange length”. In: *IEEE Transactions on Magnetics* 49.8 (2013), pp. 4937–4939.
- [135] R. H. Charles et al. “Array programming with NumPy”. In: *Nature* 585.7825 (2020), pp. 357–362.
- [136] J. D. Hunter. “Matplotlib: A 2D graphics environment”. In: *Computing in Science & Engineering* 9.3 (2007), pp. 90–95.
- [137] P. Virtanen et al. “SciPy 1.0: Fundamental Algorithms for Scientific Computing in Python”. In: *Nature Methods* 17 (2020), pp. 261–272.
- [138] N. O. Urs et al. “Origin of hysteretic magnetoelastic behavior in magnetoelectric 2-2 composites”. In: *Applied Physics Letters* 105.20 (2014), pp. 2012–2017.

- [139] N. Martin et al. "Local stress engineering of magnetic anisotropy in soft magnetic thin films". In: *Applied Physics Letters* 94.6 (2009), p. 062506.
- [140] C. Dorn and S. Wulfinhoff. *Code and data used for "Computing Barkhausen noise spectra for magnetostrictive thin film composites using efficient magnetization-magnitude preserving simulation techniques"*. 2023. DOI: 10.57892/100-15.
- [141] C. Kittel. "On the theory of ferromagnetic resonance absorption". In: *Physical Review* 73.2 (1948), p. 155.
- [142] D. G. Hwang and H. C. Kim. "The influence of plastic deformation on Barkhausen effects and magnetic properties in mild steel". In: *Journal of Physics D: Applied Physics* 21.12 (1988), p. 1807.
- [143] C. Jagadish, L. Clapham, and D. L. Atherton. "Influence of uniaxial elastic stress on power spectrum and pulse height distribution of surface Barkhausen noise in pipeline steel". In: *IEEE Transactions on Magnetics* 26.3 (1990), pp. 1160–1163.
- [144] N. J. Wiegman. "Barkhausen effect in magnetic thin films: Experimental noise spectra". In: *Applied Physics* 12 (1977), pp. 157–161.
- [145] G. Durin, A. Magni, and G. Bertotti. "Measurements of the Barkhausen effect in FeCoB amorphous alloys". In: *Journal of Magnetism and Magnetic Materials* 160 (1996), pp. 299–301.
- [146] G. Durin and S. Zapperi. "On the power spectrum of magnetization noise". In: *Journal of Magnetism and Magnetic Materials* 242 (2002), pp. 1085–1088.
- [147] G. Durin et al. "Signature of negative domain wall mass in soft magnetic materials". In: *Journal of Magnetism and Magnetic Materials* 316.2 (2007), pp. 436–441.
- [148] F. Bohn et al. "Statistical properties of Barkhausen noise in amorphous ferromagnetic films". In: *Physical Review E* 90.3 (2014), p. 032821.
- [149] T. Hamaguchi, T. Ichihara, and T. Ohtsu. "Analysis of Barkhausen noise failure caused by ESD in a GMR head". In: *2002 Electrical Overstress/Electrostatic Discharge Symposium*. IEEE. 2002, pp. 119–122.
- [150] N. Stutzke, S. Burkett, and S. E. Russek. "High-frequency noise measurements in spin-valve devices". In: *Journal of Vacuum Science & Technology A: Vacuum, Surfaces, and Films* 21.4 (2003), pp. 1167–1171.
- [151] N. Daher and G. A. Maugin. "The method of virtual power in continuum mechanics application to media presenting singular surfaces and interfaces". In: *Acta Mechanica* 60.3 (1986), pp. 217–240.
- [152] J. McCord et al. "Stress-induced remagnetization in magnetostrictive films". In: *Journal of Applied Physics*. Vol. 95. 11. American Institute of Physics AIP, 2004, pp. 6861–6863.
- [153] J. Cullen and M. Wuttig. "Domain walls in elastically soft crystals". In: *Journal of Applied Physics* 91.10 (2002), pp. 7804–7806.

- [154] C. Müller et al. “Imaging of Love Waves and Their Interaction with Magnetic Domain Walls in Magnetoelectric Magnetic Field Sensors”. In: *Advanced Electronic Materials* 8.6 (2022), p. 2200033.
- [155] R. Kikuchi. “On the minimum of magnetization reversal time”. In: *Journal of Applied Physics* 27.11 (1956), pp. 1352–1357.
- [156] A. V. Khvalkovskiy et al. “Vortex oscillations induced by spin-polarized current in a magnetic nanopillar: Analytical versus micromagnetic calculations”. In: *Physical Review B* 80.14 (2009), p. 140401.
- [157] R. Bjørk et al. “MagTense: A micromagnetic framework using the analytical demagnetization tensor”. In: *Journal of Magnetism and Magnetic Materials* 535 (2021), p. 168057.
- [158] J. E. Miltat and M. J. Donahue. “Numerical micromagnetics: Finite difference methods”. In: *Handbook of Magnetism and Advanced Magnetic Materials* 2 (2007), pp. 742–764.
- [159] A. Vansteenkiste and B. Van de Wiele. “MuMax: A new high-performance micromagnetic simulation tool”. In: *Journal of Magnetism and Magnetic Materials* 323.21 (2011), pp. 2585–2591.
- [160] C. Abert et al. “A fast finite-difference method for micromagnetics using the magnetic scalar potential”. In: *IEEE Transactions on Magnetics* 48.3 (2011), pp. 1105–1109.
- [161] D. Gross and T. Seelig. *Fracture Mechanics: With an Introduction to Micromechanics*. 3rd ed. Berlin, Germany: Springer, 2017, p. 18.